UNIVERSITY OF CALIFORNIA, SAN DIEGO

DESIGN AND MANIPULATION OF 1-D RUGATE PHOTONIC CRYSTALS OF POROUS SILICON FOR CHEMICAL SENSING APPLICATIONS

A Dissertation submitted in partial satisfaction of the requirements for the degree

Doctor of Philosophy

in

Chemistry

by

Brian Henry King

Committee in charge:

Professor Michael J. Sailor, Chair
Professor Judy Kim
Professor Andrew C. Kummel
Professor Jan Talbot
Professor William C. Trogler

2010

The dissertation of Brian Henry King is approved, and it is acceptable in quality and form for publication on microfilm and electronically:

_____

_____

_____

_____

_____

Chair

University of California, San Diego

2010

DEDICATION

In contemplating how to spend my mid-20s, the lure of the unknown pulled me toward the field of sensing. The sensors we encounter in our everyday lives distill the intricacies of physical and chemical interactions to the flash of an indicator light or the whine of a warning siren. Opening the black boxes that are sensors reveals a world of qualifications, thresholds, and probabilities that is reflective of the nuance and complexity of the reality in which we live, yet is built upon basic chemical principles that can be understood and exploited.

This dissertation is dedicated:

To the black boxes that we, in our inattention blindness, walk past every day.
May we illuminate their depths and reap the knowledge that they bring

To the balance of action and reflection,
the arcs, circles, and spirals of personal growth,
and the valiant if quixotic effort to attribute structure to the abstract

To a deeper appreciation of the tyranny of choice, and,

To the universal power of travel to extract the mind from encapsulation

TABLE OF CONTENTS

CHAPTER ONE

CHAPTER TWO

CHAPTER THREE

CHAPTER FOUR

CHAPTER FIVE

CHAPTER SIX

CHAPTER SEVEN

CHAPTER EIGHT

APPENDIX A

APPENDIX B

LIST OF FIGURES

CHAPTER ONE

CHAPTER TWO

CHAPTER THREE

CHAPTER FOUR

CHAPTER FIVE

CHAPTER SIX

CHAPTER SEVEN

CHAPTER EIGHT

APPENDIX A

APPENDIX B

LIST OF TABLES

CHAPTER THREE

CHAPTER FOUR

ACKNOWLEDGMENTS

I offer special thanks: to Professor Sailor for his continual guidance and support, and his infinite patience for the slow churn of my paper drafting machinery; to Jay Snyder for our great collaboration with NIOSH over the years; to Jamie Link for helping me get my first project off the ground; to Andrei Gramada, Adrian Garcia Sega, Travis Wong, Sam Noda, and Anne Ruminski, who I have worked closely with on projects over the years; to Anne Ruminski for making our time in rural Pennsylvannia staring at wildlife more enjoyable, and fielding my endless questions on the finer points of constructing a dissertation; to Manuel Orosco, the life of the party in and out of the office and who always seemed to know the best seminars and events for me to find free snacks; to the first main-office crew of Shawn, Manny, Luo, and Michelle. Hungrily unwrapping Shawn's generous "gift" of half a sub sandwich to discover a lump of powdered sugar is one for the books; to everyone in the Sailor lab who has contributed to my work and growth, especially the crew of gas sensing folks; to Joel Grondek for the many surfing lessons and good times at the beach; to Beniamino Sciacca and Giuseppe Barillaro for their discussions on everything thermal and optical; and to everyone who has been working and contributing to the lab over the years

Chapters two, three, four, five, six, seven and eight are, in part, reprints of the following publications:

King, Brian H.; Ruminski, Anne M.; Snyder, Jay L.; Sailor, Michael J. Optical- fiber-mounted porous silicon photonic crystals for sensing organic vapor breakthrough in activated carbon. Advanced Materials (2007) 19 (24), 4530-4534.

King, Brian H.; Gramada, Andrei; Link, Jamie R; Sailor, Michael J. Internally Referenced Ammonia Sensor Based on an Electrochemically Prepared Porous SiO_2 Photonic Crystal. Advanced Materials (2007), 19 (22), 4044-4048.

Ruminski, Anne M; King, Brian H.; Salonen, Jarno; Snyder, Jay L.; Sailor, Michael, J. Porous silicon-based optical microsensors for volatile organic analytes: effect of surface chemistry on specificity. Advanced Functional Materials (2010) Manuscript accepted for publication and published online July 2010.

King, Brian H.; Wong, Travis; Sailor, Michael J. Discrimination of pure chemical vapors by optical sensing of a thermally cycled rugate porous silica photonic crystal. Manuscript in preparation.

King, Brian H.; Sailor, Michael J. Gas sensing with electrochemically fabricated medium-wave infrared porous silicon optical filters. Manuscript in preparation

King, Brian H.; Noda, Sadafumi; Sailor, Michael J. Thermal desorption of organic vapors from porous silicon films and implications in optical vapor sensing. Manuscript in preparation

Garcia Sega, Adrian; King, Brian H.; Sailor, Michael J. Tunable porous silicon multispectral correlation filters for the remote detection of dipicolinate Manuscript in preparation.

The author of this dissertation was one of the primary authors or co-author on all publications.

VITA

June 2004	B.S. in Chemistry, Department of Chemistry and Chemical Biology, Harvard University, Cambridge, Massachusetts
June 2006	M.S. in Physical Chemistry, Department of Chemistry and Biochemistry, University of California, San Diego
September 2010	Ph.D. in Chemistry, Department of Chemistry and Biochemistry, University of California, San Diego

PUBLICATIONS

1. King, Brian H.; Wong, Travis; Sailor, Michael J. *Discrimination of pure chemical vapors by optical sensing of a thermally cycled rugate porous silica photonic crystal.* Manuscript in preparation

2. King, Brian H.; Sailor, Michael J. *Gas sensing with electrochemically fabricated medium-wave infrared porous silicon optical filters.* Manuscript in preparation

3. King, Brian H.; Noda, Sadafumi; Sailor, Michael J. *Thermal desorption of organic vapors from porous silicon films and implications in optical vapor sensing.* Manuscript in preparation

4. Garcia Sega, Adrian; King, Brian H.; Sailor, Michael J. *Tunable porous silicon multispectral correlation filters for the remote detection of dipicolinate* Manuscript in preparation.

5. Ruminski, Anne M; King, Brian H.; Salonen, Jarno; Snyder, Jay L.; Sailor, Michael, J. *Porous silicon-based optical microsensors for volatile organic analytes: effect of surface chemistry on specificity*. Advanced Functional Materials (2010) *Manuscript accepted for publication, published online July 2010.*

6. King, Brian H.; Ruminski, Anne M.; Snyder, Jay L.; Sailor, Michael J. *Optical-fiber-mounted porous silicon photonic crystals for sensing organic vapor breakthrough in activated carbon.* Advanced Materials (2007) 19 (24), 4530-4534.

7. King, Brian H.; Gramada, Andrei; Link, Jamie R; Sailor, Michael J. *Internally Referenced Ammonia Sensor Based on an Electrochemically Prepared Porous SiO_2 Photonic Crystal.* Advanced Materials (2007), 19 (22), 4044-4048.

ABSTRACT OF THE DISSERTATION

DESIGN AND MANIPULATION OF 1-D RUGATE PHOTONIC CRYSTALS OF POROUS SILICON FOR CHEMICAL SENSING APPLICATIONS

by

Brian Henry King

Doctor of Philosophy in Chemistry

University of California, San Diego, 2010

Professor Michael J. Sailor, Chair

Porous silicon rugate photonic crystals are an attractive optical sensor material due to their high surface area, naked eye response, and controllable optical, morphological, and chemical characteristics. This thesis presents new ways to improve the selectivity, reversibility, and stability against interferents of remotely interrogated porous silicon sensors.

After a brief introduction to rugate porous silicon, Chapters 2-5 present methods of directly sensing the interaction of organic vapors with the porous layer by chemical and physical sensor modulation. A 0.3 mm^2 fiber optic-coupled porous silicon sensor is constructed in Chapter 2 and implanted in a bed of activated carbon, demonstrating carbon bed end-of-service-life sensing. Chapter 3 furthers this concept by incorporating chemically modified sensor surfaces, with selectivity between water vapor, isopropanol, and heptane vapors demonstrated using acetylated and oxidized sensor chemistries.

Chapter 4 introduces physical modulation of the porous silicon sensor, with thermal modulation of the photonic crystal to 160°C employed to rapidly and repeatedly desorb methyl salicylate and octanol vapors that foul the sensor response. Thermal modulation is applied to discrimination of pure heptane, cyclohexane, and isopropanol vapors in Chapter 5 by rapidly cycling a rugate sensor between 25-80°C while exposed to partial pressures of organic vapors up to 7.5 Torr. Sensor responses to the thermally modulated sorption equilibrium allow discrimination of these pure analyte vapors.

The final three chapters describe using porous silicon as tailored interference filters that increase the specificity of standoff optical detection. In Chapter 6, the stop bands of rugate filters are tuned to match mid-infrared molecular absorbance bands, including the 1250 cm^{-1} P=O bond stretch. Standoff gas sensing is demonstrated with filters matched to the 2350cm^{-1} stretch of CO_2. In Chapter 7, selective 2-D imaging of target compounds is demonstrated by matching filters to visible emission peaks of photoluminescent dyes that bind to dipicolinic acid, found in anthrax spores. Finally,

wavelength separated, ratiometric referencing is demonstrated in Chapter 8, where a pH-responsive $NH_{3(g)}$ sensor based on a dye-infused rugate filter with two stop bands encoded into the porous layer is shown to compensate for large fluctuations in probe light intensity and increase signal to noise.

CHAPTER ONE

INTRODUCTION

1.1 Abstract

Porous silicon optical sensors have attracted recent attention as sensitive detectors of chemical and biological compounds[1, 2] due to their ease of fabrication, large surface area, range of accessible surface chemistries[3], and controllable optical and morphological properties including pore size, porosity, and refractive index profile. Chemical vapor sensing has been demonstrated with a variety of porous silicon optical structures, including Bragg mirrors[4], Fabry-Pérot films[5], microcavities [6], and rugates [7]. Rugate structures, used in this work, exhibit a sinusoidal variation of their refractive index with depth [8], resulting in an optical reflection band centered at a wavelength determined by the period and amplitude of the refractive index profile. Infiltration of chemical vapors into the porous matrix displace air from the porous voids, increasing the refractive index of the film and resulting in a red shift of the optical stop band wavelength that enables sensing by monitoring the reflectivity peak wavelength over time[9]. Rugates offer advantages over other porous silicon optical structures that include the ability to monitor sensing with the naked eye, their retention of the sensing characteristics of Fabry-Pérot interference fringes[10, 11], and the ability to construct photonic crystals with tailored optical stop bands that allow their use as optical filters for the indirect sensing of target compounds.

Sensitivity, specificity, and stability against probe light and environmental fluctuations are major challenges facing porous silicon rugate optical sensors that are addressed in this dissertation. This is accomplished by imparting chemical and physical means of class selectivity to rugate structures as direct vapor sensors, and by

tailoring the optical features of rugate-based structures for specificity as indirect sensors and for optical referencing.

1.2 Introduction

Porous silicon optical sensors are readily fabricated by an anodic etching process[12] that allows control of the nanostructure to produce porous layers with desired pore diameters, porosities, and dielectric profiles and with a native surface chemistry that readily modified[3], enabling sensing of a broad range of chemical and biological compounds[1, 2].

First discovered in 1956 by Uhlir at Bell Laboratories[13], porous silicon gained prominence in 1990 when Canham described its room temperature photoluminescence.[14, 15] As early as the late 1980s, Tobias used porous silicon as a humidity sensor[16], but the 1990s saw the rapid growth of studies on the chemical, physical, and optical properties of the material, leading to a variety of sensing applications that have applied both electrical and optical transduction approaches. Point sensors of porous silicon have been employed to detect a wide range of chemical and biological compounds, including NOx[17, 18 19 20], volatile organic compounds (VOCs),[21-24] toxins,[25] polycyclic aromatic hydrocarbons,[26] proteins,[27] DNA[28] enzyme activity[29], and explosives.[30] The high surface area of the porous silicon structure, typically ~200 m^2/cm^3 [4] provides a high density of adsorption and reaction sites amenable to chemical and biological sensing[31], and the material can act as a preconcentrator for analyte vapors due to its nanopore structure[32]. Furthermore, the ability to tailor the optical spectrum of porous silicon[8, 33] has generated interest in its

use as optical filters[34] for the indirect sensing of compounds. Recent years have seen the growth of interest in porous silicon for applications as diverse as high throughput screening[35], biomolecular barcoding[36] and personal respiratory protection[37].

1.3 Porous Si Sensors

Sensors can be classified as direct or indirect[38, 39]. Direct sensors are defined here as those materials that bind, adsorb, or otherwise physically interact with analyte molecules, resulting in a measurable change in the material properties. Direct sensing thus consists of two key steps: binding of analyte molecules, and transduction of the binding event to a measurable signal. An intrinsic property of the analyte may be sensed by transduction through the sensing material response[40], like measuring mass with a quartz crystal microbalance or refractive index by the reflectance of a light beam.[41] Alternatively, the effect of an analyte on a sensing material can be measured, like the material's conductance[42], impedance, resistance, or color.[38, 39]

Indirect sensors, in contrast, do not directly bind to target molecules. Intrinsic properties of an analyte may be measured without direct binding, as with Fourier transform infrared spectroscopy and Raman spectroscopy, which measure the vibrational and rotational energy levels of compounds. The sensing material may also be used as an electrical or optical filter for a separate sensing transducer,[34, 43 44] such as filters for the fluorescence of target dye compounds,[45] with a separate imaging system performing signal transduction. Similarly, an indirect sensor may use a primary sensing material as a trasducer that hosts a second material or compound that directly

interacts with analytes, like fiber optic sensors that monitor the color or fluorescence of a hosted immobilized indicator or label.[38]

Signal transduction with porous silicon sensors has been performed by a variety of methods, including elipsometry,[46] MALDI,[47] and resonance Raman spectroscopy [48]. The most common approaches, however, are electrical and optical transduction of direct porous silicon sensors. Electrical transduction by measurement of changes to the porous silicon capacitance[16, 49] resistance,[50] and impedance[51] have been widely applied to sensing chemical liquids[42] and vapors[17, 52]. Optical transduction gained traction in the 1990s following the discovery of room temperature porous silicon photoluminescence[14, 15], where quantum confinement in molecular wires of nanoporous porous silicon and nanoscale surface effects[53] result in a bright red-orange photoluminescence, corresponding to an energy that is larger than the bandgap energy for bulk Si. Analyte sensing has been performed by monitoring the quenching of the photoluminescence by adsorbates.[22, 54, 55]. Optical transduction by reflectance spectroscopy has also been widely applied to chemical and biological sensing[4, 28, 35, 41, 56-59] The reflection of light off of the interfaces of the porous silicon sensing layer, and off of its internal interfaces from variations in the porous silicon structure, result in optical features that shift in the presence of analytes, detailed in the next sections.

This dissertation focuses on optical reflectance sensing as a means of transduction. This approach requires little or no power to operate, can interrogate the sensor at a distance, and allows placement of the sensing material in environments of electrical interference that would disrupt the response of electrically transduced porous silicon sensors. Porous silicon optical reflectance has been used to sense organic

liquids[41] and solvents[58], biological assays[1 35], and chemical vapors.[4, 60] In the case of rugate sensors, the porous silicon nanostructure exhibits visible optical features and combines analyte binding with transduction and output to the user in a single structure, since analyte-induced shifts in the color of the rugate photonic crystal are visible to the naked eye[61].

The next sections detail the fabrication of porous silicon optical layers, the special characteristics of rugate porous silicon optical structures that are the focus of this dissertation, and the optical transduction of porous silicon sensors by reflectance spectroscopy.

1.4 Optical Vapor Sensing with Porous Si

1.4.1 Etching Mechanism and Sensor Preparation

Porous silicon may be prepared by stain etching[62], photoelectrochemical etching[12], or electrochemical[12] etching of crystalline silicon wafers. The most common approach is the anodic dissolution of single crystalline silicon in a solution of hydrofluoric acid.[12, 31] Electrochemical etching of silicon wafers is one of the simplest and cheapest means to fabricate a nanostructure with complex properties. The electrochemical etch produces a porous layer whose thickness, porosity, and average pore diameters are precisely controlled. Porous silicon is typically prepared by electrochemically corroding a silicon wafer in an aqueous solution containing hydrofluoric acid and ethanol. The process drills network of nanometer-scale holes along the <100> crystallographic direction in the Si wafer. The morphological characteristics of the porous layer are influenced by the electrochemical current

density, the electrolyte composition, and the dopant characteristics (boron or phosophorous doping and dopant concentration) of the wafer, allowing control of pore size from a few nanometers to several microns[12, 31, 63] and the creation of a variety of pore morphologies as well as complex multilayered structures. Microporous (<2nm diameter pores), mesoporous, (2-50nm) and macroporous (>50nm) layers of porous silicon can be fabricated, facilitating sensing of analytes ranging from small molecules to proteins and DNA.[64]

Over the past two decades, a number of theories have emerged on the anodic initiation and formation mechanism of porous silicon[15, 31, 63, 65-67]. Figure 1.1 depicts a commonly reported mechanism for electrochemical dissolution based on the injection and migration of holes in the silicon substrate to the silicon-electrolyte interface. The overall divalent dissolution reaction of silicon with HF can be summarized as:

$$2Si + 6HF + 2h^+ \rightarrow Si\text{-}H + H_2SiF_6 + 2\,H^+ + \tfrac{1}{2}\,H_2 \quad (1.1)$$

The method and sites of pore initiation have been debated[12, 63], with some theories favoring initiation at pits or defect sites on the silicon surface, with the initial width of the regions of pore removal controlled by the silicon space charge layer depth, and thus the applied current density[63]. Once silicon removal has initiated, a commonly reported mechanism for continued removal can be summarized as follows: In the absence of electron holes, silicon hydride is relatively stable in the hydrofluoric acid electrolyte since the comparable electron affinities of hydrogen and silicon result in a resistance to attack by fluoride ions (Step 1, Figure 1.1). A hole that reaches the interface surface, due to the applied current, destabilizes the Si-H bond and allows nucleophilic attack by a fluoride ion (Step 2), forming an Si-F bond. The polarization effect of the Si-F bond

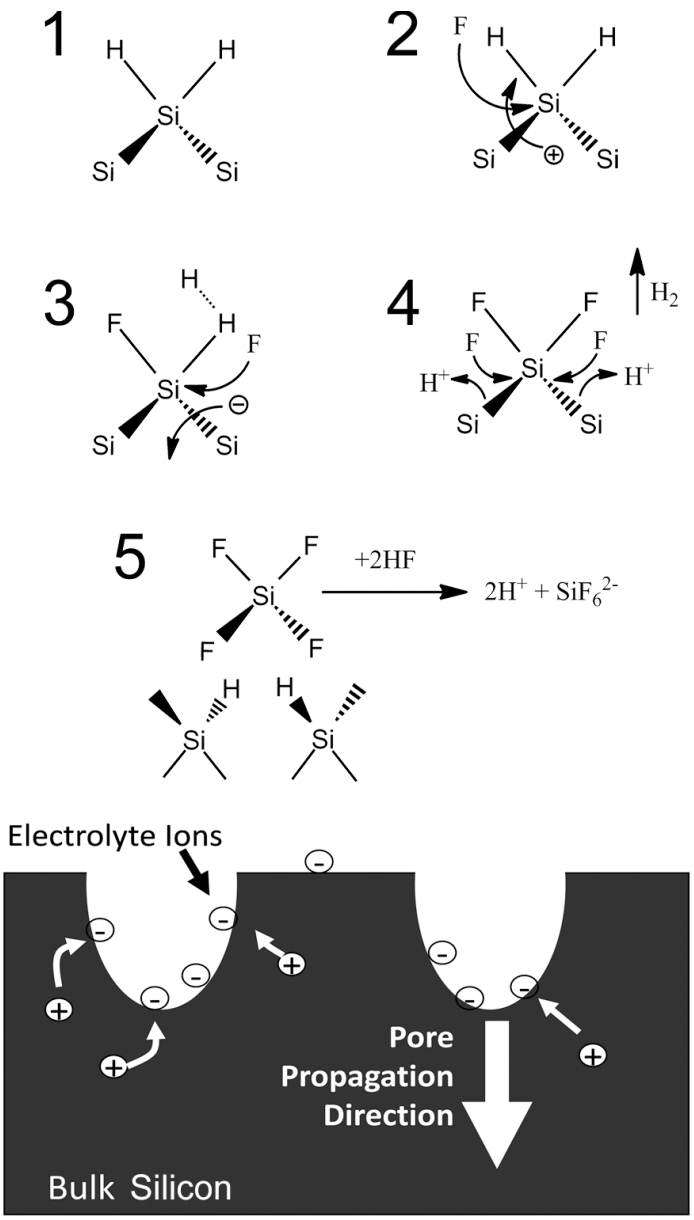

Figure 1.1 Proposed mechanism of micropore formation for the electrochemical anodization of silicon (adapted from reference 12). **Bottom:** cross sectional depiction of the etching process, showing the increase in pore depth with silicon removal.

allows a second fluoride ion to attack the remaining hydrogen bond, with the hydrogens combining to form a molecule of H_2 and resulting in injection of an electron into the substrate (Step 3). The polarization induced by the two Si-F bonds then reduces the electron density of the remaining backbonded Si-Si connections, allowing attack by HF or H_2 and removing the silicon atom from the surface as SiF_4 (Step 4), leaving the formerly backbonded silicon atoms on the surface hydride terminated. The SiF_4 readily reacts with HF to form a highly stable SiF_6^- fluroanion, with the surface returned to its 'passive' state (Step 5) until another hole is made available. Repeated silicon removal results in the growth of pores into the bulk silicon, with the preferential growth direction due to the accumulation of potential at the pore tips, and, as some have suggested[68], due to depletion of carriers from the pore walls.

Etched porous silicon layers can subsequently be removed from the silicon bulk as thin sensing films by electropolishing in a low concentration of HF electrolyte through the application of a pulse of high current density,[12] which removes silicon atoms faster than pores can propagate, detaching the porous layer from the underlying bulk.

1.4.2 Optical Transduction Approaches

1.4.2.1 Common Structures and their Optical Spectra

Since the current density applied to the electrochemical etching of silicon controls both the rate of silicon removal and the width of the porous channels,[12] a variety of optical structures have been fabricated as sensor materials by precisely controlling the current-time waveform of the fabrication process. Chemical vapor

sensing has been demonstrated with porous silicon electrochemically etched to form Bragg mirrors[4, 69], Fabry-Pérot films[5], microcavities[6, 70], and rugates [7].

Fabry-Pérot Thin Films

A Fabry-Pérot porous silicon film is perhaps the simplest of the structures mentioned above, with reflected spectra exhibiting thin film optical interference. A constant current density of the etching waveform results in straight pore channels connecting the top and bottom of the porous layer. These thin films are often referred to as "straight" etches, in contrast to the corrugated pores of rugate structures. The uniform porosity of the relatively straight pore channels results in a uniform refractive index of the layer with depth. Light striking the porous sensor reflects off of the air-porous silicon and porous silicon-substrate interfaces, with the path difference of the two reflected rays resulting in thin film interference, analogous to Bragg diffraction of X-rays in crystalline solids. The reflected optical spectrum, shown in Figure 1.2, consists of a continuous series of fringes corresponding to the periodic constructive and destructive interference of light across the optical spectrum. Fringe maxima are the result of constructive interference, occurring at:[71, 72]

$$2nL=m\lambda_m \qquad (1.2)$$

where (n) is the average refractive index of the porous layer, (m) is the fringe order, (L) the total thickness of the porous layer, and λ_m the wavelength of the fringe. The term (2nL), twice the optical thickness (nL), is referred to as the effective optical thickness (EOT) of the layer. A convenient method of determining the effective optical thickness is a Fast Fourier Transform of the porous silicon thin film's reflectivity spectrum. The Fourier transform of a plot of reflectance versus frequency yields an FFT spectrum

with a peak centered at 2nL, since the absicca of the FFT spectrum is effective optical thickness.

To see why this is so, consider equation 1.2 above for two neighboring fringe maxima at λ_1 and λ_2, which gives:

$2nL=m\lambda_1 = (m+1)\lambda_2$ (1.3)

Solving the two expressions at right for m yields $m = \lambda_2 / (\lambda_1 - \lambda_2)$, which substituted into $(m\lambda_1)$ in the equation above gives:

$$2nL = \frac{\lambda_1\lambda_2}{\lambda_1-\lambda_2} \quad (1.4)$$

Two fringe maxima at wavelengths λ_1 and λ_2 differ by $\Delta\lambda$ in wavelength (nm), corresponding to a difference in frequency (wavenumber, 10^6/nm) of $\Delta f = (1/\lambda_2 - 1/\lambda_1)$. For a reflected light or reflectivity spectrum of intensity versus frequency (wavenumber), a Fourier transform thus computes the frequency of the fringe spacing with respect to spectral frequency, yielding a plot of the intensity of the fringe-spacing frequency versus the fringe-spacing frequency. Since the fringe spacing is Δf with respect to spectral frequency, the frequency of the fringe spacing is the inverse of Δf. The Fourier transform thus computes the fringe spacing frequency:

$$\frac{1}{\Delta f} = \frac{1}{\frac{1}{\lambda 2}-\frac{1}{\lambda 1}} = \frac{\lambda_1\lambda_2}{\lambda_1-\lambda_2} \quad (1.5)$$

which is precisely the quantity 2nL from equation 1.4

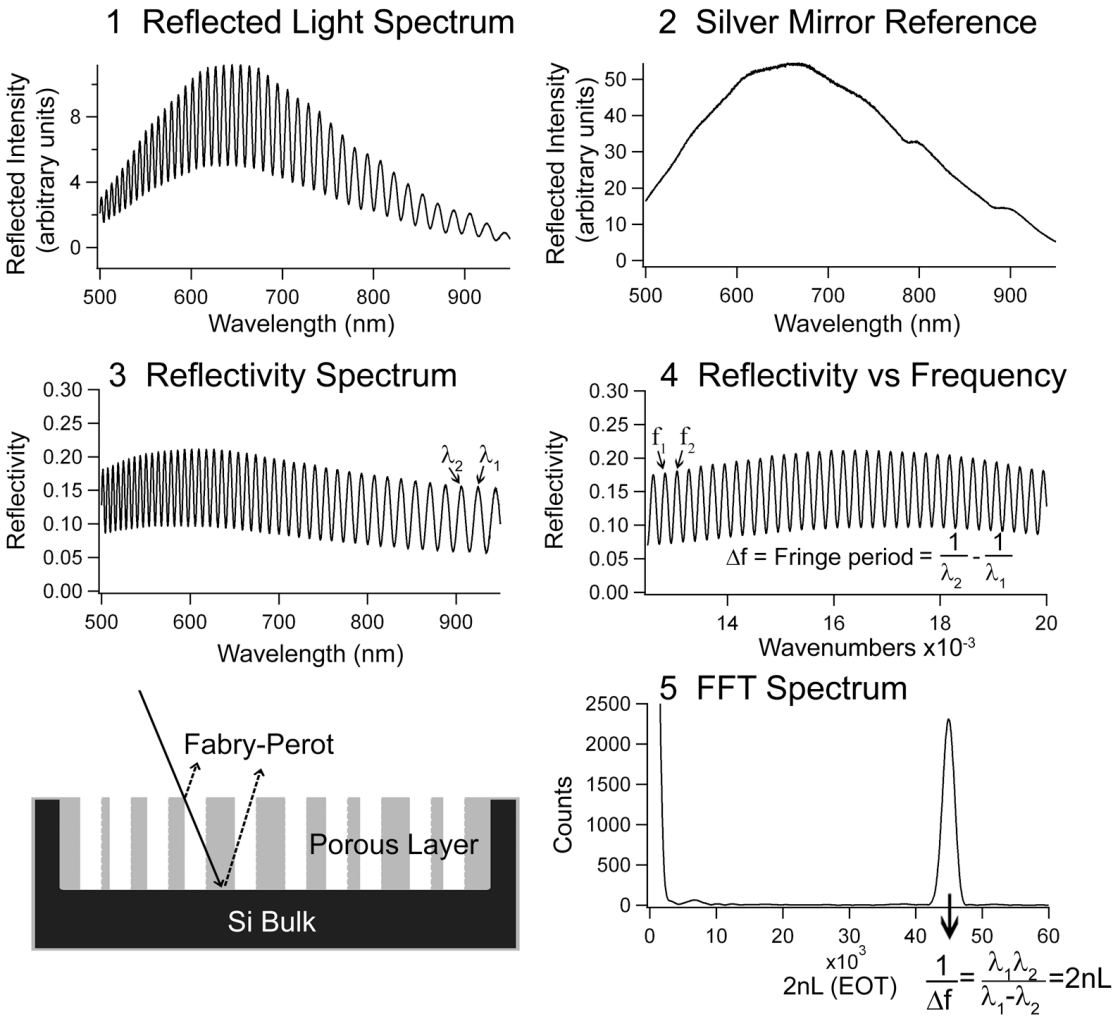

Figure 1.2 Reflectivity spectrum of a Fabry-Pérot thin film of porous silicon, described in section 1.4.2.1 of the text. **(1)** Reflected light spectrum acquired normal to the silicon surface with a broadband light source and CCD detector. **(2)** Silver mirror reflective reference, with a spectral profile due to the responsivities of the optical source and detector across the spectrum. **(3)** Reflectivity spectrum from (1) divided by (2). **(4)** Plot of reflectivity versus spectral frequency (wavenumbers), resulting in evenly spaced interference fringes. **(5)** An FFT of the frequency-domain reflectivity spectrum yields a spectral peak whose position corresponds to the effective optical thickness of the layer, 2nL (nm). **Lower left:** a thin film Fabry-Pérot porous silicon layer experiences interference of light reflecting from the top and bottom interfaces. The pore size is exaggerated for illustration. Incident rays are shown at an angle for illustration; spectra are usually taken at normal incidence.

Rugate, Bragg, and Microcavity Photonic Crystals

A single current density need not be applied over the entire course of an electrochemical etch. Steps of current density over time or continuous profiles of current density with time yield structures with different layers of porosity, and therefore different refractive index profiles with depth. As electrons move through layers of alternating high and low refractive indices, they experience periodic changes in potential as they interact with nuclei, resulting in the formation of allowed and forbidden energy levels referred to as photonic band gaps[73], similar to the way in which the periodic potential in a semiconductor crystal affects the electron motion by defining allowed and forbidden electronic energy bands.

Photonic crystals were first realized in 1987 by Eli Yablonovitch at Bell Communications Research, who by the early 90s had translated his theories into practice in making a photonic crystal by drilling a regular array of holes into a block of material.[73] Such early materials were of interest for their optical properties, but were difficult and time consuming to mechanically manufacture. Since then, photonic crystals have been employed for biological[36, 61] and chemical[4] sensing. Electrochemical fabrication provides an fast and easy means of constructing photonic crystals and tuning their optical properties by controlling the variations in the nanostructure. Unlike mechanical or physical deposition means of creating dielectric photonic structures, electrochemical fabrication of porous silicon can easily create smoothly varying profiles of the dielectric function over the depth of the layer.[8] Modern porous silicon photonic crystals are fabricated by using a computer controlled galvanostat to apply a current density waveform with a temporal resolution of

hundreds to thousands of points per second, allowing such smooth changes in the refractive index of the photonic crystal with depth.

Bragg Stacks

A porous silicon layer etched with a current-time waveform of two alternating current densities results in an A-B-A-B pattern of alternating pore morphology with depth. Bragg reflectors exhibit a relatively broad photonic stop band[39] at wavelengths determined by the depth of each layer and each layer's refractive index. Porous Bragg mirrors have been employed to detect liquids and vapors of chemical and biological compounds[4, 74, 75]

Microcavities

Microcavity structures consist of two Bragg mirrors separated by a defect layer, with the defect corresponding to a sharp dip in the photonic reflectivity band that has been utilized for several chemical and biological sensing applications[6, 70].

Rugates

Rugates were first developed in porous silicon by Berger[76] in 1997, with the term borrowed from biology to describe the corrugated profile of the structures with depth[8]. Although originally used to describe structures with sinusoidal variations in refractive index with depth, the term has since broadened to include any photonic structure with a gradually changing dielectric profile, in contrast to the sharp dielectric interfaces of a Bragg stack.[4, 74, 77] This includes "composite" rugate structures that exhibit multiple spectral stop bands, whose refractive index-depth variations take the form of the superposition of two or more sinusoidal waveforms.[8, 33, 78]

Rugates are not exclusive to porous silicon, and have been developed since the 1980s as optical coatings and photonic switches. A variety of techniques have been employed to create rugates by methods other than electrochemical etching, including evaporation[79, 80], glancing angle deposition[81], reactive sputtering[82], plasma enhanced chemical vapor deposition,[83] and vacuum evaporation[84]. However, these other methods are relatively slow and expensive, and have faced the difficulty of gradually depositing a continuously changing mix of two dielectric materials to obtain the desired profile[8]. Furthermore, while these methods create optical rugate materials, they are not porous and cannot sense chemical and biological species in the direct way that porous silicon can. The low cost and ease of fabrication of complex rugate structures of porous silicon continues to offer an attractive means of creating films with customized spectral features and direct sensing capabilities.

A sinusoidal refractive index variation with the depth of the porous layer results in an optical reflection band centered at a wavelength determined by the period and amplitude of the refractive index profile. Multiple layers of rugates can be fabricated by electrochemical dissolution of porous silicon, with each layer exhibiting separate, tailored optical stop bands, and multiple sinusoids can be combined as mentioned above into composite profiles that exhibit stop bands corresponding to each component frequency[33, 85], like rugate structures with several stop bands that have been used as spectral barcodes.[78]

In the simplest case of a single stop band rugate photonic crystal, a sinusoidal variation in the current density of the etch with time results in a sinusoidal change in the porosity of the porous silicon layer with depth. The porosity can be related to the

refractive index of the layer in air by the Bruggeman effective medium approximation[7, 86]:

$$(1-P)\,\frac{{n_{Si}}^2-{n_{avg}}^2}{{n_{Si}}^2+2{n_{avg}}^2}+\;P\;\frac{{n_{air}}^2-{n_{avg}}^2}{{n_{air}}^2+2{n_{avg}}^2}=0 \tag{1.6}$$

where n_{Si}, n_{air}, and n_{eff} are the refractive indices of the pillars of silicon, air in the porous voids, and average refractive index of the layer, and P the layer porosity. Small changes in porosity are approximately linear with changes in the average refractive index, so a sinusoidal variation of porosity with depth results in a concomitant refractive index variation. Thus, the current-time waveform of the electrochemical etch directly influences the porosity-depth profile and related refractive index-depth profile of the porous layer.

The refractive index variation over the depth of the porous rugate layer can be expressed as[8, 33]:

$$n(z)=n_{avg}+\frac{\Delta n_{avg}}{2}\sin\left(\frac{4\pi n_{avg}z}{\lambda_0}\right)=\;n_{avg}+\frac{\Delta n}{2}\sin\left(\frac{2\pi z}{d}\right) \tag{1.7}$$

where n_{avg} is the average refractive index of the filter, $n_{avg}z$ the optical path length, Δn the variation in refractive index in the undulating layers, λ_0 the resonance peak wavelength of the rugate, and d the spatial period of the index modulation, which is the physical thickness of one period of refractive index variation in the porous layer. The central wavelength of the resonance peak is therefore approximated as[33]:

$$\lambda_0 = 2n_{avg}d \tag{1.8}$$

Changing the period of the current-time etching waveform changes the physical period (d) of the refractive index-depth profile, shifting the position of the photonic stop band. This allows rugate filters to be fabricated with stop bands at wavelengths from the

ultraviolet to the infrared, as shown in Figure 1.3. The figure displays a scanning electron microscope cross sectional image of porous silicon and its corresponding porosity-depth profile and current-time etching waveform profile (notional). The layer spacing in the image corresponds to a rugate whose stop band was in the infrared (Chapter 6), and was chosen to clearly show the periodic variations in porosity, which are imaged as light and dark bands due to the changing electron density between high and low porosities. The bottom panel of the image displays a photograph of a series of rugate etches in air, fabricated with a current density varying between 12.5-50 mA/cm^2 with increasing etch waveform periods from left (blue photonic crystal) to right (red photonic crystal), resulting in an array of photonic crystal colors as the photonic stop band is tailored to positions across the visible spectrum.

1.4.2.2 Advantages of Porous Silicon Rugates

Rugate porous silicon offers several key advantages for chemical sensing. While the spectrally narrow fringes of a Fabry-Pérot layer cannot by resolved without the aid of a spectrometer, the stop band of a rugate photonic crystal imparts the material with a color visible to the naked eye, as shown in Figure 1.3. Rather than performing a Fourier transform of the Fabry-Pérot fringes to obtain the refractive index of the layer, the rugate structure acts as a physical Fourier transform, with the color of the reflected light corresponding to the average refractive index of the layer according to Equation 1.8. The physical Fourier transform of light from the rugate structure is due to the reflection or rejection of light at those frequencies corresponding to the spatial frequency of the refractive index variation. As described in the next sections,

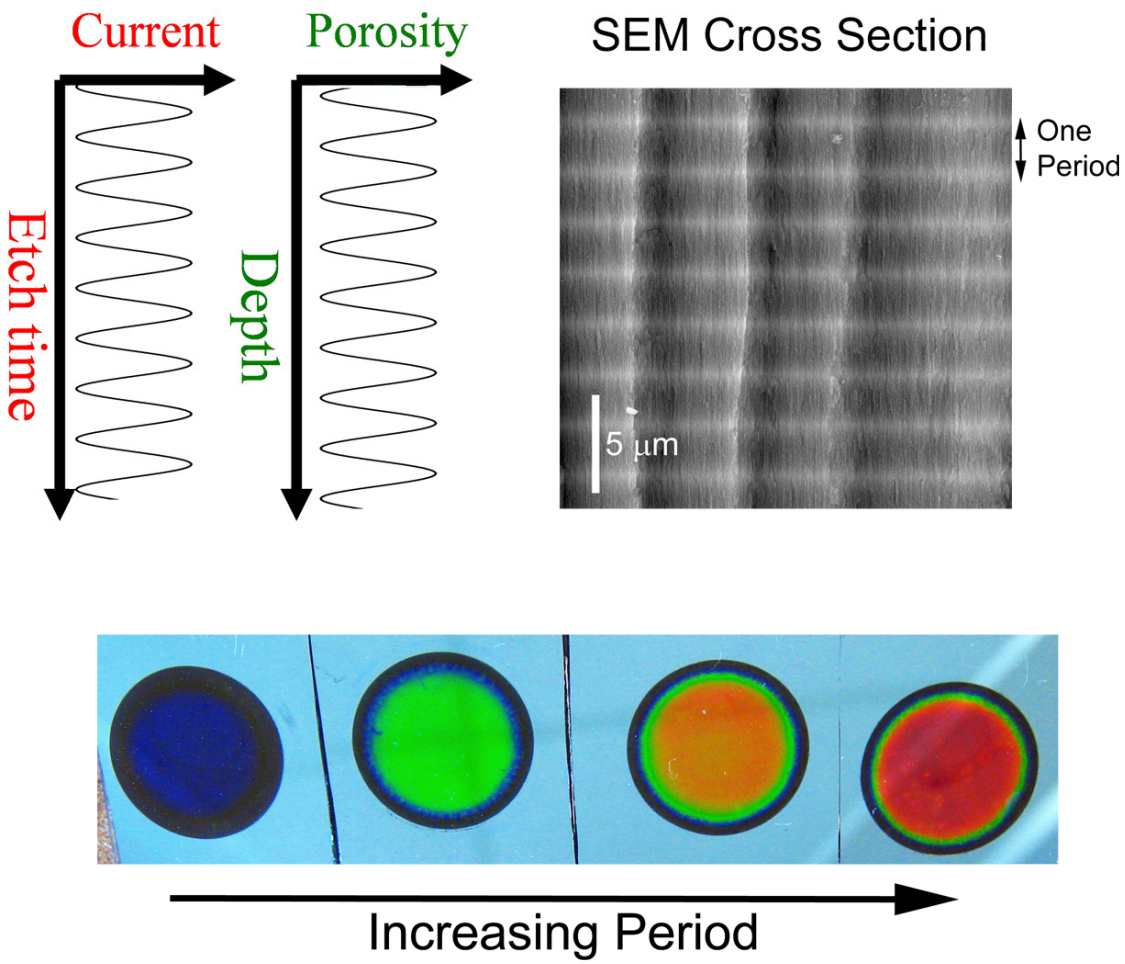

Figure 1.3 Rugate porous silicon photonic crystals. A sinusoidal variation in the current density of the electrochemical etch with time results in a corresponding modulation of the porosity with depth. A cross sectional scanning electron microscope image of a rugate filter (upper right) exhibits horizontal bands corresponding to the cyclic variations in the porosity of the layer with depth. The vertical pore channels (~10nm width) are too small to be discerned at the resolution shown. The structure acts as an optical Fourier transform of the porosity variation, with a single reflectance stop band corresponds to the period of the porosity variation imparting the photonic crystal with a color. Etches with increasingly greater periods of their current-time etching waveforms result in structures with colors that can be tuned across the visible spectrum and into the infrared (bottom). The SEM image shown here is of a structure with a stop band in the infrared, since the long period is more clearly shown in the cross sectional image.

rugate sensors need not be powered, with detection of liquids and high concentrations of vapor analytes possible by visual inspection. For example, visual inspection of rugate sensing has been applied to monitoring biological assays[87].

Second, rugate structures can be constructed to retain many of the sensing modalities of Fabry-Pérot films. As shown in Figure 1.4, the air-porous silicon top interface and porous silicon-bulk bottom interface of the porous layer result in a reflectivity spectrum that is a combination of the Fabry-Pérot interference fringes and the rugate stop band, essentially creating two sensing modalities in one package. Light rays are shown at an angle in the figure for ease of illustration, but in practice reflectance spectra are usually acquired normal to the layer surface. For comparison, the figure also shows the reflectance spectrum of a "straight etch" layer of porous silicon of the same thickness and average porosity as the rugate, but made with an etching waveform with constant current density. The interference fringes can serve as a means of error-checking the response of the rugate stop band to vapors, since both the interference fringes and the rugate stop band will shift with analyte vapor as it changes the average refractive index of the layer. This cross-check was performed throughout the work in this dissertation to ensure that any sudden changes in sensor response were not the result of the data processing methodology of tracking the rugate photonic band position. Additionally, Chapter 5 utilizes the thin film interference fringes of a rugate to relate the spectral stop band to the refractive index of the layer, and ultimately to the volume filling of the porous layer by analytes. Furthermore, in Chapter 6, the visible wavelength fringes of a rugate with a stop band in the infrared are used to determine changes in optical thickness with varying etch conditions. If the interference fringes

are not desired in the optical spectrum, short transition layers at the top and bottom interfaces that match the porous silicon refractive index to that of the interface can be incorporated in the current-time profile[8]. This interface "index matching" has been shown to greatly reduce the reflectivity of the top and bottom interfaces[10, 88, 89] and result in optical spectra absent of Fabry-Pérot interference.

Another advantage of rugates is that unlike Bragg stacks, rugate layers suppress higher order harmonics[72] and can readily by fabricated to produce photonic structures with complex optical features, including multiple stop bands.[8, 33] Chapters 6 and 7 leverage this ability to create multiple features in rugates to match target spectra . The creation of multiple spectral stop bands is also of particular importance to improving the robustness of porous silicon sensors by incorporating optical referencing. While multiple layers of Fabry-Pérot films have been used for signal referencing[71], rugate filters with multiple optical features can be constructed as a single, composite layer by superimposing two or more frequencies in the current-time waveform.[33, 78, 85]. Each superimposed frequency results in a corresponding spectral band. Chapter 8 leverages this creation of multiple rugate bands in the same physical structure to perform signal referencing.

Furthermore, rugate structures are also more robust against the effects of absorbing species that enter the optical path between an interrogating light source and detector. Interferents with gradually changing absorbance over a wide spectral range, such as many scattering species, can affect Fabry-Pérot sensors since the FFT of the spectral fringes will be convoluted by the absorption profile of the interferents.

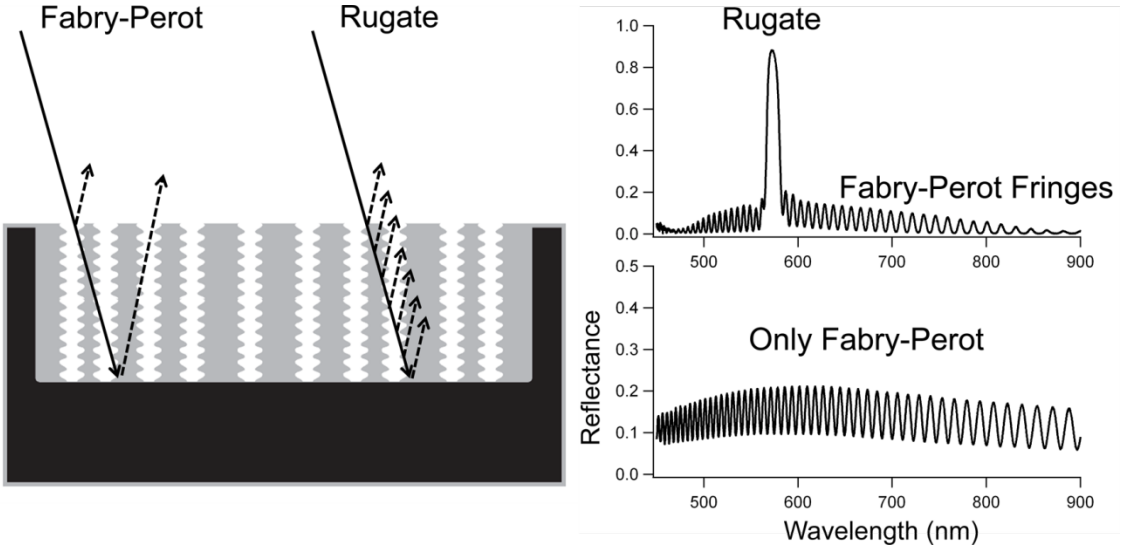

Figure 1.4 Reflectivity spectra of rugate and Fabry-Pérot porous silicon optical layers. **Left:** A rugate layer (grey) on top of the bulk silicon (black) consists of cyclically varying regions of high and low porosity with depth corresponding to the undulations of the pore width. The rugate exhibits both Fabry-Pérot thin film interference, from the air-porous Si and porous Si-substrate interfaces, and a reflectance stop band, from the reflections of light off of each section of the continuously varying interface with depth. **Top right:** a single-band rugate filter exhibits both a spectral stop band and interfacial Fabry-Pérot interference fringes. **Bottom right:** a porous layer anodized with a constant current density over the duration of the etch exhibits only Fabry-Pérot interference fringes.

Although this will affect the intensity of light reflected from a rugate photonic stop band, the spectral wavelength of narrow band rugates will be less influenced by such interferents, since the change in absorption over its narrow spectral region is small.

1.4.2.3 Transduction to Measurable Signal

The reflectivity spectrum of the rugate porous silicon photonic crystal shown in Figure 1.4 was acquired by focusing white light from a tungsten-halogen lamp through one arm of a bifurcated multimode optical fiber, with the common end of the bifurcation focused onto the photonic crystal surface at normal incidence to the porous silicon surface. Reflected light from the photonic crystal is focused back into the bifurcated end of the fiber optic cable with a lens assembly and passes through the other arm of the bifurcation to a spectrometer, which contains a diffraction grating to spread the spectrum of reflected light across a CCD sensor. Each pixel of the sensor thus corresponding to a narrow wavelength bin.

The choice of the light source, optical fiber, optical sensor structure, and detector all influence the reflectivity spectrum. The method described above is a means of white light or low coherence interferometry[39], with the latter term reflecting the characteristic of the light source. Many papers[5, 86, 90] display spectra of reflected light spectra from rugate or other porous silicon structures. It is important to distinguish between these reflected light spectra and true reflectance spectra, though both are valid means of sensing analytes with the porous structures. The former include contributions from the optical system besides the porous silicon film or photonic structure, while the latter are referenced against a highly reflective material

like a silver mirror in order to divide out the effects of the optical system, as shown in Figure 1.2

Without referencing, reflected light spectra, like those recorded with visible-range CCD spectrometer systems from Ocean Optics, exhibit a Gaussian-like or hump-like convolution of the interference fringes. This is due to the combination of the optical components in the system. Specifically, the smooth, increasing curve of the light source intensity over the visible range combines with the decreasing sensitivity of the CCD detector with higher wavelengths as well as the Gaussian-like curve of the grating spectral efficiency in the spectrometer and the relatively constant transmittance of the multimode optical fiber over the visible range. Wavelength response curves of each of these components of light source, transmission medium, and detector components are readily obtained from manufacturer datasheets or factory calibration reports. Additionally, the bottom of the fringes in Figure 1.2 show an additional convolution that "lifts" the interference minima above zero intensity. This is due to reflection and scattering off of the top porous silicon-air interface and to the coherence envelope of the system, which reduces the fringe contrast, referred to as the fringe visibility[39].

Another common low coherence arrangement for low power porous silicon sensors[91], including one built by the author that is described later in the Chapter and shown in Figure 1.8, is to use a light emitting diode (LED) as the spectral source and a photodiode or phototransistor detector. In this arrangement, the spectrum of light emitted by the LED has a Gaussian profile[39]. Phototransistors also have Gaussian spectral sensitivities across wavelengths, but in the visible the detector sensitivity

profile is monotonically increasing. The current passing from the phototransistor source to drain depends on the cumulative sum of the light source, porous silicon modulator, and photodiode sensitivity across all wavelengths, and is typically a logarithmic function of the total irradiance reaching the detector. The voltage response across the phototransistor collector can range from approximately linear to logarithmic with the current, depending on the mode of operation. A higher coherence light source can also be used to interrogate porous silicon photonic crystals by reflecting laser light off of the structure and monitoring the reflected intensity of an interference fringe or the rugate peak,[92] with the voltage response of the detector again depending on the components of the optical system.

More generally, output voltage of an optical system can be expressed as[39]:

$$V = q\left(\int_{\lambda} S(\lambda)F(\lambda)M(\lambda)D(\lambda)d\lambda\right)^{p} \tag{1.9}$$

where S(λ) is the spectral power distribution of the source, F(λ) the spectral transmission of the optical fiber, M(λ) the spectral modulation of the spectral element (the porous silicon photonic crystal), and D(λ) the spectral responsivity of the detector. The parameter p represents the proportionality between the voltage output and the received optical power, and q is a factor for the electronic circuitry producing the voltage. As mentioned, sources may include LEDs, lasers, or white light sources. For a CCD spectrometer, the equation above corresponds to the voltage for each pixel, integrated across that pixel's bin of a narrow range of wavelengths, with the width of the bin determined by the grating or prism in the spectrometer and by other detector optical components. For fiber optic-based sensors, the source, fiber, and sensor

(modulator) terms in Equation 1.9 are first integrated over the length of the fiber, and the integral over wavelengths summed over the modes of propagation in the fiber.[39]

Porous silicon rugate photonic crystals can thus be optically interrogated in a variety of ways. To better understand the sensor response over the entire visible spectrum, this dissertation focus on white light interrogation with spectrometer acquisition over a broad wavelength range. This allows for a comprehensive understanding of the spectral changes in the photonic sensors.

1.4.3 Sensing Motif

The sensing motif of rugate porous silicon is shown in Figure 1.5. In Figure 1.5, a rugate photonic crystal with a single spectral stop band (top of figure) was dosed with a high concentration of toluene vapor. Infiltration of toluene into the porous layer red shifted the stop band and changed the observable color of the crystals from green to red, as shown in photographs of the material before and during dosing.

The direct sensing principal based on changes in the refractive index of the porous layer is similar for rugate, Bragg stack, and Fabry-Pérot structures. In the absence of analytes, the porous layer has an average refractive index consisting of a combination of the index of the silicon matrix and the index of the material in the porous voids, typically air or nitrogen for vapor sensors. Analytes that infiltrate the porous layer and enter the porous voids change the average refractive index. For a Fabry-Pérot thin film, this is detected as a change in the EOT of the layer ($2n_{avg}L$), with the fringes shifting their spectral positions since[5]:

$$2n_{avg} L / m = \lambda_m \quad (1.10)$$

Monitoring the Fourier transform of reflectance spectra therefore allows sensing by monitoring changes in the effective optical thickness, $2n_{avg}L$.

Similarly, analyte infiltration shifts the spectral position of a rugate stop band, since the central wavelength of the reflectance peak corresponds to ($2n_{avg}d$), as given in equation 1.8. [8, 61] Shifts in the rugate stop band can be monitored by white light reflectance spectroscopy[5] by Gaussian fitting the rugate spectral band and monitoring its wavelength over time as analytes are introduced. This sensing methodology has been applied to both chemical[7] and biological sensing with rugate photonic crystals. As pictured in Figure 1.5, large changes in the refractive index due to a high degree of analyte loading into the porous silicon result in spectral shifts of the photonic stop band that are visible to the naked eye as color changes. For instance, Orosco covered a rugate porous silicon photonic crystal with a zein protein layer in an enzymatic assay. Digestion of the protein layer resulted in cleavage products that infiltrated the porous silicon, changing its color in a fast, easy to read assay[93]. Another related approach to sensing with rugate photonic crystals is to monitor the intensity of a laser beam reflected off of one wavelength of the stop band or off of an interference fringe, with changes in intensity corresponding to shifts of the fringe or rugate band[92].

Degree of spectral response to analytes

For liquid analytes that fully penetrate the porous structure, porous silicon acts as a refractometer. In contrast, the spectral response of porous silicon sensors to vapor analytes depends in small measure on the refractive index of the penetrating analyte but is dominated by the effects of surface-analyte interactions that dictate vapor adsorption

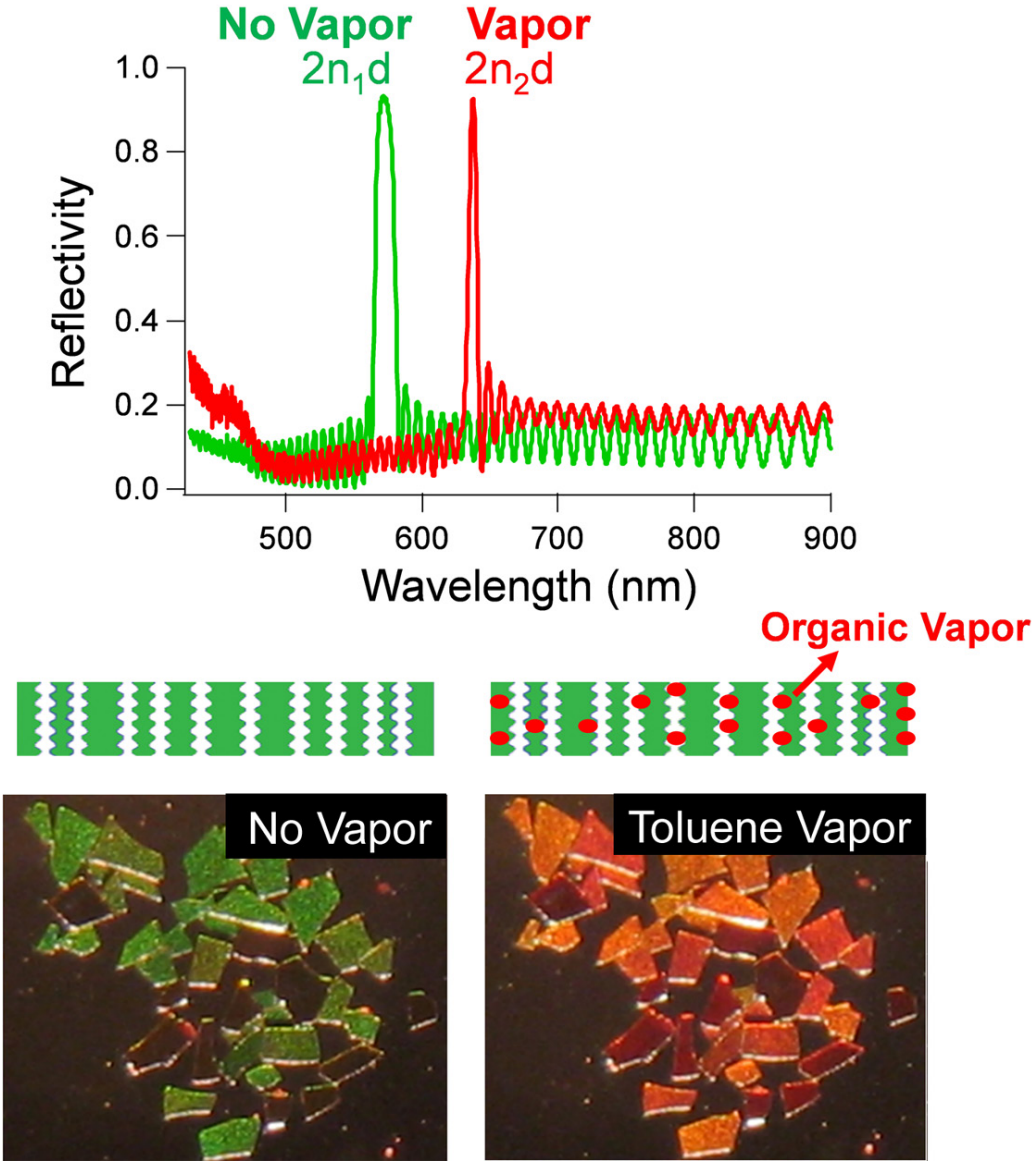

Figure 1.5 Vapor sensing methodology. Vapor or liquid analytes that infiltrate the porous silicon matrix change the average refractive index, n, of the porous layer, resulting in a red shift of the spectral stop band. **Top:** reflectivity spectrum of a porous silicon filter before and after exposure to a high concentration of Toluene vapor. **Middle:** cross section depiction of the pore channels in the filter layer before and after vapor exposure. **Bottom:** photographs of fractured porous silicon rugate photonic crystals and their apparent color in the absence and presence of analyte vapor

into the porous matrix. Similarly, the response of porous silicon sensors in biological sensing can be dominated by the binding efficiency or electrostatic attraction of biological species to the porous silicon surface.[86, 94]

As a refractometer, porous silicon photonic crystals have been used for sensing organic solvents,[7, 95] since for a given class of solvents such as alcohols or alkanes, the pore penetration of liquid analytes is comparable and the sensor response will be dominated by difference in analyte refractive index. The top plot in Figure 1.6 displays the change in the average refractive index of the porous silicon layer as a function of the fraction of the porous volume that is loaded with an organic analyte. More details on this calculation and example programming code are given in Appendix A.4. The relationship between the porosity of the porous layer and the refractive indices of the analyte, silicon, and medium (chosen as air here) is expressed by the three component Bruggeman effective medium approximation as [86]:

$$(1-P)\,\frac{{n_{Si}}^2-{n_{avg}}^2}{{n_{Si}}^2+2{n_{avg}}^2}+\;(P-fP)\frac{{n_{air}}^2-{n_{avg}}^2}{{n_{air}}^2+2{n_{avg}}^2}+\;(fP)\frac{{n_{fill}}^2-{n_{avg}}^2}{{n_{fill}}^2+2{n_{avg}}^2}=0 \qquad (1.11)$$

where f is the volume filling factor, ranging from 0 to 1, and P is porosity, from 0 to 1. The term n_{fill} is the refractive index of the analyte filling the pores, n_{avg} is the average index of the porous layer, and n_{air} is the refractive index of the medium, in this case ambient air. The plots in Figure 1.6 were calculated by using a typical porous silicon porosity of 65% and silicon refractive index of n=4.1, which corresponds to the refractive index of silicon at ~545nm.

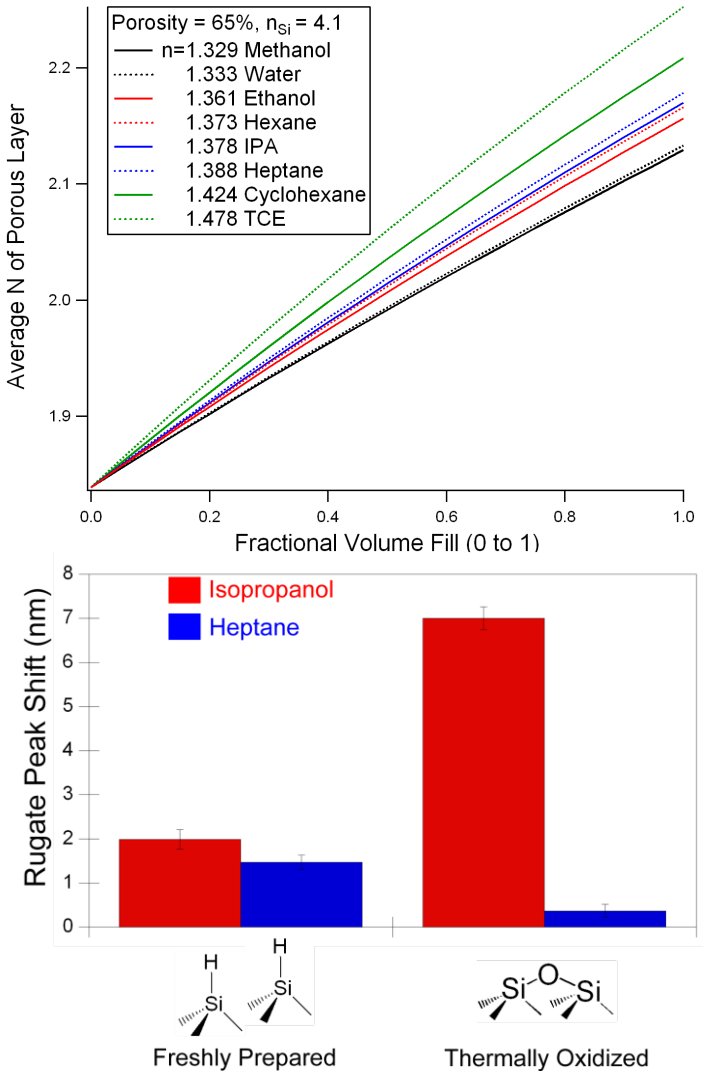

Figure 1.6 Influence of the analyte refractive index and analyte-pore surface interaction on the response of the photonic crystal sensors. **Top:** Infiltration of the pores by analyte vapors increases the average refractive index of the porous layer. The average index is plotted against the fractional volume filling of the pores (1.0 = completely filled) for several analytes (see Appendix A.4). For liquid analytes that fully penetrate the porous structure, the sensor acts as a refractometer, with the degree spectral shift determined by analyte refractive index. For vapor sensors, the surface chemistry of the porous layer drives the response. **Bottom:** Despite having very similar refractive indices, equal vapor concentrations of heptane and isopropanol shift a rugate spectral peak differently depending on the surface chemistry of the sensor, which determines the degree of analyte loading and adsorption. 500ppm of isopropanol and heptane were separately introduced to freshly prepared (bottom left) and thermally oxidized (bottom right) rugate filters and the photonic stop band shifts recorded. Error bars represent one standard deviation over multiple rugate filters tested.

Although isopropanol (IPA) and heptane have similar refractive indices, and thus exert similar shifts on the average refractive index of the layer for a given volume of analyte in the pores, the response of a rugate photonic crystal to the same concentration of the two vapors is dominated by the surface chemistry of the sensor. Sensed as vapors, these analytes have drastically different levels of partitioning and adsorption into the porous layer due to their respective analyte-surface interactions. As shown in the bottom plot of Figure 1.6, surface chemistry is a dominant influence on the response of porous silicon sensors to vapor analytes. While heptane and isopropanol load comparably into the weakly polar, freshly prepared silicon hydride surface of a rugate porous silicon sensor, resulting in similar wavelength shifts of the rugate spectral band for both analytes, a similarly fabricated rugate photonic crystal that has been thermally oxidized to produce a polar pore surface preferentially adsorbs isopropanol over heptane. Rugate porous silicon sensors with modified surface chemistries can thus be used to impart class selectivity, as discussed later in this Chapter and in Chapters 2 and 3.

1.4.4 Sensor Operation and Interface

Transduction of a sensing event yields a raw, measurable signal that is typically processed before providing output to the user, as depicted in Figure 1.7. Processing often includes integrating spectrometer responses over short time segments (typically 5-200msec for the reflected white light spectroscopy configuration described above), averaging spectra to decrease noise, subtracting a “dark” spectrum from each spectrum acquired to compensate for detector noise, and spectral referencing. For Fabry-Pérot

interference fringes, processing may include performing an FFT of the spectrum, Gaussian fitting the result, and plotting and monitoring the fitted peak position over time. For white light interrogation of rugate photonic crystals, this processing may include Gaussian fitting of the rugate spectral band and monitoring the wavelength of the fit over time.

For an LED-phototransistor optical interrogation system, the voltage or current is typically monitored over time. A simple microcontroller can perform basic processing functions, as shown in Figure 1.8. In this figure, a rugate porous silicon photonic crystal with a stop band matched to the spectral emission wavelength of an LED was positioned in the optical path by removing the porous layer from the bulk silicon and gluing it to the polished face of a phototransistor package. The microcontroller was programmed, using the open source Arduino language, to flash the red illumination LED, acquire voltage readings before and during each flash, and subtract the "dark" reading before each flash from the reading under LED illumination as a means of correcting for the ambient light level. In the presence of vapor analytes, the rugate spectral band red shifts, allowing more LED light to strike the phototransistor in the sensor, which changes voltage of the detector circuit. More details are given in Appendix A.1. At preset voltage thresholds, the color of the indicator LED and its pattern of blinking change to indicate the concentration of analyte present. Boards with additional processing functions including averaging and integration of data from other sensors have been demonstrated. This example demonstrates the ease with which rugate porous silicon sensors can be incorporated

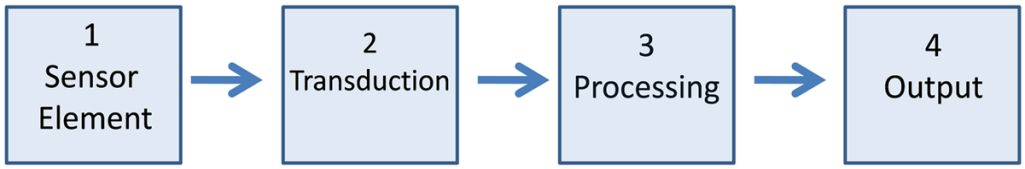

Figure 1.7 The components of a simple optical sensor system consisting of (1) a sensor element like porous silicon, where interaction with the target analyte takes place, (2) transduction of the binding event through changes in the optical spectrum, and detection by an optical detector, (3) processing of the raw signal output, such as Gaussian fitting the spectral peaks, Fourier transforming optical interference fringes, signal referencing, dark spectrum correction, and comparison of the processed value to set thresholds, and (4) output to the user, such as a live plot of processed values, a text display, or indicator lights tripped at predetermined thresholds.

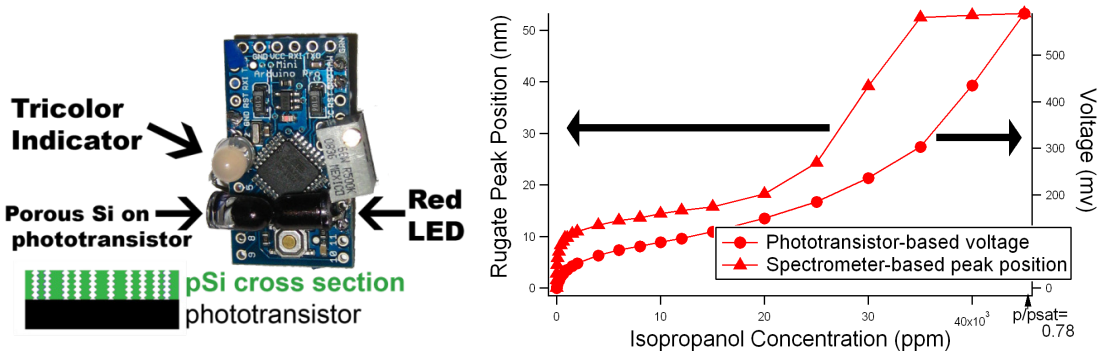

Figure 1.8 **Left:** A porous Si sensor on top of an Arduino microcontroller board powered by a coin cell battery. The Arduino microcontroller acts as the processing step in Figure 1.7. The porous Si film, glued to a phototransistor, senses vapors by changing the amount of light passing through it from an LED illumination source, since the rugate spectral stop band is tailored to match the LED emission band. Vapors that penetrate the porous layer shift the photonic band off resonance with the LED light, allowing a greater intensity to reach the phototransistor. The microcontroller processes voltage readings, performs corrections, and alerts the user when sensor thresholds are met. **Right:** Calibration of the voltage from the board at left to isopropanol vapor concentration (right axis) and comparison to the rugate spectral shift measured by a reflectance off the photonic crystal with a white light source and CCD spectrometer (left axis). See appendix A.1 for details.

into low power, small form factor sensing systems with minimal processing requirements.

The plot at the right of Figure 1.8 shows the influence of the optical system on the sensor response, displaying the difference in the response of the rugate spectral peak position to isopropanol, as determined by white light reflectance with a CCD detector, to the response of the spectral peak as determined by the voltage of the porous silicon-attached phototransistor circuit of the LED-phototransistor arrangement.

1.5 Meeting Optical Sensing Challenges

Ideally, a sensor should exhibit excellent sensitivity, specificity, zero drift, reversibility, and stability against interferents. This dissertation addresses new approaches to improving several of these key components with porous silicon rugate optical sensors. The following sections outline methods and principles in the literature for improving porous silicon optical sensor sensitivity, specificity, and stability.

1.5.1 Sensitivity

Porous silicon has been used to optically sense alcohol vapor concentrations as low as 250ppb, alkanes at ppm levels,[5, 96, 97] and organophosphate chemical agents at concentrations of a few hundred ppm.[98] Proteins in solution have been detected at concentrations of 1pM [27, 99], and DNA at concentrations as little as 2fM[27, 28, 99],

Sensitivity is imparted by the pore size of matrix and by its surface chemistry, which can be modified through simple or extensive functionalization[3]. Sensitivity toward specific analytes, as well as imparting sensors with class-specific sensitivity by

modification of the sensor surface chemistry, is discussed in the next section on selectivity. The extent of both adsorption and capillary condensation of vapors into porous silicon optical sensors are influenced by the surface affinity of analytes the porous matrix, which can be tailored using various chemical modifications [5, 96, 97] detailed later.

Decreasing the pore size of the porous silicon sensor is a key means of improving its sensitivity toward vapor analytes, and can be controlled by changing the current density of the etching waveform[31] and the dopant level of the crystalline silicon wafer[12]. Chemical stain etching [100, 101], which degrades porous silicon without the application of an electrochemical bias, has also been used to create microporous layers with small pore diameters. Although analyte vapors will adsorb onto the surface of meso and macroporous silicon, nanoscale pores possess an additional capability to concentrate a vapor, known as microcapillary condensation.[102] The smaller the pore radius, the lower the partial pressure at which condensation can occur at a given temperature.[103] Microcapillary condensation is a nanoscale phenomenon that provides an additional means of increasing sensitivity by spontaneously concentrating volatile molecules[104]. The pore diameter at which capillary condensation occurs for a given partial pressure of vapor analyte, P, is given by[104]:

$$d = -\frac{4\gamma M}{\rho RT \ln\left(\frac{p}{p_0}\right)} \tag{1.12}$$

where ρ, γ, and M are the vapor density, surface tension, and molecular weight of the analyte and P_0 is the saturation vapor pressure[7]. The smaller the average pore diameter, the lower the partial pressure at which capillary condensation will occur.

This capillary condensation is responsible for the visibly observable, large (~100nm) spectral shifts of the rugate stop band upon vapor exposure that turn green rugate photonic crystals red. An example of this was shown in Figure 1.5.

1.5.2 Selectivity

Porous silicon has been imparted with selectivity toward analytes through a number of approaches. Six approaches to achieving chemical and biological selectivity are described below:

1. Lock and key approach

In this approach to specificity, porous silicon is conjugated to a specific capture probe for a target species[105, 106]. Commonly employed in biosensing, this approach is highly specific and has been used to detect targeted antibodies,[107] aptamers,[59] and complementary DNA strands.[28] Specificity comes with a tradeoff, since a separate sensor must be constructed for each new target analyte, and capture probes that tightly bind their targets can have poor reversibility[105]. An example of this approach was developed by Dancil and coworkers, who attached biotinylated protein A to the surface of porous silicon[59] to specifically detect an antibody, human Immunoglobulin G (IgG). A similar detection scheme was demonstrated by Schwartz et al.[108]

2. Chemically Reactive Surface

The porous silicon surface can directly react with some chemical species, or be loaded with catalysts that react with specific compounds. For instance, Sohn loaded porous SiO_2 micropore channels with a copper ion catalyst[25] for the detection of fluorophosphonate nerve agents, and Rocchia modified ozone oxidized porous silicon

with 3-amino-1-propanol[109], with the resulting amine groups on the sensor surface reactive toward carbon dioxide to form carbamate species. Hydrogen has been sensed with porous silicon by inclusion of a palladium hydrogen trap in the porous layer[110], and hydrofluoric acid has been detected by its reaction with oxidized porous silicon,[111] which degrades the oxidized porous layer leading to a change in porosity, and therefore the average refractive index and spectral properties of the sensor.

3. Physisorption / Surface Interaction

The surface of porous silicon has been extensively tailored due to the large library of reactions available for modifying silicon-hydrogen and silicon-silicon bonds[3]. Methods include hydrosilylation,[112] radical coupling,[113] Grignard reactions,[114] and thermal carbonization with acetylene[115]. One of the simplest surface reactions of freshly prepared porous silicon is oxidation. Freshly prepared porous silicon rapidly reacts with water vapor and oxygen at ambient conditions to form a thin oxide layer that slowly grows with storage time in air.[12, 95] Wet thermal oxidation can control the depth of the oxidized layer from a few atomic layers up to oxidation of the entire nanostructure to form SiO_2 at high temperatures, typically >800°C.[12] The stability and surface hydrophilicity of oxidized porous silicon is used in Chapters 3,4,5,7, and 8, and sensors with a number of other surface modifications are tested for their response to organic vapors in Chapter 3 to impart class selectivity toward volatile organic analytes.

The porous photonic crystal surface chemistry has a profound effect on analyte vapor sorption, but sorption can also be modulated physically by heating or cooling the porous layer. Methods of thermal cycling to discriminate organic vapors have been employed with metal oxide and other sensor types,[116-118] but have not been investigate

with porous silicon. Chapters 4 and 5 examine the effect of thermal modulation on analyte sorption in porous silicon rugate photonic sensors, as well as the ability to discriminate vapors by their thermally modulated optical properties.

4. Size exclusion

The ability to construct layers of porous silicon with different pore geometries has led to molecular selectivity by size exclusion. For instance, Orosco constructed a double layer of mesoporous silicon for this purpose, as shown in Figure 1.9 [93] The upper layer consisted of large ~100nm diameter pores and hosted a protease, while the lower layer consisted of small ~6nm pores that the protease could not penetrate. Upon addition of a substrate, small digestion products infiltrated the lower porous layer, allowing real-time optical sensing and size separation of the digestion products. In addition to stacks of porous silicon layers of different pore sizes, lateral pore diameter gradients of porous silicon have also been fabricated and used for the size separation of molecules.[119]

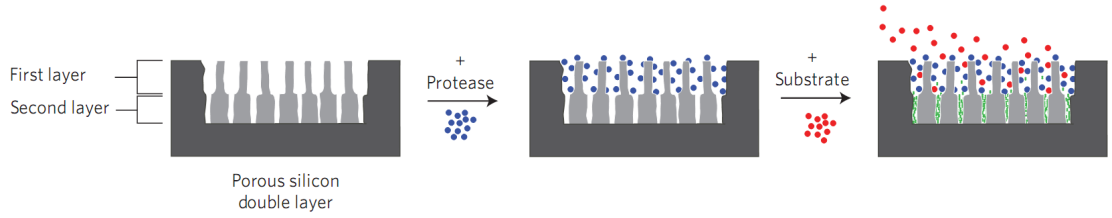

Figure 1.9 Example of achieving selectivity by size exclusion, adapted from reference 92. A double layer of porous silicon was constructed with a top layer of large, ~100nm pores loaded with active protease (pepsin, blue) that is too large to infiltrate the smaller ~6nm pores below. Addition of a substrate (α-casein, red) results in a digestion product that is small enough to penetrate the lower layer. The enzymatic reaction was monitored in real time by optical reflectivity.

5. Arrays

Arrays are central to odor discrimination by the mammalian olfactory system, in which thousands of receptors in the olfactory epithelium send responses through neurons to olfactory centers in the brain for processing[105, 120]. Rather than a ligand-specific receptor for every chemical compound, each olfactory receptor is sensitive toward many analytes, with the aggregate response pattern used to identify odors. Although very few porous silicon arrays have been reported, sensing arrays are commonplace in vapor sensing with other sensing materials[121], including fiber optic bead-based arrays[122], cross reactive metal oxide arrays,[105, 123] polymer arrays of various polythiophenes,[124] carbon black-polymer resistor arrays[125, 126] and thin film acoustic wave microsensor arrays[127]. The lateral distribution of porous silicon pore sizes described above[119] in discussing size exclusion can be considered a lateral array of porous silicon.

In contrast to the arrays described above, which vary the material or coating of each sensor element but use a single transduction methodology, a different type of array-based sensing uses multiple, differing transduction methods and sensing materials. These "arrays" are often referred to as orthogonal sensors, since they combine responses from sensors that use different operating principles, like reflectance sensing with porous silicon, pholuminescence quenching, Fourier transform infrared spectroscopy, Raman spectroscopy, fluorescence detection, ion mobility spectroscopy, mass spectroscopy, surface Plasmon resonance, or other methods. Many high-end commercial sensors consist of multiple, orthogonal sensors packaged together, with the results of each type of sensor pooled and algorithms employed to describe the total

response of the system. For instance, in 2010 Smiths Detection offered the HGVI, a hand-held multi-sensor detector package that combines ion mobility spectrometry, photo ionization detection, and Taguchi gas sensors (metal oxide sensors). Orthogonal methodologies help to reduce false positives, since interferents affects one type of sense may have no effect on a different sensing methodology.

6. Indirect Sensor Leveraging other Materials or Techniques

Porous silicon can be used as a high surface area host for analytes, with sensing specificity and transduction accomplished by methods not involving the porous layer. For instance, it has served as the matrix in matrix-assisted laser desorption/ionization (MALDI),[47] and porous silicon hosting silver nanoparticles has been used for sensing by surface-enhance Raman spectroscopy[128]. Alternatively, porous silicon can used both as a host material and to perform optical transduction, but as an indirect sensor that does not directly interact with target analytes. For instance, the porous layer can serve as a host for an indicator dye, as is done with a multi-band rugate photonic crystals of porous silicon in Chapter 8.

The passive optical properties of porous silicon can also be used in conjunction with another optical transducer. In Chapters 6 and 7, sensing specificity is imparted by tailoring the passive optical spectral properties of rugate-based porous silicon filters. The filters do not transduce the presence of target molecules directly. Instead, they are placed in the beam path of other optical detection methodologies. In Chapter 6 the passive optical properties of rugate filters are used in conjunction with FTIR to impart specificity toward target compounds by matching infrared vibrational bands, and in

Chapter 7 tailored filters matching fluorescence dye spectra are used in conjunction with a visible spectrum digital camera sensor.

1.5.3 Referencing and Stability to Interferents

Fluctuations in probe light intensity, absorbing or scattering species in the optical path, and changes in temperature, pressure, or humidity can all affect the sensor response of porous silicon optical sensors and lead to false positives. Optical referencing or "ratiometric" sensing can be accomplished in several ways.

Fiber optic sensor systems, for example, commonly employ temporal, frequency, spatial, or wavelength separated referencing.[39] The last two methods are most commonly used with porous silicon optical sensors. In spatially separated referencing, a reference channel is physically distinct. Numerous configurations are possible, but typically involve splitting light from the illumination source to a separate reference detector, bypassing the sensor, or using a duplicate interrogation source, sensor, and detector in a physically separate reference channel, with the sensing element in the reference channel sealed and unable to interact with analyte vapors but experiencing temperature or other changes to be mitigated by referencing.[38, 39]

In wavelength separated referencing, the signal and reference channels often share the same optical path, but correspond to different spectral features at separated wavelengths. This simplifies the referencing approach, and ensures that interferents or probe light fluctuations are experienced by both the signal and reference channels. Two examples of referencing with electrochemically fabricated porous silicon are given in Figure 1.10 and 1.11. As shown in figure 1.10, Pacholski and coworkers constructed a

self-referencing double layer of porous silicon. The top "signal" layer was functionalized with protein A and used to sense the binding of IgG, while the bottom "reference" layer provided a means of eliminating the effects of nonspecific binding.[71] In another example, a double layer rugate stack was constructed by Ruminski[90], shown in Figure 1.11, as means of referencing the porous silicon optical sensor response to variable relative humidity. The upper rugate layer in the figure was etched and modified by hydrosilylation with 1-dodecene, with the lower layer modified with undecylenic acid. Both layers were stabilized by electrochemical grafting of $-CH_3$ groups, resulting in a hydrophobic upper layer and hydrophilic bottom layer. The differential in the responses of the two layers allowed sensing of volatile organic vapors in variable levels of relative humidity, with the response to humidity eliminated by referencing one layer's response to the other.

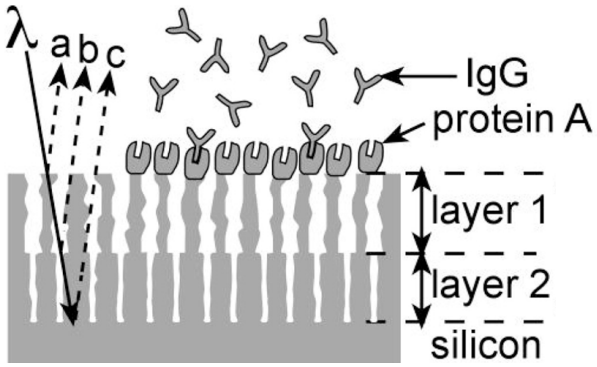

Figure 1.10 Example of signal referencing with a double layer of porous silica,[71] adapted from reference 70. Protein A was immobilized to the surface of the top layer, with its binding to IgG detected by changes in the reflectivity of the top layer. The bottom layer was not functionalized with protein A and served as a referencing channel for nonspecific changes

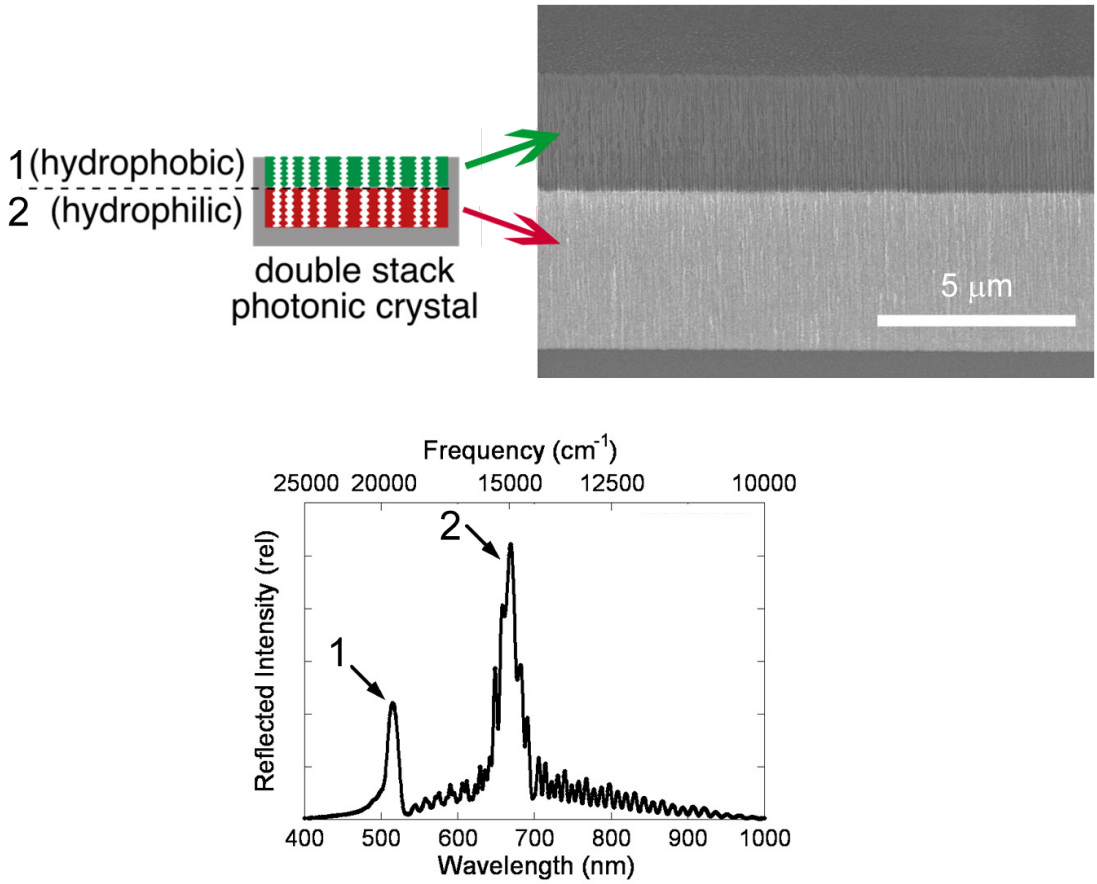

Figure 1.11 Example of vapor sensor referencing for the compensation of humidity using a double layer of rugate porous silicon composed of a hydrophobic and hydrophilic layer[90]. Adapted and redrawn from reference 89. Top left: cross sectional depiction of the double layer stack. Top right: cross sectional SEM image showing the two distinct layers. Bottom: reflected light spectrum of the double layer stack, with one rugate stop band corresponding to each of the layers.

In the examples above, double layer stacks of porous silicon were used as signal and reference layers. Chapter 8 improves upon this by investigating a composite porous silicon rugate structure fabricated with a current-time etching waveform composed of the superposition of two sine waves with different frequencies, resulting in a single porous silicon layer that exhibits two spectral stop bands. This structure enables wavelength separated signal referencing in which the signal and reference channels are not just in the same optical path, but are encoded into the same layer of material. While each layer in a double layer stack may experience different interferents, the composite layer ensures that the signal and reference channels experience uniform effects.

Finally, another method of avoiding interferents in the optical path is to reduce the segment of the optical path open to air. Rather than directing light from a bifurcated fiber through air, nitrogen, or a biological medium to the sensor surface, films of rugate porous silicon may be directly attached to optical fibers, greatly reducing the effects of any transient absorbing species in the optical path. The next Chapter introduces a porous silicon-coupled optical fiber that couples interrogating and reflected white light directly into a porous silicon sensing layer that is coupled with epoxy to an optical fiber.

CHAPTER TWO

OPTICAL FIBER-MOUNTED POROUS SILICON PHOTONIC CRYSTALS FOR SENSING ORGANIC VAPOR BREAKTHROUGH IN ACTIVATED CARBON

2.1 Abstract

The following four chapters explore the capabilities of rugate porous silicon photonic crystals to act as direct sensors for organic vapors, with the porous layer acting as the recognition element that reversibly adsorbs target analytes and as the means of optical transduction of the sensing event. Here, a microsensor for volatile organic compounds (VOCs) was prepared by adhering a 0.5 mm-diameter porous Si 1-D photonic crystal to the distal end of an optical fiber. The photonic crystal was prepared by programmed electrochemical dissolution of Si in an aqueous hydrofluoric acid and ethanol electrolyte. The wavelength of the reflected stop band from the photonic crystal shifts to the red when a volatile organic species enters the porous matrix. The optical fiber-based porous Si sensor responds to a broad range of VOCs (isopropanol, cyclohexane, and trichloroethylene), and exhibits a relatively low response to water vapor. The microsensor can be embedded in an activated carbon filtration bed, providing a means to monitor near end-of-service-life by responding to the breakthrough of organic vapors in advance of their detection in the effluent by gas chromatography. This chapter describes the construction, vapor response, and implications of these freshly prepared porous silicon optical layers coupled to optical fibers. Following this, Chapter 3 extends these observations to study chemically modified porous silicon surfaces for inducing specificity of the optic fiber-coupled sensors to classes of analytes.

2.2 Introduction

Fiber-optic-based sensors have been applied to a variety of remote sensing problems: measurement of pressure, humidity, vapor-phase chemicals, and aqueous biomolecules are leading examples[39, 129-133]. With a width of only a few tens to hundreds of microns, these sensors require little power to operate, are impervious to electrical interference, and can be multiplexed together into distributed sensor configurations[39, 130, 132]. Fiber sensors may be extrinsic or intrinsic, depending on how the measured parameter is optically transduced[39]; intrinsic sensors, like interferometric and Fabry-Pérot cavity devices, leverage the fiber's inherent optical properties to transform a parameter such as mechanical stress into an optical signal [131, 134, 135]. Extrinsic sensors, such as bead-based arrays[129] and polymer caps[133], immobilize an indicator or label on the distal end of the fiber, using only the light-carrying capability of the fiber to transduce the sensor signal. In this work, an extrinsic sensor for volatile organic compounds (VOCs) is created by adhering a 0.5 mm-diameter porous Si photonic crystal to an optical fiber. Remote sensing with such a device is demonstrated by detecting breakthrough of VOCs in an activated carbon filtration bed.

There is a growing need for sensors that can monitor the residual adsorption capacity of activated carbon filtration cartridges in gas masks and other personal protective equipment[136]. Typically, these sensors operate by detecting organic vapors as they break through a filter bed of activated carbon. Despite advancements in end-of-service-life sensor technologies[130, 137, 138], the need persists for a very small, low-power, and cost-effective sensor. In the United States, government health and safety regulations require the detection of VOCs prior to depletion of the carbon bed's

adsorption capacity, yet these regulations have not yet been enforced due to a lack of suitable sensing devices[139, 140].

2.3 Experimental

2.3.1 Sensor construction

Porous Si samples displaying a single spectral reflectance peak were prepared from single-crystal, (100)-oriented highly boron-doped p-type Si (Siltronix, 1.0-1.2 mΩ-cm resistivity) by electrochemical etching in a 3:1 v:v solution of aqueous hydrofluoric acid:ethanol (49% hydrofluoric acid from Fisher Scientific, Inc). Etching was performed in a Teflon cell with a platinum mesh counter electrode and a galvanostat (Princeton Applied Research Model 363) under computer control (LabView, National Instruments). The current waveform was sinusoidal, with a period of 6.9 s, varying between 10 and 50 mA/cm^2, applied for 75 cycles (518 s). The porous layer was detached from the bulk Si by applying a current of 2.7 mA/cm^2 for 2 minutes in a 3.3% hydrofluoric acid:ethanol solution.

2.3.2 Optical Fiber Selection and Preparation

Although vapor sensing with porous silicon has been performed by laser interferometry at specific visible and near-infrared wavelengths[92], white light reflectance spectroscopy was employed here to more completely understand the optical response of the sensor to analyte vapors across the full visible spectrum. Multimode optical fiber was therefore selected. A low hydroxyl content fiber was chosen for its more consistent transmittance profile across visible wavelengths. Fiber with a

relatively large diameter (600 μm core, low OH, Thorlabs Inc.) and wide numerical aperture (0.48) was selected for ease of fabrication and coupling of light, both between the optical fiber and the porous Si layer and between the proximal end of the optical fiber and distal Y-branch of the bifurcated fiber leading to the light source and CCD detector. Attachment of the porous layer was performed by first scoring the fiber with a diamond scribe, cleaving the fiber, stripping the polymer jacketing at both ends (Thorlabs T28S48), and preparing each cleave by polishing with progressively finer aluminum oxide micron lapping sheets (Thorlabs). Transparent 30-minute epoxy was (Devcon No. 14310) was partially cured for 20 minutes to prevent full epoxy infiltration into the porous layer, then applied to the prepared fiber and coupled to the porous Si film. Attached porous layers were cured in air for 24 hours, then coupled to the fiber optic interrogation system by threading the proximal end of the fiber sensor into an SMA bare fiber terminator (Thorlabs) that in turn coupled to the distal end of the Y-branch bifurcated optical assembly, picture in Figure 2.1. Coupling to the optical interrogation system by direct end-to-end butting of SMA cables is less efficient than precision angular fiber cleaving and splicing[39], but for the short distance of the fiber sensor presented here and high intensity of the tungsten-halogen light source such losses did not affect fiber performance, and had a negligible effect on the signal to noise of the CCD detector. Scanning electron microscopy was performed on gold-sputtered porous silicon samples using an FEI Quanta 600 instrument. Thickness measurements were taken by examining cross sections of the porous layers, as shown in Figure 2.2 (bottom).

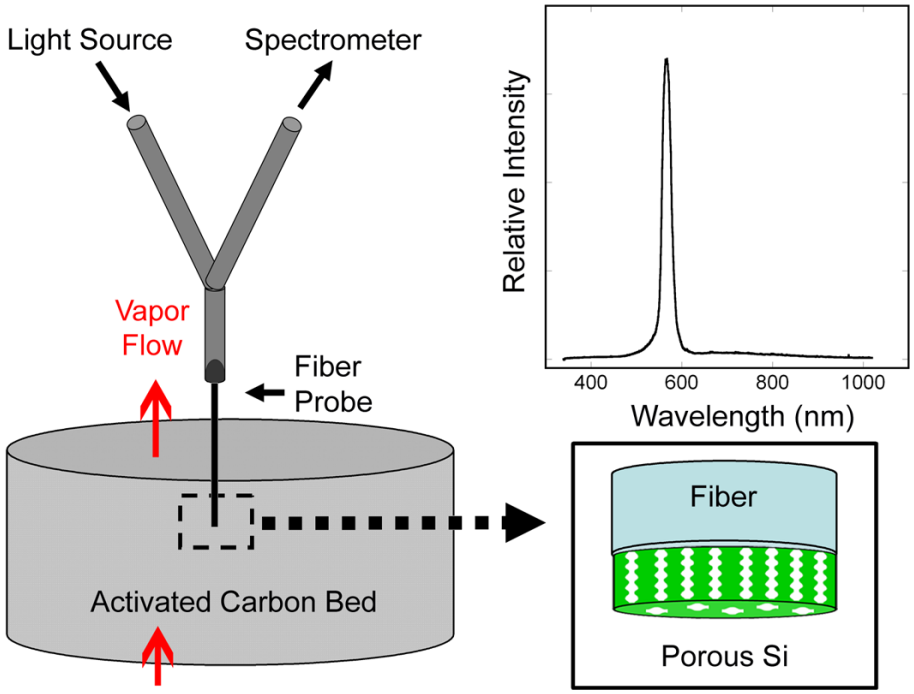

Figure 2.1 Diagram depicting the experimental setup for the in-situ monitoring of VOC breakthrough in an activated charcoal filtration bed. A porous Si photonic crystal is attached to a silica-core optical fiber (bottom right) and embedded in an activated carbon bed (left). A spectrometer monitors the reflected light spectrum from the photonic crystal (upper right). A red-shift in the spectrum is indicative of the presence of free organic vapors in the carbon bed.

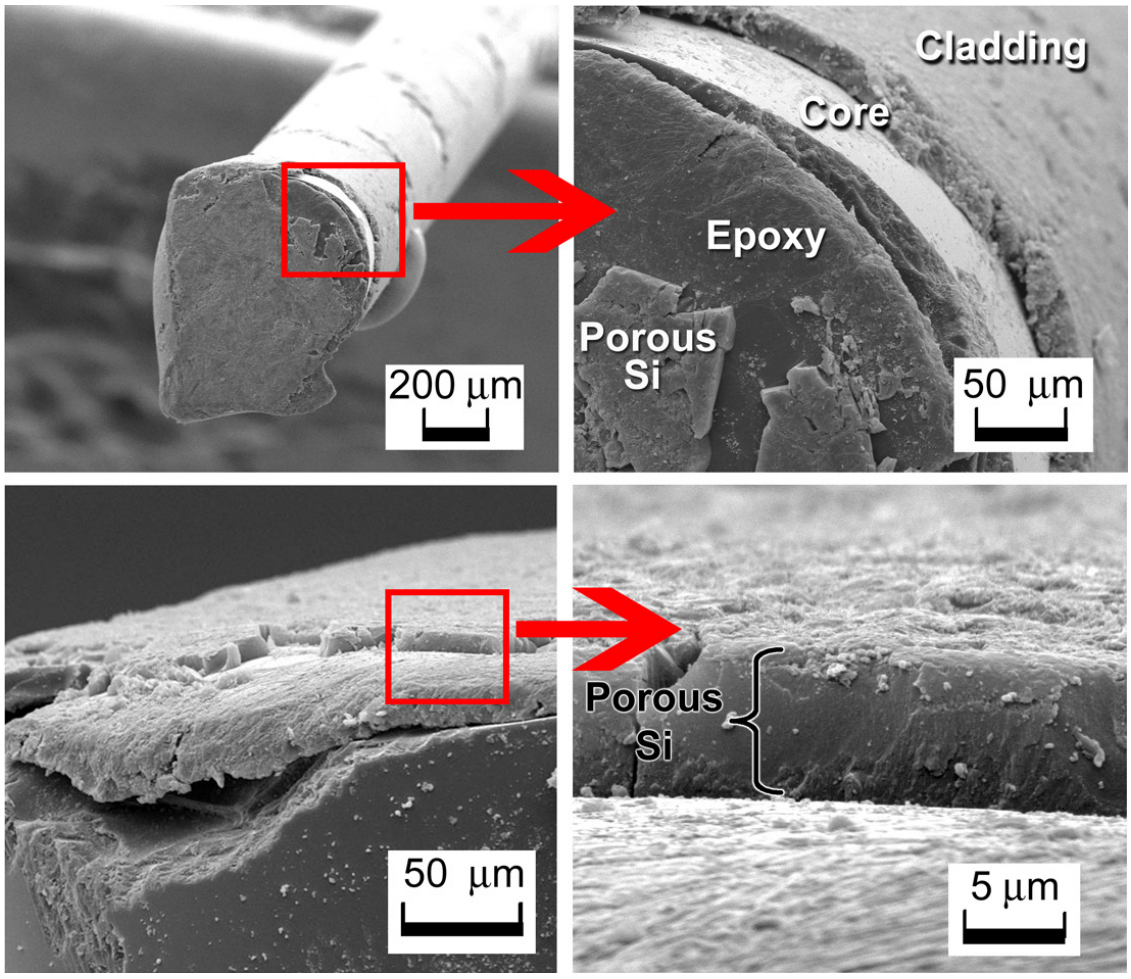

Figure 2.2 Scanning electron micrographs of porous Si attached to an optical fiber. The porous Si film, epoxy layer, optical fiber core, and optical fiber cladding are shown in the upper right image. The lower panel images show a profile, cross sectional view of the attached porous layer on top of the epoxy. An image of a poorly cleaved region of one of the optical fibers is shown at lower left since it more clearly shows the individual sections of optical fiber, epoxy, and porous silicon.

2.3.3 Vapor Dosing Measurements

The optical fiber with attached photonic crystal sensor was inserted into a glass ampoule filled with activated carbon and placed in a computer-controlled dosing system. A nitrogen carrier gas flow rate was set to 1 L/minute using a mass flow controller (Escort LC pump, MSA). Analytes were injected with a low-volume liquid flow pump (Valco M6) into a metal (Swagelok) T-junction. The junction was wrapped in heating tape and maintained at 50 ºC with a PID controller (RKC Rex D100) using feedback from a thermocouple probe. A short length of polypropylene tubing connected the metal T-junction to the carbon ampoule, with the ampoule outflow connected to a separate plastic T-junction, pictured in Figure 2.4. Each glass ampoule contained two sections (100 mg and 50 mg beds) of activated carbon (Anasorb coconut shell carbon, SKC Inc.) separated by glass wool with the fiber probe positioned between the two sections (referred to as mid-bed in the text); the longer 1.5 cm carbon packing containing 100 mg of carbon was connected to the analyte inflow, while the shorter length of packed carbon containing 50 mg of carbon was emptied for fiber insertion and repacked to a length of 0.9-1.1 cm. Gas chromatographic (SRI 8610) sampling of the effluent gas was performed downstream of this second section of bed. The optical fiber ran through the length of the junction and into the ampoule, with the outlet of the junction packed with glass wool to keep the carbon in place. The proximal end of the optical fiber was coupled to the distal end of a Y-branch bifurcated optical fiber (600 micron core, Ocean Optics Inc.) with a fiber coupler (Thorlabs). A tungsten halogen light source (Ocean Optics LS-1) illuminated one Y branch of the

bifurcation, with a spectrometer (Ocean Optics USB2000) monitoring the reflected light from the other branch, as illustrated in Figure 2.1.

2.3.4 Data Processing and Analysis

For each run, the sensor reflectance spectrum and gas chromatographic response were recorded simultaneously on separate computers. Collection began several minutes before analyte introduction to establish a baseline response. The same fiber-coupled sensor was inserted into a fresh ampoule of carbon for each trial. Reflectance spectra were recorded every 9 s and gas chromatographic readings were obtained every 2 minutes. GC and reflectance spectral files were matched with their computer time stamps, and the spectra (Figure 2.4) were zeroed horizontally such that time zero corresponds to the introduction of analyte flow in each run. Each reflectance spectrum collected (example shown in Figure 2.1) was fit with a Gaussian function using the data analysis and plotting program Igor Pro (Wavemetrics, Inc.) to determine the peak wavelength (λ_{max}). In Figure 2.3, the fiber optic sensor response to the various analytes was characterized with no activated carbon present. In Figures 2.4 and 2.5, the fiber probe was inserted into carbon ampoules, and the shift in the peak wavelength was plotted as a function of time alongside plots of concentration determined from the GC.

2.4 Results and Discussion

2.4.1 Fabricating a Sub-millimeter Sensor

The porous Si photonic crystal was prepared by electrochemical dissolution of boron-doped p++ Si in a solution of aqueous hydrofluoric acid and ethanol. The current density applied during this process affects the pore size and porosity of the resulting structure[24, 35, 61]. A photonic crystal generated by application of a periodic current waveform yields a porous layer with spatially varying porosity in the z-direction (normal to the wafer surface). In the present work, a sinusoidal waveform is used, and the resulting samples display a single sharp spectral reflectivity peak (top right plot of Figure 2.1), at a wavelength determined by the periodicity of the refractive index in the porous layer [85, 141]. The porous Si photonic crystal film was removed from the Si wafer using an electropolishing reaction[35, 61]. It was rinsed gently with ethanol, dried at ambient temperature with a stream of pure N_2, and affixed to the end of a cleaved silica-core optical fiber with transparent epoxy. A scanning electron microscope image of the resulting sensor structure is shown in Figure 2.2. The thickness of the porous Si sensing layer is 8 microns, with a diameter of ~500 microns.

2.4.2 Sensing Motif

The wavelength of the reflectance peak maximum, λ_{max}, is influenced by the refractive index of the periodic porous structure. Displacement of air in the pores with an organic compound results in a red shift in λ_{max} [9, 97]. In order to characterize the dose-response behavior, spectra are obtained by introducing white light into one arm of a bifurcated optical fiber, and measuring light reflected from the porous Si sample in the

other arm with a spectrometer as shown in Figure 2.1. The sensor was placed in a chamber with a continuous stream of nitrogen, and controlled concentrations of analytes were introduced upstream of the sensor chamber by means of a precision liquid pump (Milligat, GlobalFIA). The liquid injection zone was heated to ensure complete vaporization and mixing of the analyte in the gas carrier stream.

2.4.3 Response to Vapors

The responses of the sensor to vapors of the four analytes isopropyl alcohol (IPA), cyclohexane, trichloroethylene (TCE), and water using nitrogen as a carrier gas are presented in Figure 2.3. The concentrations of each of the organic analytes were verified with a gas chromatograph whose sample inlet was connected to the sampling chamber. The photonic crystal is sensitive to a broad class of organic vapors, and the high surface area of the porous layer provides sensitivity toward many adsorbates[61]. For the organic analytes tested here, the relative sensor response, measured as the slope of the concentration-$\Delta\lambda_{max}$ curves of Figure 2.3, is IPA > TCE > cyclohexane > H_2O, corresponding to slopes of 1.52, 0.37, 0.27, and 0.06 nm per 1000 ppmv respectively). The magnitude of the expected red shift ($\Delta\lambda_{max}$) depends on both the refractive index and the amount of analyte captured in the porous matrix. The amount of a particular analyte captured is directly related to the relative affinity of the surface for the analyte and inversely related to the vapor pressure of the analyte [5]. In general, analytes with lower vapor pressures will exhibit a greater affinity for a surface. Indeed, the observed trend in $\Delta\lambda_{max}$ tracks inversely with analyte vapor pressure for the organic molecules

studied; the values of the saturation vapor pressures of IPA, TCE, and cyclohexane at 20 °C are 31, 59, and 78 Torr, respectively[142].

Water, with a vapor pressure of 17.5 Torr at 20 °C, is predicted to display the largest value for the slope of the concentration-$\Delta\lambda_{max}$ curve. However, H_2O displays the smallest slope of the series depicted in Figure 2.3. The response of porous Si sensors to different analytes has been shown to be somewhat dependent on surface chemistry [97]. In the present case, the freshly-prepared porous Si films are hydrogen-terminated, although the processing steps generate a mixed hydride-oxide surface. This surface is relatively hydrophobic. The very weak response to H_2O is indicative of the very low affinity of the hydrophobic porous Si surface for H_2O, [22] and underscores the importance of a stable surface chemistry in determining sensitivity for this type of sensor [97]; continual exposure to an ambient environment gradually oxidizes the as-prepared porous Si surface and increases the H_2O response relative to organic vapors.

The observed trend in sensitivity of the sensor towards the different analytes also corresponds to a trend in decreasing solvent refractive index: TCE (n = 1.4773) > cyclohexane (1.4235) > IPA (1.377) > H_2O (1.333) [143]. However, the differences in refractive index are relatively small and the effects of surface affinity on analyte loading are expected to play a larger role in determining the sensitivity observed.

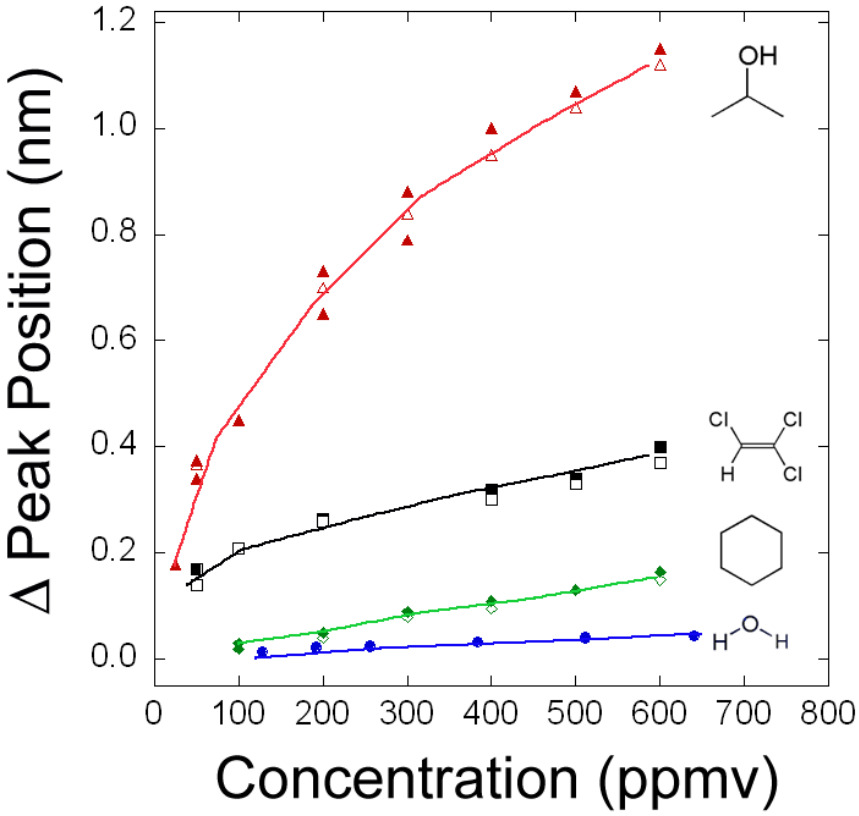

Figure 2.3 Porous Si sensor response to IPA, TCE, cyclohexane, and water in the 50 – 600 ppmv range. Two identically prepared sensors, shown as open and filled symbols, were simultaneously exposed to various concentrations of each vapor. Spline curves are drawn to guide the eye.

2.4.4 Sensing Carbon Bed Vapor Breakthrough

Detection of organic vapors breaking through a bed of activated carbon was performed using the analytes IPA, cyclohexane, TCE, and TCE in 63% relative humidity, each at a steady-state concentration of 300 parts per million by volume (ppmv), equivalent to 737, 1303, and 1612 mg/m^3 for IPA, cyclohexane, and TCE respectively. The responses of the sensor, located within the ampoule containing the carbon bed, and the gas chromatograph responses, sampled downstream from the ampoule, are shown in Figures 2.4 and 2.5. The porous Si probe senses VOCs in the carbon bed before detection downstream by the gas chromatograph. For all of the organic analytes studied, the red shift of λ_{max} in the photonic crystal is many times greater than the λ_{max} noise level, and the shift occurs tens of minutes before an analogous response is observed by gas chromatography.

Humidity exerts a significant influence on the response of the sensor to organic analytes. A sensor was embedded in activated carbon and challenged with TCE in the presence of 63% relative humidity (RH), Figure 2.5. The value of $\Delta\lambda_{max}$ for the sensor exposed to 300 ppmv of TCE in RH was 0.84 nm after 100 minutes, while in pure nitrogen at 63% RH the red shift was 0.87 for the same time span. After 200 minutes, the sensor in pure nitrogen at 63% RH shifted by 1.06 nm, approaching an asymptote of 1.2 nm. Thus, despite the low sensitivity of the sensor to water vapor (Figure 2.3), at high concentrations (~14,900 ppmv) water vapor accounts for much of the observed sensor response; in the absence of water vapor (0% RH), the shift was only 0.14 nm.

Humidity also significantly affects the TCE breakthrough curve, reflected in Figure 2.5. The large change in the sensor response at high humidity is consistent with

the presence of a high concentration of water vapor (~14,900 ppmv at 20º C [143]) relative to the VOC concentration (300 ppmv). The flame ionization detector used in the gas chromatograph is not sensitive to water, so the carbon bed breakthrough curves plotted on the right hand axis of Figure 2.5 represent detection of only the TCE component in the effluent. The shape of this response curve is consistent with the adsorption of a binary mixture of water and TCE on activated carbon[144-146].

Activated carbon with few inorganic impurities and little surface oxide is highly nonpolar and exhibits only weak van der Waals interactions with water at low vapor pressures. However, water vapor does adsorb when present at high concentrations due to adsorbate-adsorbate interactions that lead to cluster formation and eventual pore filling in activated carbon[147]. Adams[148] and Linders[146] separately showed that little water is absorbed on activated carbon below 30% RH, with adsorption strongly increasing above 45%. The binary adsorption of an organic solvent and water vapor in activated carbon is influenced by the miscibility of the two compounds in the adsorbed phase. Miscible solvents such as an ethanol:H_2O mixture adsorb according to their multi-component equilibrium[146], while an immiscible mixture such as TCE:water vapor is modeled by the independent co-adsorption of the two components. In the latter model, the immiscible organic compound is adsorbed into the micropore volume not occupied by water[146], with concomitant displacement of water from hydrophobic micropores[145] rather than partitioning of the hydrophobic organic compound into the water layer. A miscible solvent pair traverses a bed of activated carbon as a single

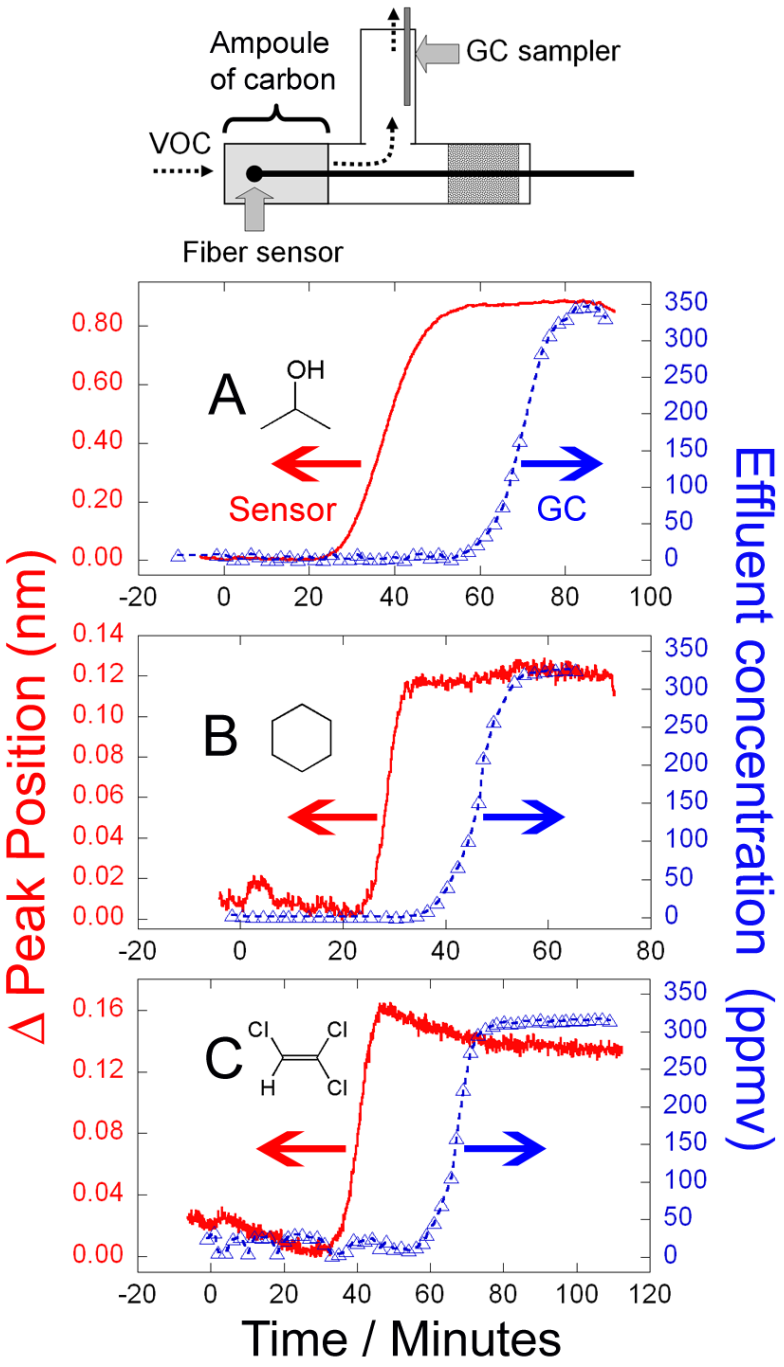

Figure 2.4 Response curves of the porous Si sensor embedded in a carbon bed (solid, left axes, red; acquired every 9 s), and gas concentrations determined by GC and sampled at the outflow of the carbon bed (dotted, right axes, blue; acquired every 2 min). Vapor flows of isopropyl alcohol (A), cyclohexane (B), and trichloroethylene (C) were tested. The analyte concentration in the carrier stream was 300 ppmv for each. In each trial, the implanted sensor responded to analyte in advance of the analyte's detection by the gas chromatograph.

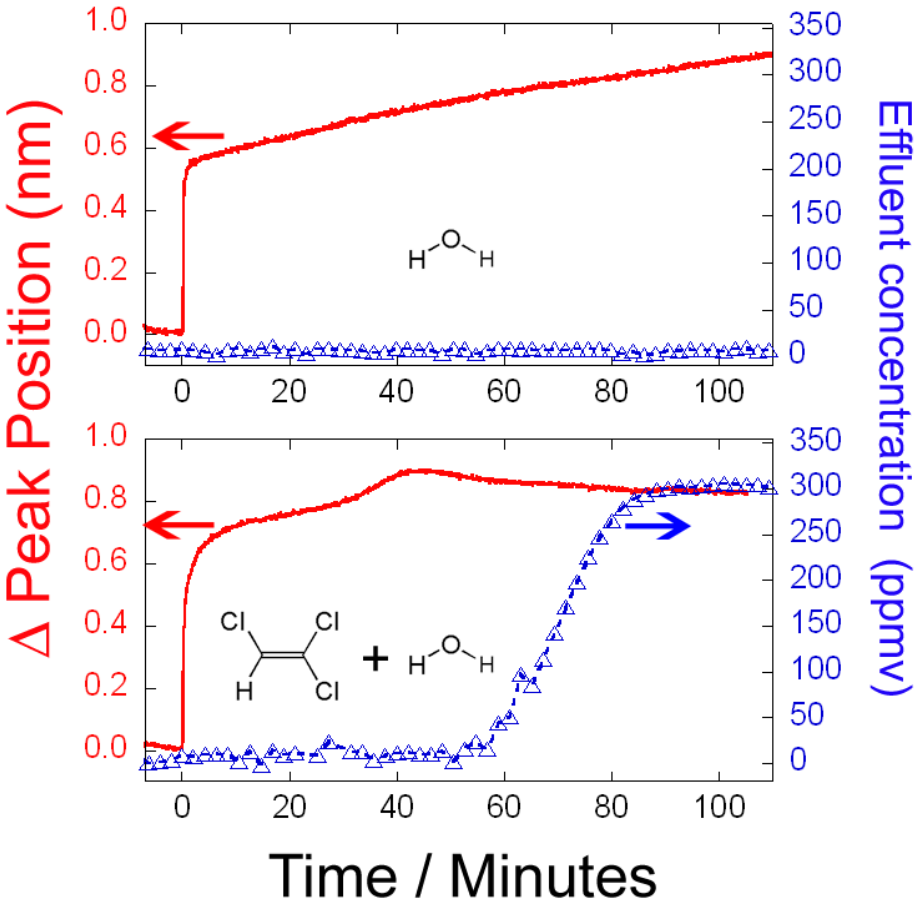

Figure 2.5 Top: Response curve of the carbon bed-implanted porous Si sensor (solid, left axis, red) to a flow of 63% relative humidity (RH) in N_2 compared to the FID detector response of the gas chromatograph (triangles, right axis, blue). **Bottom:** Response curves of the embedded sensor recorded after introduction of a mixture of 300 ppmv trichloroethylene (TCE) and 14,900 ppmv water vapor (63% RH) in N_2. The porous Si sensor was embedded in activated carbon, while the gas chromatograph inlet was positioned at the outflow of the carbon bed. The nominal RH of the N_2 gas in the carbon bed before time = 0 is 0%. The additional sensor response contribution of the TCE in the humid stream is shown in the bottom plot.

front, while an immiscible mixture of two components may not progress through the bed uniformly. In the present system this is observed for the TCE/water vapor mixture; the sensor detects TCE almost 40 min after it detects the change in RH (Figure 2.5). The initial response of the ampoule-embedded sensor is consistent with the sensor response to 63% RH alone, with the high concentration of water vapor rapidly traversing the carbon bed. After 35 minutes in the flow of TCE and water vapor, the value of λ_{max} sharply increases, corresponding to the time at which the embedded sensor responds to pure TCE at 0% R.H. This additional shift of λ_{max} in the presence of the mixed vapors indicates an incomplete initial pore filling by water vapor followed by TCE adsorption into part of the residual pore volume. However, the total increase in $\Delta\lambda_{max}$ is slightly less than the simple arithmetic sum of the separate TCE and 63% R.H. responses due to the concomitant displacement of water from some micropores upon TCE adsorption.

2.4.5 Comparison of Sensor and Gas Chromatograph Responses to Vapors

The time delay between the porous Si sensor and gas chromatograph responses to vapors, shown in Figure 2.4, is due to the additional bed length of activated carbon between the sensor, implanted into the carbon bed, and the gas chromatograph sampling line, positioned at the outflow of the carbon bed. To ensure that this delay is due to the additional carbon bed length after the sensor and not a difference in sensor and gas chromatograph response times, the fiber sensor was placed outside of the bed and to sample the same effluent flow as the GC, as pictured in Figure 2.6. The simultaneous responses of the fiber-optic sensor and gas chromatograph were recorded

for a flow of 1000 ppm IPA through the carbon bed. The responses are nearly temporally coincident, with the slight delay in chromatograph response due in part to the longer sampling time (2 min per acquisition) than the fiber sensor (9 sec per acquisition). A plot of the change in reflected peak position, $\Delta\lambda_{max}$, versus the gas concentration measured by the chromatograph (bottom plot in 2.6) displays an overall response shape that is in good agreement with the calibration data (triangles) of the fiber to IPA in the absence of a carbon bed (Figure 2.3).

2.4.6 Implications

This work has demonstrated that a sub-millimeter porous Si sensor embedded in an activated carbon filter bed responds to volatile organic compounds, and can be used to indicate end-of-service life prior to complete saturation of the carbon bed. A number of devices designed to detect VOCs in carbon beds have been implemented, but with limited success [130, 137, 138, 149]. Dye-based, colorimetric indicators, for instance, are limited by functional group selectivity, restricting their utility as broad-class sensors [138]. Electrical transduction sensors have proven more effective, yet metal oxide sensors require large currents to operate at elevated temperatures, and chemiresistor and semiconductor sensors, such as those based on arrays of carbon black organic polymer composites[137, 138], are susceptible to RH and require a large form factor that is difficult to implant in a carbon bed. Recently, Caron and coworkers[150] studied the use of a porous borosilicate fiber as a potential end-of-service life sensor that responded to VOCs in the 1000 ppmv range. Like the porous Si sensor in the present work, it

combined the advantages of optical transduction with the high surface area of a porous microstructure.

The optical fiber-based porous Si sensor described in this work responds to different classes of VOCs. Although the sensor displays a lower response to water vapor than to organics at comparable concentrations, in practical use the water vapor concentration is several orders of magnitude greater than the VOC concentration, which significantly impacts the sensor response. It should be possible to further limit the response of the sensor to water vapor by altering the porous Si surface with covalently attached, hydrophobic hydrocarbons[3, 97, 151], or to distinguish water vapor from VOCs by analyzing differential responses from two or more fiber sensors possessing different surface chemistries, as is detailed in Chapter 3. For a filter end-of-service-life application, however, the sensor's response to water vapor does not entirely detract from its applicability; regardless of whether the carbon bed adsorbs water vapor or VOCs, its adsorption capacity is diminished, rendering the activated carbon filter less effective at protecting its user. Although only one porous Si sensor was implanted in the carbon bed, the small form factor of the device allows designs in which several sensors can be placed at different carbon bed positions. Such a configuration should enable real-time, low power detection and it may also prove useful in modeling the diffusion of organic compounds through activated carbon[137, 152, 153] and in developing models of gas-solid diffusion [154] to better understand adsorption phenomena.

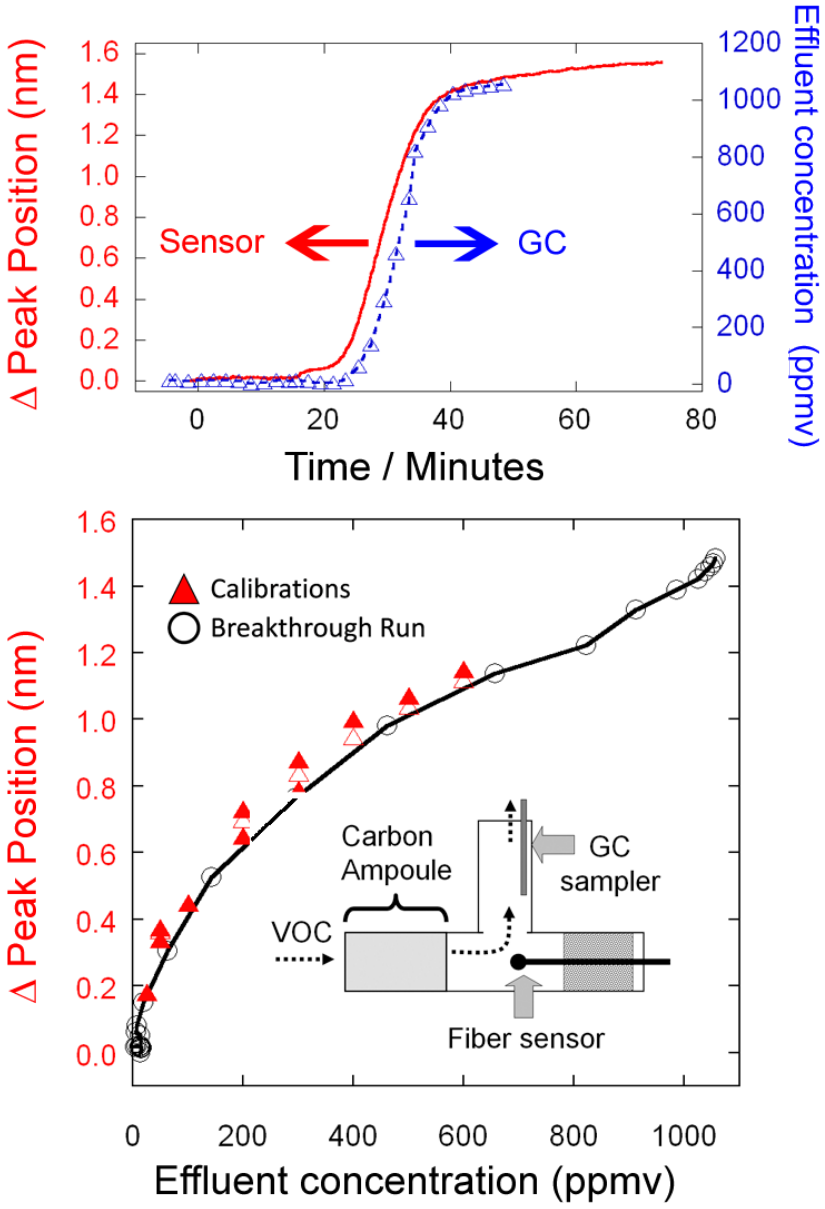

Figure 2.6. Top graph: Porous Si sensor (solid curve, left axis) and gas chromatograph (triangles/dotted, right axis) responses to a flow of 1000 ppmv isopropyl alcohol. The sensor probe and gas chromatograph were both positioned to sample the effluent of the carbon bed, with the configuration depicted in the cartoon at bottom right. **Bottom graph:** The sensor response is plotted against the chromatograph-measured effluent concentration (open circles). A spline curve is drawn to guide the eye. Calibration data of the sensor response to IPA from Figure 2.3 is added for comparison (open and closed triangles) and exhibits good agreement with the breakthrough measurements.

2.5 Conclusions

A sub-millimeter point sensor for organic vapors was constructed by coupling freshly prepared porous silicon to a multimode optical fiber. The sensor response to four analyte vapors was calibrated from 50-600 ppmv. Implanting the porous silicon-coupled optical fiber into a bed of activated carbon in a flow of vapor allowed sensing of organic vapors breaking through the bed, with implications to carbon filtration cartridge end-of-service-life detection.

Chapter two, in part or in full, is a reprint (with co-author permission) of the material as it appears in the following publication: King, Brian H.; Ruminski, Anne M.; Snyder, Jay L.; Sailor, Michael J. *Optical- fiber-mounted porous silicon photonic crystals for sensing organic vapor breakthrough in activated carbon.* Advanced Materials (2007) 19 (24), 4530-4534. The author of this dissertation is one of the primary authors of this publication.

CHAPTER THREE

CHEMICALLY MODIFIED POROUS SILICON-BASED OPTICAL SENSORS FOR VOLATILE ORGANIC ANALYTES

3.1 Abstract

Chapter 2 detailed an optical sensor constructed by adhering a freshly prepared porous Si film to a 600μm optical fiber, with applications in remote sensing and vapor breakthrough detection in carbon filtration cartridges. In this chapter, the effect of surface chemistry on the stability and specificity of the sensors is examined.

Sensing of the volatile organic compounds (VOCs) isopropyl alcohol (IPA) and heptane in air using sub-mm porous silicon-based sensor elements is demonstrated for analyte concentrations ranging from 50-800 ppm. The sensor elements are prepared as 1-D photonic crystals (rugate filters) by programmed electrochemical etch of highly doped p++ silicon, with sensing achieved by measurement of the wavelength of the photonic resonance band in the reflectance spectrum as a function of analyte concentration. The stability and response of the sensors is quantified as a function of surface chemistry, using the following modification methods: ozone oxidation, thermal oxidation, thermal hydrosilylation with 1-dodecene, electrochemical methylation, thermal reaction with dicholorodimethylsilane and thermal carbonization with acetylene. The thermally oxidized and the dichlorodimethylsilane-modified materials show the greatest stability under atmospheric conditions. Optical microsensors are then prepared by removal of the porous layer from the Si substrate and attachment to the distal end of optical fibers. The acetylated porous Si microsensor displays a greater response to heptane than to IPA, while the other chemical modifications display a greater response to IPA than to heptane. The thermal oxide sensor displays a strong response to water vapor, while the acetylated material shows a relatively weak response. The results demonstrate the viability of such optical

microsensors, and suggest that a combination of optical fiber sensors with different surface chemistries can be used to classify VOC analytes. Application of the miniature sensors to the detection of VOC breakthrough in a full-scale activated carbon respirator cartridge simulator is demonstrated.

3.2 Introduction

The use of porous Si has been explored for various environmental sensing applications. The photoluminescence,[22, 55, 155] refractive index[21, 46] and dielectric constant[16, 156] of porous Si are very sensitive to the presence of molecules in the pores. Volatile organic compounds,[21-23] explosives[30] and polycyclic aromatic hydrocarbons[26] have all been detected, with detection limits of a few ppb reported for some of these compounds.[157]

Porous Si offers many advantages as a chemical sensing platform. The porous layer contains a high specific surface area for analyte adsorption (in the range of a few hundred m^2 per cm^3) [31], the surface chemistry can be tailored,[3] and the porous layer is easy to produce [12].

Porous Si photonic crystals can be fabricated from highly doped p-type silicon by applying a sinusoidal anodic current during an electrochemical etch. This etching waveform produces a porous film with a periodic modulation in porosity and refractive index in the <100> direction of the silicon wafer, resulting in a rugate optical structure with continuously varying refractive index profile with depth.[158] The reflectivity spectrum contains a sharp spectral peak at a wavelength corresponding to the period of the sinusoidal etching waveform. Reflectivity peak wavelengths are also dependent on

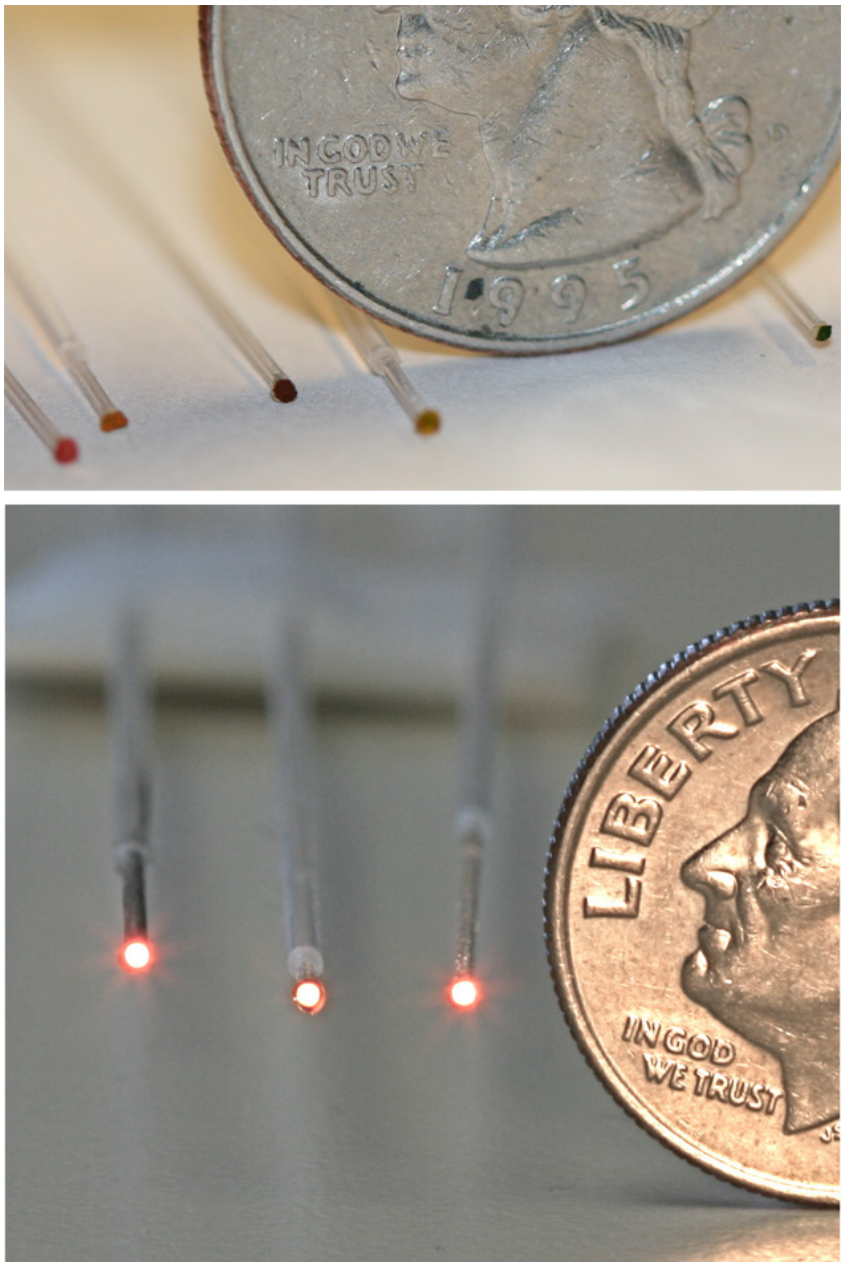

Figure 3.1 600 μm diameter porous photonic crystals, electrochemically etched from silicon, are chemically modified and attached to the tip of optical fibers. Surface modifications consisting of hydride, oxide, hydrocarbon, and carbide species are studied; the response to various VOC analytes depends on the surface chemistry on the porous Si particle. Top: rugate porous : the etch parameters determine the spectral reflectivity peak wavelength in rugate porous Si photonic crystals, allowing a material with a range of colors to be fabricated. Bottom: white light is passed through the optical fiber, reflecting off the porous Si and returning through the fiber to a spectrometer.

the refractive index of the porous film. When a substance enters the pores the refractive index of the porous layer increases, yielding a red shift in the reflectivity peak. The shift of the reflectivity peak provides a means to quantify the amount of chemical in an analyte matrix.

The chemical functionality of the surface species dictates the vapor response and the stability of the porous Si sensor.[3, 112, 159] In particular, grafting of chemical functionalities via formation of Si-C bonds has been found to be a convenient reaction to prepare stable sensors that display a degree of chemical selectivity. Grafting can be achieved by electrochemical reduction of alkyl halides[160] or by hydrosilylation of terminal alkenes.[161-163] Whereas the native surface of porous Si contains hydrophobic, air-reactive Si-H species, grafting of aliphatic hydrocarbons generates a similarly hydrophobic but significantly more stable surface. Using aliphatic compounds that contain specific functional groups such as carboxylate provides a means to incorporate different surface affinity properties while retaining the chemical stability of the Si-C bonded sensor surface.[90] A carbonaceous species can also be grafted to the porous Si surface by thermal decomposition of acetylene on a native porous Si surface.[164] Although less well-defined than the hydrosilylation route, the "hydrocarbonized" porous film is environmentally stable[165] and its chemical sensing capabilities have been demonstrated.[166-169]

In this work, porous Si rugate optical structures were prepared with the different chemical modifications described above, and the response of the photonic crystals to hydrophilic (isopropanol) and hydrophobic (heptane) analytes quantified. The stability of each sensor type was examined over a period of 15 days. From this

screening, two sensor chemistries (thermal oxide and acetylene carbonization) with acceptable stability and displaying significantly different analyte responses were incorporated into remote optical sensors by adhering sensor films of each chemistry to the ends of silica optical fibers. These optical fiber sensors have small footprint of <1 mm diameter and are impervious to electrical interference, since the spectral detector may be placed at a distance from the sensor head. The suitability of the fiber-based microsensors in a remote sensing application is demonstrated by monitoring the organic vapor breakthrough of analytes through a bed of activated carbon. We find that microsensors modified with acetylene effectively minimize interference from fluctuations in relative humidity.

3.3 Experimental

3.3.1 Sensor Construction

Single-crystalline highly doped p-type Si wafers (0.0008-0.0012 Ω–cm resistivity, (100) polished, B-doped) were purchased from Siltronix Corp. All reagents were used as-received unless otherwise noted. Aqueous HF (49%), isopropanol, acetic acid, undecylenic acid and lithium iodide were purchased from VWR International. Heptane, dodecene, iodomethane and silanization solution I (~5% dichlorodimethylsilane in heptane) were purchased from Sigma-Aldrich. Pure ethanol was purchased from Rossville Gold Shield Chemical Company. Acetonitrile was purchased from EM Sciences, and purified using a two-column solid-state purification system (Glasscontour System), then transferred to a glovebox (Vacuum Atmospheres Company) without exposure to air, and stored over activated molecular sieves.

Oxygen was purchased from Westair Gases & Equipment, acetylene from Airgas, Inc., and nitrogen from Praxair, Inc. Optical fibers (600 micron silica core, low OH) were purchased from Thorlabs, Inc. Liquid epoxy DGEBA resin (Epotuf 37-140 diglycidyl ether of bisphenol-A) was provided by Reichhold, Inc. Liquid epoxy DGEBPB (D.E.R. 354 diglycidyl ether of bisphenol-F) and Novolac (D.E.N 438 epoxy novolac resin) were furnished by the Dow Chemical Company. Curing agents (Ancamine 2432, 2423, 2587, and MCA) were provided by Air Products and Chemicals. 2-Ton binary epoxy was purchased from ITW Devcon.

Porous Si samples containing a single spectral reflectance peak were prepared by anodization of highly doped p-type Si wafers in a 3:1 v:v solution of aqueous hydrofluoric acid:ethanol in a two-electrode configuration using a platinum ring counter-electrode. Etching was performed in a Teflon etching cell using a galvanostat (Princeton Applied Research Model 363) under computer control (LabView, National Instruments). The porous layer was etched using a sinusoidal current density waveform varying between 13.3 and 66.4 mA/cm^2 with a period ranging between 8 and 11.5 seconds for an etch duration ~10 min. The electrolyte solution was mixed during the etching process to minimize hydrogen bubble formation on the sample surface and to encourage etchant solution exchange in the porous film.[158] Fiber sensors required the detachment of the porous layer from the bulk Si. The porous layer was detached by applying a current of 3.8 mA/cm^2 for 8 min. in a 3.3% hydrofluoric acid in ethanol solution. Free standing porous Si was attached to optical fiber with partially cured mixture of epoxy resin and the amine curing agent, and allowed to cure for two days before use. The ratio of resin to curing agent was determined using the amine value

(curing agents) and epoxide equivalent weights of each component from the respective certificates of analysis. Fiber optic-coupled sensors tested in sections 3.4.6-3.4.7 were constructed with the binary mixture of Bis-A and the aliphatic amine Ancamine 2432. Photographs of constructed sensors are shown in Figure 3.1

3.3.2 Sensor Characterization

Gravimetric Determination of Porosity:

Five repetitions of each sample etch type were prepared. Samples were weighed before etching (m_1), after etching (m_2), and after dissolving the porous layer with a 0.1M basic solution of KOH in water and ethanol (m_3). The following equation was used to determine the porosity fraction:[170]

$$Porosity\ Fraction = \frac{m_1 - m_2}{m_1 - m_3} \tag{3.1}$$

Scanning Electron Microscopy:

Porous layer thickness was measured with a Phillips XL30 environmental scanning electron microscope (SEM) imaging in secondary electron mode with an accelerating voltage of 10 keV was used. Porous Si tipped optical fibers were sputter-coated with chromium prior to acquisition to avoid sample charging.

Infrared Spectroscopy:

Surface modification was verified through attenuated total reflectance Fourier-transform infrared (ATR-FTIR) spectroscopy. Spectra were recorded using a Thermo Scientific Nicolet 6700 FTIR with a Smart iTR diamond ATR attachment. Spectral resolution was 4 cm^{-1} and 64 interferograms were averaged per spectrum.

Water Contact Angle Measurements:

Sessile drop contact angle measurements were collected on three samples of each surface chemistry, using a digital camera and Adobe Photoshop CS2 for analysis. Using a glass syringe, a 5 μL drop of deionized (Millipore) water was delivered to the chip surface to form a water droplet. Contact angles were measured on both sides of the droplet and averaged.

3.3.3 Surface Modifications

Surface modifications were performed by Anne M. Ruminski. Briefly, thermally oxidized samples (Si-O-Si) were prepared by inserting as-prepared H-terminated porous Si samples (Si-H) in a tube furnace (Lindberg/Blue M, Thermo Fisher Scientific, Waltham, MA) under air at 600 °C for 90 min. Ozone oxidation (Si-OH) was achieved by placing as-prepared Si-H samples in a flowing stream of ozone (Ozone Solutions, product ID OZV-8, flux of 8 g h^{-1}) for 4 min. Silanization of samples (Si-O-Si$(CH_3)_2$-O-Si) was performed by the immersion of ozone oxidized samples in ~5% dichlorodimethylsilane in heptane under inert conditions on a Schlenk line. The samples were heated to 105 °C for 8.5 hours, cooled, and rinsed with dichloromethane and ethanol. Porous samples were functionalized with dodecene (Si-$(CH_2)_{11}CH_3$) via a hydrosilylation reaction.[3] Samples were placed in a flask and covered with neat dodecene. The flask was subjected to three freeze-pump-thaw cycles on a Schlenk line (vacuum gas manifold). Samples were heated to 150 °C under nitrogen for 3 h, then cooled and rinsed with dichloromethane and ethanol. Si-CH_3 samples were prepared from Si-H samples by reductive electrochemical grafting of

CH_3I.[160] The Si-H sample was placed in an electrochemical cell with a glass cap fitted with a stopcock and a counter electrode feed-through. The vessel was attached to a Schlenk line and filled with nitrogen. The sample (working electrode) and the Pt counter electrode were then immersed in 4 mL of acetonitrile containing 0.2 M iodomethane and 0.2 M lithium iodide. A cathodic current of 5 mA cm^{-2} was applied for 2 min. Several types of acetylated samples (Si-C) were prepared, by performing the acetylation reaction at various temperatures: an Si-H sample was placed in a ceramic boat and inserted into a tube furnace under a nitrogen flow of 2 L min^{-1}. After ten min, the furnace was set to the desired temperature (300, 485 or 500 °C). Once the furnace reached the temperature set point, acetylene gas was introduced to the samples at a flow rate of 1 L min^{-1}. After 30 min, the acetylene flow was terminated and the oven was allowed to cool to room temperature.

3.3.4 Vapor Dosing Measurements

Reflected light spectra of the samples in the visible region were taken from 345-1045nm with a CCD spectrometer (Ocean Optics USB4000) with a tungsten-halogen light source (Ocean Optics LS-1) connected with a Y-branch 600um diameter, bifurcated multimode optical fiber. The common end of the bifurcated fiber was focused with an objective lens to a $2mm^2$ spot size and positioned normal to the porous silica surface for bulk-attached chip samples. Figure 3.2 displays a nominal reflectance spectrum. Spectra of the fiber-mounted porous Si samples were obtained by coupling

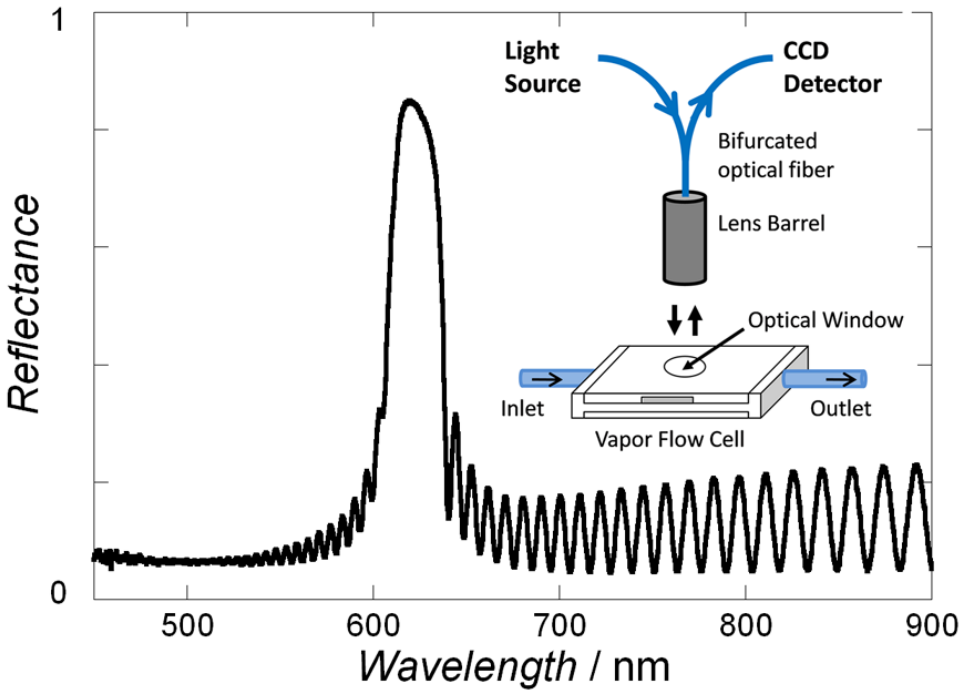

Figure 3.2 Typical reflectance spectrum of the porous Si rugate filters used in this study. The sample is etched using a sine wave, which results in a one-dimensional photonic crystal. This spectrum is of a native surface (Si-H terminated) sample. The reflectance spectrum is acquired at normal incidence, as indicated in the inset. Bulk-attached sensor chips, studied to assess surface chemistry influences on vapor dosing before creating optical fiber-mounted sensors, were studied by mounting each chip in a vapor flow with a glass optical window, as shown.

the optical fiber to the bifurcated fiber optic cable with a standard fiber coupler (Thorlabs, Inc.).

Porous Si chips testing and fiber stability testing were performed by exposing samples to 500 ppm IPA and heptane using a computer-controlled vapor dosing system. Nitrogen carrier gas was set to a flow rate of 1.5 L min^{-1} using a mass flow controller (Alicat Scientific). Analyte was injected with a low-volume liquid flow pump (MilliGAT 6nl-10ml/min, GlbalFIA) into a brass block heated to ~45 °C to flash vaporize analyte into the carrier flow. The outflow of the vaporization block was united with a separate nitrogen purge line, also controlled with a mass flow controller, at a computer controlled four-way valve. The nitrogen and vapor lines could be switched between two valve outlets, with one line flowing to the sample and the other to a waste stream. Vapor concentrations were validated with a gas chromatograph (SRI Instruments 8610C with FID detector).

Calibration of the optical fibers to vapor analytes and breakthrough monitoring of vapors in carbon beds were performed using a similar vapor dosing system configuration, with the following differences. Air flow rate was set at 32 L min^{-1} using a Miller Nelson HCS-401 air conditioning system (Miller Nelson Instruments, a unit of assay technology, Livermore, CA). The Miller-Nelson system was also used to set the relative humidity of the air stream. Analyte was injected as described above. Breakthroughs of activated carbon beds were performed with a custom built APR cartridge simulator consisting of a stainless steel box with inlet and outlet threaded ports on the top and bottom faces for introducing air flow. Inside the box was a small cylinder with a removable top and bottom containing 50 g of activated carbon, as

pictured in Figure 3.12. Fiber optic sensors were threaded into the simulator box, along with a small tube to draw samples to a gas chromatograph. The fibers and GC probes were located halfway into the depth of the bed. The bed was filled with RVG 12x20 granular activated carbon (Calgon Carbon Corporation) immediately prior to vapor break-through measurements. A second tube was tapped into the outflow of the carbon bed simulator to sample vapors exiting the bed, and led to a separate port on the 10-port multivalve gas chromatograph.

The gas chromatograph (SRI model 8610) was programmed to automatically sample the two (cartridge mid-bed and output) gas streams and quantify the concentrations. All components could be separated in under 2 min. This permitted simultaneous monitoring of the mid-bed and exhaust of the cartridge simulator at 4-min intervals. The GC responses for heptane and isopropanol were calibrated by filling a 10-L sampling bag with 6 L of air and injecting a known amount of liquid analyte with a microliter syringe. The vapor and air were mixed by kneading the gas bag, then a sample withdrawn from the bag with a pressure-tight gas sampling syringe and mixed with at the desired ratio with conditioned air to dilute the sample. The desired dilution was then injected directly into the gas sampling loop of the gas sampling valve, and the process repeated for at least 5 vapor concentrations to build a multi-segment concentration calibration curve of the GC for each analyte.

Figure 3.2 displays the reflected light spectrum of a sample before vapor introduction. Each spectrum collected was fit with a Gaussian function in LabView to determine the peak wavelength (λ_{max}). The peak wavelength of each sensor was

monitored over time, with changes in peak position from the baseline in nitrogen plotted for various analyte exposures.

3.4 Results and Discussion

3.4.1 Preparation and Characterization of Porous Si Photonic Crystals

Porous Si samples were prepared by electrochemical etch of highly doped p++ type silicon in an ethanolic HF solution. The current was varied sinusoidally, producing a film containing layers with a continuously varying "rugate" porosity-depth profile.[9, 158] The layered structure acts as a one-dimensional photonic crystal displaying a single peak in the reflectance spectrum, at a wavelength determined by the period of the sine wave used in the current-time etch waveform. All samples were etched with the same minimum and maximum current density of 13.3 and 66.4 mA/cm^2, the HF concentration (3:1 v:v HF:ethanol), and etch duration. The current periodicity was adjusted in order to produce a reflectance peak located at ~650 nm after chemical modification, shown in Figure 3.2. Nominally, an etchwave period of 10 seconds was applied, resulting in a porosity of 74.2% +- 0.6% and a thickness of 13.27 +/- 0.06 um. Sample porosity was determined by gravimetric analysis [170] by weighing samples before etching, after etching and after dissolution of the porous layer with a 0.1M KOH solution in water and ethanol.

The various chemical modification reactions were performed immediately after etching the samples. Nine different chemical reactions from the literature were employed to generate distinct surface functionalities. Table 3.1 summarizes the chemical reaction chemistries, the idealized type of surface it generates, and the

measured sessile drop contact angles. Confirmation of surface species after chemical modification was performed by A.M.R. using attenuated total reflectance Fourier transform infrared (ATR-FTIR) spectroscopy. The oxidation methods all tend to generate hydrophilic surfaces. Ozone oxidation produces a more hydrophilic surface than thermal oxidation, presumably due to the presence of a larger amount of surface Si-OH species. The ATR-FTIR spectra support this interpretation; along with the asymmetric Si-O-Si and Si-O stretching vibrations at 1025 cm^{-1} and 780 cm^{-1}, respectively, a strong band assigned to *v* O-H is observed at 3350 cm^{-1} for the ozone-oxidized material. This species is detected as a minor component in the ATR-FTIR spectrum of the thermally treated material. At the temperature used in the thermal oxidation reaction, hydroxylated (Si-OH) surfaces are known to undergo dehydration to generate the more hydrophobic Si-O-Si surface.[171-173] The asymmetric Si-O-Si and Si-O stretching vibrations for the thermally oxidized material appeared in the FTIR spectrum at 1033 and 808 cm^{-1}, respectively.

Several of the chemical modification methods of Table 3.1 result in hydrophobic material as a result of creating either aliphatic hydrocarbons or silicon carbide-like species on the surface. The silicon carbide-like species are generated by pyrolysis of acetylene on the surface of a freshly prepared (hydrogen-terminated) porous Si chip. [174] Previous studies report that the temperature of the pyrolysis reaction plays a key role in determining the degree of hydrophobicity or hydrophilicity of the resulting "hydrocarbonized" porous film.[115, 169] In this study, three different pyrolysis temperatures (300, 485 and 500 °C) were used to prepare hydrocarbonized samples. For all of the preparations, ATR-FTIR spectra display a prominent broad band at 1000

cm^{-1}. This band appears in a region of the FTIR spectrum (1050-1150 cm^{-1}) that is generally associated with silicon oxides. However, the band remained after samples were soaked in an ethanolic solution of HF, suggesting that the band cannot be due to oxide (silicon oxides rapidly dissolve in HF solutions). On the basis of density functional theory calculations, Salonen and coworkers assigned the 1000 cm^{-1} band of thermally carbonized porous Si to C-H stretching vibrations from a species in which the carbon atom is back-bonded to Si atoms.[165] This assignment is consistent with the other bands observed in the FTIR spectrum, which include C-H stretching (~2900 cm^{-1}) and bending (~1385 cm^{-1}) vibrations.[164] Contact angle measurements of the actetylene-treated, hydrocarbonized samples were less consistent than with the other chemical modifications. The water contact angle was observed to decrease as a function of time, and the footprint of the drop on the sample was often not round. We ascribe this to surface heterogeneity; presumably the acetylation chemistry produces a mixture of hydrophobic and hydrophilic domains.

Three chemical modification methods were used to place aliphatic hydrocarbon species on the porous Si surface: a long hydrocarbon chain was bonded to the surface through a thermal hydrosilylation reaction with 1-dodecene,[175] a methyl group was attached by electrochemical reduction of methyl iodide, and a dimethylsiloxy group was attached by thermal reaction of an ozone-oxidized sample with dichlorodimethylsilane. ATR-FTIR spectra confirmed the presence of the aliphatic or methyl species. The aliphatic species displayed bands assigned to C-H stretching and deformation modes at 2966, 2926, 2858 and 1469 cm^{-1}, and the methyl-capped surfaces displayed a distinctive band associated with the methyl rocking mode at 769 cm^{-1}.[160]

Both of the surface preparations that produce surface-bound methyl species (electrochemical reduction of CH_3I or reaction with dichlorodimethylsilane) generate material that displays the same contact angle.

Table 3.1 Surface Chemistries Prepared on Porous Si Samples[a]

Process	Chemical Reaction	Surface Species	Contact Angle (°)[a]	r = Δλ(Heptane) / Δλ(IPA)
Native surface	-	Si-H	102 ± 3	0.74
Ozone oxidation[176]	Si-H + O_3 =>	Si-O-Si, Si-OH	11 ± 1	0.053
Thermal oxidation (600 °C, 90 m)[97]	Si-H + O_2 =>	Si-O-Si	20 ± 1	0.11
Hydrosilylation with 1-dodecene[175]	Si-H + CH_2=$CH_2(CH_2)_9CH_3$ =>	Si-$(CH_2)_{11}CH_3$	119 ± 2	0.69
Electrochemical methylation[160]	Si-H + CH_3I =>	Si-CH_3	102 ± 3	0.92
Ozone oxidation + dichlorodimethylsilane[159]	(a) Si-H + O_3 => Si-OH (b) 2 Si-OH + $Cl_2Si(CH_3)_2$ =>	Si-O-Si$(CH_3)_2$-O-Si	101 ± 1	0.49
Thermal acetylation (300 °C, 30 m)[165]	Si-H + H-C≡C-H =>	"Si-C"	53 ± 3	0.75
Thermal acetylation (485 °C, 30 m)[165]	Si-H + H-C≡C-H =>	"Si-C"	80 ± 3	5.0
Thermal acetylation (500 °C, 30 m)[165]	Si-H + H-C≡C-H =>	"Si-C"	76 ± 7	2.9

[a] Contact angle measurements were performed on the same day as chemical functionalization.

3.4.2 Response of Chemically Modified Porous Si to Analyte Vapors

In order to select a surface chemistry that contrasts with the oxidized sensor surface, a stable hydrophobic sensor surface is desired. The relative hydrophobicity of chemically modified porous Si chips was evaluated by comparing the optical response of each sample to isopropanol and to heptane vapors. Each of the two analytes was introduced individually into a nitrogen stream at a concentration of 500 ppm. The peak

position of the reflectivity peak was determined using a Gaussian fit of the spectra, and the wavelength shift of the reflectivity peak was recorded, as shown in Figure 3.3. A response ratio was determined by dividing the sensor response to 500 ppm heptane by the response to 500 ppm isopropanol, producing a response factor "r" as defined in eq. 3.2:

$$r = \frac{\Delta\lambda_{\text{heptane}}}{\Delta\lambda_{\text{isopropanol}}} \tag{3.2}$$

Calculated r values of the chemically modified porous Si chips are listed in Table 3.1. Larger values of r indicate a greater degree of hydrophobicity. As might be expected from the relatively large quantity of surface Si-OH species, ozone-oxidized samples display the smallest r value (0.053), followed closely by thermally oxidized samples (0.11). This result is in agreement with water contact angles, where ozone-oxidized samples had the smallest contact angle followed by thermally oxidized.

Other samples with r values less than 1.0 include chips that were: acetylated at 150 °C or at 300 °C; reacted with dichlorodimethylsilane; functionalized with dodecene; electrochemically methylated; or unmodified (presenting a native, hydride-terminated porous Si-H surface). Water contact angle measurements on hydride-terminated porous Si indicate a relatively hydrophobic surface, however the value of contact angle steadily decreases upon exposure to air, indicative of slow oxidation of the surface hydrides to produce hydrophilic Si-O-Si and Si-OH species. Samples that were electrochemically methylated and surfaces modified with 1-dodecene displayed the same or a larger water contact angle, respectively, relative to the native Si-H

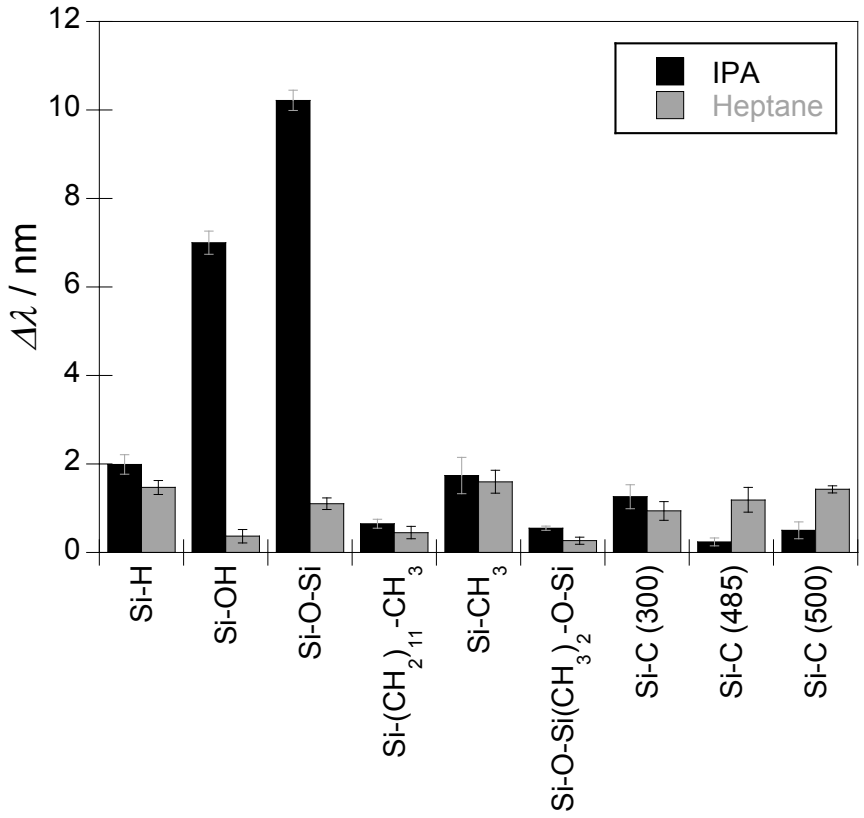

Figure 3.3 Response of chemically modified porous Si photonic crystal samples to isopropanol (IPA) and heptane vapors. Vertical bars indicate the increase in wavelength ($\Delta\lambda$) of the resonant spectral peak of the photonic crystal relative to the sample in pure N_2, for the indicated surface chemistries. Simplified surface chemistries are described in Table 3.2: Si-H (native surface of porous Si); Si-OH (ozone oxidized); Si-O-Si (thermally oxidized at 600 °C); Si-$(CH_2)_{11}CH_3$ (hydrosilylated with dodecene); Si-CH_3 (electrochemically methylated); Si-O-Si$(CH_3)_2$-O-Si (modified with dimethylsiloxane); Si-C (acetylated at the indicated temperature, in °C). Analyte concentrations are 500 ppm isopropanol and 500 ppm heptane. Values are the average of 5 samples; error bars represent one standard deviation.

samples. ATR-FTIR spectra of these samples reveal the presence of residual Si-H species on these surfaces. As with the as-etched porous Si-H samples, air oxidation is expected to generate surfaces that are less hydrophobic than expected.

Although the samples reacted with dichlorodimethylsilane and the electrochemically methylated samples displayed the same water contact angle, the dimethylsiloxy terminated samples exhibit a significantly smaller r value than the methyl terminated samples. We attribute this difference to the presence of the Si-O bonds attaching the dimethylsilyl species to the surface and the underlying oxidized porous Si material. Liquid water only probes the hydrophobic methyl groups on the outermost layer, whereas water vapors can penetrate to the more hydrophilic oxides. The electrochemically methylated material has much less oxide and so is expected to exhibit hydrophobic characteristics to both liquid and gas phase water. The water contact angles of the thermally acetylated samples showed no obvious correlation with the measured r value, attributed to the surface heterogeneity produced by the acetylation reaction.

Only two samples exhibited r values greater than 1.0: the acetylated samples prepared at 500°C (r = 2.9) and at 485°C (r = 5.0). The ATR-FTIR spectra of the samples prepared at 485 °C displayed more intense C-H stretches at 3055 and 2900 cm^{-1} than samples prepared at 500 °C, indicative of a greater degree of hydrophobicity that is consistent with the relative r values measured and with previous studies.[177] Acetylated samples prepared at temperatures > 500 °C appear black and lack an observable reflectivity spectrum. Salonen and coworkers have proposed that the reaction of acetylene with porous Si at temperatures > 500 °C could lead to significant

carbonization,[165] and the black appearance is attributed to carbonaceous deposits on the porous Si surface.

3.4.3 Stability of Chemically Modified Bulk-Attached Porous Si Sensors

In order to screen the surface modifications for surface chemistries that yield stable, contrasting responses to the analytes, the reproducibility of the vapor response of the chemically modified porous Si chips was examined over a period of 15 days for bulk-attached porous Si layers.

Seven of the ten surface types were studied: native surface (Si-H), ozone oxidized (Si-OH), thermally oxidized (Si-O-Si), dodecyl terminated (Si-$(CH_2)_{11}CH_3$), methyl terminated (Si-CH_3), dimethylsiloxy terminated (Si-O-Si$(CH_3)_2$-O-Si), and acetylated at 485°C (Si-C). Samples were stored at ambient in the laboratory atmosphere and then exposed to 500 ppm of isopropanol and heptane vapors 1, 8 and 15 days after chemical modification. Figure 3.4 displays the average responses and r value of each chemically modified sample. ATR-FTIR spectra were acquired for every sample on each of the three sampling days.

Samples with the native Si-H surface displayed a slight increase in their response to isopropanol over the 15-day period, with the ATR-FTIR spectra of the native samples displaying an increase in the band associated with Si-O-Si stretching vibrations at 1050 cm^{-1}. Ozone oxidized samples displayed no change in analyte response or in the ATR-FTIR spectrum, within the error limits of the experiments. Thermally oxidized samples displayed an increase in response to isopropanol during the first 8 days, though the response was stable from that point on. No significant

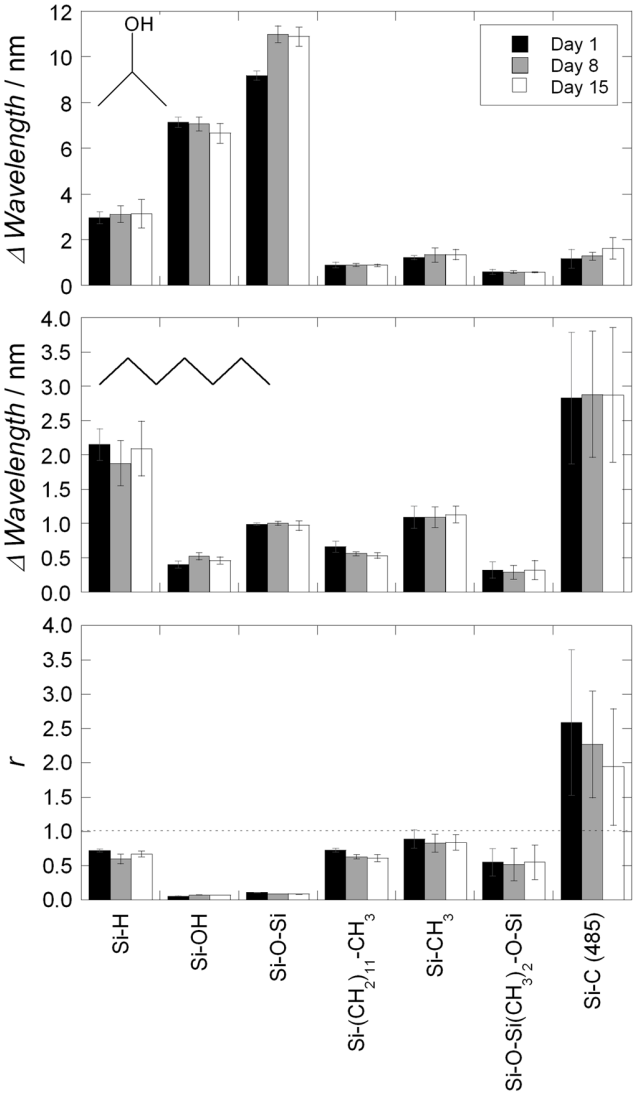

Figure 3.4 Response of chemically modified porous Si photonic crystal samples to isopropanol and heptane vapors as a function of storage time (in air). **Top and Middle:** Vertical bars indicate the increase in wavelength ($\Delta\lambda$) of the resonant spectral peak of the photonic crystal upon exposure to 500 ppm isopropanol (Top) or 500 ppm heptane (Middle), for the indicated surface chemistries. Responses measured on day 1 (black bar), day 8 (grey bar) and day 15 (white bar). **Bottom**: r value, the ratio of the heptane response to the isopropanol response (see eq. 3.2). Horizontal dashed line at r = 1.0 separates samples that display a greater response to heptane (r > 1) from those that display a greater response to isopropanol (r < 1). Values are the average of 5-6 samples; error bars represent one standard deviation. Simplified surface chemistries are described in Table 1: Si-H (native surface of porous Si); Si-OH (ozone oxidized); Si-O-Si (thermally oxidized at 600 °C); Si-$(CH_2)_{11}CH_3$ (hydrosilylated with dodecene); Si-CH_3 (electrochemically methylated); Si-O-Si$(CH_3)_2$-O-Si (modified with dimethylsiloxane); Si-C (485) (acetylated at 485 °C).

change was observed in the heptane response. No detectable changes were apparent in the ATR-FTIR spectra during the 15-day period.

Samples modified with dodecyl, methyl and dimethylsiloxy groups retained the same response to heptane and isopropanol vapors within the error limits for the duration of the 15-day test. However, ATR-FTIR spectra of dodecyl modified samples displayed prominent Si-O-Si and C-H bands at day 1, which decreased in intensity by day 8. No further changes in the ATR-FTIR spectra were noted at day 15. ATR-FTIR spectra of electrochemically methylated samples showed a slight growth of the oxide band at 1050 cm^{-1}, while spectra of the dimethylsiloxy modified samples remained the same over the 15-day period.

Overall, the average heptane and isopropanol response of samples reacted with acetylene at 485°C showed a slight increase in heptane response a larger percent increase in isopropanol response, leading to a net decrease in the response ratio r over the 15-day period. This may be due to oxidation of surface Si-H species that were not reacted with the acetylene to form Si-C. Surface heterogeneity could contribute to this partial surface coverage of Si-C bonds. There was also large variation in analyte response between individual samples, leading to the large error bars in the data shown in Figure 3.4. We attribute this variation to surface heterogeneity, which was also evident in the water contact angle measurements. To correct for this, optimization of the acetylation procedure is needed. For example, Jalkanen and coworkers place samples in a sealed quartz tube under a flow of nitrogen followed by acetylene prior to placement of the sample and tube into a furnace.[77]

As a result of the above vapor dosing evaluations, the thermally oxidized and acetylated (485°C) surface chemistries were chosen for coupling to optical fibers as contrasting hydrophilic and hydrophobic porous layers. For comparison, sensors with the native Si-H surface were also coupled to optical fibers and employed in remote sensing applications.

3.4.4 Remote Sensing by Attachment of Free Standing Porous Si Films to Optical Fibers

Sensors with a small form factor are amenable to volume volume-constrained sensing environments like activated carbon filtration cartridges [37]. The chip-based porous Si sensors discussed so far have a diameter of ~ 1.2 cm. Previous work has shown that the active porous sensing layer can be removed from the Si substrate and fractured into particles of <500 μm diameter.[24, 61] Referred to as "smart dust," the small particles retain the gas adsorption properties and sensing capability of the original bulk-attached films.[9] In this work, such freestanding porous Si particles were attached to the tip of 600 micron diameter optical fibers (Figure 3.5) as previously demonstrated in Chapter 2.[37] The process produces no significant change in the reflectivity spectrum relative to the original chip-based sensors. The small size of the optical fibers allows multiple sensor probes to be placed in a remote location of limited space.

To better differentiate between classes of analyte vapors, three porous Si surface chemistries covering a range of hydrophobic/hydrophilic characteristics were chosen. Chemical modifications that displayed large differences in their relative

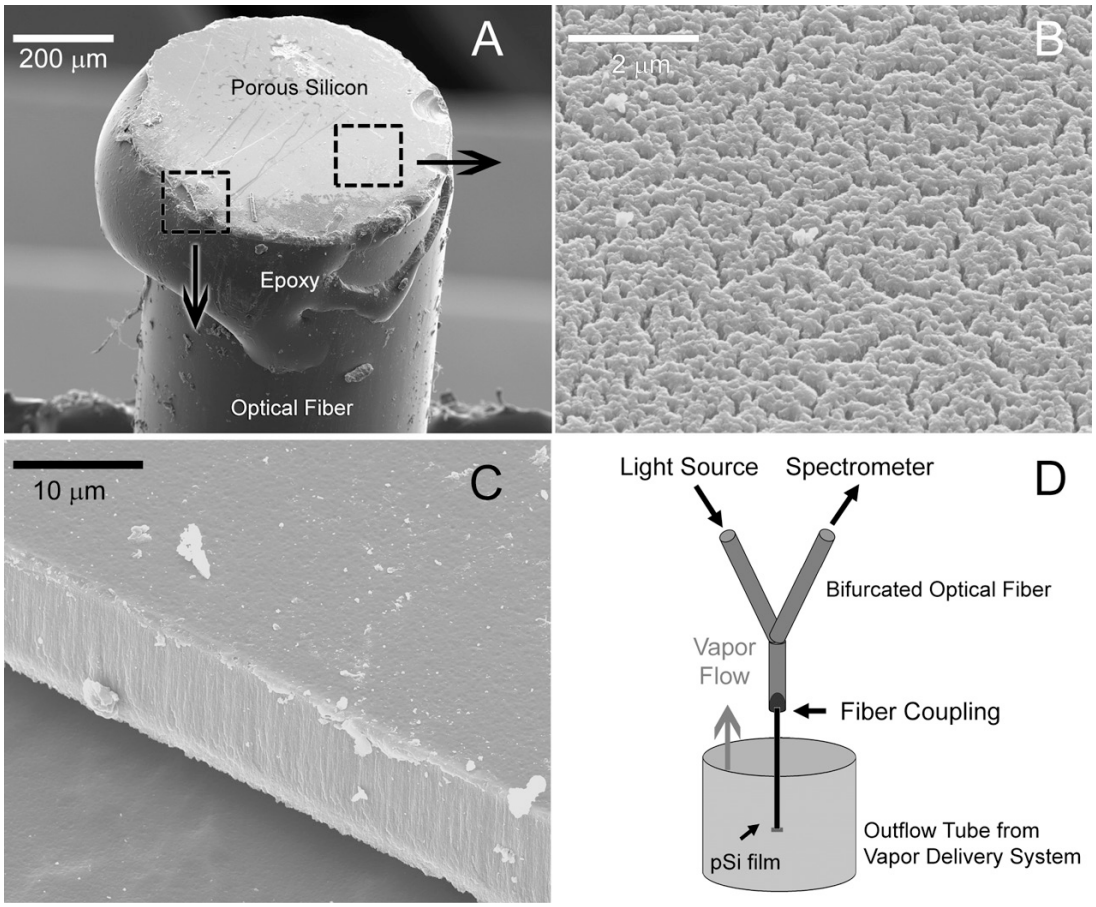

Figure 3.5 **A:** Scanning electron microscope (SEM) image of an optical fiber capped with a porous Si vapor sensor (rugate filter). The porous Si layer was prepared as a freestanding film and attached to the glass fiber with epoxy. **B:** planar surface view SEM image of the porous Si. **C:** profile view of the porous Si layer on top of the epoxy. The vertical striations in the middle of the image are the pore channels in the material. **D:** Schematic depicting the optical configuration used for testing remote sensing. The fiber-coupled porous Si sensor was inserted into the outflow tube of the vapor delivery system to test the sensor response to different concentrations of heptane and isopropanol. The proximal end of the fiber was coupled to a bifurcated optical cable, with a white light source at one arm and a spectrometer at the other.

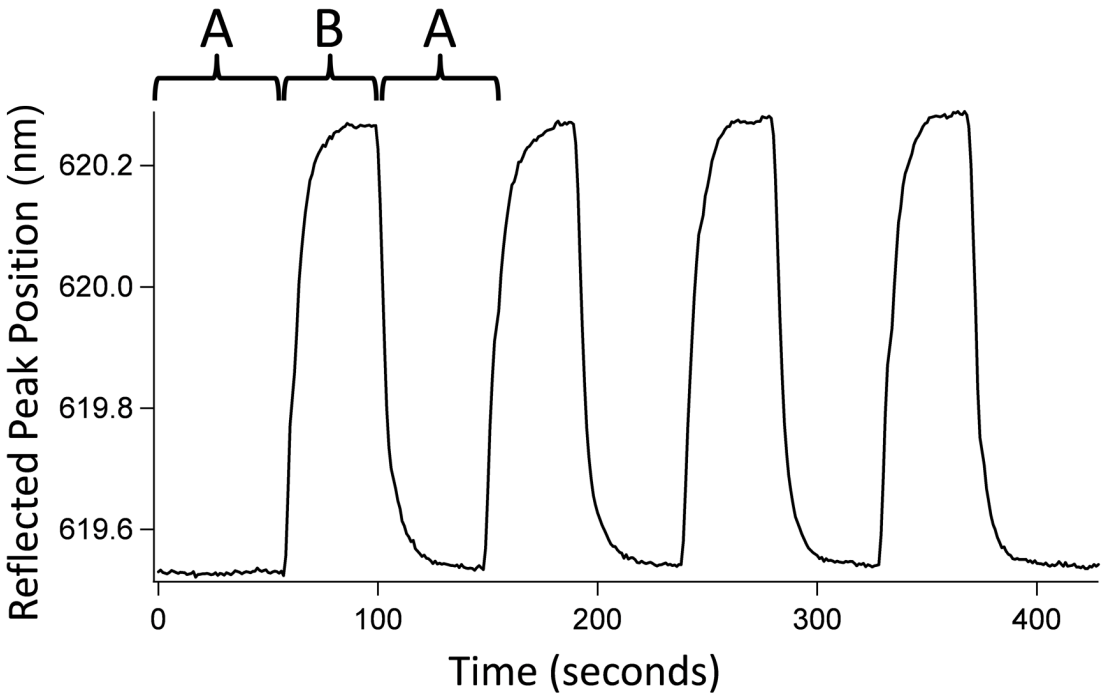

Figure 3.6 Reversibility of the sensor response to repeated 500 ppm doses of isopropanol. A thermally oxidized porous Si photonic crystal was coupled to an optical fiber and placed in the outflow tubing of the vapor delivery system as depicted in Figure 3.5. The sensor was exposed to alternating segements of pure nitrogen at 1L/min for 50 sec (segement A) and 500 ppm of isopropanol in nitrogen at the same flow rate for 40 sec (segment B).

analyte responses, based on r values, were used in the fiber-based sensor experiments: native surface porous Si (Si-H, r = 0.74), thermally oxidized (Si-O-Si, r = 0.11), and thermal acetylation at 485 °C (Si-C, r = 5.0). Because the acetylation chemistry was highly variable, a single batch of acetylated porous Si films were used for all the fibers in this study.

Porous Si photonic crystals were etched as described above. After etching, the porous layer was removed from the bulk Si using an electropolishing etch. The free-standing porous Si films were then immediately functionalized by a thermal treatment in either air (Si-O-Si) or acetylene (Si-C) as described in section 3.4.1, or left unmodified in the case of the native surface chemistry (Si-H). Optical fiber was cleaved to a desired length, stripped at both ends of the outer cladding layer, and polished on aluminum oxide lapping film to provide a smooth tip for optimal light coupling. The free-standing 500μm diameter porous Si particles were attached to the tips of the fibers using a partially cured Bisphenol A epoxy/modified aliphatic amine curing agent mixture and allowed to cure at room temperature for two days before use. Other adhesive mixes were evaluated as described in section 3.4.5.

The fiber-coupled porous Si sensors responded to low concentration doses of analyte vapors in less than a minute. In Figure 3.6, an oxidized porous Si sample coupled to an optical fiber was exposed to repeated cycles of a flow of pure nitrogen for 40s followed by 500 ppm IPA for 50s. The change in the spectral peak position of the photonic crystal over time is plotted in the figure, and exhibits a reversible response to organic vapor and a fast equilibration time, reaching an equilibrated response to each vapor exposure in less than a minute. This fast, reproducible response is desirable for

concentration monitoring applications, like monitoring activated carbon beds for organic breakthrough as detailed in section 3.4.7.

3.4.5 Adhesive Selection for Fiber Optic Porous Si Attachment

In contrast to the relatively stable response of the thermally oxidized porous Si layers, the acetylene-reacted surface chemistry (Si-C) exhibited degradation over two weeks for bulk-attached porous Si chips, as shown in Figure 3.4. The choice of adhesive used to mount porous Si films to the optical fiber may further exacerbate this degradation. In Chapter 2, a widely available epoxy adhesive was used for porous Si fiber mounting as a common, cheap means of fiber coupling. A multitude of adhesives are available for coupling the films to the optical fibers. Adhesion of one material to another can be grouped into several mechanisms: electrostatic attraction, adhesion by mechanical interlocking, and the formation of chemical bonds [178, 179]. Adhesives that chemically bond, like silane coupling agents, are not preferable since they may alter the desired surface chemistry of the porous Si films.

Urethane or isocyanate adhesives generally bond by the reaction of isocyanate groups with primary and secondary hydroxyl groups. Since this may allow bonding of the adhesive to the porous Si sensor surface, resulting in an altered vapor response, such adhesives are undesirable [178]. Acrylic adhesives cure by chain growth polymerization of acrylic monomers [178]. To prevent premature polymerization, commercial monomers have inhibitors added, which may leech into the porous structure and effect the sensor response. The low viscosity of these adhesives is also undesirable for preventing penetration of adhesive into the porous layer. Cyanoacrylate

and methyl methacrylate formulations (Loctite 495, Loctite 409) were briefly tested for coupling porous Si to the optical fibers, but the response of the fiber-coupled sensors to analyte vapors was found to be highly variable.

With epoxy adhesives, the dominant adhesive force is electrostatic attraction of polar groups between the cross-linked epoxy polymer and surface. Typically, precursor backbone molecules containing epoxide groups are cross-linked by step or chain-growth polymerization, with the resulting polar polymer linkages from the epoxy ring reaction providing adhesion [179]. Epoxies are cheap, durable, and exhibit good chemical resistance and low reactivity. Based on these factors, epoxy was selected as the adhesive for sensor construction.

3.4.5.1 Epoxy Formulations

Despite the advantages of epoxies as an adhesive class, the specific epoxy used in Chapter 2 resulted in Si-C acetylated-surface sensors with a highly variable response, as shown in Figure 3.7. In this figure, the response ratio (heptane:ipa) of several sensors constructed with 2-Ton epoxy (Chapter 2) is compared to the Bis-A-Ancamine 2432 epoxy formulation selected in this chapter. The 2-Ton epoxy significantly decreases the consistency of the sensor response for the Si-C surface, while showing no impact on the thermally oxidized surface. Components of the 2-Ton epoxy may have leeched into the porous matrix and promoted oxidation of Si-OH and Si-H species that had not been reacted to form Si-C in the surface preparation. Additionally, the variability may be due to the mechanical properties of the epoxy and

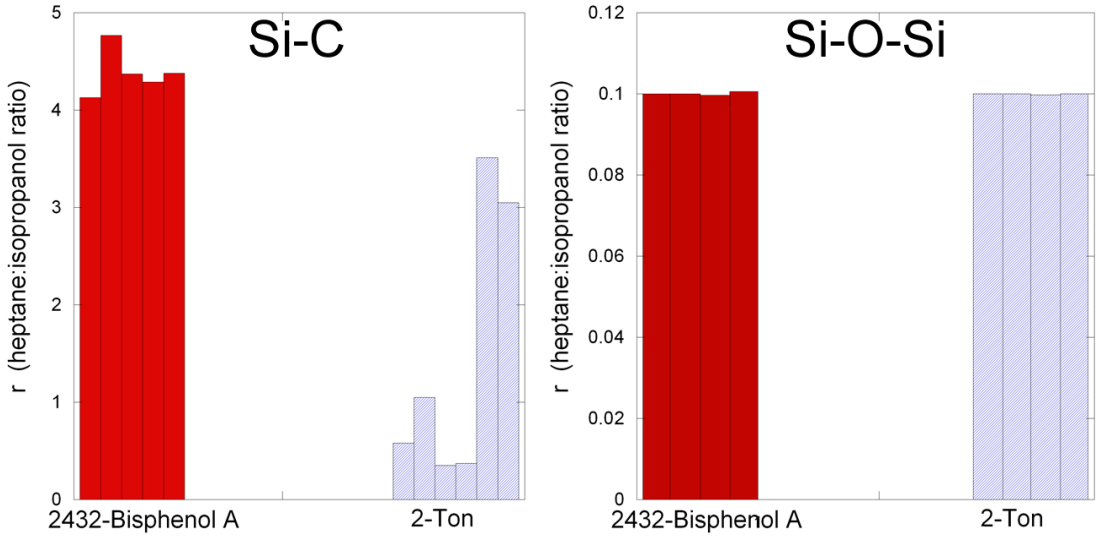

Figure 3.7 Influence of the epoxy used to attach the porous Si films to the optical fiber. As seen in Figures 3.3 and 3.4, the acetytlated surface chemistry (Si-C) (left) has a high variability of the bulk-attached sensor response. This variability is exacerbated by using 2-Ton epoxy, which contains filler materials, compared to more pure epoxy components, such as Ancamine 2432 and Bisphenol A (diglycidyl ether of bisphenol-A). Each vertical bar represents a separate porous Si-coupled optical fiber. The thermally oxidized surface chemistry (right) exhibited excellent consistency among the responses of each sensor regardless of the type of adhesive used. All responses were evaluated 24 hours after porous Si chemical modification and attachment to optical fibers.

inconsistencies of the epoxy cure, of the contact with the porous layer surface, and of the degree of penetration of epoxy components into the sensor surface.

2-Ton binary epoxy (ITW Devcon) contains the widely used diglycidal ether of bisphenol A (DGEBA) epoxy resin. The second component, according to materials safety data sheets, contains an aminoethyl piperazine (aliphatic amine) curing agent and nonylphenol nonreactive diluents. These nonreactive diluents compose 75% of the second component weight, suggesting their role in the response variability. Such low

molecular weight materials can be drawn into the surface of porous adherends [178], and solvents in the adhesive can swell the adherend or degrade parts of the surface. To improve consistency of the fiber-coupled sensor responses, commercial epoxies with nonreactive components were avoided. Instead, known resins and curing agents were selected and mixed in proper stoichiometric ratios.[180]

To accomplish this selection of a suitable diluent-free, filler-free epoxy formulation, data sheets of adhesive properties from several companies (Air Products, DOW Chemical, ITW Devcon, Hexion Corporation, Reichhold Inc.) were first screened for desirable physical and chemical epoxy properties, including a high viscosity to prevent porous layer penetration, fast cure times at room temperature, low color (Gardner scale), and excellent aqueous and chemical resistance. Water and chemical resistance was assessed by examining published studies of the weight change of cured epoxies exposed to liquid chemicals over time[181]. Three epoxy resins and four curing agents were selected for basic screening. The resins were: DEGBA (Bis-A), a very common epoxy resin; DGEBF (Bis-F, diglycidyl ether of bisphenol F), a resin with improved solvent resistance compared to Bis A [182]; and a Novolac (glycidyl ethers of phenolic novolac) resin, with multi-epoxy functionality[182] and the stability of the phenol-formaldehyde backbone[183]. The multiple epoxide groups in the novolac resin allow a high cross-link density, resulting in excellent temperature, chemical, solvent, and humidity stability.

Aliphatic and cycloaliphatic amine curing agents were chosen based on published chemical and physical properties [184]. Epoxy curing agents include various primary or secondary polyamines, cyclic amines, anhydrides, and polyamids[182].

Primary and secondary amines are highly reactive with epoxy, with multifunctional amines reacting with polymer resins through step- growth poymerization of the epoxide resin with the curing agent, resulting in highly crosslinked networks[178]. For instance, the reaction of a primary amine with an epoxide group proceeds as:

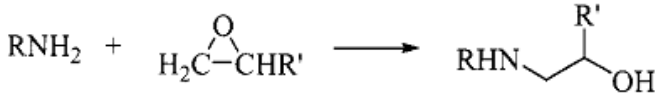

(3.3)

The secondary amines that are generated may then further react with another epoxide group, with the hydroxyls thus formed then reacting with additional epoxy groups to form an ether linkage. This allows cross linking of the resin and curing agent [178]. Several aliphatic and cycloaliphatic amines with good chemical resistance and low curing temperature were selected[184]. Although simple amines can cure epoxide polymers rapidly, liquid diamines or polyamines with flexible backbones lead to tougher, more flexible cured adhesives[178], useful in the remote sensing application here. Therefore, curing agents consisted of: Ancamine 2432, a modified aliphatic amine with very good chemical resistance and a low temperature cure; Ancamine 2423, a modified cycloaliphatic amine with low color and good water and acid resistance; Ancamine 2587, a modified cycloaliphatic polyamine that also shows excellent solvent resistance; and Ancamine MCA, another modified cycloaliphatic amine with good chemical resistance .

3.4.5.2 Influence of Epoxy on Acetylated Fiber Stability

The bulk-attached acetylated porous Si layers exhibited a steady decrease in the sensor response ratio of heptane:IPA at 500ppm over the 15-day study period for bulk-attached chips stored at ambient. Binary epoxy formulations using known resins and curing agents, free of filler materials and diluents, were assessed to determine the resin-curing agent pair that yields the least additional degradation of the acetylene response ratio as well as the best consistency in sensor response over multiple samples. The additional degradation of Si-C surfaces may occur from the breakdown of filler materials or unreacted resin or curing agent components [178] that promote oxidation of inreacted surface bonds. Further, variability may arise from the consistency of the attachment methodology, due to the viscosity and cure characteristics of each resin-curing agent pair, which influence the morphological properties of the porous Si-epoxy interface and degree of penetration of the epoxy into the porous Si layer. In Figure 3.8, the response ratio of acetylated (485°C) fiber-coupled sensors is plotted over 15 days for parings of four curing agents and three epoxy resins. The resins (Bisphenol A, Bisphenol F, and Novolac) are designated by different symbol shapes in the plots. Each of the four panels corresponds to a curing agent (Ancamine 2432, MCA, 2587, and 2423) as previously described. As before, the ratio (heptane:ipa response) was determined by dosing each fiber twice with 500 ppm heptane and 500 ppm IPA.

The response ratios over time for each of the resin-curing agent pairs is similar, with the Ancamine 2432 yielding the most consistent response. The DGEBA and Novolac resins also exhibited more consistent responses than the DGEBF (Bisphenol-F) resin. The response of a bulk-attached acetylated sample chip is shown in the upper

left panel, for comparison of the chip response to the fiber-mounted film response. All fiber-coupled films exhibited lower initial response ratios and a greater rate of degradation of the response ratio over time than the bulk-attached chips. As described in the next section, where lift-off films of acetylated porous Si were physically mounted to the optical fibers without adhesive, this greater degradation rate may be due not to the adhesive but to the increased diffusion and flow of ambient air into the porous structure for lifted-off films, compared to layers attached to bulk on one side[185]. In contrast to the acetylated porous Si films, the thermally oxidized surface chemistry was highly consistent (Figure 3.7) and stable, displaying no discernible difference in response ratio between bulk-attached chip sensors and lifted-off, fiber-coupled sensor films.

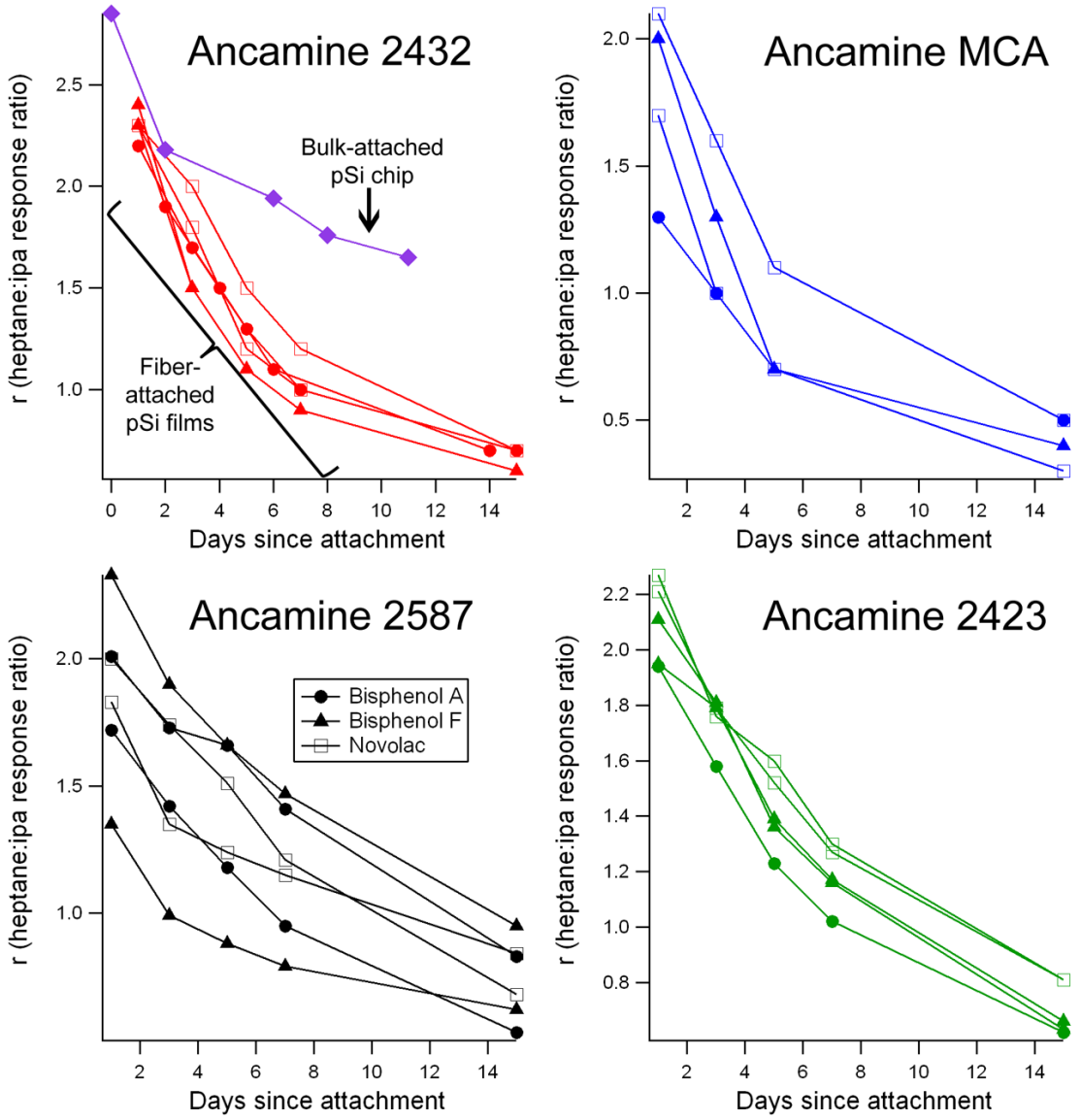

Figure 3.8 Response of acetylated (Si-C, 485°C) porous Si photonic crystal samples to isopropanol and heptane vapors as a function of storage time (in air) for various epoxy resins and curing agents. The vertical axis shows the ratio of the heptane:isopropanol response of each fiber at 500ppm. Each solid line represents a seprate porous Si-coupled optical fiber sample. The four panels represent different epoxy curing agents used in each sensor's adhesive formulation (Ancamine 2432, MCA, 2587, and 2423), while the data point symbols represent the resin utilized (Bisphenol A, Bisphenol F, and Novalac). All resin-curing agent pairs exhibited similar degradation of the response ratio over 15 days, though adhesive fomulations with Ancamine 2432 showed the least variation among resins and among multiple samples of each resin. The response of the acetylated porous Si not lifted off from the bulk (bulk-attached) ias diamonds in the upper left plot for comparison.

3.4.5.3 Adhesive-free Fiber Mounting of Freestanding Porous Si

For the acetylated porous Si (485°C reaction temperature), a greater rate of degradation of the sensor response ratio was observed for fiber-mounted films compared to that of the bulk-attached chips. The degradation rate appeared relatively independent of the choice of epoxy resin and curing agent (Figure 3.8), indicating that the epoxy formulation had a negligible effect on the sensor surface.

Instead, the act of lifting the porous Si layer from the bulk Si chip may be responsible for the higher degradation rate of the heptane:IPA ratio, since lifted-off layers were acetylated as free standing films while bulk-attached chips were acetylated with only one side of the porous layer exposed to acetylene, with the other side of the layer attached to bulk silicon. Differences in acetylene reaction dynamics may have yielded lift-off films with considerably less surface coverage of Si-C, since the temperatures and accessible pore surface strongly influence resulting surface properties in the acetylation reaction[186, 187]. Less Si-C coverage, in turn, allows for more oxidation of the samples over time, consistent with the observed decrease in the heptane:IPA response ratio. Further, the act of lifting off the porous Si layer may allow better penetration of ambient oxygen and water vapor into the samples, contributing to oxidation of surface sites not reacted with acetylene.

To compare the response of free-standing porous Si layers coupled to fibers with and without adhesive, acetylated porous Si films were placed inside a porous metal cap (Mott Corporation) as pictured in Figure 3.9. This allowed optical interrogation of the porous Si film by physically butting the film against the end of a polished 600um optical fiber. The response ratio of the metal-capped fiber over time

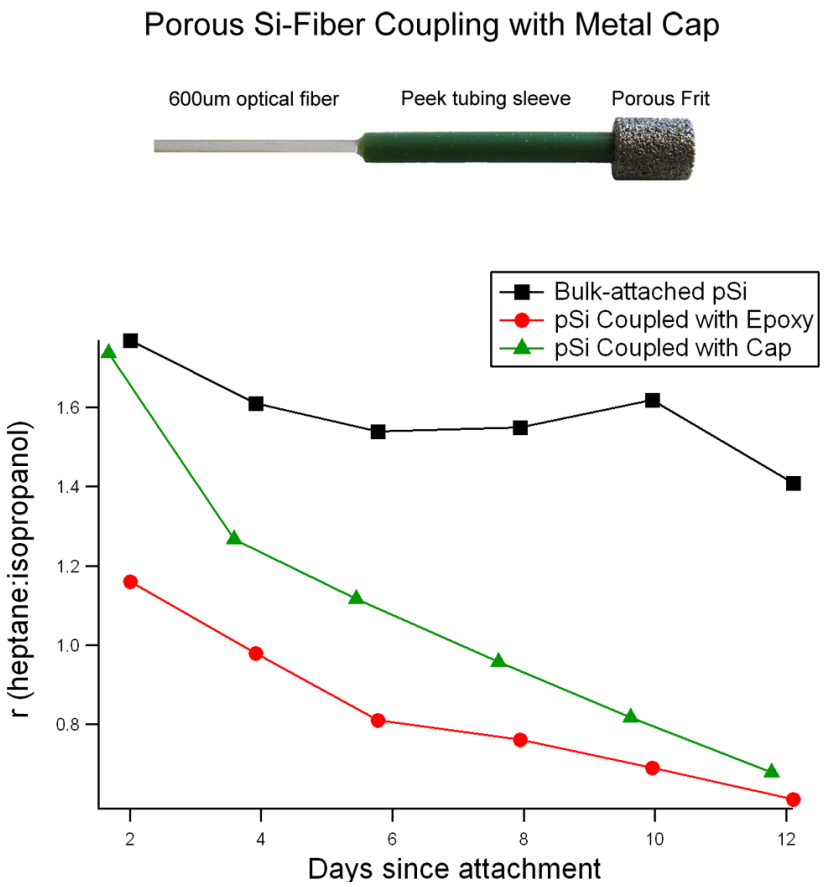

Figure 3.9 Response ratio (heptane 500ppm to isopropanol 500ppm) over time of acetylated (Si-C, 485° C) porous Si film, comparing physical (1) attachment of a piece of the porous Si film to the optical fiber by placing the film in a porous frit butted to the distal end of the fiber, to (2) a section of the same film attached to the optical fiber with adhesive (Bis-A / Ancamine 2432), to (3) a porous Si layer similarly acetylated (Si-C, 485°C) but not removed from the bulk Si or attached to an optical fiber. Both lifted-off porous layers show similar response curves, with the ratio of the responses degrading more quickly than the bulk-attached porous silicon.

exhibited a similar response-time profile as the sample coupled to the fiber the epoxy (DGEBA-Ancamine 2432), where both were constructed using the same acetylated porous Si film. A separate acetylated sample was prepared by acetylation of a bulk-attached porous Si chip at 485°C, which exhibited a lesser rate of degradation of the heptane:IPA response ratio. This is consistent with the differences in the acetylation

process between liftoff films and chips, not the choice of diluents-free epoxy, being responsible for the greater decrease of surface stability of Si-C liftoffs than bulk-attached chips.

3.4.5.4 Adhesive Selection Summary

In summary, the thermally oxidized surface chemistry provides a relatively stable and highly reproducible hydrophilic surface. Thermal acetylation at 485°C yields a hydrophobic surface (large ratio r) that slowly degrades over two weeks, with the rate of degradation higher for lifted-off films than for bulk-attached chips. The large fractional content of nonreactive fillers in the 2-Ton epoxy used in Chapter 2 yielded mechanical and chemical properties that resulted in inconsistent attachment and sensors responses. Using epoxy resin and curing agent components without filler or diluents resulted in significantly greater consistency (Figure 3.7) with small differences in the degradation profiles of the various epoxy formulations. Coupling free standing layers to the optical fibers with epoxy yields a smaller sensor footprint than cupping the film to the fiber mechanically with a cap, with both approaches yielding similar stability profiles of the sensor material, indicating that the higher degradation rate of lifted-off Si-C films than chips is due to differences in the acetylene reaction conditions. Based on the physical properties of the epoxy choices including color, aqueous and solvent resistance, and observed sensor-coupled consistency, Ancamine 2432 and DGEBA were selected as the binary adhesive pair used in the sections below. To compare calibration and breakthrough monitoring with fibers of various surface

chemistries, all vapor calibrations and carbon bed breakthrough experiments were performed with fibers aged 2 days after attachment of the porous Si film to the fiber.

3.4.6 Calibration of Porous Silicon-Coupled Fibers to Isopropanol, Heptane, and Relative Humidity

The proximal end of each porous Si-tipped optical fiber was coupled to a bifurcated optical fiber assembly, with one arm of the bifurcation leading to a light source and the other to a CCD spectrometer. The spectrum of light reflected off of the porous Si sensor could therefore be monitored from the epoxy-attached side of the porous film, leaving the other end open to analyte vapor penetration (Figure 3.5). The sensors were calibrated with isopropanol and heptane vapors in a carrier flow of ambient air. Reflectivity peak spectral positions were recorded in air at ~36% relative humidity and room temperature. Analyte concentrations of 50, 100, 200, 400, 500, 600 and 800 ppm were introduced sequentially, with an air purge in between each dose to return the sensor response to the initial baseline reading. Results are displayed in Figure 3.10. As expected, exposure to isopropanol produces the largest wavelength shift in the Si-O-Si sample, followed by Si-H and Si-C. The wavelength shift measured for the Si-H and Si-C samples is linear with IPA concentration over the range tested, while the Si-O-Si sample response curve increases more sharply at lower concentrations. All three surface chemistry types display a relatively linear response to heptane vapor, with Si-C samples displaying the greatest change in reflectivity peak wavelength upon exposure to heptane, followed by Si-H and then Si-O-Si. The inversion of responses between Si-O-Si and Si-C to the vapors, in which Si-O-Si

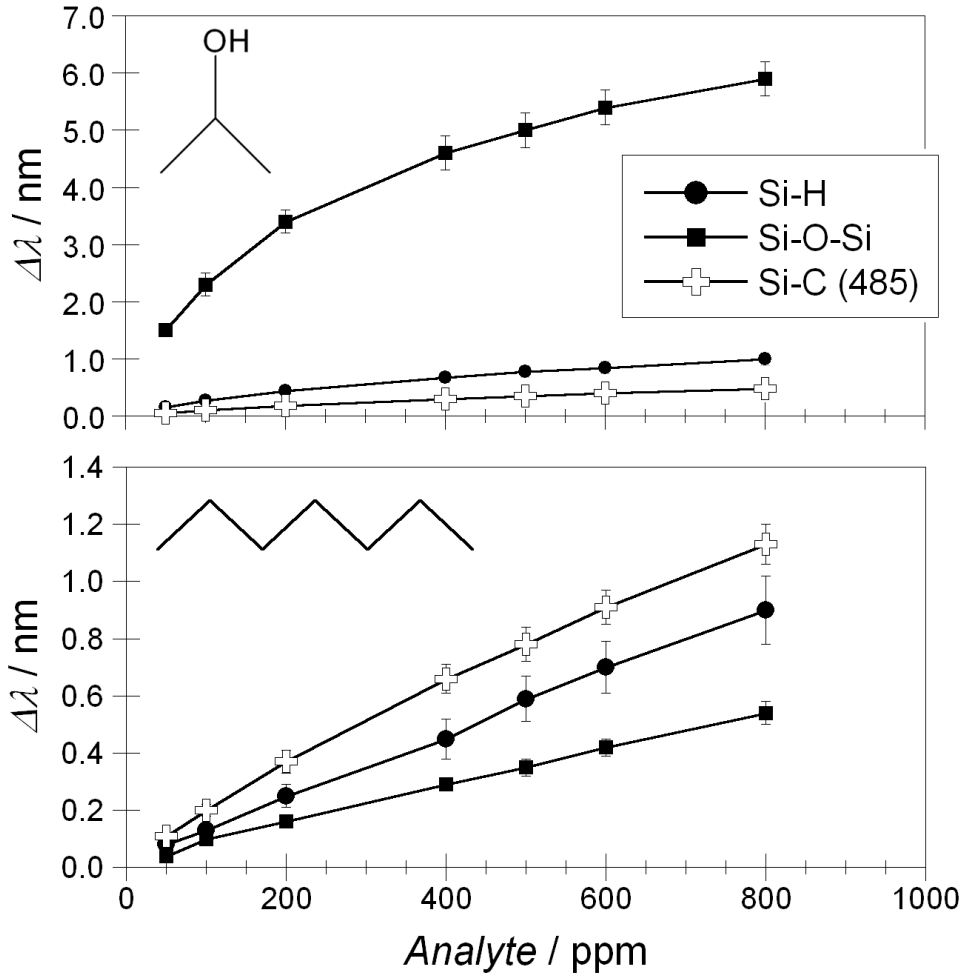

Figure 3.10 Dose-response curves for fiber-mounted optical porous Si sensors exposed to the analytes isopropanol (top plot) and heptane (bottom plot). Surface chemistries on the porous Si samples were: hydrogen-terminated (Si-H, circles), thermally oxidized (Si-O-Si, squares) or thermally reacted with acetylene at 485 °C (Si-C, plus sign symbols). Lines between points are included as a guide to the eye. Values displayed represent an average of 6-9 samples, error bars correspond to 1 standard deviation.

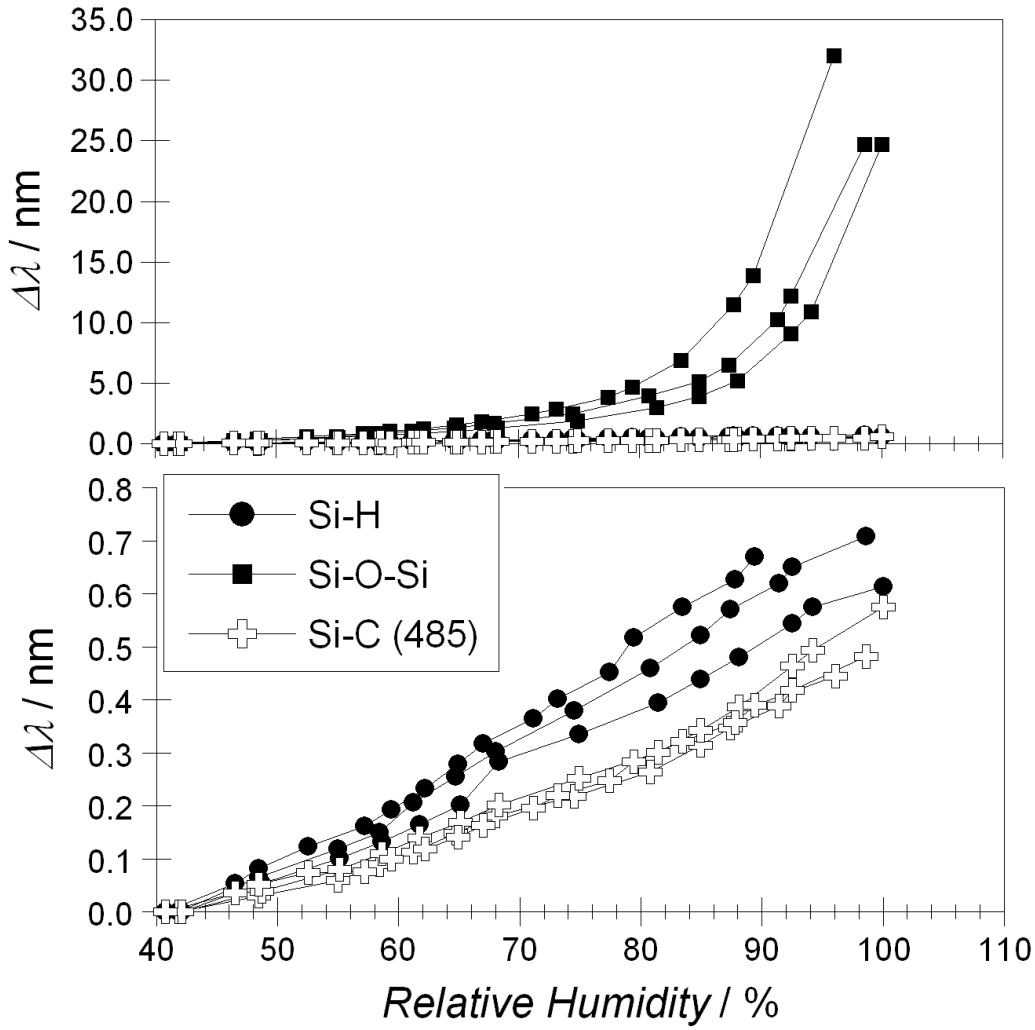

Figure 3.11. Response of fiber-mounted optical porous Si sensors to relative humidity (RH). Samples are: native surface porous Si (Si-H, gray circles), thermally oxidized (Si-O-Si, black squares) and thermally reacted with acetylene at 485 °C (Si-C, white plus symbols). All data points represent the change in wavelength of the reflectivity peak as a function of RH, relative to the wavelength value at RH = 41.5%. Data from 9 samples are shown, representing 3 samples for each of the 3 different surface chemistries. (Top) Chart comparing all three sample types. (Bottom) Plot expanded along the y-axis, showing only the Si-H and the Si-C samples.

exhibits a greater response to IPA than Si-C while Si-C exhibits a greater response to heptane than Si-O-Si, is expected, based on the r values discussed above (heptane:ipa response ratio) for bulk-attached chip samples and on the difference in hydrophobicity between the oxidized and thermally acetylated surfaces. The freshly prepared Si-H samples, with a surface hydrophobicity between that of Si-C and Si-O-Si, exhibits a response to each vapor between those of the other surface chemistries tested, as expected.

The permissible exposure limits (PEL) for volatile organic compounds published by the Occupational Safety and Health Administration (OSHA) is generally reported as a time weighted average (TWA), where the value is the average VOC exposure limit over a set time (usually eight hours). The OSHA PEL (TWA) for isopropanol is 500 parts per million (ppm),[188] and for heptane it is 500 ppm.[188] As shown in Figure 3.10, the fiber-mounted porous Si sensors are capable of detecting these analytes at lower concentrations than the two OSHA PELs.

To probe the effects of relative humidity (RH) on the porous Si capped fiber sensors, samples were exposed to stepped increments of ~5% RH beginning at a RH ~ 41.5% (Figure 3.11) in a flow of 32L/min of air. Due to the long time required to decrease the RH in the Miller-Nelson conditioning system, purging of the samples was not performed between RH values. Hysteresis of sample response therefore was not examined. The response curves are similar to the isopropanol curves, and an expected trend for a polar analyte: the oxidized Si-O-Si sample displays the largest response. Si-H samples display the next largest response, followed by Si-C samples. The dose-response curves of Si-H and Si-C samples are approximately linear; Si-O-Si exhibits a

decrease in sensitivity with increasing concentration. Figure 3.11 compares the response of the 3 surface chemistries. Relative humidity exerts a large effect on the reflectivity peak position of the oxidized sample since the polar surface facilitates greater adsorption of the water vapor, producing a total wavelength shift of 30 nm when relative humidity changes from 41.5% to 99%. By comparison, the more hydrophobic Si-H and Si-C samples display relatively minor responses of < 0.8 nm over the same relative humidity change. The results are consistent with the measured sessile drop water contact angle measurements, where thermally oxidized (Si-O-Si) chips show a small contact angle of 20°, while the corresponding value for Si-H is 102°.

3.4.7 Sensing Vapor Breakthrough in Activated Carbon Respiratory Cartridges

Optical fibers with chemically responsive sensor heads on their distal end are widely used as remote sensors[131, 133, 189, 190] for detecting vapor-phase organic compounds[38, 133], relative humidity[38] and aqueous biomolecules.[129, 191, 192] The small form factor (diameters of a few hundred microns and active regions < 1 mm) allows their use in volume-constrained applications, such as the activated carbon filtration cartridge of an air purifying respirator (APR).[37, 150] Health and safety regulations in the United States require the use of end-of-service life (ESL) indicators on APRs but allow for the use of service life calculators.[139, 140] However, these calculators may require a level of expertise not present in many industrial settings and are subject to the variability of environmental conditions which could result in overexposure to vapor contaminants. End-of-service life indicator cartridges would improve the safety of the

APR user by shifting the burden of service life determination from the user to an electronic ESL system,[139, 140] as mentioned in Chapter 2.

In the last chapter, native porous Si (Si-H)-capped optical fibers were used to demonstrate sensing of analyte breakthrough in a small ampoule packed with activated carbon.[37] Although this demonstrated proof-of-principle, the Si-H chemistry used in that work is not sufficiently stable to be of practical use. In the present work, we find that chemically modified porous Si-capped fibers display improved stability under relevant environmental conditions. The fibers were tested in a full-size activated carbon respiratory cartridge simulator. The cartridge simulator contained two sampling ports for a conventional gas chromatograph (GC), one at the middle of the bed of activated carbon (mid bed) and a second located at the air outlet of the simulator box (end bed). Three holes were tapped into the cartridge chamber to accommodate the fiber sensors, and the entire assembly was placed in a stainless steel containment vessel, as picture in Figure 3.12.

Three porous Si-coupled fibers containing the Si-H, Si-O-Si, and Si-C surface chemistries described above were positioned at the mid-point of the carbon bed and the bed filled with activated carbon. In Figure 3.13, air containing 500 ppm isopropanol was passed through the cartridge chamber. The responses of the porous Si sensors and the GC probes are shown. To establish an initial baseline of the sensor response, the position of the reflectivity peak of the sensors was monitored in the carbon bed with no air flow for 5 min prior to introduction of the 500ppm vapor stream in air, with the reflectivity peak position of the sensors remaining constant during this period. Air

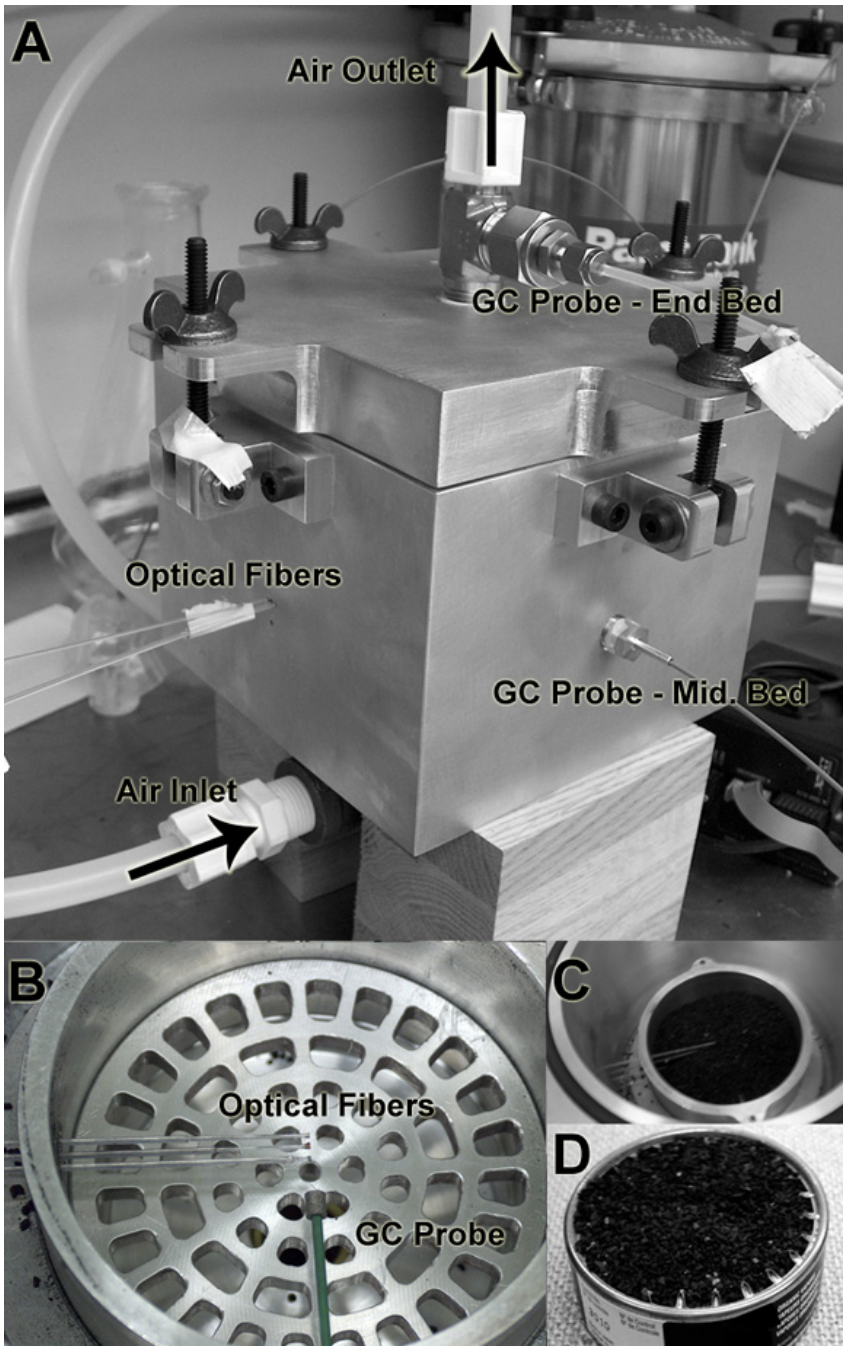

Figure 3.12 Respirator cartridge simulator. **A:** Simulator box containing air inlet and outlet, GC probe ports at mid-bed and air outlet, and holes for the porous Si tipped optical fibers. **B:** Inside the simulator box is a smaller chamber that can hold 50 g of activated carbon. Optical fibers and the mid bed GC probe are visible. **C:** The smaller chamber partially filled with activated carbon particles. When completely filled, the carbon is kept in place by filter paper placed on the bottom and top of the chamber. **D:** An opened commercial activated carbon respirator filtration pack for comparison.

flow (containing isopropanol at a relative humidity of ~36%) was then initiated at a rate of 32 L min^{-1} (time = 0 in Figure 3.13). The reflectivity peak of the Si-O-Si porous Si sample displays an initial blue shift in the first few minutes of the air-vapor flow, as the humidity in the carbon bed stabilizes (RH for ambient laboratory air = 42%, conditioned air = 36%, measured by a EdgeTech Dewmaster chilled mirror hygrometer). As demonstrated above (Figure 3.11), the Si-C and Si-H sensors show a much lower dependence on relative humidity, and the signal from these two sensors is relatively stable during the transition from RH = 42% to RH = 36%. After ~75 min of isopropanol vapor flow, the porous Si-tipped fiber sensors display a gradual red shift of the reflectivity peak, indicating the breakthrough of isopropanol into the region of the carbon bed occupied by the fiber sensors. The magnitude of the red shift is consistent with a 500 ppm isopropanol concentration, based on the calibrations discussed shown in Figure 3.10. Detection of isopropanol by the fiber sensors is confirmed by the response recorded from the two GC probes placed mid-bed and at the outlet end of the carbon bed. The ~30 min delay of the mid-bed GC measurement relative to the signals from the three fiber sensors is attributed to slight positional differences of the fibers and the GC probe within the carbon bed.

The improvement in stability afforded by the two chemistries (Si-O-Si and Si-C) is apparent in the response traces of Figure 3.13. The as-etched porous Si particle (Si-H) displays a significant blue shift during the course of the dosing run. This is attributed to oxidation of the hydride material. Conversion of the Si component of the porous Si matrix to silicon oxide results in a decrease in refractive index of the material, which is manifested as a blue shift in the spectral resonance. The samples

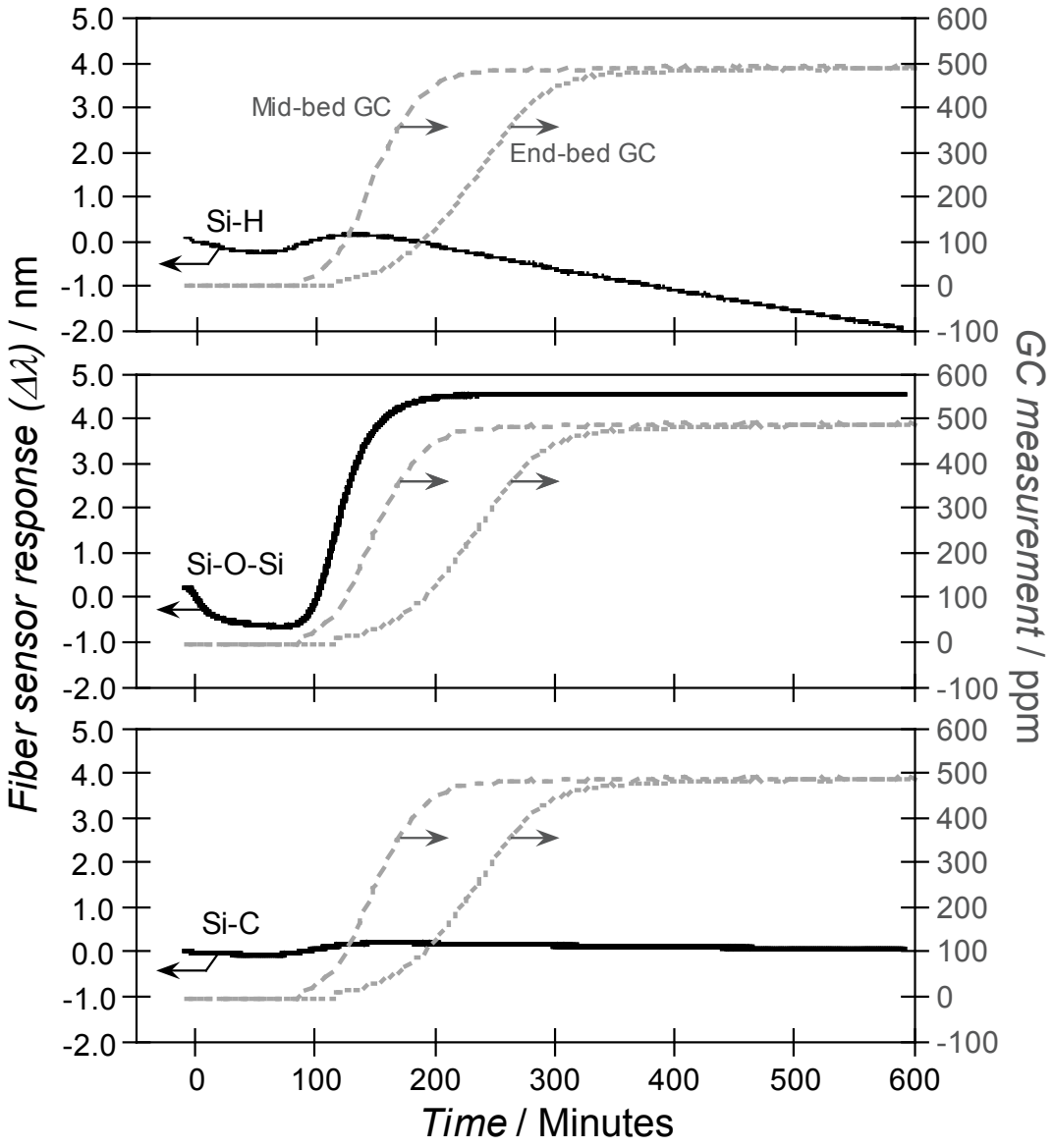

Figure 3.13 Response of porous Si optical sensors embedded in a carbon bed, demonstrating the detection of isopropanol breakthrough. Vapor breakthrough is monitored by gas chromatograph (GC) probes (right y-axis) at mid bed (gray long dash) and at the outlet of the bed (gray short dash), and by fiber-mounted porous Si sensors (left y-axis) that consisted of chemistries: (top) as-etched (Si-H), (middle) thermally oxidized (Si-O-Si), and (bottom) thermally reacted with acetylene at 485 °C (Si-C). Optical sensor data points were obtained every 20 sec. GC data points were obtained every 4 min. 500 ppm isopropanol flow was initiated at time = 0 in a carrier gas of air at 36% relative humidity.

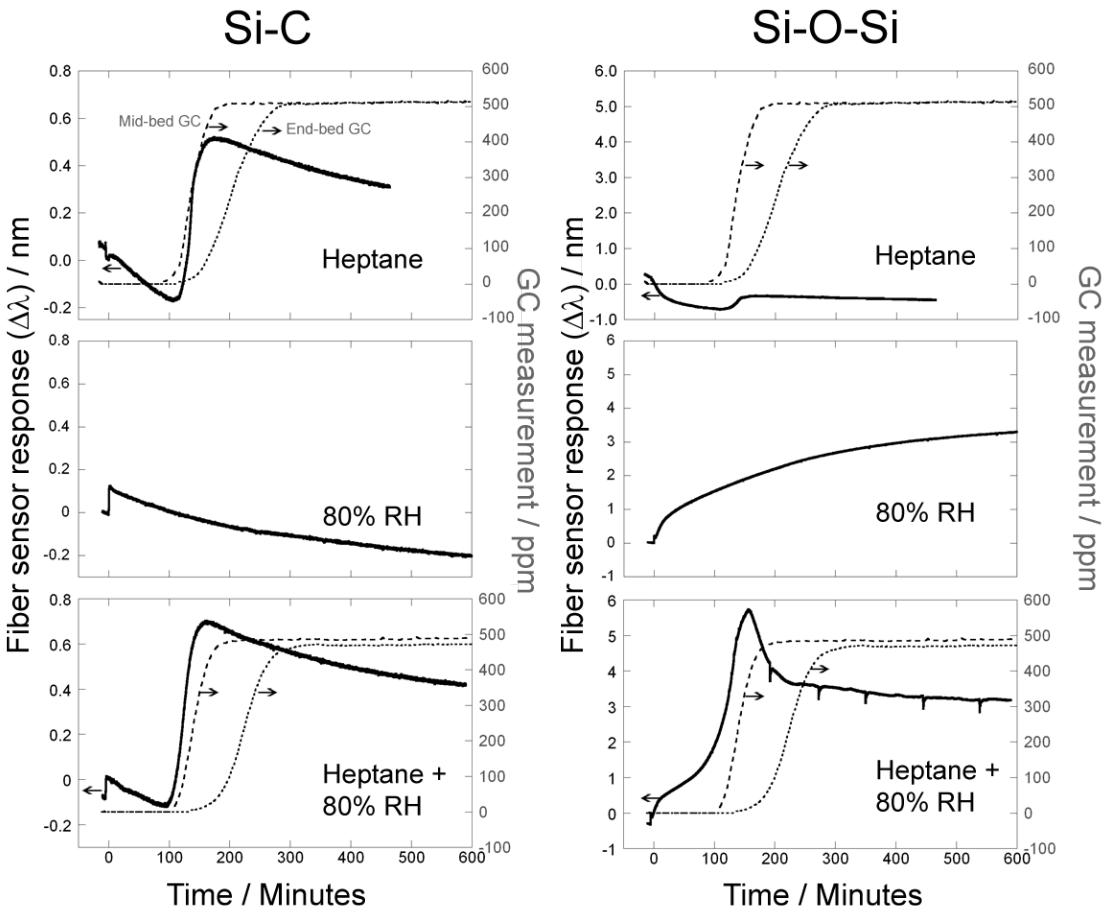

Figure 3.14 Response of porous Si optical sensors embedded in a carbon bed, demonstrating the detection of heptane, water vapor, and heptane-water vapor breakthrough. Vapor breakthrough is monitored by gas chromatograph (GC) probes (right y-axes) at mid bed (gray long dash) and at the outlet of the bed (gray short dash), and by fiber-mounted porous Si sensors (left y-axes). The left column shows response of acetylated Si-C (485°C) sensors, while the right column shows the response of thermally oxidized Si-O-Si sensors. **Top row**: 500 ppm of heptane was flowed through the carbon bed with a carrier stream of air at 36% relative humidity. **Middle row:** 80% relative humidity was flowed through the bed. No GC response is shown since the GC detector was insensitive to water vapor. **Bottom row:** 500 ppm heptane in a carrier stream of 80% relative humidity was flowed through the bed. All analyte flows began at time t=0 minutes. Optical sensor data points were obtained every 20 sec. GC data points were obtained every 4 min.

with Si-O-Si or Si-C chemistries do not display such a blue shift, consistent with the known stability of these two surfaces over the duration of the experiment.[165, 193]

In Figure 3.14, three porous Si-coupled fibers containing the Si-H, Si-O-Si, and Si-C surface chemistries were positioned in the carbon bed as described above, and the bed exposed to heptane vapors. Each row of Figure 3.14 shows a separate analyte breakthrough run of a carbon bed, with new porous Si-coupled sensors used in each run to maintain the 2-day age of the sensors, allowing for consistency of the sensor response. The two columns correspond to the Si-C and Si-O-Si fibers used in each run. Following the same methodology as the IPA run above, a set of 3 sensors was implanted in the carbon bed and exposed to 500 ppm heptane vapor (top row, Figure 3.14). In contrast to the 500 ppm IPA vapor exposure run, the response to heptane was greater for the Si-C fiber than the Si-O-Si, as expected from the calibrations of the surface chemistries above. The acetylene-reacted sensor exhibits a blue shifting baseline both before and after analyte detection, indicating slow oxidation in air of areas of the heterogenous sensor surface. As, with the IPA carbon bed breakthrough run, the sensors successfully detected heptane breaking through the activated carbon at the mid-bed location in advance of the vapor breakthrough through the entire depth of the cartridge, with the latter detected by the end-bed GC sampling.

The middle row of Figure 3.14 shows a carbon bed breakthrough monitoring run with a flow of 80% RH. As the high concentration of RH breaks through to the sensor position, the oxidized sensor exhibits a large spectral shift as expected. The acetylated sensor exhibits a slight, smooth decrease in sensor position, which may be due to the oxidation of surface sites not converted from Si-H to Si-C in the reaction

with acetylene. GC response curves are not shown for these RH-only breakthrough runs since the flame ionization detector is insensitive to water vapor.

Finally, the third row of Figure 3.14 shows the sensor responses of Si-C and Si-O-Si optical fiber probes to the carbon bed breakthrough of 500 ppm heptane in 80% RH. The acetylated sensor surface exhibits a response consistent with that of the sensor exposed to the breakthrough of 500 ppm heptane at a lower relative humidity (36%). In contrast, the Si-O-Si sensor exhibits a response consisting primarily of the sensor response to 80% RH. The peak in the sensor response over time at ~150 minutes is due to water vapor rollup, discussed in the next section. The small vertical, periodic spikes in the response after ~150 minutes are due to the Miller-Nelson humidity conditioning system and correspond to each time the water reservoir in the system was filled with fresh, cold water, with the momentary (<1min) lower temperature in the reservoir resulting in a drop in the water vapor delivered to the air stream, and manifested as short drops in sensor response as the water vapor-heptane flow passes the sensor.

3.4.8 Observation of Water Vapor Rollup

The response of the oxidized fiber to the breakthrough of 500 ppm heptane in a flow of 80% RH through the carbon bed exhibits a peak in spectral response before leveling to a slowly equilibrating spectral peak shift, as seen in Figure 3.14 and plotted again in Figure 3.15. This response peak corresponds to the commonly observed phenomenom of water vapor “rollup”, where breakthrough concentrations temporarily exceed the incoming concentrations due to displacement of adsorbed water in the

carbon bed by the organic vapor. [194-197] Vapor rollup is also observed in multianalyte flow systems where competition between analyte vapors results in preferential adsorption of one species[198]. Here, it is a result of the faster rate of progression of the high RH water vapor front through the carbon bed [147] than the organic vapor.

Figure 3.15 displays the observed spectral response to the mid-bed breakthrough of 80% RH and 500 ppm heptane, and the corresponding breakthrough concentration over time (right side) and gas phase concentration versus the distance into the carbon bed (left), with vapor flowing from left to right. The zone boundaries are at the centers of the mixture component wavefronts and are adapted from the Wood-Snyder zones of vapor concentrations[195, 196]. The effect of the mutual exclusion of the adsorption volume in the activated carbon is depicted. The lower affinity of the water vapor to the activated carbon [147] results in its faster traversal of the carbon bed. In Zone 3, only water vapor is adsorbing onto the carbon. As heptane breaks through the bed more slowly, the wavefront of the vapor displaces water already adsorbed from the high humidity wavefront, pushing the displaced water in front of the heptane at a "rollup" concentration higher than that of the high humidity water vapor alone (Zone 2). This rollup front of extra displaced vapor induces a large sensor response. As this rollup front of displaced water moves past the porous Si sensor location, the sensor response then decreases to an equilibrium response, corresponding to the water vapor and heptane in equilibrium with the activated carbon (Zone 1). The progression of these wavefronts through the carbon bed was observed with the oxidized fiber due to its hydrophilicity and large water vapor response. The more hydrophobic freshly

prepared and Si-C sensor surface exhibited no such effect, since its response to water vapor is minimal relative to its response to heptane (Figure 3.14).

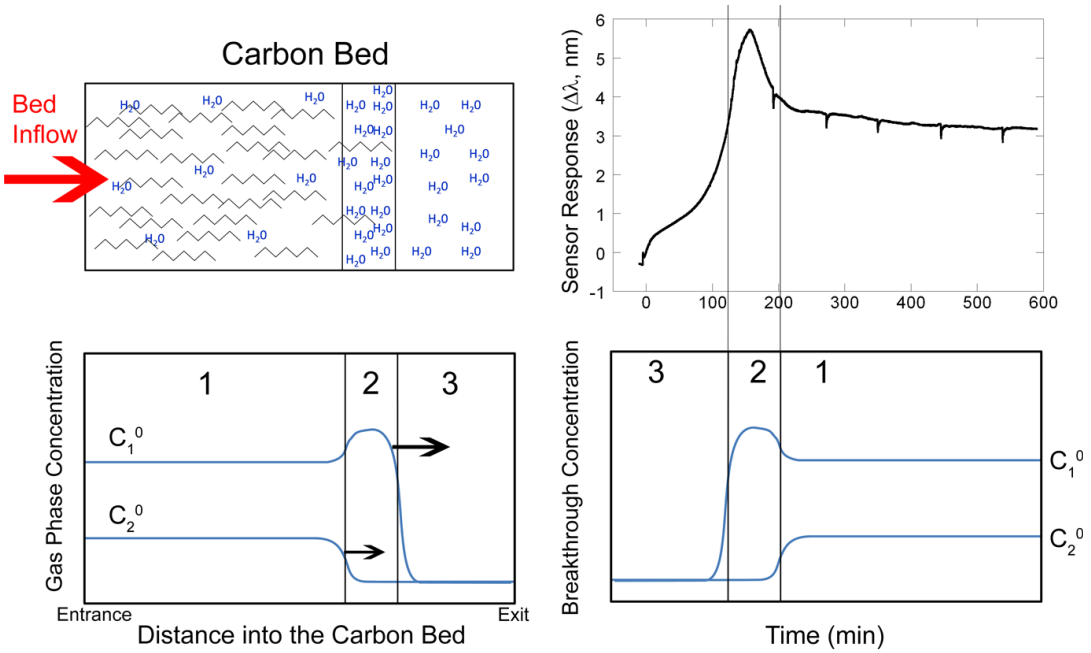

Figure 3.15 Observation of water vapor rollup for the oxidized porous Si sensor exposed to 500 ppm heptane in a flow of air with 80% relative humidity. **Left column:** a depiction of the carbon bed (top) and corresponding cartoon of the Wood-Snyder [196] zones of vapor concentrations C_1^0 and C_2^0 (bottom) versus the depth of the carbon bed, where C_1^0 = 80% relative humidity and C_2^0 = 500 ppm heptane. In most of Zone 1, the carbon is at equilibrium with both vapors (water and heptane) in the mixed input stream. In most of Zone 2, water vapor is at equilibrium at a higher "rollup" concentration than that entering the bed due to displacement by the heptane vapor front,. In Zone 3, water vapor is adsorbing from this higher concentration. Arrows (bottom left) indicate the direction of the vapor fronts as they progress through the carbon bed. **Right column:** porous Si-coupled fiber sensor response to the heptane-water vapor mixture over time (top) and the corresponding Wood-Snyder zones of vapor concentrations at the location of the fiber optic sensor (bottom) for the mixture. The porous Si sensor responds to both water vapor and heptane, while the GC detector (response shown in Figure 3.14) responds only to heptane.

3.5 Conclusions

The response of porous-Si-based optical sensors to analyte vapors is strongly influenced by surface chemistry. When challenged with two VOC analytes intended to probe surface hydrophobicity/hydrophilicity, all but one of the sensor types tested responded more to polar isopropanol than to nonpolar heptane. Only the "hydrocarbonized" surface, prepared by thermal decomposition of acetylene on an as-prepared porous Si sample, responded more strongly to the hydrophobic analyte. When stored in ambient conditions (laboratory air), all surfaces including the oxidized sensors exhibit relatively stable responses to the VOCs over 15 days, while the acetylated surfaces (Si-C) show a gradual decrease in their responses to heptane relative to their response to IPA. This may be due to the oxidation of unreacted surface sites for samples lacking complete Si-C surface coverage. Native porous Si (Si-H) reacts with air and displays significant drift during atmospheric testing, while acetylated (485°C Si-C)and thermally oxidized (Si-O-Si) exhibit far less drift over the sampling periods examined and appear most suitable for environmental monitoring.

A small (sub-mm) film of either the Si-C or the Si-O-Si sample can be attached to the distal end of an optical fiber with minimal degradation in optical sensor response and excellent response time to vapors and reversibility. The two different optical fiber sensors display divergent responses to the isopropanol and heptane analytes used in this study (Si-O-Si porous Si-coupled optical fibers respond more to isopropanol than heptane vapors, whereas Si-C porous Si-coupled optical fibers respond more to heptane than isopropanol vapors. This suggests that such chemistries can be used to classify different analytes in a microsensor system. The Si-C modified (acetylated at 485°C)

porous Si sensor displays the lowest response to humidity of the fiber sensors tested. Although significantly reduced, the response of this material to changing RH must still be considered in the design of sensors that are intended to operate in open environments.

The feasibility of the fiber-mounted sensors for monitoring residual service life of activated carbon respirator cartridges was also demonstrated .[165, 193] By automating the determination of end-of-service life for respiratory cartridges, the burden of calculating and tracking cartridge replacement times is shifted away from the user. The divergent responses observed in the calibration of the Si-C and Si-O-Si surface chemistries to concentrations of heptane and IPA were also observed with fibers monitoring the breakthrough of the analytes in a full-size activated carbon filtration cartridge simulator. Furthermore, the phenomenon of water vapor rollup, in which the an organic vapor front traversing an activated carbon bed displaces the water vapor adsorbed from a front ahead of it, creating a peak in the sensor response over time, was observed with the water-sensitive Si-O-Si fiber for a mixed flow of heptane in high humidity.

Chapter three, in part or in full, is a reprint (with co-author permission) of the material as it appears in the following manuscript submitted for publication: *Porous silicon-based optical microsensors for volatile organic analytes: effect of surface chemistry on specificity*. Advanced Functional Materials (2010) *Manuscript accepted for publication, published online July 2010.* The author of this dissertation is the one of the primary authors of this publication.

CHAPTER FOUR

THERMAL DESORPTION OF ORGANIC VAPORS FROM POROUS SILICON FILMS: IMPLICATIONS IN OPTICAL VAPOR SENSING

4.1 Abstract

In the last chapter, class-specific analyte specificity was demonstrated by modifying the surface chemistry of porous silicon optical sensors. The next two chapters describe a means of physically modifying the adsorption equilibrium of porous silicon to analyte vapors by thermal modulation. The ability and implications of applying a thermal pulse to the sensor after exposure to low volatility, slowly desorbing analytes is described here. Sensors balance a tradeoff between high sensitivity and reversibility, but thermal modulation allows vapors trapped in the porous layer that "foul" the sensor [132] to be expelled. Following this, Chapter 5 details a thermal modulation methodology to discriminate vapors of pure high volatility analytes. Both chapters test the porous silicon optical sensors under ambient pressures with vapors flowing over the surface of the porous silicon to better approximate field use conditions than sensors tested in sealed-chamber[60] environments.

Here, a 1-D porous silicon photonic crystal exhibiting a single visible light reflectivity peak was used to optically sense the low volatility vapors methyl salicylate and octanol. Freshly prepared and oxidized sensor materials were examined, exhibiting slow desorption and retention of the vapors at ambient after 1.5 hours, but rapidly expelling vapors when heating with a thermal pulse, resetting the sensor to its baseline response. Cycles of vapor dosing, followed by thermal refreshing, were consistent and repeatable. As the sensor was heater, the temperature at which the rate of change of the optical response was greatest was unique to each vapor expelled and differed between the oxidized and freshly prepared porous materials.

4.2 Introduction

Porous silicon optical sensors have attracted recent attention as sensitive detectors of chemical and biological compounds[1, 2] due to their ease of fabrication, large surface area, range of accessible surface chemistries[3], and controllable optical and morphological properties including pore size, porosity, and refractive index profile. Chemical vapor sensing has been demonstrated with a variety of porous silicon optical structures, including Bragg mirrors[4], Fabry-Pérot films[5], microcavities [6], and rugates [7]. Rugate structures, used in this work, exhibit a sinusoidal variation of the refractive index with layer depth[8], resulting in an optical reflection band centered at a wavelength determined by the period and amplitude of the refractive index profile. Infiltration of chemical vapors into the porous matrix displace air from the porous voids, increasing the refractive index of the film and resulting in a red wavelength shift of the stop band position that enables sensing by monitoring the reflectivity peak wavelength over time[9].

Porous silicon sensors exhibit zero-point baseline drift, long recovery times for low volatility organic vapors, and the gradual accumulation of vapor molecules in the porous matrix that leads to reduced sensitivity and dynamic range of the sensors [90, 95]. Although alternate sensing materials like metal oxides exhibit low drift and good recovery to baseline after sensing, their high temperature of operation is not desirable for portable, low power sensor applications[199]. In this work, a thermal pulse is applied to porous silicon optical sensors to refresh the sensor response after exposure to low volatility vapor analytes.

Thermal sensor refresh is commonly used in variety of materials[200], including capacitive polyimide humidity sensors[201] and metal oxide films, with some studies assessing the response profile of the sensor when heated to inform analyte identification[123, 202]. On porous silicon, studies have focused on thermal sensor refresh for electrically transduced devices, including capacitive sensors with integrated resistive heaters[203, 204] or thermoelectric[205] heaters , electrical phase-based sensors with integrated resistive heaters for humidity sensing[206], and designs that do not directly sense with porous Si but use the material as a preconcentrator reservoir that expels vapors when heated[32, 207], passing them over other sensing elements. Although optical transduction provides a number of advantages, including remote sensing applications[24, 37, 38] and a low susceptibility of the sensor element to electrical interference, little work has been performed on refreshing optical sensors for organic vapor applications. Salem[95] constructed rugate porous Si optical sensors for vapors that were subjected to thermal cycles to assess the durability of the sensor, but did not apply the thermal profile to expunge analyte vapors or address characteristics of the sensor response when heating.

In the work below, rugate porous silicon and oxidized porous silica films were optically transduced by reflected light spectrometry and exposed to low volatility analyte vapors to examine the efficacy and characteristics of desorbing vapors from the sensor materials. Octanol was selected for its low volatility, as well as methyl salicylate, which is of additional interest for its use as a stimulant for the sulfur mustard chemical warfare agent[208]. Isopropanol was selected to contrast the ambient recovery response of the sensor to a high volatility organic vapor.

4.3 Materials and Methods

4.3.1 Sensor Preparation

Porous silicon rugate optical films were prepared from single-crystal, (100)-oriented highly boron-doped, p-type Si (Siltronix, 1-1.2 mΩ-cm resistivity) by electrochemical etching in 3:1 v:v solution of aqueous hydrofluoric acid (49%, Fisher Scientific):ethanol (Rossville Gold Shield Chemical). Etching was performed in a Teflon cell with a platinum ring counter electrode and a galvanostat (Kepco BOP 50-4D) under computer control (Lab View, National Instruments.) The current density waveform of the rugate etch was varied in time t sinusoidally according to:

$$I(t) = I_{min} + \frac{\Delta I}{2}\left[\sin\left(\frac{2\pi t}{p}\right) + 1\right] \quad (4.1)$$

where I_{min} = 12.5 mA/cm^2, ΔI=50 mA/cm^2. The period was p=6.2 seconds for as-etched optical structures and p=7.73s for the structures subsequently oxidized, so that both types of sensor material exhibited a rugate stop band reflectance peak at the same wavelength, centered at 568nm. Since the fresh samples oxidize upon heating, multiple samples were prepared under identical etch parameters from the same 4" silicon wafer, with a stop band central peak deviation of +/-3nm among all samples utilized. Oxidized samples were placed in a tube furnace (Lindberg Blue) for 45 minutes at 800°C in ambient air and allowed to slowly cool. Samples were cut to 4x4mm squares to reduce the thermal mass on the heater and decrease the heating and cooling times.

4.3.2 Sensor Characterization

Gravimetric Determination of Porosity

Samples were weighed before etching (m1), after etching (m2), and after dissolving the porous layer with a 0.1M basic solution of KOH in water and rinsing with ethanol (m3). The following equation was used to determine the porosity of the freshly prepared sample[170]:

$$\text{Porosity} = (m_1 - m_2) / (m_1 - m_3) \quad (4.2)$$

Five samples had an average porosity of 65% +/-2%. For oxidized samples, the different density of the oxidized (2.21 g/cm^3) etched layer than the bulk silicon (2.33 g/cm^3) must be considered. The porosity of an oxidized sample is $(V_{total}-V_{SiO2}) / V_{total}$, where the total volume removed after etching and dissolution is $V_{total} = (m_1-m_3)/2.33$ and the silica volume, for a weight (m_4) of the porous layer after oxidation, is $V_{SiO2} =(m_3-m_4)/2.21$. Oxidized optical sensors had an average porosity of 29%+-2% for 5 oxidized samples.

Characterization by FTIR, SEM and BET

Fourier transform infrared (FTIR) spectra were recorded with a Thermo Scientific Nicolet 6700 FTIR with an MCT/A detector and KBr beamsplitter using a resolution of 2 cm^{-1} and an average of 128 scans, collected in attenuated total reflection mode with a smart iTR diamond accessory.

Scanning electron microscopy was used to determine porous silicon layer thickness by cutting and imaging cross sections with a Phillips XL30 Field Emission ESEM in secondary electron mode and an accelerating voltage of 10kV. BET nitrogen adsorption measurements (Micromeritics ASAP 2010) of freshly prepared and

oxidized samples were taken at 77K, with the samples first degassed in situ at 323 K until a static vacuum of $5x10^{-5}$ Torr was reached. Average pore diameters of 8um and 6um were determined for oxidized and freshly prepared structures, respectively.

4.3.2 Vapor Dosing

The vapor delivery system consisted of a flow of dry (medical) air controlled to a constant flow of 500sccm with an electronic mass flow controller (Alicat Scientific) that branched at a 3-way valve into two lines, with one line vapor-free purge flow and the other line flowing into a vapor bubbler. The two lines rejoined at a second downstream valve, with the valve outflow connected to the sample vapor flow cell, depicted in Figure 4.1. A 125mL sealed Erlenmeyer flask served as a ballast for concentration mixing, placed between the output valve and the sample cell. The vapor bubbler line was itself split into two lines, one bubbled through liquid analyte and one flowing a dilution stream of nitrogen, to dilute the saturated concentration of the vapor bubbler to 67% P / P_{sat}. Each of the lines in the vapor-line split was flow-controlled with a dial-adjusted flow mixer (Cole-Parmer), and rejoined to form a diluted vapor line that met with the vapor-free purge line at the downstream valve before the sample flow cell. Glass bubblers with porous glass diffuser-tipped top assemblies were filled with liquid analytes and maintained at 25°C +-2°C in a thermostatted water bath (HAAKE D8). Liquid methyl salicylate, isopropanol, and 1-octanol were purchased from Sigma-Aldrich. The output flow of the system to the sample cell was checked for flow rate losses with an electronic mass flow meter (Alicat Scientific).

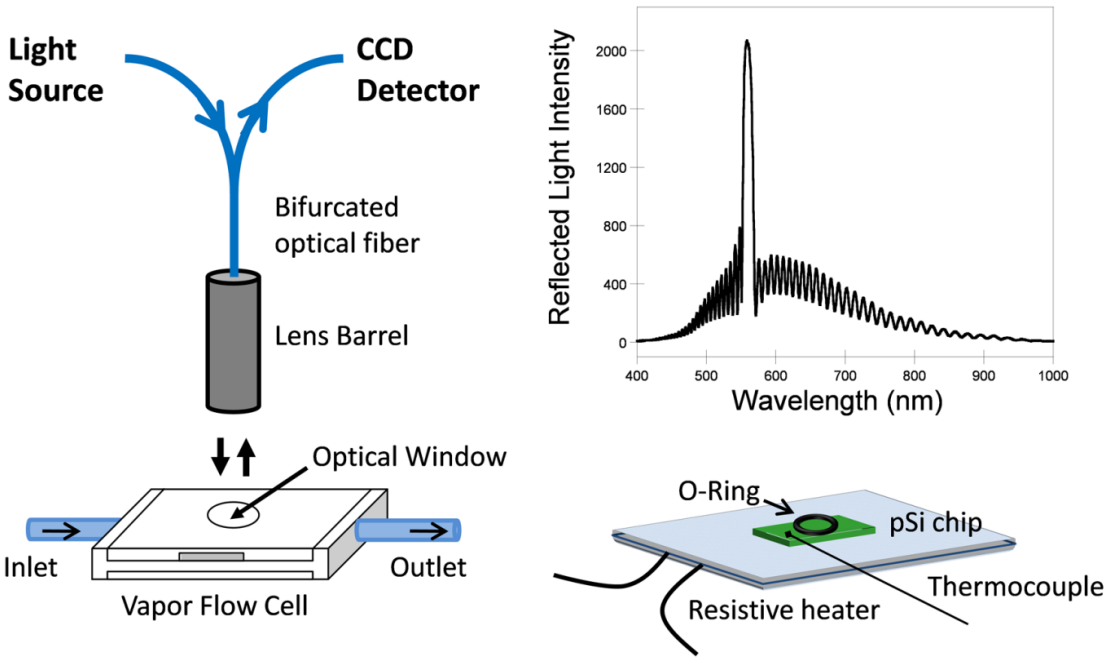

Figure 4.1 Sensor configuration. The porous Si was sealed into a Teflon vapor flow cell and the backside heated with a resistive think film heater. **Left**: the optical sensing configuration. **Right**: sensor chip assembly. **Top right**: reflected visible light spectrum of the porous silicon

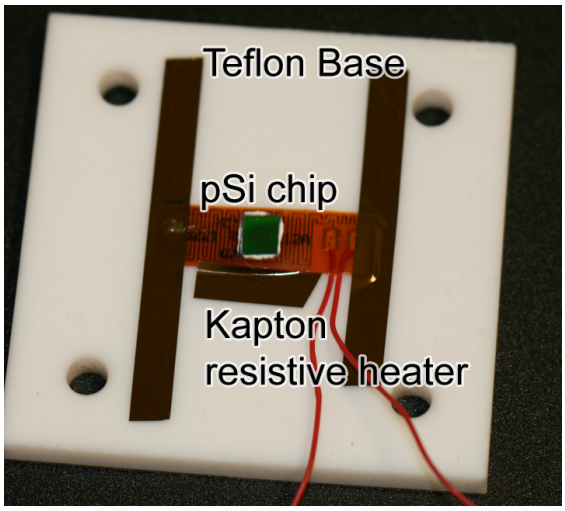

Figure 4.2 Picture of porous silicon sample mounted onto the resistive heater with thermal paste, on top of a Teflon bottom plate. A thermocouple was then attached to the surface of the porous silicon chip, and the assembly mounted with an o-ring seal into the Teflon flow cell. The heater is secured to the Teflon base with Kapton high temperature tape.

The sample vapor cell is drawn in Figure 4.1 and consisted of a Teflon cell with Swagelok input and output ports and a glass optical window to allow visible light interrogation of the sample. A Kapton O-ring on top of the sample sealed it to the glass window. The backside of the sensor was coated with a thin layer of thermal compound (AOS) and placed on a resistive heater (Minco) atop the Teflon bottom plate of the cell as pictured in Figure 4.2. A fine-gauge thermocouple (Omega) was attached to the top of the sensor with Kapton high temperature tape (VWR) in an area not covered by the interrogating light beam, and temperature readings recorded by computer with an Extech 383273 serial interface multimeter.

4.3.3 Choice of Heater

The thin film heater used in these experiments proved sufficient for rapid heating up 200°C. The desorption profiles of the sensor response to temperature in section 4.4.5 is influenced by the heating rate of the material. Unlike thermally programmed desorption, where the heating rate is linearly ramped, the heating profile was a function of the heater power specifications and total heat transfer of the system. The warm up time of a sample is a function of the material's mass and specific heat, the temperature increase desired, and the power of the heater, and can be expressed as[209]:

$$t = \frac{m\, C_p (T_f - T_i)}{BP} \tag{4.3}$$

where m is the mass of the porous silicon chip, C_p the specific heat of silicon, T_f and T_i the initial and final temperatures, P the power of the heat after losses, and B a constant

that depends on the units selected. An estimate of the conductive losses to the Teflon plate can be expressed as[209]:

$$Loss\ (watts) = \frac{KA(T_f - T_i)}{3.412\ L} \quad (4.4)$$

where K is the thermal conductivity of the Teflon in contact with the heater, A the cross sectional area, and L=1/8" the thickness of the Teflon plate. Given the average chip dimension of 4mm^2 and mass of 0.055g, for heating from 25 to 160°C with the 13Ω heater at 8.5 volts the warm up time is calculated as 26 seconds. This number provides an estimate of the minimum heat up time. The observed heating time was 160s, and is longer because the estimate above does not include radiative, convective, and other conductive losses in the system. Since the purpose of this chapter is to demonstrate the ability to refresh porous Si optical sensors, the heater configuration detailed above had acceptable power specifications. In Chapter 5, rapid thermal cycling of porous silicon is probed. For that system, a more powerful thermoelectric Peltier heater/cooler system with computer control was selected.

4.3.4 Reflected Light Spectra

Reflected light spectra of the samples in the visible region were taken from 345-1045nm with a CCD spectrometer (Ocean Optics USB4000) and a tungsten-halogen light source (Ocean Optics LS-1) connected with a Y-branch bifurcated optical fiber. The common end of the bifurcated fiber was focused with an objective lens to a 2 mm^2 spot size on the sample and positioned normal to the porous silicon sample surface. Figure 4.1 displays the reflected light spectrum of a sample before vapor introduction. Each spectrum collected was fit with a Gaussian function (Igor Pro,

Wavemetrics, Inc.) to determine the peak wavelength (λ_{max}), and λ_{max} plotted against time. Spectra were acquired at a rate of 1HZ.

4.4 Results and Discussion

4.4.1 Pore Size and Distribution

The nitrogen absorption curves for the fresh and oven oxidized sensor materials are shown in Figure 4.3, with relevant nitrogen BET data of the average pore size, desorption-branch pore opening pore size, and surface area compiled in Table 4.1. The BET constant, C_{BET}, represents the affinity between the nitrogen molecule and the sample surface and provides an indication of the surface polarity, with low values (<50) indicative of hydrophobic surfaces. As expected, the oxidized porous Si had a ~3 times greater C_{BET} than freshly prepared material. The nitrogen absorption isotherm is type IV with an H2 hysteresis, typical of mesoporous materials[104].

Figure 4.4 displays the pore size distribution of both sensor types, along with a plan-view SEM of the pore network of the freshly prepared sensor. Unlike template porous materials like porous alumina[210] or zeolites[147] that have highly uniform pore sizes, porous silicon exhibits a broader distribution of pore diameters. The implication of the difference in pore size between the freshly prepared and oxidized sensor materials are discussed in the following sections.

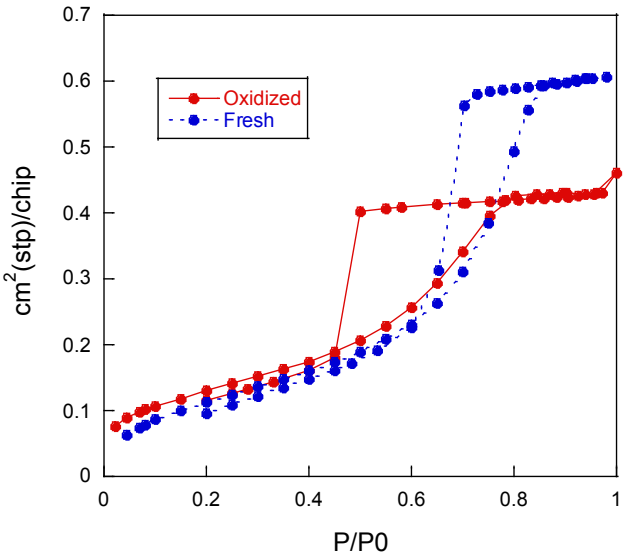

Figure 4.3 Nitrogen absorption (bottom segments) and desorption (top segments of curves) of fresh and oxidized porous silicon as a function of its partial pressure, taken at 77K.

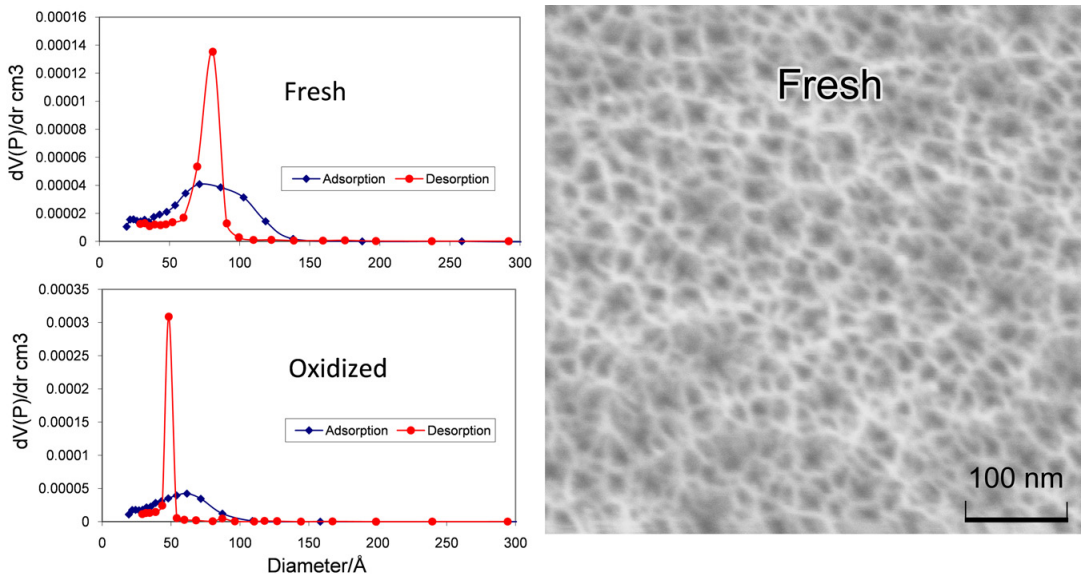

Figure 4.4 Left: Volume change with pore radius plotted as a function of the pore diameter, in Angstroms, displaying the pore size distribution of the fresh and oxidized photonic structures. **Right:** Plan-view SEM of the porous Si surface showing the network of pore channels.

Table 4.1 N_2 Adsorption Isotherm Values of the Porous Materials

	Fresh (Si-H)	Oxidized (Si-O-Si)
Average pore diameter (Å)	81	59
Opening pore diameter (Å)	79	49
S_{BET} m^2 (STP) /chip	0.462	0.488
V cm^3 (STP) /chip	0.607	0.429
C_{BET} [a]	26	66

[a] The C_{BET} constant represents the affinity between the nitrogen molecule and the sample surface, providing an indication of surface polarity. Low values (<50) are indicative of hydrophobic surfaces.

4.4.2 Recovery of Porous Si Sensors at Ambient Temperature

Freshly etched Si-H porous silicon and oxidized SiO_2 porous silica optical films were exposed to vapors of methyl salicylate (MeS) and octanol and allowed to recover in air. The central stop band wavelength, λ_0, was recorded as the sensors were dosed and allowed to recover, shown in Figure 4.5. Each exposure run consisted of a baseline in dry air for 5 min, exposure of each sensor chip to analyte vapor for 3 min, and recovery of the sensor in dry air. Isopropanol (IPA) exhibits complete recovery of the sensor after ~1 hour and contrasts the relatively fast recovery rate of the high volatility analyte to the slow and incomplete recovery of MeS and Octanol, with saturated vapor pressures of 45.5, 0.078, and 0.034 Torr at 25°C for IPA, octanol, and MeS, respectively[211].

The initial spike observed in sensor response, lasting for several seconds and beginning when the a vapor was introduced, was due to a momentary concentration spike when accumulated pressure in the vapor line tubing was released when switching from nitrogen to vapor. In Figure 4.5 this initial response is predominantly observed in the oxidized samples due to their higher sensitivity to vapor. This transient spike is also

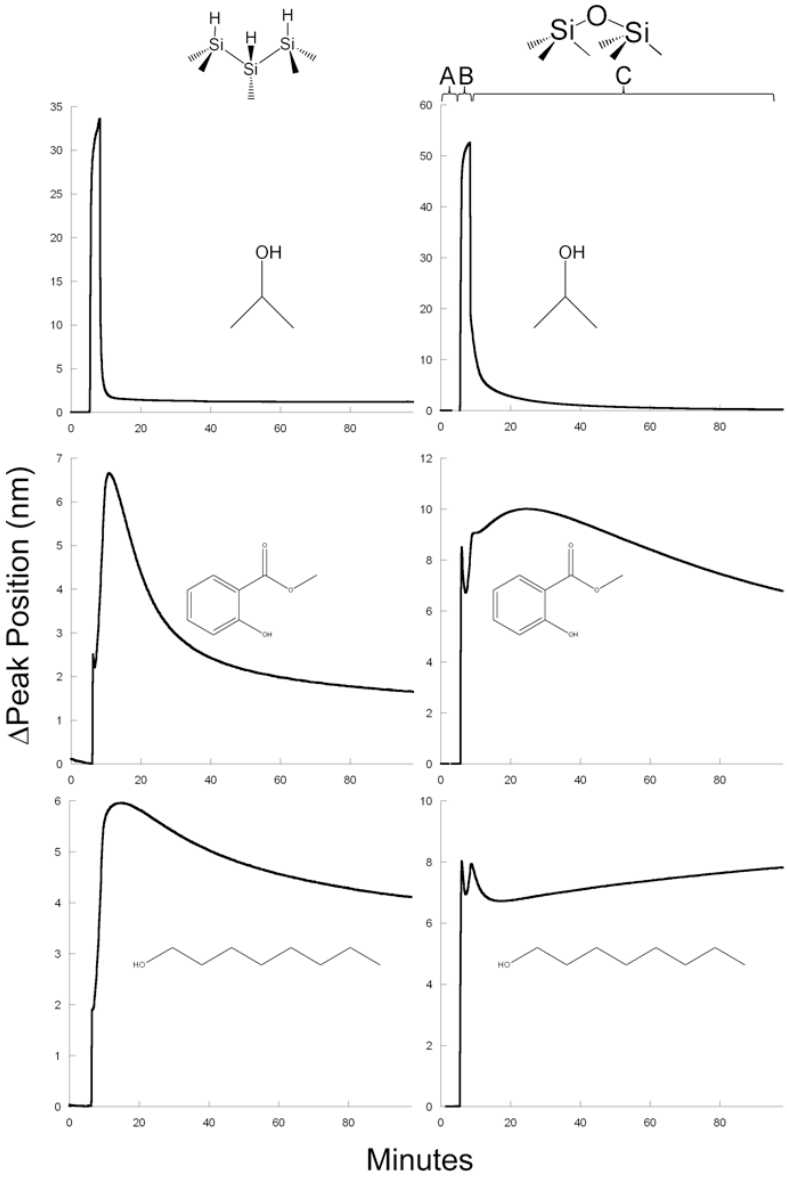

Figure 4.5 The spectral position of the reflected rugate peak during for a dose of analyte vapor, with recovery at ambient temperature. Section A: sensor baseline in medical (dry) air for 5 min. Section B: vapor (top: isopropanol; middle: methyl salicylate; bottom: octanol) was introduced for 3 min. Section C: the sensor was allowed to recover in a flow of dry air without heating. **Left:** freshly prepared porous Si. **Right:** thermally oxidized porous SiO2

present in the oxidized thermally cycled doses in Figure 4.7, but does not appear in other runs since the valve switching procedure was optimized. The initial transient spike, which was followed by 3 minutes of continual vapor dosing, had no discernible effect on the ambient and thermally-refreshed desorption studied here. After 1.5 hours, the fresh and oxidized MeS and octanol-dosed samples showed only modest recovery to the initial baseline. After 12 hours, MeS samples recovered to 5-10% above the initial baseline. Octanol samples showed significantly less recovery, decreasing to only 25-35% above the initial baseline after 12 hours day at ambient. The presence of these trapped vapors after long recovery periods was confirmed by FTIR, as detailed later. Freshly prepared samples show significantly faster recovery of both analytes than oxidized samples. This is due to the weaker interaction of the Si-H sample surface to the moderately polar analytes compared to the polar SiO_2 surface, as well as from the larger pore size of the fresh samples (6nm diameter compared to 8nm diameter oxidized) and the thinner layer thickness of the fresh samples (12.4um compared to 16.2um for oxidized) that allowed for faster diffusion from the layer.

Capillary condensation occurs in pores whose diameter is below the Kelvin diameter d, described by:

$$d = -\frac{4\gamma M}{\rho RT \ln(\frac{p}{p_0})} \tag{4.5}$$

where ρ, γ, and M are the vapor density, surface tension, and molecular weight of the analyte, P_0 is the saturation vapor pressure, and P the applied partial pressure[7]. Using the relevant physical properties of each analyte [211], the Kelvin diameter, below which capillary condensation occurs, was calculated at 67% P /P_{sat} as 3.2nm for IPA, 8.5nm

for octanol, and 10.4nm for methyl salicylate. The sensors in this study were thus exposed to vapor concentrations at which capillary condensation can occur for MeS and octanol. Though the samples were above the calculated Kelvin diameter for IPA at this concentration with capillary condensation not expected, the higher vapor pressure of IPA resulted in greater loading into the porous film and resulted in a large shift in rugate peak position compared to the other analytes.

4.4.3 Thermal Refresh of Sensor Response

Briefly, freshly prepared and oxidized sensor chips were subjected to cycles of vapor dosing and thermal refreshing, shown in Figures 4.6 and 4.7. To contrast the cycles of thermally refreshed analyte exposure to repeated exposure at ambient without refreshing, the sensor was exposed to regular doses of analyte vapor at ambient with the time between doses corresponding to that of the thermally refreshed exposure cycles, shown in Figure 4.8.

In Figures 4 6 and 4.7, for each cycles the porous layers were allowed to establish a baseline in dry air for 5 minutes, exposed to analyte for 3 minutes, allowed to partially recover in air for 3 minutes, then heated to 160°C and allowed to cool under dry air to 26°C. The partial recovery in air demonstrated the slow recovery of the sensor after analyte exposure for each cycle before the application of the thermal pulse. The bottom row in each figure displays the temperature-time profiles of each exposure run. The rightmost column of each figure displays a run in which the sensor was not exposed to vapor but was subjected to a thermal pulse and heated to 160°C. These

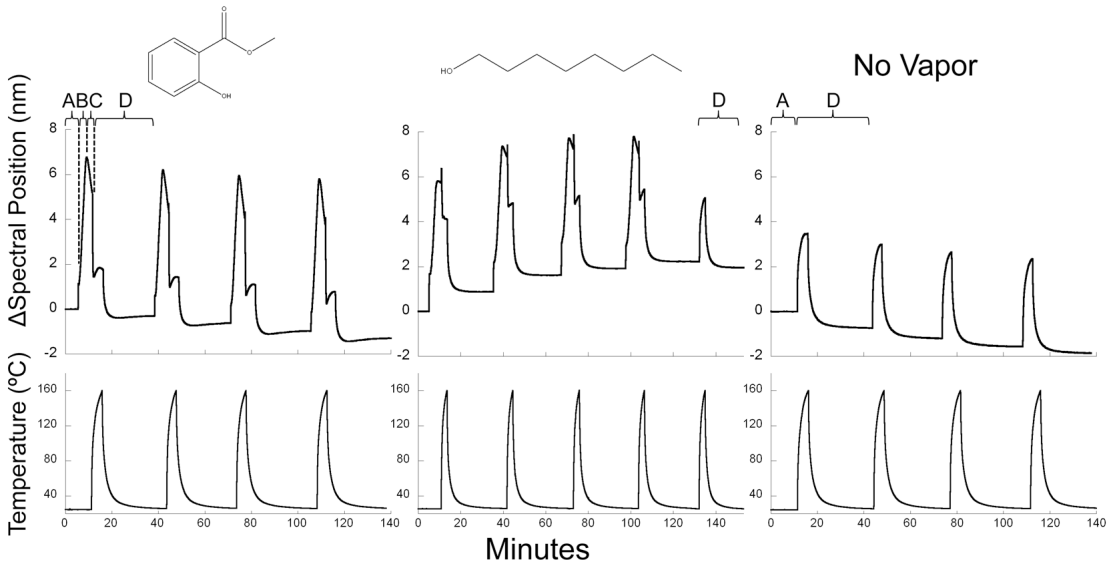

Figure 4.6 Thermal refresh of freshly prepared porous Si over cycles of analyte exposure. Top panels display the shift in rugate peak position over time. Bottom panels display the temperature versus time. Following an initial baseline (segment A), each cycle consists of exposure to analyte for 3 min (B), a flow of dry air for 3 min (C) to demonstrate slow recovery without heating, and a thermal pulse (D) and recovery in air to demonstrate a refresh of the sensor response. For octanol (middle panels), an additional heat pulse was applied after the last dose-heat cycle to desorb trapped vapor from the layer.

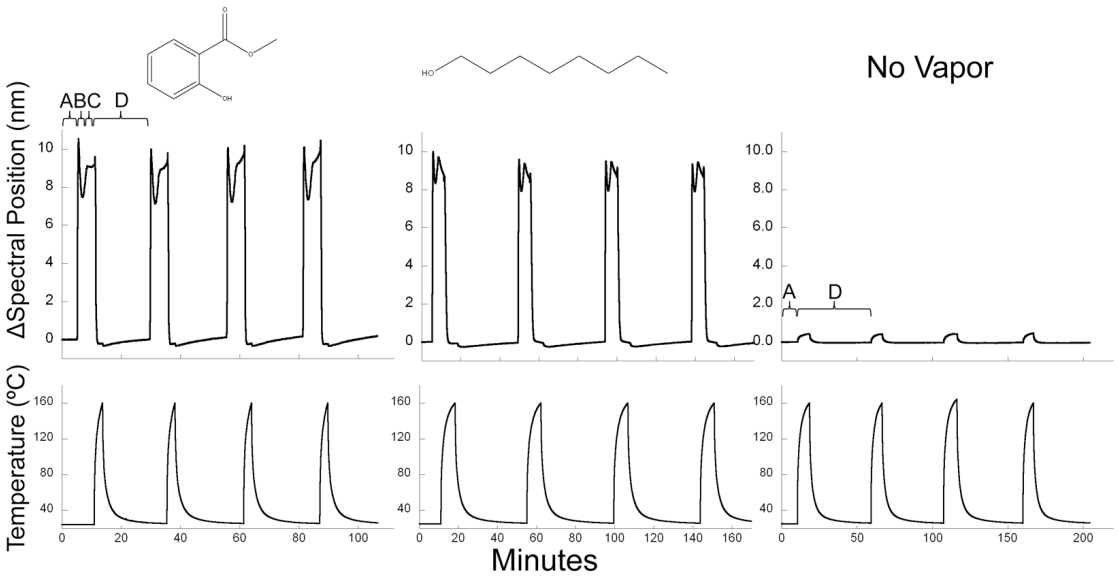

Figure 4.7 Thermal refresh of oxidized porous SiO_2 over cycles of analyte exposure. Top panels display the shift in rugate peak position over time. Bottom panels display the temperature versus time. Following an initial baseline (segment A), each cycle consists of exposure to analyte for 3 min (B), a flow of dry air for 3 min (C) to demonstrate slow recovery without heating, and a thermal pulse (D) followed by recovery in air to demonstrate the refresh of the sensor response.

traces display the intrinsic changes in rugate peak wavelength due to the temperature increase, without the influence of analyte vapors.

The change in spectral position of the rugate peak when heated after vapor exposure, labeled as section D, exhibits a hook shaped response for the fresh Si-H sensor surface and a smaller response spike for the oxidized surface. These features are due to the intrinsic change in the spectral band when heated. As the sensor temperature increases, vapors are expelled and a large reduction in the peak position is observed, but as the temperature continues to increase the peak position increases due to the refractive index change of the porous layer with temperature. This intrinsic change recovers to the initial ambient baseline as the sensor cools. The freshly prepared porous silicon samples also display decrease in the spectral peak position after each cycle of heating, for both the MeS vapor-dosed run and the cycles in which only heating was applied with no vapor dosing. This spectral blueshift is due to an increased rate of oxidation of the porous silicon at elevated temperatures, as conversion of porous silicon to silica lowers the average refractive index of the optical layer.

The freshly prepared, porous silicon sample exposed to octanol exhibits a baseline increase with each vapor cycle, indicating that the refresh temperature-time profile was not sufficient to thermal reset the sensor response. An additional thermal cycle after vapor exposure, pictured in Figure 4.6, was sufficient to decrease the sensor response to baseline level before the cycle of vapor exposure and heating, and as expected, thermal pulses to higher temperatures and for longer times resulted in complete removal of octanol from the layer, with two cycles to 190°C with the same heater configuration fully expelling octanol from the sensor, confirmed by FTIR.

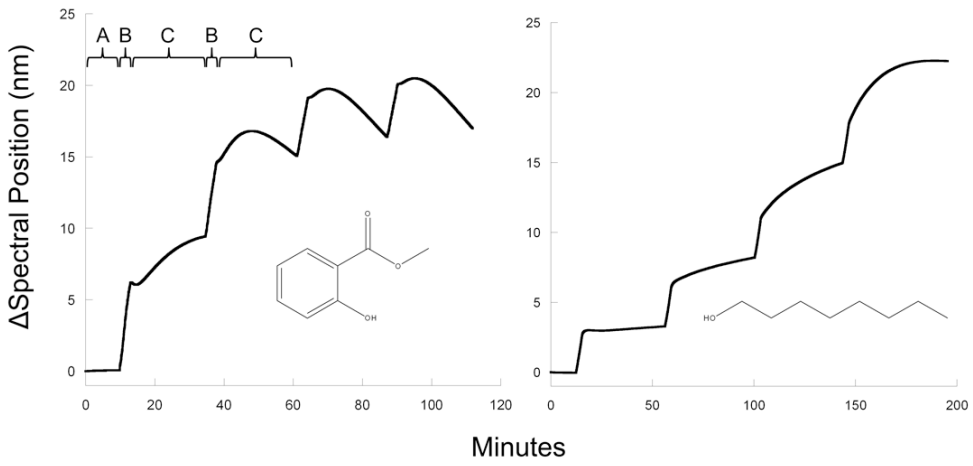

Figure 4.8 Shift in peak position versus time of the accumulation of analytes in oxidized porous SiO_2 over cycles of analyte exposure without thermal reset pulses. The time scales of the baseline in air, analyte exposures, and partial recovery to the baseline in air match those of the Figures 4.6 and 4.7. The first few segments of exposure and recovery are labeled at left, and correspond to the segments in Figures 4.6and 4.7.

The detriments of sensing low volatility vapors without thermally refreshing are exemplified in Figure 4.8, where multiple vapor exposures results in a steady accumulation of analytes and a loss of the sensor's dynamic range .

As mentioned, vapor exposure of the oxidized porous silica followed by thermal reset exhibits an initial spike in sensor response due to pressure buildup in the bubbler line of the vapor delivery. Figure 4.9 shows the difference in sensor response between a configuration with a two-way valve selecting between pure air and vapor/air lines, and a four-way valve with continuous flow-through to avoid pressure buildup. The four-way valve design was utilized for the multiple analyte, sequential dose-refresh cycles shown in Figure 4.13 below. While optimization of the two-way valve switching by turning the downstream valve (upper right diagram) before the upstream valve resulted in a greatly reduced initial spike, the four-way valve configuration eliminated initial spikes. The initial spike is broadened by the presence of the mixing ballast before the sample cell. The effect of a ballast on the concentration changeover time for a constant flow rate system is modeled in Appendix A.3.

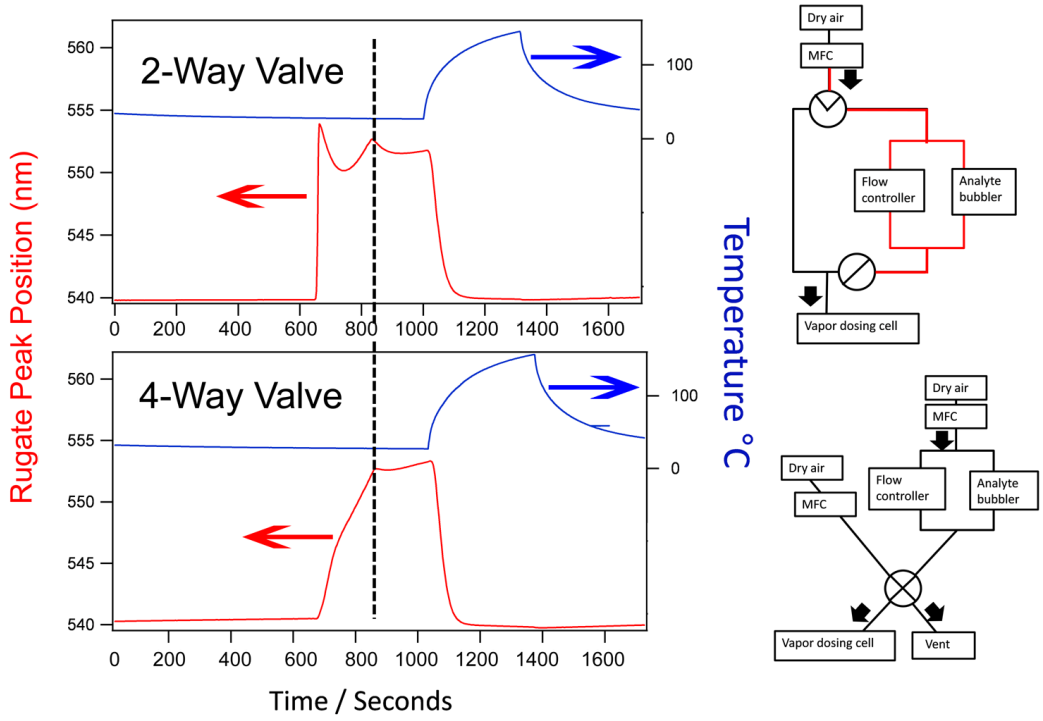

Figure 4.9 Left: Analyte dose and thermal refresh using a 2-way versus a 4-way valve immediately before the sample flow cell. After a baseline in dry air, methyl salicylate vapor was introduced for 3 min at time t=650sec (top plot) or t=700sec (bottom plot) . The vertical line indicates the end of the methyl salicylate dose, which was followed by 3 min of dry air flow before applying the thermal pulse. Temperature versus time is indicated on the right axis. **Right:** Schematics of the two configurations. The initial spike in the 2-way valve run is due to momentary pressure buildup in the analyte line, shown in red. With the flow-through configuration, no such spike was observed.

4.4.4 Temperature Dependence of Sensor Refractive Index

The plots in the right hand columns of Figures 4.6 and 4.7 display the intrinsic shift of the sensor's spectral peak position with temperature as it was heated under a flow of dry air, with no analyte exposure. The first cycle of each of these sensor shift versus, time traces is plotted in the left column of Figure 4.10, with the corresponding temperature vs. time traces below. Plotting the spectral peak shift versus temperature yields linear heating and cooling profiles of the sensor response to temperature, as shown in the right hand column of Figure 4.10.

Since the fresh sample oxidizes at higher temperatures, the cooling cycle follows a curve at a lower response than the heating segment. Oxidization is not linear with temperature and occurs faster at higher temperatures, consistent with the observed linearity of the sensor shift vs temperature response deviating most above 140°C due to increasingly faster oxidation. The spectral response to temperature was determined by fitting each curve between 40 and 140°C, with values of $d\lambda/dT$ given in Table 4.2.

The thin film interference fringes of the spectra, shown in Figure 4.2, were utilized to calculate the change in optical thickness with temperature, $d(2n_{avg}L)/dT$, by performing a Fourier transform of each spectrum in the vapor exposure runs[86] to determine the effective optical thickness $2n_{avg}L$ at each time point. Traces of $2n_{avg}L$ versus temperature were then fit between 40 and 140°C, where L is the cross sectional layer thickness and n_{avg} is the average refractive index of the porous layer.

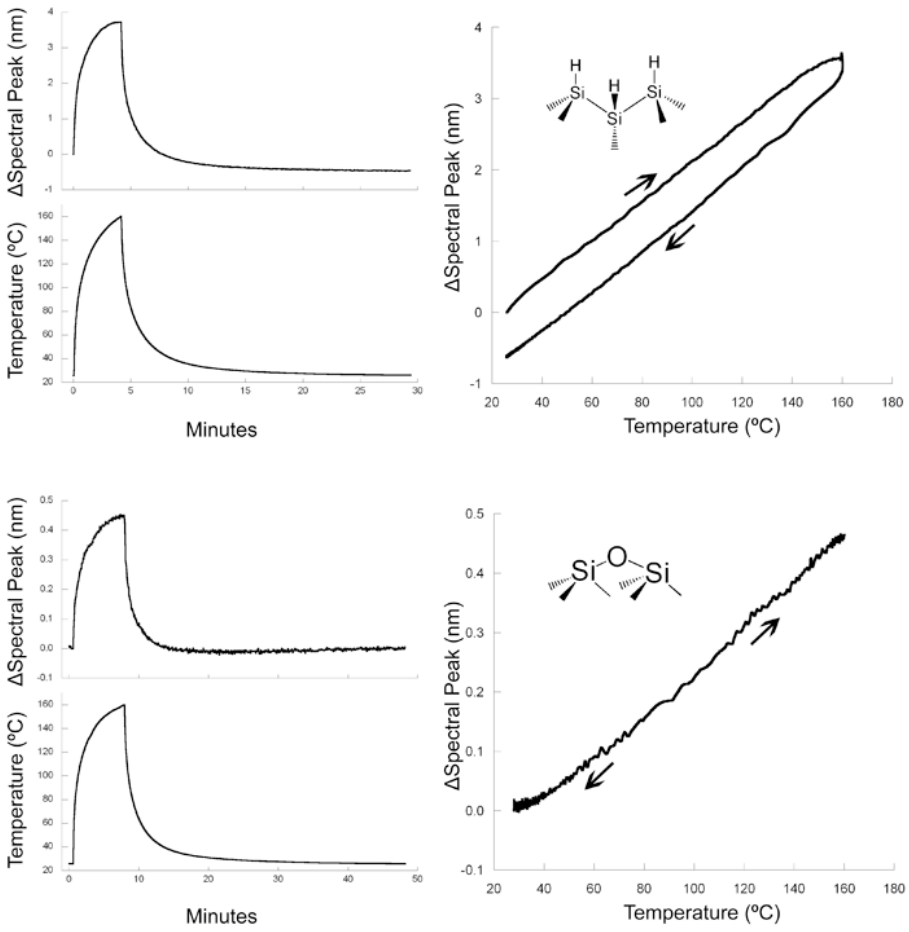

Figure 4.10 Left: Spectral peak shift and temperature versus time for porous Si (top) and porous SiO_2 (bottom) for one cycle of heating under dry air with no vapor exposure. The spectral position shifts with temperature. **Right**: spectral shift versus temperature for porous Si (top) exhibiting a blue shift in wavelength due to oxidation, and spectral shift versus temperature of SiO_2 (bottom) showing a return to the initial wavelength after cooling.

Table 4.2 Measured optical response to heating[1]

	Fresh (Si-H)	Oxidized (SiO_2)
$d\lambda/dT$	$2.8x10^{-2}$	$3.7x10^{-3}$
$d(2n_{avg}L)/dT$	2.8	0.60
$n_{material}$ (Si or SiO_2) at 25°C	4.3	1.46
$dn_{material}/dT$ (Si or SiO2)	$5.1x10^{-4}$	$1.2x10^{-5}$

[1] λ is in nm, T in °C

The refractive index of each sensor material was then determined by first calculating the average refractive index of the porous layer, n_{avg}. The average index was determined by dividing the value of $2n_{avg}L$ at 25°C, taken at the beginning of each run, by twice the thickness L of the layer, determined by SEM. The average layer refractive index is commonly related by the layer porosity to the material refractive index of porous silicon and silica with the Bruggeman effective medium approximation [212]:

$$(1-P)\,\frac{{n_{material}}^2-{n_{avg}}^2}{{n_{material}}^2+2{n_{avg}}^2}+\;P\;\frac{{n_{air}}^2-{n_{avg}}^2}{{n_{air}}^2+2{n_{avg}}^2}=0 \qquad (4.6)$$

where P is the porosity of the layer and $n_{material}$, n_{avg}, and n_{air} the refractive indices of the layer material (silicon or silica), the averaged layer, and air filling the porous voids, respectively.

Calculated silicon and oxidized SiO_2 values of $n_{material}$ are given in Table 4.2. The observed change in the material‘s refractive index was similarly determined by calculating $n_{material}$ at 40 and 140°C for freshly prepared and oxidized sensors, then dividing the difference at those temperatures by ΔT=100°C. Literature values of $n_{material}$ and the temperature coefficient of the refractive index $dn_{material}/dT$ for silicon and several glasses are compiled in Table 4.3.

The thermo-optic coefficient of the refractive index for silicon, dn_{Si}/dT, is commonly reported as $\sim 2x10^{-4}$ [213, 214] That value does not apply here, since it is determined at laser communication wavelengths of ~1.5um and $dn_{material}/dT$ exhibits a strong wavelength dependence[215] that increases significantly at lower wavelengths, both for silicon[216] and for silica[217]. The rugate peak wavelength for the freshly prepared and oxidized samples was 568nm, and values in Table 4.3 were selected from the literature accordingly. In Table 4.3, the refractive index of silicon is reported for λ=570 nm at 25°C[218], and dn/dT is based on Jellison's[215] observations between 400-700nm, with the value at 568nm chosen. The temperature coefficient for fused silica is based on Toyoda's measurements from 450-1500nm and is for λ=550nm at 25°C. The refractive index of SiO_2 is taken at the sodium d-line, λ=589 nm. Lithosil-Q is a synthetic fused silica from Schott glass, and BK7 is a borosilicate crown glass. Values for these materials were provided as references to common optical glasses, with $n_{material}$ for both taken at the e-line (546 nm) at 25°C, and $dn_{material}/dT$ between 60 and 80°C.

Properties of BK7 are also displayed since the p++ Boron-doped wafers contain a small amount of borosilicate upon oxidation. However, the approximately 10^{20} dopant density[219] of the wafers yields a very small overall mass fraction of the material, since $1x10^{20}$ atoms per cm^3 = $1.8x10^{-3}$ g/cm^3 compared to the silicon density of 2.33 g/cm^3. Other glasses containing lanthanides, lead, fluorine, barium, and so forth were deemed not appropriate.

Changes in $n_{material}$ with temperature and wavelength can be expressed more generally through parameters fit experimentally to each type of glass by applying a temperature-dependent form of the Sellemeier equation[220]. Data sets of these fit

parameters were used in the calculation of Lithosil-Q and BK7 values. For instance, at a wavelength λ, the equation below expresses the change in refractive index for a temperature T relative to a reference temperature T_0 , with D_0, D_1, D_2, E_0, E_1, and λ_{TK} as fit constants :

$$\Delta n_{abs}\,(\lambda, T) = \frac{n^2(\lambda,T_0)-1}{2n(\lambda,T_0)}\left(D_0\Delta T + D_1T^2 + D_2T^3 + \frac{E_0\Delta T + E_1\Delta T^2}{\lambda^2-\lambda^2{}_{TK}}\right) \quad (4.7)$$

In this equation, the absolute index n_{abs} is the material refractive index relative to vacuum. The index relative to air is then:

$$n_{rel}\,(\lambda, T) = \frac{n_{abs}(\lambda,T)}{n_{air}(\lambda,T,p)} \quad (4.8)$$

at air pressure p. These equations can then be used to calculate dn_{abs}/dT and dn_{rel}/dT of a material.

The measured n_{SiO2} is in excellent agreement with the literature value, both equal to 1.46. The calculated material thermo-optic coefficient, dn_{SiO2}/dT ($1.2x10^{-5}$), lies between literature values for fused silica and synthetic Lithosil-Q silica. Calculated values for silicon have a greater difference from the literature, with the n_{Si}=4.3 higher than the literature value of 4.0, and dn_{Si}/dT=5.1x10-4 somewhat higher than the reference value of 4.7x10-4.

Typically, both the thermo-optic coefficient described above and a thermal expansion coefficient are considered, and influences due to a change in pressure with temperature from lattice stress have also been suggested[221]. However, contributions from the thermal expansion coefficient are typically an order of magnitude smaller than the thermal-optic coefficient[39, 222]. For instance, Bragg fiber gratings, similar to the oxidized silica multilayer rugate structures described here, experience a wavelength

shift contribution from thermal expansion of the silica core that is less than a tenth that from the thermo-optic refractive index change[223].

Table 4.3 Material Temperature Coefficients

Material	n	dn/dT
Silicon	4.03 [218] 4.01 [224]	4.7×10^{-4} [215]
Fused Silica		1.3×10^{-5} [217]
SiO_2	1.459-1.475 [225]	
Lithosil-Q (fused silica)	1.458 [220]	1.04×10^{-5} [220]
Borosilicate BK7	1.517 [220]	3.1×10^{-6} [220]

4.4.5 Thermal Desorption of Vapors from Porous Silicon

Spectral shifts with temperature of the sensor refreshed after vapor exposure are displayed in Figure 4.11. For clarity, only the first refresh cycle of each series is shown. These profiles represent the desorption of the analytes from the porous matrix as the temperature increases. The shift in the sensor peak position with temperature was corrected for the intrinsic thermal refractive index changes of silicon and SiO_2, described in the previous section. Using those calculated temperature coefficients, the spectral peak position was corrected by $\lambda_0' = \lambda_0 - (T-T_{25^\circ})(d\lambda/dT)$, where λ_0' is the corrected spectral position, λ_0 the spectral position at 25°C, and T the temperature. Corrected curves are displayed as solid lines, with uncompensated profiles displayed as dashed lines. The initial vertical increase in response at 25°C in each panel corresponds to the increase in spectral position upon vapor dosing, and is followed by a

slight decrease during the 3 minute recovery period in air that took place after dosing but before heating. The spectral position shift with temperature is seen as the horizontal segment of each trace that extends rightward from the vertical line of initial vapor response.

The second derivative of these curves represents the maximum rate of change of the spectral position with temperature. Since uniform thermal profiles were applied to each run, this characteristic desorption temperature can be compared for each analyte/material pair. As shown in Figure 4.11, the temperature of the maximum rate of sensor shift for the freshly prepared sensor was T= 72°C for MeS and T=79°C for octanol. The corresponding characteristic temperatures for the oxidized porous silica were significantly higher, with T=105°C for MeS and T=113°C for octanol. As with the differences in the ambient temperature desorption curves shown in Figure 4.5, the higher characteristic temperatures of the oxidized porous silica, compared to the freshly prepared material, are due to the stronger interaction of the oxygen atoms in the SiO_2 surface with the polar analytes than the interaction of the weakly polar Si-H porous silicon. The higher temperatures may also be due to the increased Van der Waals forces exerted on the analytes condensed as liquids or adsorbed as multilayers in the porous silica due to its smaller pore diameter of 6nm, compared to 8nm for the freshly prepared porous silicon. The smaller pore size of the oxidized material is also consistent with its sharper temperature transition, with the change in sensor response at the characteristic temperature occurring over a smaller temperature range than the freshly prepared sensor, as shown in Figure 4.11. Characteristic temperatures T at

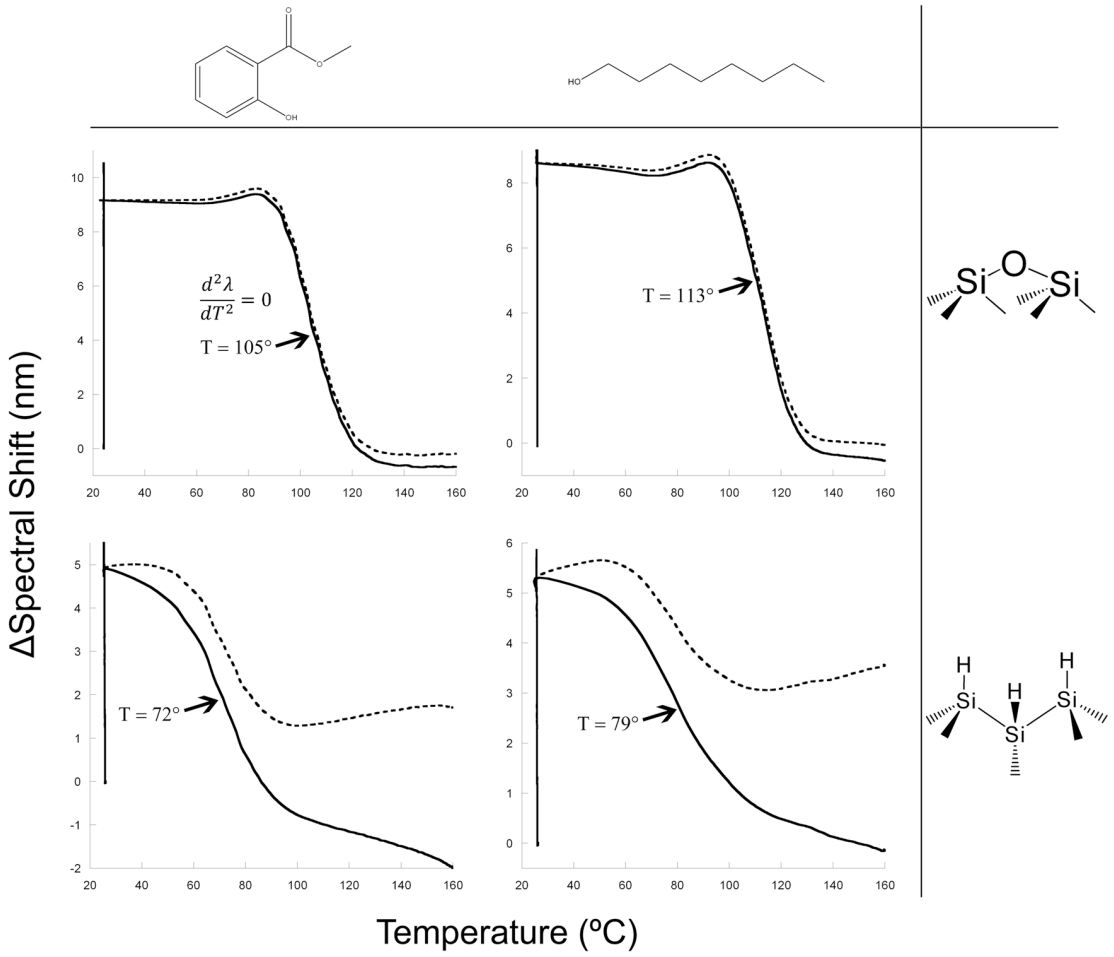

Figure 4.11 Spectral shifts versus temperature for one cycle of vapor dosing followed by heating. Vertical lines at the left of each panel are the spectral shift at 25°C upon vapor exposure, followed by a partial decrease of the peak position in the 3 min of post-exposure air flow before heating. The temperatures of the maximum heating rate, determined by the second derivative of the curves, are indicated. Dotted lines indicate spectral data with no correction for the native change in spectral position with temperature. Solid lines are the peak positions with temperature corrected for the observed native shifts (Figure 4.6). **Top row**: porous SiO_2 exposure to methyl salicylate (left) and octanol (right). **Bottom row**: freshly prepared porous Si exposure to the analytes.

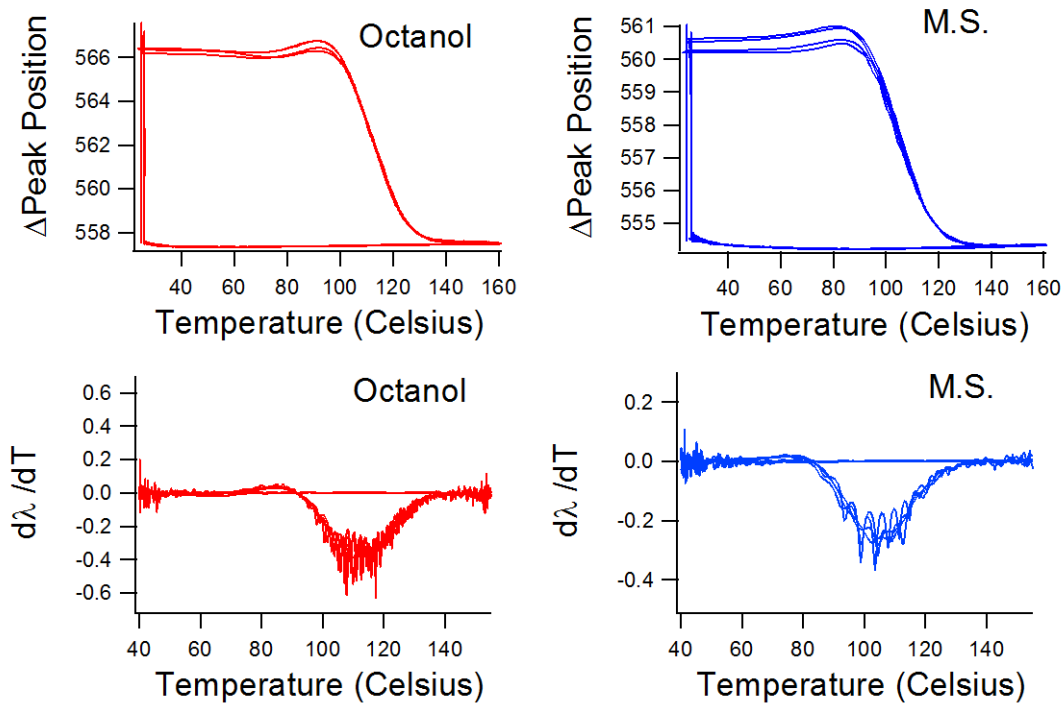

Figure 4.12 **Top:** Spectral shifts versus temperature for multiple cycles of vapor dosing and heating of the oxidized porous SiO_2. The spectral shift over several cycles is show consistent shift-temperature profiles for each cycle. **Bottom:** Derivative of the peak position-temperature plots. The center of a Gaussian fit of the derivative peaks in the lower row were used to determine the temperature at which the change in peak position is greatest for each analyte.

which $d^2\lambda / dT^2 = 0$ were calculated for the other cycles in each run and for the uncorrected spectral shift profiles, and found to agree within +/-1°C for the oxidized runs and +/-2°C for the runs with freshly prepared porous Si, with the greater variability of the latter resulting from gradual oxidation with each temperature cycle. Figure 4.12 displays the spectral peak position shift versus temperature (top row) and the derivative of the peak shift versus temperature (bottom row) over all cycles for the oxidized sensor repeated vapor doses. The profiles were consistent over many cycles. The derivative shifts versus temperature profiles were fit with a Gaussian function between 80 and 140°C, and the central temperature of the Gaussian fit taken as the T at which $d^2\lambda/dT^2 = 0$.

4.4.6 Sensor Reuse Over Multiple Vapor Exposures

The stable baseline of the oxidized porous silica sensor over repeated thermal cycles and vapor exposures makes it suitable as a durable sensing material. Periodic thermal pulses were applied to the porous silica sensor under dry air, as shown in Figure 4.13. The sensor was then subjected to cycles of analyte exposure and thermal refresh, alternating between isopropanol, methyl salicylate, and octanol. Each cycle of vapor exposure consisted of exposure to analyte for 3 min, recovery under dry air for 3 min, and application of a thermal pulse to 160°C. The temperature-time profile is displayed in the bottom panel of the figure for comparison.

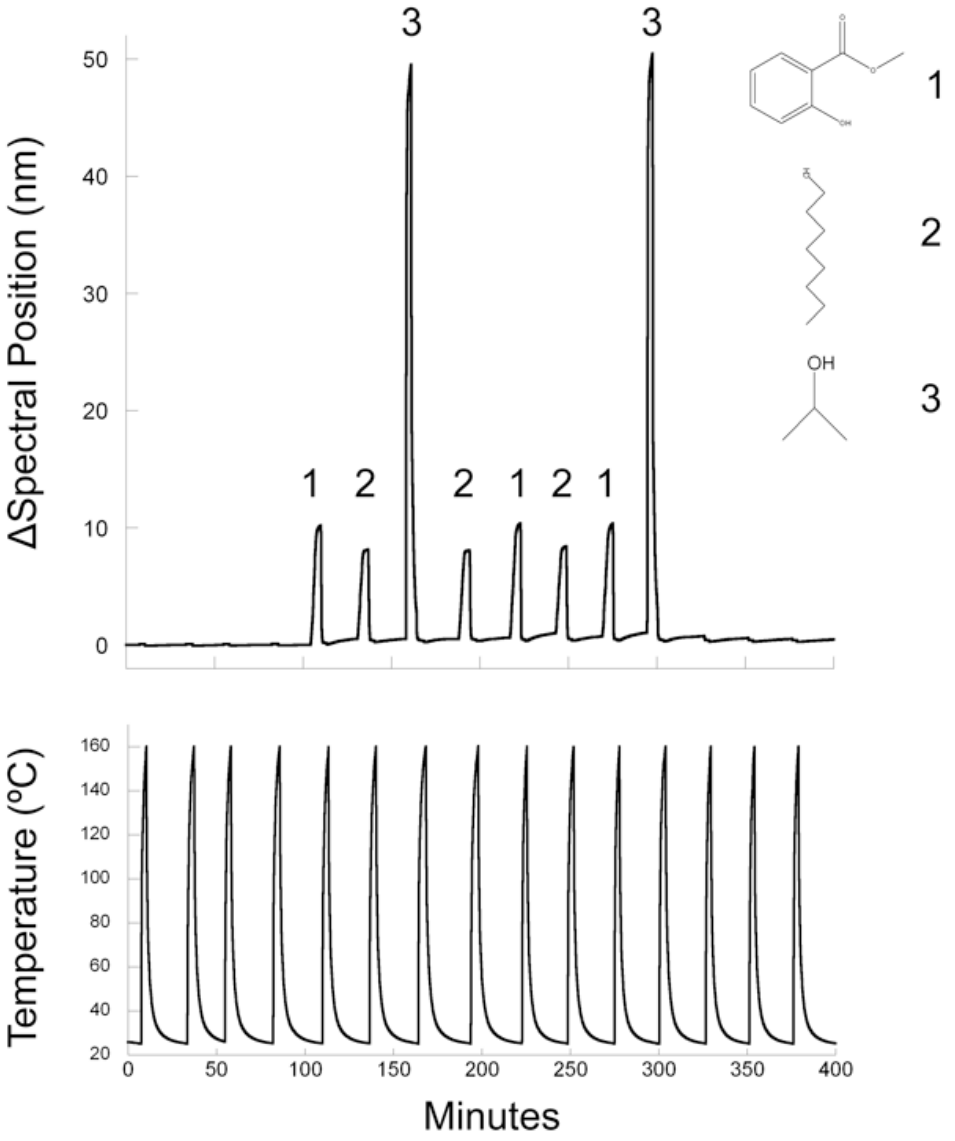

Figure 4.13 Continual thermal refresh of oxidized porous SiO_2. Cycles under dry air are followed by cycles of consisting of 3 min of analyte exposure, 3 min of recovery under dry air, and a thermal pulse and recovery under dry air. Isopropanol, methyl salicylate, and octanol were alternatively introduced to the sensor as indicated.

4.4.7 FTIR Analysis of Thermally Refreshed Filters

ATR-FTIR spectra of sensor surface was taken before and after each of the cycled vapor exposure runs, as shown in Figure 4.14. Spectra were acquired for both the thermally refreshed and the ambient temperature runs, and for both oxidized and freshly prepared materials. While the oxidized sensor chips could be reused for multiple runs, with no change in FTIR features after multiple thermal refresh cycles, the fresh sensor chips oxidized in air with each thermal pulse and required separate, identically etched samples for each new vapor run.

Spectra of freshly prepared porous Si are shown in the left column of Figure 4.14. All exhibit peaks from the $\nu(SiH_x)$ stretches at 2112and 2087 cm^{-1}, $\delta(SiH_2)$ at 907cm^{-1}, and $\delta(SiH_x)$ at 623cm^{-1}. Cycled heating of the fresh sample, without any exposure to vapor (right column of Figure 4.6), resulted in the growth of a $\nu(SiO)$ band at 1009 cm^{-1} as shown in the second row of Figure 4.14. While dosing the fresh sensor with MeS and applying thermal refresh pulses yielded the same result of slight oxidation, dosing with octanol and applying a single thermal refresh pulse after each dose showed additional infrared peaks that correspond to the octanol not desorbed from the porous matrix (third row, $\nu(CH$) at 2855, 2922,and 2958 cm^{-1} and $\delta(CH)$ at 1466 cm^{-1}). When additional thermal pulses to the same temperature were applied after octanol vapor exposure, the analyte was effectively desorbed and the FTIR peaks of octanol in the sensor eliminated (fourth row). FTIR spectra of the fully oxidized porous silica are shown in the right column, and exhibit a strong $\nu(Si\text{-}O\text{-}Si)$ stretch at 1020 cm^{-1}. Heating of the oxidized sample without exposure to analyte yielded the

same spectrum as heating the sensor after exposure to analyte, with the latter shown in the second row.

In contrast, FTIR spectra of the sensor after the vapor accumulation runs in which no thermal refresh was applied (Figure 4.8) exhibit additional infrared peaks corresponding to adsorbed analytes, as shown in the bottom two right hand panels of Figure 4.14. The spectrum after octanol accumulation exhibits alkyl stretch peaks ν(C-H) at 2858, 2928, and 2960 cm^{-1}[1226] and that of MeS after accumulation exhibits a ν(C=O) stretch at 1680cm^{-1}, ν(Ph) at 1616, 1587, 1487, 1444, and 1306 cm^{-1}, and δ(OH)at 1334 cm^{-1} [227]. The FTIR spectra of liquid octanol and MeS are displayed in Figure 4.15, with key peaks that were exhibited in the spectra above labeled: ν(CH) at 2853, 2924, and 1464 cm^{-1}, δ(CH) at 1464 cm^{-1}, and ν(OH) at 3325 cm^{-1} for octanol; ν(C=O) at 1673 cm^{-1}, ν(Ph) at 1616, 1584, 1484, 1439, and 1302 cm^{-1}, and δ(OH) at 1334 cm^{-1} for MeS.

Figure 4.16 displays the ATR-FTIR spectra of the AOS thermal compound that applied to the backside of the sensor chips to facilitate thermal contact with the heater. Spectra of two porous SiO_2 samples are also displayed. One sample was kept free of contamination and exhibits only an Si-O-Si absorption above 1000 cm^{-1}. The other sample (middle plot) was contaminated with a small amount of the thermal paste, clearly shown in the spectrum. The plots highlight the need for careful handling of the small sensor chips.

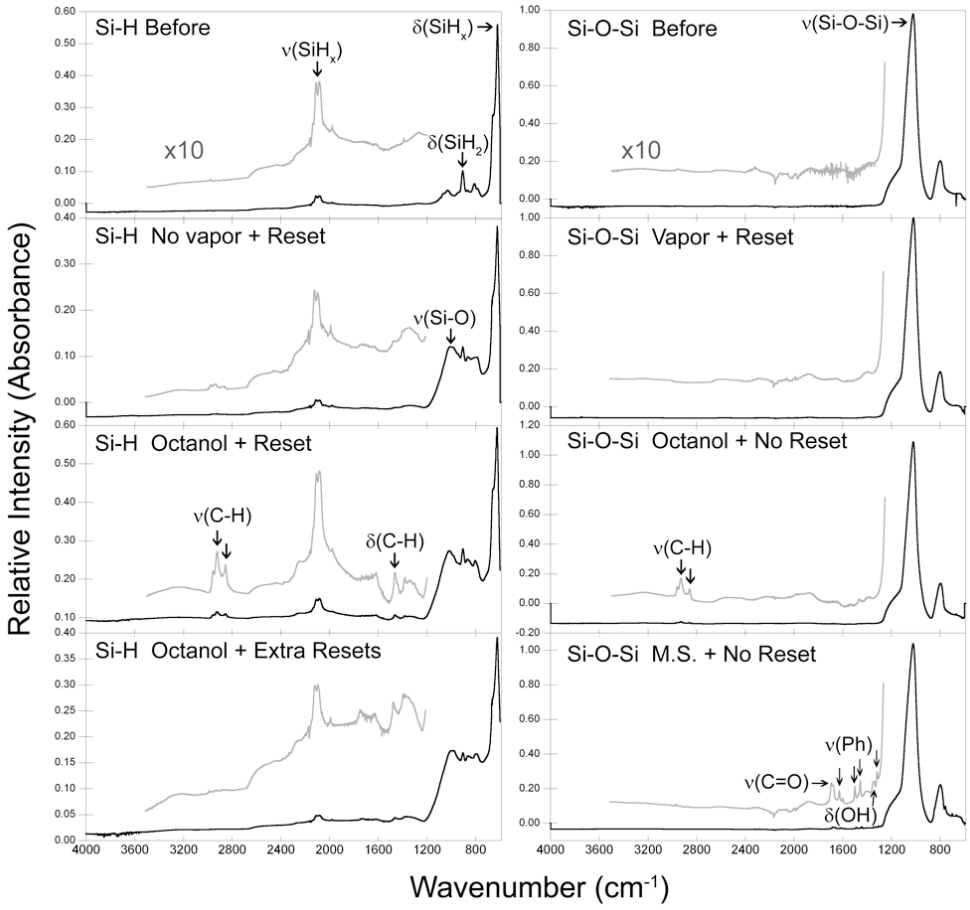

Figure 4.14 ATR-FTIR spectra. **Left:** freshly prepared porous Si. **Right**: oxidized SiO_2. When the sensors are heated in air with no analyte exposure, the SiO_2 shows no change in FTIR peaks, while the fresh Si sensor exhibits oxidation. After analyte exposure followed by heating, the SiO_2 again show no change while the Si sensor exhibits oxidation. In the case of octanol with the fresh Si sensor, trapped vapor is visible in the FTIR after a single thermal pulse (third row), but eliminated after multiple thermal pulses (fourth row). The bottom two panels at right show the accumulation of vapors in the SiO_2 structure (Figure 4.5) after several exposures if no thermal refresh is applied.

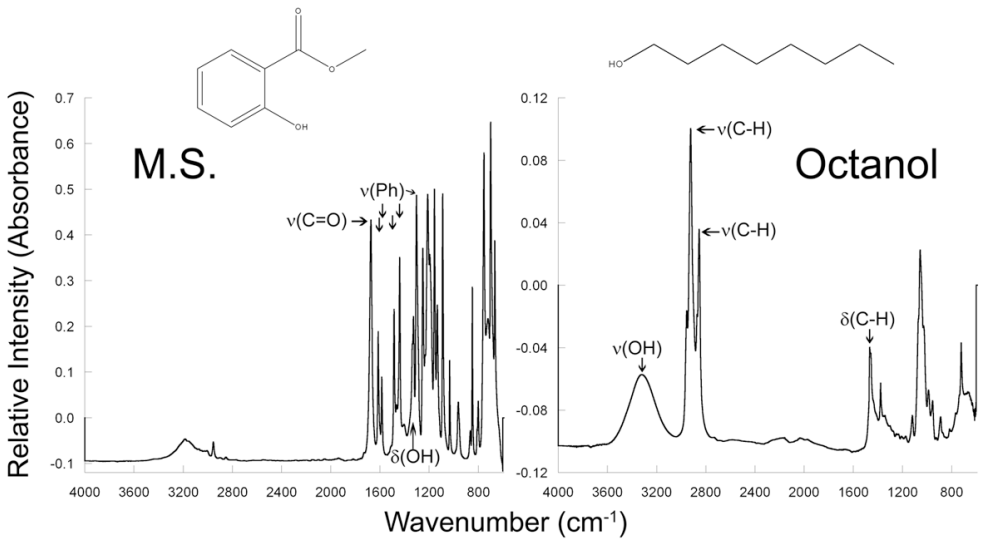

Figure 4.15 ATR-FTIR spectra of liquid methyl salicylate (left) and liquid octanol (right). Features present in the porous Si exposed to analytes (Figure 4.9) are noted.

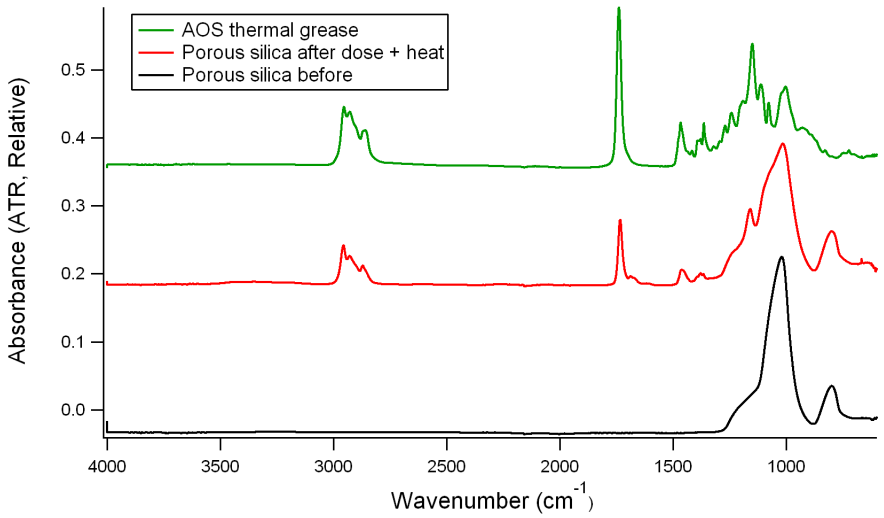

Figure 4.16 ATR-FTIR spectra of oxidized SiO_2 before heating (bottom) and after heating (second from bottom) compared to the thermal paste used to contact the heater with the sensor chip. The sample after heating was contaminated with the thermal grease compound or copper tape glue, as indicated by the 2800-2900cm-1 C-H stretches of the organic compounds in both. Care must be taken in the handling of the 5x5 mm sensor chips.

4.5 Conclusions

Porous silicon and silica rugate optical layers exhibited retention and slow desorption of methyl salicylate and octanol vapors at ambient temperature. Application of a thermal pulse rapidly refreshed the oxidized silica sensors to their initial baseline, and refreshed the freshly prepared silicon sensors to a lowered baseline due to thermal oxidation. For porous silica, the thermal refresh methodology was repeatable and consistent over multiple cycles of vapor exposure and thermal refresh to 160°C. The temperature at which the maximum rate of sensor response occurred was unique to each vapor and sensor material combination, suggesting the ability to discriminate vapors through optical sensing of the porous layers during the thermal refresh. . Periodic thermal pulses allowed for the continuous detection of sequentially administered methyl salicylate, isopropanol, and octanol vapors that would otherwise not fully desorb from the porous layer in the sensor sampling period.

Chapter four, in part or in full, is a reprint (with co-author permission) of the material as it appears in the following publication: King, Brian H.; Noda, Sadafumi; Sailor, Michael J. *Thermal desorption of organic vapors from porous silicon films and implications in optical vapor sensing*. Manuscript in preparation The author of this dissertation is the primary author of this manuscript.

CHAPTER FIVE

DISCRIMINATION OF PURE CHEMICAL VAPORS BY OPTICAL SENSING OF A THERMALLY CYCLED RUGATE POROUS SILICA PHOTONIC CRYSTAL

5.1 Abstract

The last chapter explored the influence of a thermal pulse to desorb low volatility organic vapors from porous silicon, and noted the difference in characteristic desorption profiles between analytes. In this chapter, a methodology is presented for the discrimination of pure volatile organic vapors based on optically sensing shifts in the spectral resonance band of a thermally cycled rugate porous silica photonic crystal. The thermal response profile of the stop band as the sensor is cycled enables separation of sensor responses for analyte partial pressures from 0-7.5 Torr. The sensor response to temperature modulation while exposed to vapor flows was consistent with the equilibrium adsorption isotherms of the sensor. At the lower isopropanol concentrations, a delay in the sensor response is observed when heated , due to its slower equilibration.

5.2 Introduction

Optical porous silicon sensing films, electrochemically fabricated by etching crystalline silicon in aqueous hydrofluoric acid, have been employed to detect a wide range chemical and biological compounds, including volatile organic vapors[60, 90], explosives[30], DNA[28, 99], and proteins[59, 87]. Their large surface area [60], ease of fabrication, range of accessible surface chemistries[3], and controllable optical and morphological properties including pore size, porosity, and refractive index allow the porous material to be tailored to specific sensing applications. Chemical vapor sensing has been demonstrated with various porous silicon optical structures including Bragg mirrors[4], Fabry-Pérot films[5], microcavities[6], and rugate filters[7]. Sinusoidal variations in the porous silicon refractive index with depth result in rugate filters[8] with a

reflection stop band at a wavelength determined by the amplitude and period of the refractive index modulation. Infiltration of chemical vapors into the porous film shifts this spectral peak by increasing the refractive index of the porous layer thereby enabling transduction of ambient vapors by monitoring the magnitude and time evolution of the reflected stop band or "rugate peak" wavelength[9].

Porous silicon vapor sensing has largely been performed at ambient temperatures, with the vapor-sensor equilibrium passively monitored. Thermal pulses have been used with electrically transduced porous silicon sensors to refresh the porous matrix after analyte exposure [203, 204], but little work has been conducted on porous silicon exploring the use of thermal modulation to gain vapor discrimination information. Foucaran[205] constructed a thermoelectrically cooled capacitive porous silicon humidity sensor based on thermally modulating the dew point, but these and other humidity sensors have focused on high analyte concentrations in which capillary condensation occurs in the porous layer[228], and have transduced sensing electrically. Here, optically sensed porous silica is rapidly thermally cycled while exposed to low concentrations of analyte vapors, and the thermal modulation response used to inform analyte concentration and discrimination.

Thermal cycling has been utilized on other materials to improve sensor discrimination and selectivity capabilities. Lee[117] has reviewed temperature modulation techniques applied to metal oxide sensors. Notably, Nakata applied sinusoidal temperature cycles to semiconductor conductivity sensors and assessed the characteristic conductance-temperature profiles of the sensor exposed to light hydrocarbons[118]. Helig also applied sinusoidal temperature profiles, modulating a tin

oxide resistivity sensor to extract analyte-specific characteristics for CO and NO_2. More recently, Semancik and Raman have used programmed temperature profiles on arrays of metal oxide films to separate analyte behavior based on conductivity measurements[123, 229]. In each case, high temperatures ranging from 200-600°C were employed and chemical transduction was electrically based.

Here, an optically interrogated oxidized porous silica sensor is used for chemical vapor transduction. After an initial investigation of the isothermal vapor response of the sensor, the optical film was rapidly cycled over a low temperature range and exposed to volatile organic compounds, with the optical shifts of the rugate peak monitored over the temperature modulations and used to inform vapor concentration and discrimination. The sensor is modulated between 25-80°C, and exposed to vapor partial pressures ranging from 0-7.5 Torr (a few hundred to several thousand ppm). Oxidized porous silica, fabricated by heating porous silicon to high temperatures in humid air, was chosen primarily due to its greater stability than freshly prepared porous silicon[7, 31] as well as its heightened sensitivity to analyte vapors from the decrease in pore size with oxide growth. Three volatile organic analytes are assessed. Heptane and isopropanol were chosen to compare polar and nonpolar analytes with comparable vapor pressures at 25°C, with cyclohexane chosen to compare the response of a higher volatility nonpolar analyte.

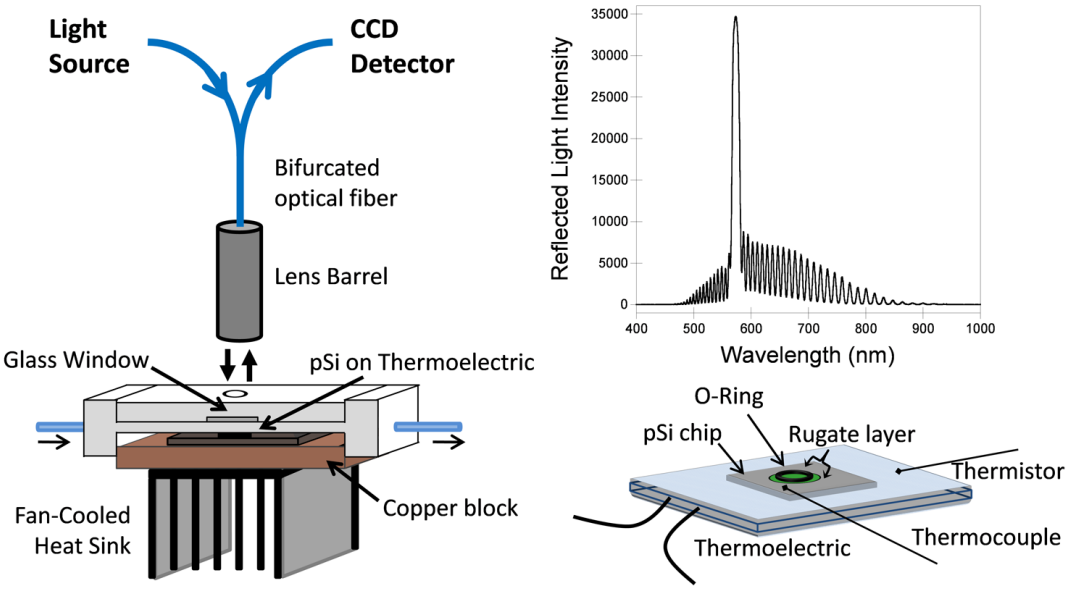

Figure 5.1 Sensor experimental configuration. The porous Si was sealed into a vapor flow cell and a Peltier thermoelectric contacted to the backside to heat and cool the chip. Temperature readings were taken with a thermocouple directly attached to the silicon chip, with a thermistor coupled to the thermoelectric to validate the thermocouple reading. Visible spectra of the rugate layer, taken through an optical window in the flow cell, exhibit a spectral peak that red shifts with vapor exposure. The wavelength shift of the spectral peak was taken as the measurand (rugate peak shift). A continuous flow of nitrogen with a partial pressure of vapor was continuously delivered to the flow cell at a rate of 1 L/min.

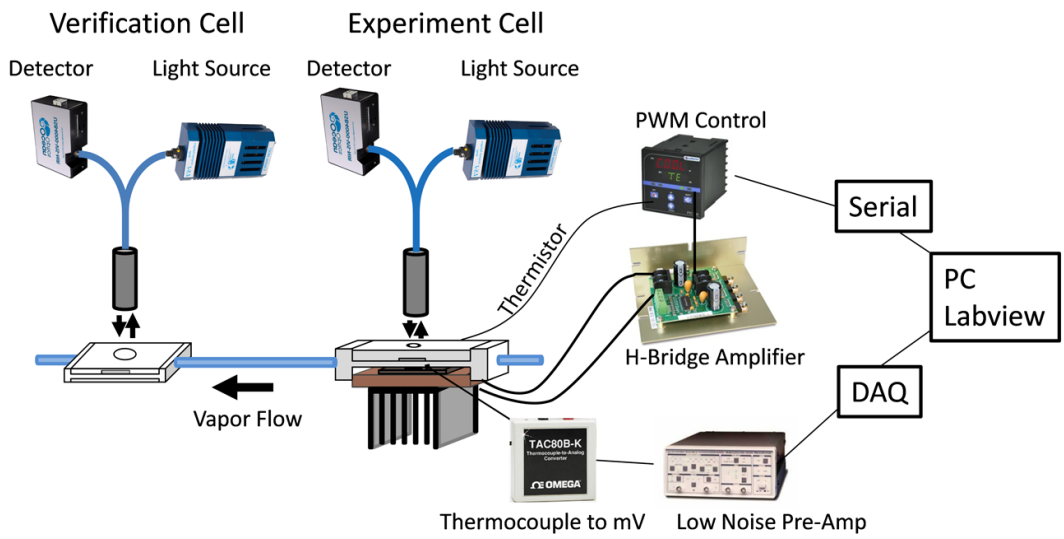

Figure 5.2 Expanded diagram of acquisition configuration. A second vapor flow cell was connected serially to the outflow of the thermally cycled cell to validate responses and check for vapor delivery system abnormalities. Temperature readings were converted to voltage at 1mV / °C, amplified, filtered, acquired by a data acquisition card and processed in LabView. The thermoelectric was driven by a controller unit under manual computer control and operated in pulse width modulated mode through an H-bridge amplifier. The thermistor was used to validate thermocouple readings and to control the thermoelectric in constant-temperature isothermal experiments. Manual control of the thermoelectric power was employed for temperature cycling experiments.

5.3 Materials and Methods

5.3.1 Sensor Preparation

Porous silicon rugate optical films were prepared from single-crystal, (100)-oriented highly boron-doped p-type Si (Siltronix, 1-1.2 mΩ-cm resistivity) by electrochemical etching in 3:1 v:v solution of aqueous hydrofluoric acid (49%, Fisher Scientific):ethanol (Rossville Gold Shield Chemical). Etching was performed in a Teflon cell with a platinum ring counter electrode and a galvanostat (Kepco BOP 50-4D) under computer control (Lab View, National Instruments.) The current density waveform of the rugate etch was varied in time (t) sinusoidally according to:

$$I(t) = I_{min} + \frac{\Delta I}{2}\left[\sin\left(\frac{2\pi t}{p}\right) + 1\right] \quad (5.1)$$

where I_{min} = 12.5 mA/cm^2 and ΔI=50 mA/cm^2 with a period of p=7.73s. Porous silica was generated by oxidizing the porous Si layers in a tube furnace (Lindberg Blue) for 45 minutes at 800°C in ambient air, resulting in a rugate peak at ~570nm as shown in Figure 5.1.

5.3 2 Sensor Characterization

Gravimetric Determination of Porosity

Samples were weighed before etching (m1), after etching (m2), after oxidation (m3) and after dissolving the porous layer (m4) with a 1:1 solution of aqueous HF:ethanol, followed by rinsing with ethanol. Since for oxidized samples the density of the oxidized (2.21 g/cm^3) etched layer differs from that of the bulk silicon (2.33

g/cm^3), volumes of each must be considered. The following equation was used to determine the porosity of the oxidized samples[170]:

$$\text{Porosity} = (V_{total}-V_{SiO2}) / V_{total} \quad (5.2)$$

where the total volume removed after etching and dissolution is $V_{total} = (m_1-m_4)/2.33$ and the silica volume after oxidation is $V_{SiO2} =(m_4-m_3)/2.21$. Oxidized optical sensors had an average porosity of 29%+-2% for 5 oxidized samples.

Scanning Electron Microscopy

Scanning electron microscopy was used to determine porous silica layer thickness by cutting and imaging cross sections with a Phillips XL30 Field Emission ESEM in secondary electron mode and an accelerating voltage of 10kV.

Fourier Transform Infrared Spectroscopy

Oxidation of the porous layer and its surface stability before and after thermal cycling and vapor dosing was verified through attenuated total reflectance FTIR spectroscopy. Spectra were recorded with a Thermo Scientific Nicolet 6700 FTIR with a Smart iTR diamond ATR attachment using a resolution of 2 cm^{-1} and an average of 128 scans.

Pore Size Determination

Nitrogen adsorption-desorption isotherms of the porous SiO_2 were recorded at 77 K using a Micromeritics ASAP 2010 volumetric apparatus. Samples were first degassed *in situ* at 323 K until a static vacuum of 5×10^{-5} Torr was reached. Pore dimensions were determined using the BdB method. An opening pore diameter of 4.9nm and average pore diameter of 5.9nm were determined.

5.3.3 Vapor Dosing and Thermal Cycling Vapor Dosing

A schematic of the vapor delivery system is shown in Appendix image A.2.1. The vapor delivery system consisted of two electronic mass flow controllers (Alicat Scientific) pooled into a vapor delivery line and two controllers pooled into a nitrogen line. The Teflon tubing of the vapor line flowed horizontally into a heated stainless steel vaporization block maintained at 50°C to promote full vaporization. Peek tubing from the outflow of a low-flow liquid pump (MilliGAT 6nl-10ml/min, GlbalFIA) was inserted into a vertical tap in the heated block fitted with Swagelok seals to inject analytes into the flow stream, with the calibrated pump rate of liquid analyte delivery and nitrogen flow rate determining the vapor concentration. Solenoid valves before and after the block prevented back pressure to the flow controllers. The outflow of the vaporization block was united with the nitrogen flow line at a computer controlled four-way valve, with the nitrogen and vapor lines switched between two valve outlets, one to the flow cell and the other to a waste stream. Both lines were maintained at a flow of 1 L/min. Vapor concentrations were validated with a gas chromatograph (SRI Instruments 8610C with FID detector).

Several of the short-range 0-7.5 Torr isothermal equilibrium runs were repeated with a bubbler-based concentration delivery system consisting of two glass bubblers filled with liquid analyte and connected in series, in the place of the heated injection block. The bubblers were placed in a temperature controlled bath (Thermo Scientific Neslab RTE740) maintained within 0.1°C, and set to 0, -5.83, and 12°C for isopropanol, heptane, and cyclohexane respectively, such that the saturated vapor pressures were comparable. After passing through bubblers, the vapor line was diluted

with a flow of N2 to the desired concentration, with flow in both lines controlled by electronic mass flow controllers (Alicat Scientific).

Sensor Mounting and Thermal Cycling

The backside of the sensor chip was coated with thermal paste (AOS Thermal Compounds) and placed on a thermoelectric Peltier module driven in pulse width modulation mode by a PID controller unit (Ferrotec FTC100), with a copper block heat sink and an aluminum, fan-cooled heat sink underneath the thermoelectric (Figure 5.1). Isothermal experiments utilized the PID controller algorithm to maintain temperature within 0.1°C. For temperature cycling, the copper block was removed and the controller unit placed in manual mode, with a serial connection executing power control through LabView. A thermocouple was placed on the silicon top surface of the sensor chip with Kapton high temperature tape (VWR) outside of the optical interrogation area. A thermistor affixed to the thermoelectric Peltier was used to validate thermocouple readings. The thermocouple temperature reading was converted to voltage (Omega TAC80B-K) and amplified (Stanford Research SR560 low noise preamplifer) before DAQ acquisition into LabView. The sensor's vapor flow cell is drawn in Figure 5.1 and consisted of a Teflon cell with Swagelok input and output ports and a glass optical window to allow optical interrogation of the sample. A Kapton O-ring on top of the sample sealed the sensor to the glass window.

Reflected Light Spectra

Reflected light spectra of the samples in the visible region were taken from 345-1045nm with a CCD spectrometer (Ocean Optics USB4000) with a tungsten-halogen lig ht source (Ocean Optics LS-1) connected with a Y-branch 600um diameter,

bifurcated multimode optical fiber. The common end of the bifurcated fiber was focused with an objective lens to a $2mm^2$ spot size and positioned normal to the porous silica surface. Figure 1 displays the reflected light spectrum of a sample before vapor introduction. Each rugate spectrum collected was fit with a Gaussian function in LabView to determine the peak wavelength (λ_{max}). Rugate spectra and temperature readings were acquired at a rate of 5Hz for temperature cycling runs, 1 Hz for equilibrium-shift isothermal adsorption-desorption dosing, and 9 Hz for isothermal desorption rate experiments.

A second verifier sensor chip and CCD system was connected serially to the outflow of the thermally modulated vapor flow cell (Figure 5.2) to monitor the vapor delivery system for abnormalities. The liquid pumps sometimes exhibited periodic cutouts in pumping activity, presumably due to liquid analyte swelling inner seals after several days. Abnormalities were monitored and any runs showing abnormalities were discarded and repeated.

5.4 Results and Discussion

5.4.1 Isothermal Equilibrium Spectral Shifts

First, the sensor was held at a constant temperature and exposed to vapors of volatile analytes to probe the effect of temperature on the vapor porous silica adsorption equilibrium.

Wavelength shifts of the rugate stop band were first assessed at 25°C over a full range of vapor pressures, from pure nitrogen to vapor saturation, and for the analytes isopropanol, heptane and cyclohexane. A flow of 1L/min of nitrogen was passed over

sensor as depicted in Figure 5.1. The partial pressure of the vapor in the flow stream was incrementally increased to saturation and likewise decreased, with the sensor response allowed to equilibrate to a steady level at each concentration. Spectra were acquired once per second and the average equilibrium rugate central peak position for each concentration segment was determined. The equilibrated sensor response, taken as the shift of the rugate peak wavelength at a given vapor concentration relative to the peak position during an initial baseline in nitrogen, is plotted against vapor concentration for each analyte in the top row of Figure 5.3. The step-wise cycle of adsorption and desorption of vapors was performed twice for each analyte, with the difference in datasets below the error band of each concentration segment.

As shown in the top row of Figure 5.3, the porous silica exhibits a type IV isotherm with an H2 hysteresis loop[64], common for mesoporous materials. The initial rise with increasing concentration corresponds to monolayer absorption, with the upwardly sloped initial linear region indicating multilayer adsorption followed by a sudden increase in adsorption due to capillary condensation. Approaching saturated vapor concentrations, the sensor response plateaus at the analyte saturated vapor pressure since the analyte sorption is limited by the finite open pore volume of the solid porous matrix. The hysteresis in porous adsorbents commonly derives from interconnected, networked pores and from the inkbottle shape of the pores, where desorption from wider sections of a pore cannot occur until desorption from the narrow neck above takes place at a lower vapor partial pressure. The corrugated pores of the

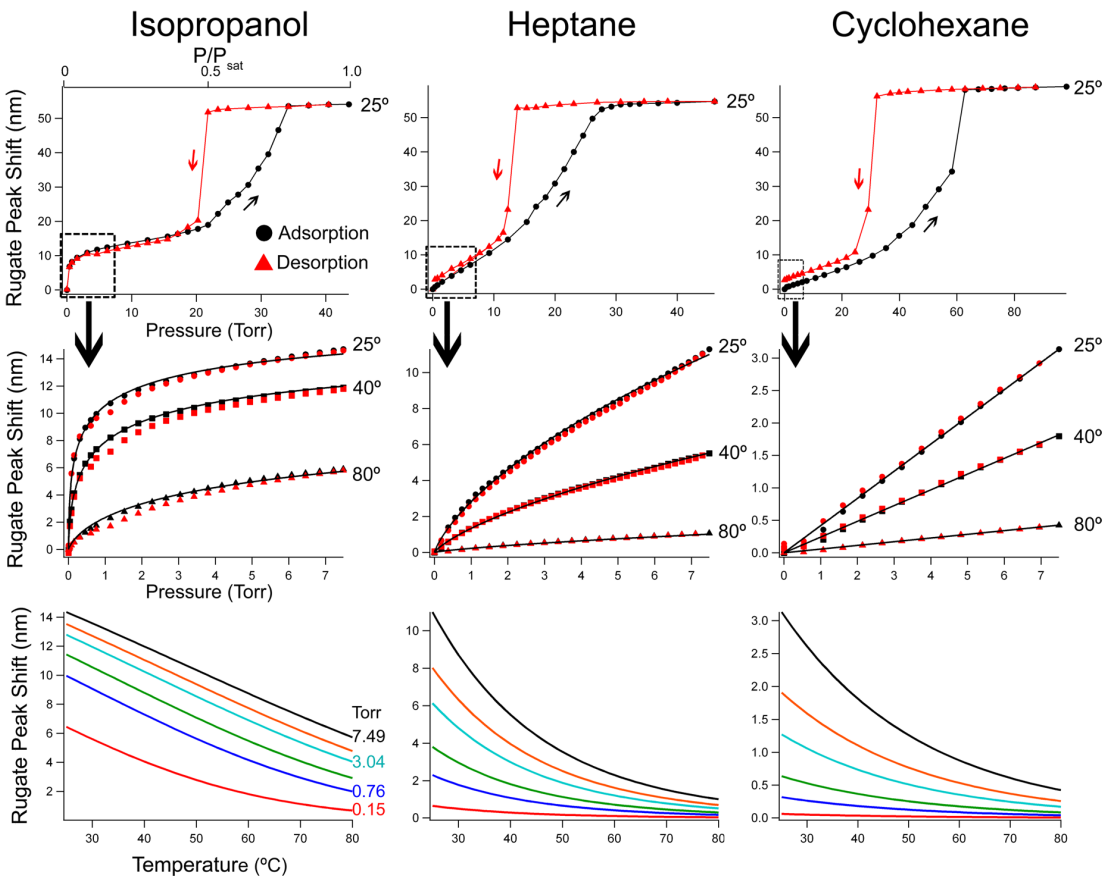

Figure 5.3 Isothermal peak shifts of the sensor at equilibrium with concentrations (pressures) of analyte vapor. **Top row:** at 25°C the vapor concentration was progressively increased step-wise to saturation, then decreased step-wise, with the sensor allowed to equilibrate to each concentration step. Pressures are the analyte partial pressures in the applied nitrogen stream, with the total pressure of the stream at ambient. Lines are drawn to guide the eye. **Middle row:** at three temperatures for each analyte, the partial pressure (concentration) was progressively increased to 7.5 Torr then progressively decreased, to obtain equilibrium spectral shifts at each pressure. The solid lines are fits of the data to the Toth temperature-dependent isotherm equations. **Bottom row**: Using the Toth isotherm fits, the spectral shifts as a function of temperature were calculated for various analyte pressures. Six are shown above, with labels on four. These differences with temperature of these curves suggest a discrimination methodology based on modulating the temperature of the sensor.

rugate porous silica layer exacerbate these constriction effects. Cyclohexane and heptane also exhibit a degree of low-pressure hysteresis, which may indicate a degree of irreversible uptake of the analyte from the smallest pores for concentrations above the capillary condensation point. The large separation between absorption and desorption segments characteristic of the H2 loop indicates a disordered pore system with a nonuniform distribution of pores sizes. This nonuniformity of electrochemically fabricated porous silica is well known [12, 228] and was confirmed here through SEM plan-view imagery of the sensor surface and through nitrogen absorption BET analysis, in which the porous silica layer exhibited a 49 Angstrom opening pore diameter and 59 Angstrom closing diameter.

The sudden decrease in sensor response with decreasing analyte partial pressure in the desorption curve is ascribed to the disappearance of the liquid meniscus from sudden vaporization of the condensed liquid between adjacent pore walls, leaving an adsorbed multilayer. This closure point corresponds to the Kelvin diameter d, expressed as [228]:

$$d = -\frac{4\gamma M}{\rho RT \ln\left(\frac{p}{p_0}\right)} \tag{5.3}$$

where ρ, γ, and M are the vapor density, surface tension, and molecular weight of the analyte, p_0 is the saturation vapor pressure, and p the applied pressure [7]. Using the relevant physical properties of each analyte [211], the Kelvin diameter for the partial pressure of the inflection point of each analyte's desorption curve were calculated as 1.8, 1.8, and 1.6nm for the respective observed desorption partial pressures of 0.3 P/P_{sat} for cycloxane, 0.27 P/P_{sat} for heptane, and 0.45 P/P_{sat} for isopropanol. Given the

nitrogen desorption opening pore diameter of 4.9nm, this implies a multilayer thickness immediately after the desorption drop of approximately (4.9-1.8)/2 = 1.6nm on the pore wall. A simple multipoint BET fit was also performed on the isothermal, equilibrated vapor dosing data in row 1 of Figure 5.3 in order to determine the BET constant, C_{BET}. The BET constant represents the affinity between the vapor and the sample surface, and was determined to be C_{BET} = 66 for nitrogen adsorption-desorption (77K under vacuum). For the vapor isothermal dosings, C_{BET} = 2 for cyclohexane, 2 for heptane, and 220 for isopropanol. The large difference between isopropanol and the other analytes is due to the strong affinity of the polar molecule to the oxygen electrons on the SiO_2 surface.

Second, having characterized the sensor response at 25°C up to saturated pressures, the sensor was next assessed from vapor pressures from zero to 7.5 Torr with finer steps of pressure and at three temperatures, as shown in the second row of Figure 5.3. These low vapor concentrations are most germane to sensing applications. Equilibrated sensor responses for vapor pressures incremented up to and then down from 7.5 Torr were determined over two absorption-desorption step-wise cycles for each analyte, with corresponding vapor concentrations in each cycles exhibiting differences in peak shifts less than the error band of each segment (<0.1nm). The adsorption-desorption cycles over this concentration range showed no appreciable hysteresis, as expected since the maximum pressure of 7.5 Torr is well below the capillary condensation point for each analyte. Although cyclohexane and heptane both exhibited a small degree of low-pressure hysteresis for desorption from saturation (Figure 5.3, row 1), this hysteresis was not observed for desorption from 7.5 Torr.

The Toth isotherm is commonly used to experimentally fit complex adsorption systems [185]. Here, a set of temperature dependent Toth isotherm equations were applied to experimentally fit the low pressure region of the equilibrium response. These fits are plotted as the solid black curves in the second row of Figure 5.3 and were found to fit the experimental data at each temperature well. For a pressure P, with fitting parameters b_0, Q, t_0, α, χ, and $C_{\mu s,0}$, the temperature dependent Toth equations can be expressed as [185]:

$$C_\mu = C_{\mu s} \frac{bP}{[1+(bP)^t]^{1/t}} \tag{5.4}$$

$$b = b_\infty \exp\left(\frac{Q}{RT}\right) = b_0 \exp\left[\frac{Q}{RT_0}\left(\frac{T_0}{T} - 1\right)\right] \tag{5.5}$$

$$t = t_0 + \alpha\left(1 - \frac{T_0}{T}\right) \tag{5.6}$$

$$C_{\mu s} = C_{\mu s,0} \exp\left[\chi\left(1 - \frac{T}{T_0}\right)\right] \tag{5.7}$$

where C is the sensor response corresponding to the amount of adsorbed analytes, T_0 = 25°C, Q is the isosteric heat of adsorption at zero loading, and T is the temperature in degrees Celsius. The fit parameters were obtained using a published MATLAB optimization routine adopted from Do. D.D. [185] to minimize the residual between the experimental data and the fit. The empirical model defined by Equation (4) permits the calculation of the sensor response to any given pressure and temperature within the fitting range of 0-7.5 Torr and 25-80 °C for the fits given in the second row of Figure 5.3. The calculated shifts in the rugate peak wavelength, from a baseline of the sensor in the absence of vapor, are plotted versus temperature in the third row of Figure 5.3. Curves for several example vapor pressures are displayed for each analyte. The

empirically calculated shift in sensor response from 25-80°C and the difference in the functional forms of these shifts between isopropanol and the nonpolar analytes suggests that temperature modulation may yield shift-temperature curves with unique characteristics for each analyte. In the next section, a temperature modulation methodology is employed to assess the effectiveness of analyte identification and quantification based on sensor shift-temperature responses.

5.4.2 Rapid Thermal Cycling if the Porous Sensor

The empirically calculated sensor shifts with temperature for the range of partial pressures of the three analytes, described in the previous section, suggest that thermally cycling the sensor can generate information to classify each analyte's concentration and identity. To test this, the sensor was thermally cycled from 25-80°C and exposed to a constant flow of vapor as shown in Figure 5.4. The copper block mounted below the thermoelectric Peltier module, shown in Figure 5.1, was removed to decrease the response time of the temperature cycling, in which the thermoelectric was used to actively heat and cool the sensor sample. For 23 partial pressures of the three analytes, ranging from 0-7.5 Torr, the sensor was cycled under a constant flow of pure nitrogen, then exposed to the same flow rate of analyte vapor in nitrogen for 8 cycles, and finally cycled again under pure nitrogen. This sequence of baseline, dosing, and purging over repeated thermal cycles is shown for one concentration of isopropanol in Figure 5.4. The thermal cycling also served to prevent vapor buildup in the porous silica matrix by repeatedly desorbing vapors. The sensor's baseline and

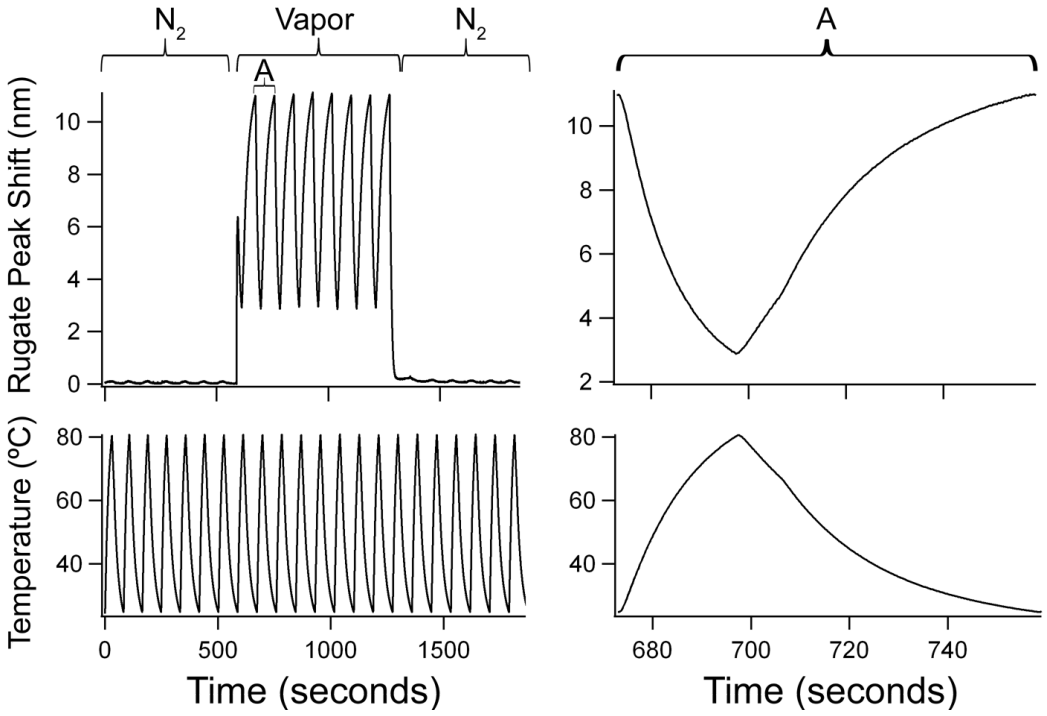

Figure 5.4 Temperature cycling methodology. **Left:** The sensor was continuously temperature cycled from 25-80° C with simultaneous spectral acquisition. The sensor was first allowed to establish a baseline in nitrogen for 7 cycles, then exposed to vapor over 8 cycles, and finally exposed to nitrogen for 7 cycles. This method was repeated for 23 concentration steps from 0-7.5 Torr for each of 3 analytes. The plot above is for 3.80 Torr of IPA. **Right:** magnification of one heating cycle under a flow of vapor (marked A in the left panel).

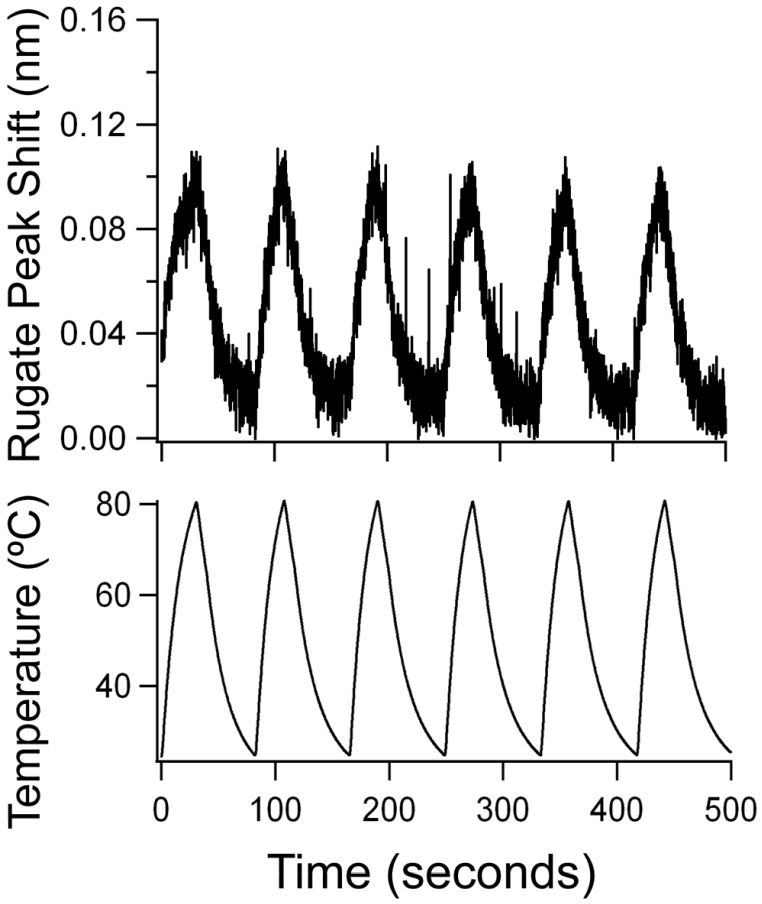

Figure 5.5 Sensor intrinsic peak shift with temperature in nitrogen. A small, highly reproducible spectral shift is observed upon heating in nitrogen due to a thermal change in the refractive index of the SiO_2. The first 6 thermal cycles from Figure 5.4 are displayed above, in which the sensor was exposed to a flow of pure nitrogen while thermally cycled.

purge (N_2) rugate peak wavelengths were found to be steady across all runs, with the sensor's chemical stability verified through FTIR spectra of the sensor acquired before and after the 69 vapor exposure runs. FTIR spectra showed no discernible change in surface functionality, nor infrared stretches from any of the analytes, with the sensor's spectra dominated by a strong ν(Si-O-Si) stretch at 1020 cm^{-1} and a very weak ν(OH) at 3350 cm^{-1}.

Thermally cycling the sensor under pure nitrogen exhibits a small, consistent change in spectral peak position due to the change of the porous SiO_2 refractive index with temperature, as described in section 4.2. This intrinsic peak shift due to the thermal coefficient of the refractive index was approximately 0.1nm from 25-80°C and was consistent for all 69 of the N_2-vapor-N_2 cycled runs (23 concentrations, 3 analytes). This intrinsic shift of the rugate spectral band with temperature is shown in Figure 5.5.

By thermally cycling the sensor, the sampling rate was also increased relative to the sensor at ambient, since no delay was necessary for the sensor to return to baseline as the vapors desorb and diffuse out of the layer. Instead, each thermal cycle acted to reset the sensor response. Figure 5.6 shows an isothermal absorption-desorption of 3.80 Torr isopropanol at 25°C. The sensor was monitored under a flow of nitrogen, exposed to isopropanol, then exposed again pure nitrogen. The time required for the sensor response to recover 95% to the initial baseline position in nitrogen was greater than the time for 9 thermal cycling events (Figure 5.4), each of which can sample a new vapor concentration or analyte.

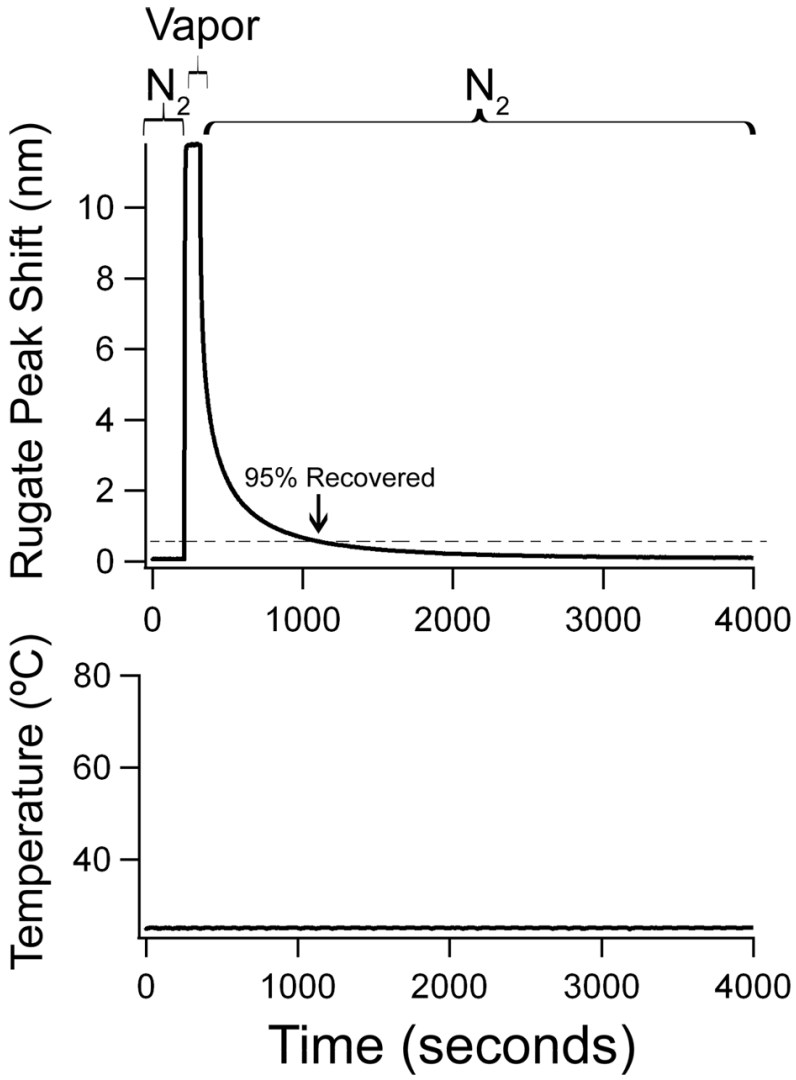

Figure 5.6 Vapor dose and purge of the sensor at 25° C. As a comparison to the sensing acquisition time of the thermal cycles in Figure 5.4, the sensor was allowed to establish a baseline in pure nitrogen, then exposed to 3.80 Torr isopropanol and allowed to equilibrate, then exposed to pure nitrogen, each at a flow of 1 L/min. The time taken to recover to 95% of the baseline is greater than the time to complete 9 thermal cycles by the method used in this study.

5.4.3 Shift-Temperature Characteristics of Thermally Cycled Sensor

The spectral shift of the rugate peak position was plotted against temperature for the thermally cycled vapor exposure cycles. The sensor baseline was taken as the rugate peak position under pure nitrogen at 25°C at the beginning of each run. Figure 5.7 displays the resulting characteristic shift-temperature curves for a vapor partial pressure of 7.5 Torr. Normalization of the sensor response curves for different partial pressures of a given analyte shows little discernible difference in the shift-temperature curves from 0-7.5 Torr except at low pressures (<2 Torr) where a diffusion delay for isopropanol may be present, discussed later. Arrows indicate the heating (desorption) and cooling (adsorption) branches. The curves of each vapor cycle for a given concentration of an analyte are highly repeatable, with each plot displaying an overlay of the last 7 vapor cycles of each run. The first cycle of each vapor run was excluded, since the initial portion of heating branch was not exposed to a full concentration of vapor due to a ~1sec delay due to the length of flow cell connector tubing before vapor was passed over the sensor surface.

The empirically calculated Toth isotherm shift-temperature curves are displayed in Figure 5.7 (dotted blue lines) for comparison. The shifts based on the equilibrium isotherm data collected at three temperatures follow the same functional form as the thermally cycled plots for each analyte but have a consistently greater rugate peak shift. This is expected, since the thermally cycled spectra are transient in temperature while the isothermal-based shifts were allowed to equilibrate to each concentration at each temperature resulting in larger adsorption and desorption shifts than the peak shifts from the unequilibrated, thermally cycled measurements.

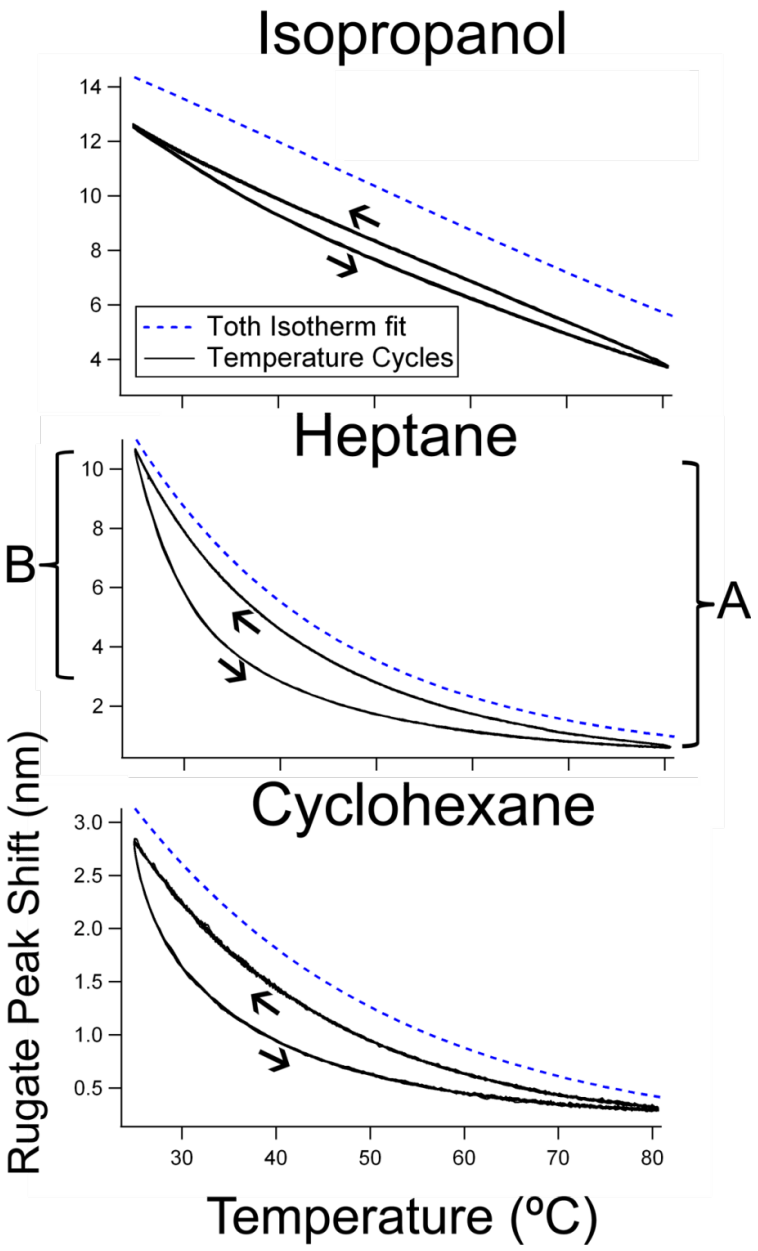

Figure 5.7 Spectral shift vs temperature, collected by the cycled methodology (Figure 5.4) at a pressure of 7.49 Torr for each analyte. For each plot, the last 7 cycles of the vapor exposure are overlaid, with no discernible difference between cycles. These curves represent the nominal shape of the peak shift vs. temperature for each analyte, with overlays of normalized response curves at each analyte pressure showing no deviations except at the lowest concentrations tested. For each curve, the zero point was taken as the peak wavelength under nitrogen flow at 25° C. Parameter (A) represents the spectral shift between 25-80° C; (B) the shift between 25-40° C. Curves based on Toth isotherm fits are overlaid (dotted), representing sensor responses at equilibrium.

The peak shift-temperature profiles of nonpolar heptane and cyclohexane exhibit a markedly more saddle-shaped response than isopropanol. Isopropanol's smaller decrease in sensor response with increasing temperature is consistent with its stronger interaction to the oxidized surface compared to the other analytes, since the surface is predominantly Si-O-Si with a small contribution of Si-OH surface bonds, as seen in FTIR spectra of the sensor. Isopropanol has also been shown to hydrogen bond to silica surfaces[230]. The strong surface interaction of isopropanol results in a less dramatic shift in the sorption equilibrium with temperature than that observed with heptane and cyclohexane, as well as in a slower isothermal desorption process from the adsorbed, loaded state to the equilibrium state in nitrogen, as discussed in section 3.6. The shift-temperature profiles of heptane and cyclohexane exhibit sharper changes in the sensor response with temperature. Since the sensor response is a measure of the amount of adsorbed analyte in the porous layer, the different sensor response profiles suggest a vapor-sensor sorption equilibrium dominated by analyte self-affinity in the cases of cyclohexane and heptane, compared to the surface affinity dominance of the isopropanol interaction. Indeed, the shift-temperature profiles of heptane and cyclohexane appear consistent with the exponential change in the vapor pressure of the analytes with temperature[211]. The importance of analyte-analyte self affinity interactions in the observed behavior of the two nonpolar analytes may be due to their lower surface affinities, particularly if multilayer adsorption occurs on preferred adsorption sites before a full adsorption monolayer is formed[231]. At a given

temperature, the sensor response to heptane is greater than to cyclohexane. This may be due in part to the ability of the heptane molecule to conform to microporous adsorption sites on the heterogenous[12, 232] pore surface, while cyclohexane is more rigid and adsorbs to sites of a preferred size[233, 234]

Binary analyte mixtures were briefly examined and exhibited shift-temperature profiles consistent with a combination of the individual components. The sensor was thermally cycled under a vapor flow mixture of 0.87 Torr heptane and 3.61Torr cyclohexane, with the resulting spectral shift versus temperature profile exhibiting the nominal concave up, saddled shape of the individual components. A mixture of 0.09 Torr isopropanol and 3.61 Torr cyclohexane exhibited a smooth shift-temperature response with a shape between that of the near-linear and saddled component responses. This averaged response may indicate incomplete surface coverage that allowed separate adsorption sites of the immiscible mixture components at these pressures. This is consistent with the isopropanol concentration of 0.09 Torr being well below the first monolayer plateau of the adsorption-desorption isopropanol experiment in Figure 5.3. The lack of kinks or additional features in the heating profile of the mixture implies a difficult identification of components in multicomponent vapor streams. However, analyte discrimination of discrete, pure analytes was highly effective, discussed below.

5.4.4 Response Space for Analyte Pressure and Temperature Ranges

The plots of sensor spectral peak shift versus temperature from the thermal cycling methodology, depicted for a few of the vapor concentrations (partial pressures) in Figure 5.7, are slices of a three dimensional response space of the sensor's shift with temperature and partial pressure. In Figure 5.8, the peak shift (nm shift) of thermal cycles at several applied vapor concentrations are displayed as response-temperature slices in a three dimensional pressure-temperature-sensor response plot for each analyte. The zero shift floor of these plots are data from the thermal cycles in nitrogen before and after each temperature-cycled vapor exposure. Black spheres represent response-pressure slices for the three temperatures at which the isothermal, equilibrated sensor dosings (Figure 5.3, row 2) were collected. As mentioned, the shifts (nm) of the thermally cycled sensor are less than the shifts observed for the isothermal, equilibrated runs since the temperature cycles allow only a transient, partial equilibration of vapor with the sensor surface at the high and low temperatures. This difference is more pronounced for the more slowly adsorbing and desorbing isopropanol than the other analytes, and decreases with increasing concentration due to the faster kinetics of the higher concentration gradients[185].

5.4.5 Distinguishing Pure Analytes by Thermal Cycling

The shift-temperature profiles described in the previous two sections were utilized to discriminate between pure analyte vapors at multiple concentrations by plotting the total sensor shift from 25-80°C against the vapor partial pressure, shown in Figure 5.9. Error bars represent the standard deviation of the shifts of the last 7 thermal

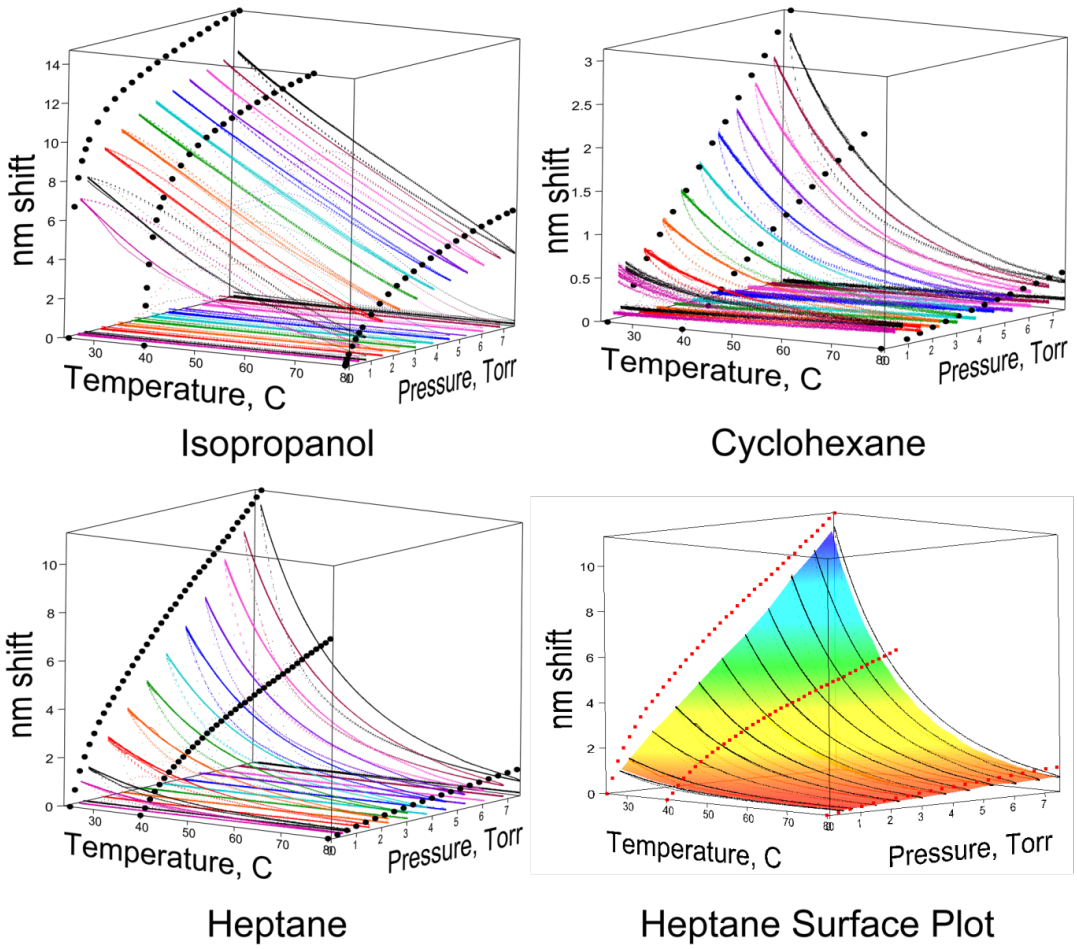

Figure 5.8 The spectral shift plotted as a function of analyte partial pressure and temperature defines a response space. Isothermal shifts at equilibrated concentrations (partial pressures), first shown in Figure 5.3, are shown as black spheres (nm-pressure slices). Spectral shifts at constant applied analyte partial pressures from the thermally cycled methodology (Figure 5.7) are shown as a separate color for each pressure (nm-temperature slices). **Lower right:** the cooling curves of the temperature cycles were taken to form a response surface for heptane (color surface). Red spheres show the isothermal adsorption-desorption peak shift data over the partial pressure. The figure is colored according to the nm shift (red to blue as low to high)

cycles of the sensor under vapor flow for each analyte and partial pressure, following the methodology described earlier (Figure 5.4). This shift in the thermally cycled sensor response under vapor flow is identified as parameter (A) in the shift-temperature profiles of Figure 5.7. With increasing vapor concentration, a larger difference in the spectral peak position between 25-80°C is observed for each analyte. At each vapor partial pressure, these thermally cycled peak position shifts are compared in the figure to the peak shift difference between the isothermal adsorption run at 25°C and the isothermal run at 80°C (Figure 5.3, second row). As with the shift-temperature plots (examples shown in Figure 5.7), the shifts based on the isothermal peak shifts between 25 and 80°C are greater than the thermally cycled shifts, since the isothermal sensor was allowed to equilibrate to the vapor at each concentration for each temperature, while the thermally cycled shifts were taken at transient temperatures with adsorption and desorption not allowed to fully equilibrate.

This difference between the thermally cycled and isothermal-difference plots decreases with increasing concentration, most notably for isopropanol. This is presumably due to the faster diffusion and equilibration of vapor within the 15.9 μm porous layer as the vapor concentration gradient is increased. For heptane and cyclohexane, this single 25-80°C shift parameter is uniquely mapped to each partial pressure, allowing concentration determination for a known analyte. For isopropanol, the parameter (A) also yields a one-to-one mapping with pressure, but between 1-7.5 Torr the change in this parameter with pressure is small, since the sensor exhibits a response plateau to vapor adsorption in this range (Figure 2, left column) at both 25°C and 80°C, corresponding to the adsorption pressures below capillary condensation.

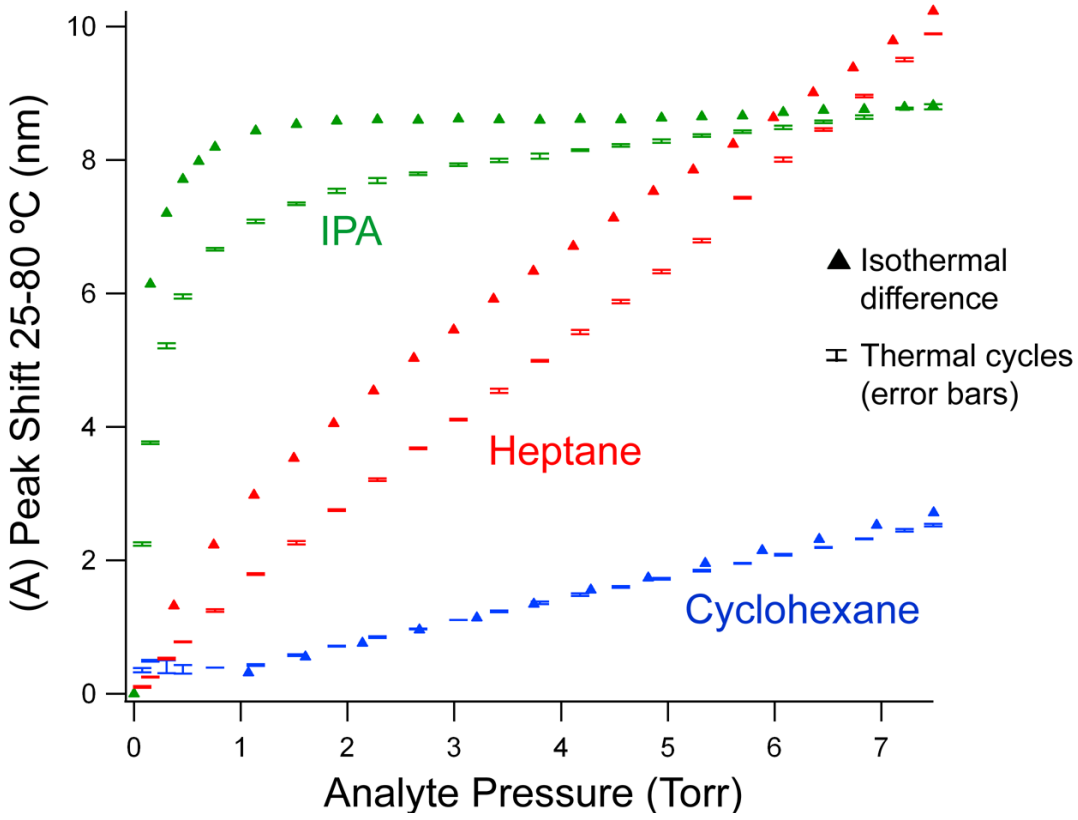

Figure 5.9 Vapor discrimination based on the spectral shift of the sensor cycled between 25-80°C. The spectral shift from 25-80°C is plotted versus analyte concentration. The average shifts from the thermal cycling method, parameter (A) from Figure 5.7, are plotted with error bars based on shifts from the last 7 vapor exposure cycles at each concentration. For comparison, the difference in spectral shifts from the isothermal, equilibrated exposures between 25°C and 80°C (Figure 5.3, row 2) are also displayed (triangles).

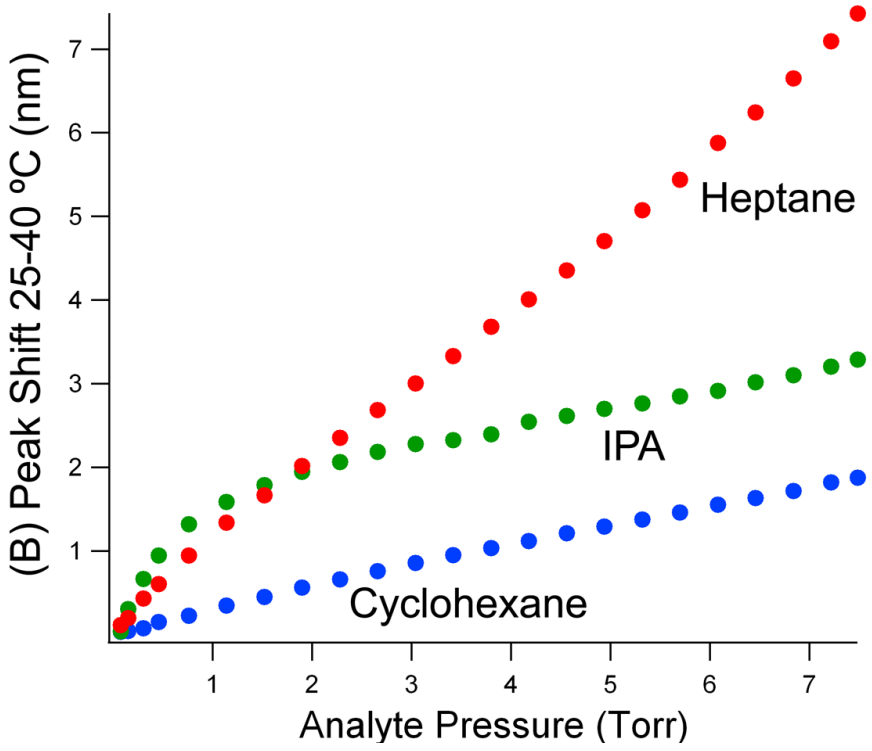

Figure 5.10 Vapor discrimination based on the spectral shift from 25-40°C from the thermally cycled methodology (Parameter (B) in Figure 5.7) for vapor concentrations from 0-7.5 Torr.

A second parameter was chosen to describe the shape of the shift-temperature profiles, in which the nonpolar analytes exhibited a sharper drop in sensor response with temperature that yielded concave up, saddled profiles, while isopropanol exhibited a much longer exponential profile that appeared almost linear for the conditions of pressure and temperature used in this study. The second parameter, labeled (B) in Figure 5.7, was taken as the sensor shift of the heating leg from 25-40°C. Figure 5.10 displays a plot of (B) versus analyte concentration. The large initial drop to 40°C for heptane due to its saddled profile is apparent.

Plotting parameters A and B as a function of pressure yields excellent separation between each pressure-analyte combination (Figure 5.11), allowing for unique identification of both vapor identity and concentration for pure analytes, within the bounds of the partial pressures and chemicals tested. Convergence of the heptane and cyclohexane sensor responses was observed below 0.3 Torr, as shown in Figure 5.11.

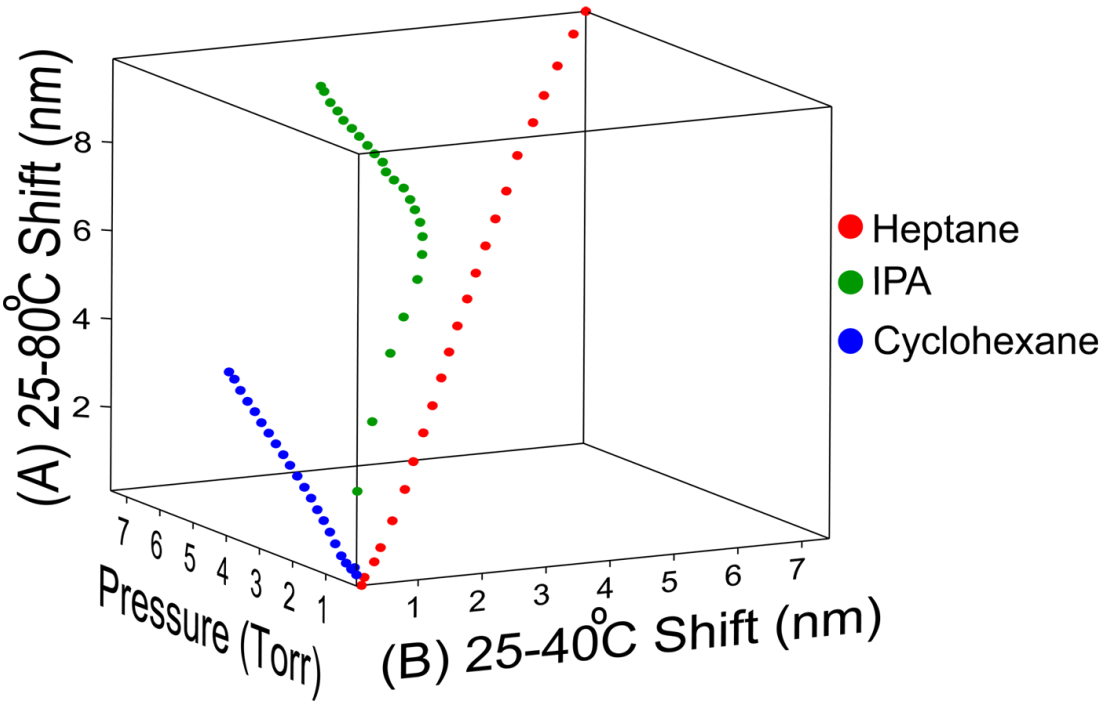

Figure 5.11 Discrimination of pure vapors based on the thermally cycled spectral shifts. The spectral shift between 25-40° C (B) was used to quantify the shape of the spectral shift vs. temperature curves (Figure 5.4). Combined with the total spectral shift between 25-80° C (A), these two parameters show excellent discrimination of the three analytes between 0-7.49 Torr.

5.4.6 Deviation of Response-Temperature Characteristics at Low Concentrations

The shift-temperature profiles shown in Figure 5.7 are representative of each analyte's response for most partial pressures. At low pressures of isopropanol below 2 Torr, however, a deviation from this response was observed. Figure 5.12 displays the shift-temperature profiles at several concentrations of isopropanol. As before, each profile consists of seven overlaid cycles collected under rapid thermal cycling. The empirically calculated curves, from the Toth isotherm fit of the sensor's equilibrium vapor isotherms, are plotted for comparison (dotted blue lines). At higher concentrations, the shift-temperature profile of isopropanol matches the profile calculated from the fitted Toth isotherms. As the concentration is decreased, the heating profile protrudes rightward to higher temperatures, so that for a given decrease in sensor response, a higher temperature is required. This bowing of the heating curve is likely due to the slowed diffusion of isopropanol from the ~16 μm porous layer at low concentrations[235] relative to the heating rate, resulting in a lag in the sensor response at low concentrations, as detailed below. The cooling leg does not exhibit such behavior since the cooling time of the sensor on the thermoelectric was twice the heating time, and the equilibration time of vapors when introduced at constant temperatures is faster than their equilibration upon vapor removal.

Heptane exhibits no such change in the shift-temperature profile, as shown in Figure 5.13. Also, for the 0.15 Torr concentration shown in this figure, the heptane peak shift, relative to the zero point in nitrogen at 25°C, appears to increase between 50-80°C. This is due to the change in refractive index of the porous SiO_2 mentioned

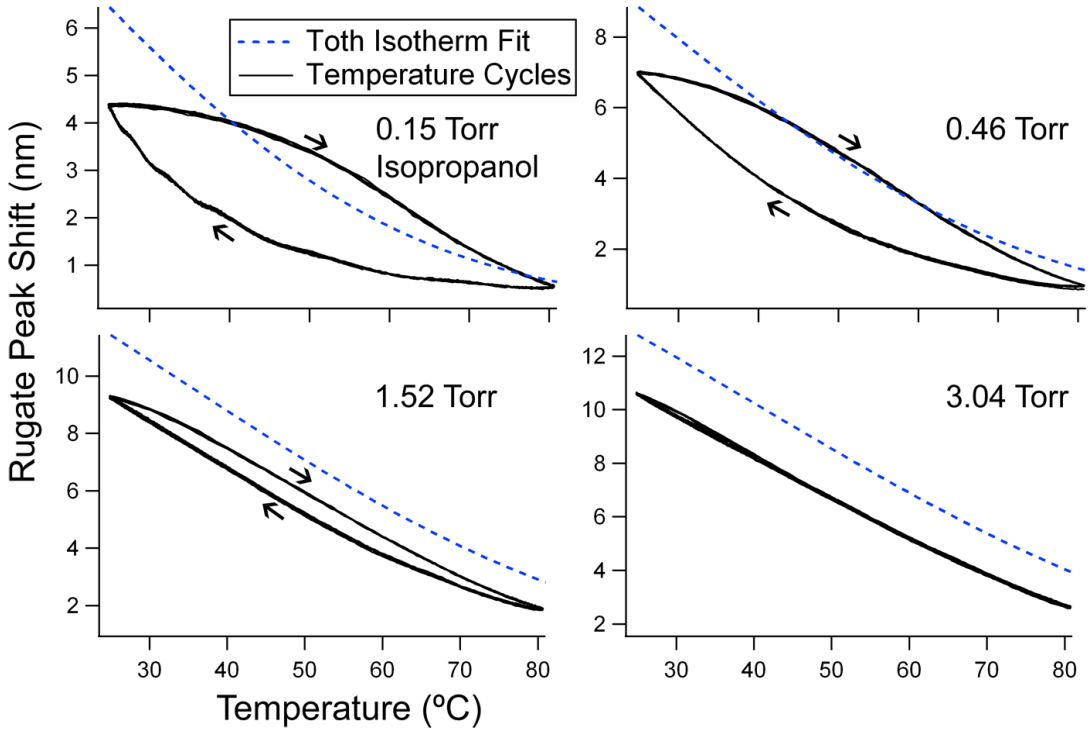

Figure 5.12 Deviation from the nominal peak shift versus temperature profiles for low isopropanol concentrations. The slowed kinetics of IPA exiting the porous sensor results in an increasing lag in desorption with decreasing concentration, observed here below 2 Torr. The peak shift vs. temperature profiles determined from the Toth isotherm fits are overlaid (dotted curves) for comparison.

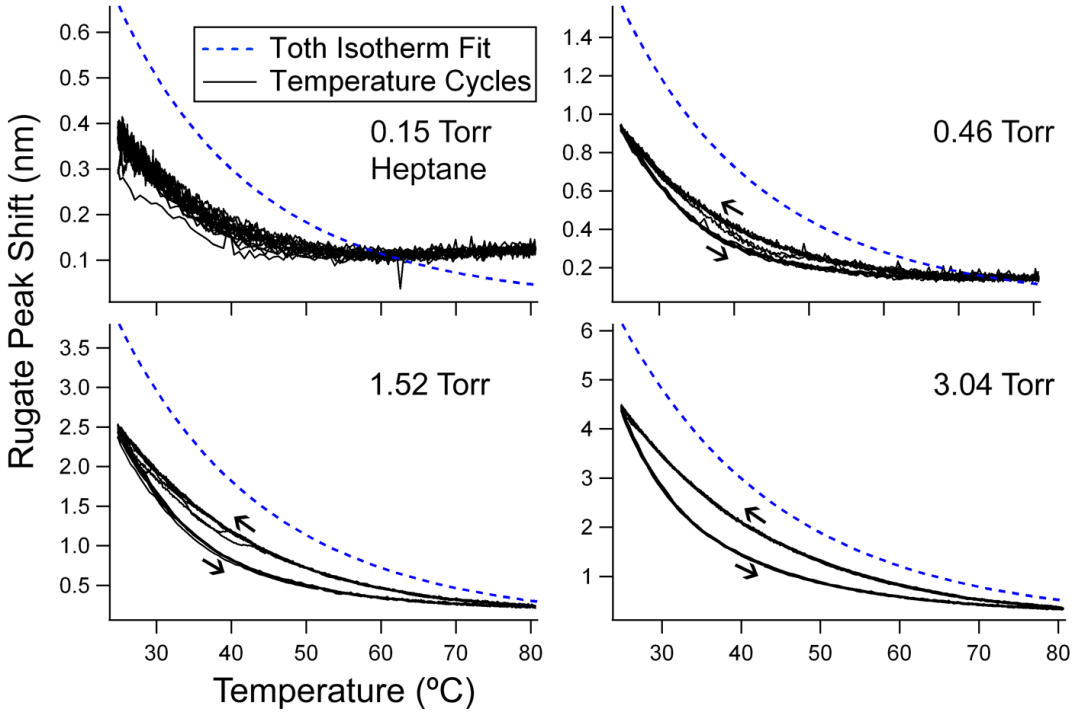

Figure 5.13 Examples of heptane peak shift vs temperature profiles at low concentrations (partial pressures). In contrast to the deviation from nominal shape for IPA at low concentrations, heptane and cyclohexane exhibit a consistent, saddled curve in its cycled temperature response. Each plot is an overlay of the 8 thermal cycles taken under constant vapor exposure for each concentration. Blue dotted lines show the peak shift vs. temperature profiles determined from the Toth isotherm fits for comparison.

earlier and shown in Figure 5.6. The observed <0.1nm increase in heptane response is consistent with the 0.1nm shift of the sensor in pure nitrogen between 25-80°C. Cyclohexane, however, exhibits a change in the shift-temperature relationship for partial pressures below 0.4 Torr, exhibiting the same increasingly bowed shape of the heating curve as the concentration of the cycled run was lowered.

To test the influence of the heating rate on the outward bowing of the shift-temperature response, observed at low concentrations of isopropanol, four heating rates were applied to the sensor. The sensor was thermally cycled between 25-80°C, and the rugate peak position recorded over time as before, with the peak shift taken relative to the rugate stop band position in nitrogen at 25°C, before introduction of a flow 0.76 Torr isopropanol vapor flow. At this concentration, the isopropanol response versus temperature exhibits an outward bowing of the heating leg with the inflection point near 50°C. In Figure 5.14, the heating leg of one cycle of the shift-temperature profile for four different heating rates is shown. The right panel displays the heating rate, dT/dt (°C/sec) as a function of temperature. For heating rates I and II, power was linearly increased to the thermoelectric, resulting in relatively flat heating profiles. For heating rates III and IV, the thermoelectric was driven at a constant, high power output as was done in the thermal cycles above, resulting in a decrease in the rate with temperature as thermal losses increase. Increasing the heating rate increases the outward bowing of the shift-temperature response, indicating that this lag in response may be desorption rate or diffusion rate limited, with the increase in the lag with lower concentrations due to increasingly slower diffusion kinetics of the vapors exiting the

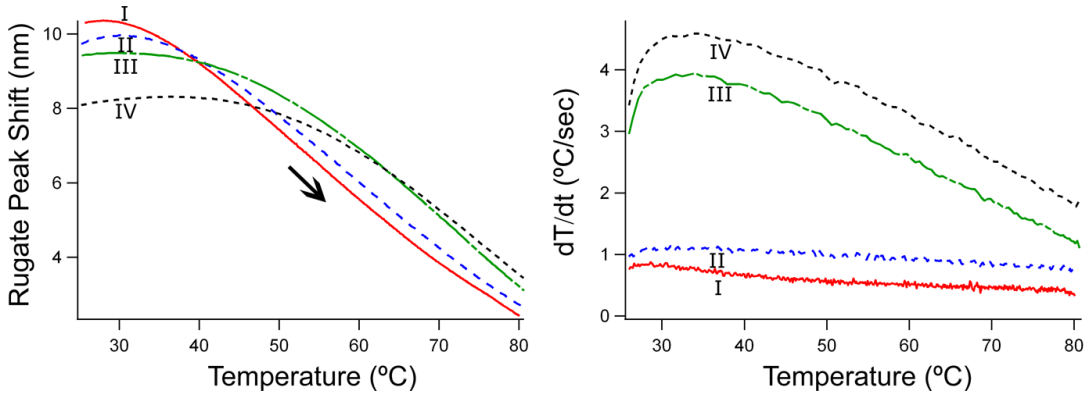

Figure 5.14 Dependence of the desorption shift-temperature profile on the heating rate for low concentrations of isopropanol. The heating segment of one temperature cycle for the sensor under a flow of 1 L/min 0.76 Torr IPA is shown for four heating rates, with I – IV corresponding to slowest to fastest. **Left**: the lag due to slow IPA desorption at this analyte pressure increases with faster heating (IV>III>II>I). **Right:** the heating rate is plotted for each of the heating profiles, where T is the temperature (°C) and t the time (seconds). Rates I and II were applied by linearly increasing the power to the thermoelectric. Rates III and IV represent a single high turn-on power supplied to heat the thermoelectric as utilized in the thermal cycling collections.

16 μm layer. High heating rates warm the sensor chip faster than isopropanol vapors can desorb and exit the layer, resulting in the thermal 'lag' observed. The different peak shift starting points of the cycle at 25°C are due to the transient temperature of the sensor undergoing thermal cycling, with faster heating rates allowing the sensor less time to equilibrate to vapor at 25°C and decreasing the sensor response to vapor relative to that at thermal equilibrium.

5.4.7 Comparison of Isothermal Desorption Rates

The thermally cycled sensor was heated from 25-80°C in 29sec and cooled to 25°C in 60sec in the thermally cycled runs with isopropanol, heptane, and cyclohexane discussed in sections 3.2.-3.4 above. To compare these times to the equilibration times of each analyte, a series of isothermal vapor dosings were performed, shown in Figure 5.15. At each temperature, a constant partial pressure of analyte vapor was introduced into the flow over the sensor, and the sensor response allowed to equilibrate. The flow over the sensor was then switched to an equal flow rate of pure nitrogen, and the decrease in rugate peak shift recorded and plotted over time. This process was repeated at several temperatures from 25-80°C. A few of the temperatures tested are shown in Figure 5.15, with two trials performed at each temperature. The data rate for these acquisitions ranged from 5-9 Hz. As showed in the figure, the sensor response after a 7.49 Torr dose of isopropanol does not equilibrate to a steady-state baseline after 30s, while the other analytes do so in less than 10s for all temperatures between 25-80°C at the same concentration. The isopropanol response does eventually equilibrate and recover to its initial baseline value after >10 mins. The increase in noise for the higher temperature plots is due to the smaller absolute shifts of the rugate peak at elevated temperatures. In Figure 5.15, the vapor flow was switched to pure nitrogen at time t=0sec for all plots. The consistent ~1sec delay before the sensor response is a delay due to the length of tubing connecting the valve switching between pure nitrogen and analyte vapor in the vapor delivery system to the vapor flow cell, with a front of vapor in the ~16cm^3 of tubing (0.5m,¼") at a flow rate of 1L/min requiring ~1 sec to reach the sample.

The shift in rugate spectral peak position in these curves represents the change in the total amount of analyte within the porous matrix, both adsorbed to the surface and present as vapors within the layer. Thus, although the relative contributions of the desorption rate of analyte from the surface and the diffusion rate of the analyte out of the porous matrix cannot be easily separated, the overall equilibration times of vapor exiting the 16μm porous layer can be compared. The equilibration of isopropanol to the nitrogen stream, after removal of the vapor stream, is clearly an order of magnitude greater than the other analytes. After 29sec, only the isopropanol run at 80°C has recovered to a steady baseline value, while at all temperatures the heptane and cyclohexane recover to steady-state values in less than half this time. Lowering the concentration of vapor results in slower equilibration times due to the lower concentration gradient between the porous layer and pure nitrogen above, as shown in the top plot of Figure 5.15 [185]. The observed equilibration times of isopropanol at various temperatures, compared to the significantly faster equilibration times of heptane and cyclohexane, support the observation of a lag in the isopropanol shift-temperature response at lower concentrations.

The cooling time of the thermally cycled sensor was twice the heating time. Additionally, analysis of the equilibration time of the sensor to isopropanol, tested at both 7.49 and 0.76 Torr for several constant temperatures, showed that the times taken to equilibrate from a stream of pure nitrogen to a stream of vapor (diffusion into the layer and adsorption) were less than half the times taken to equilibrate from a stream of

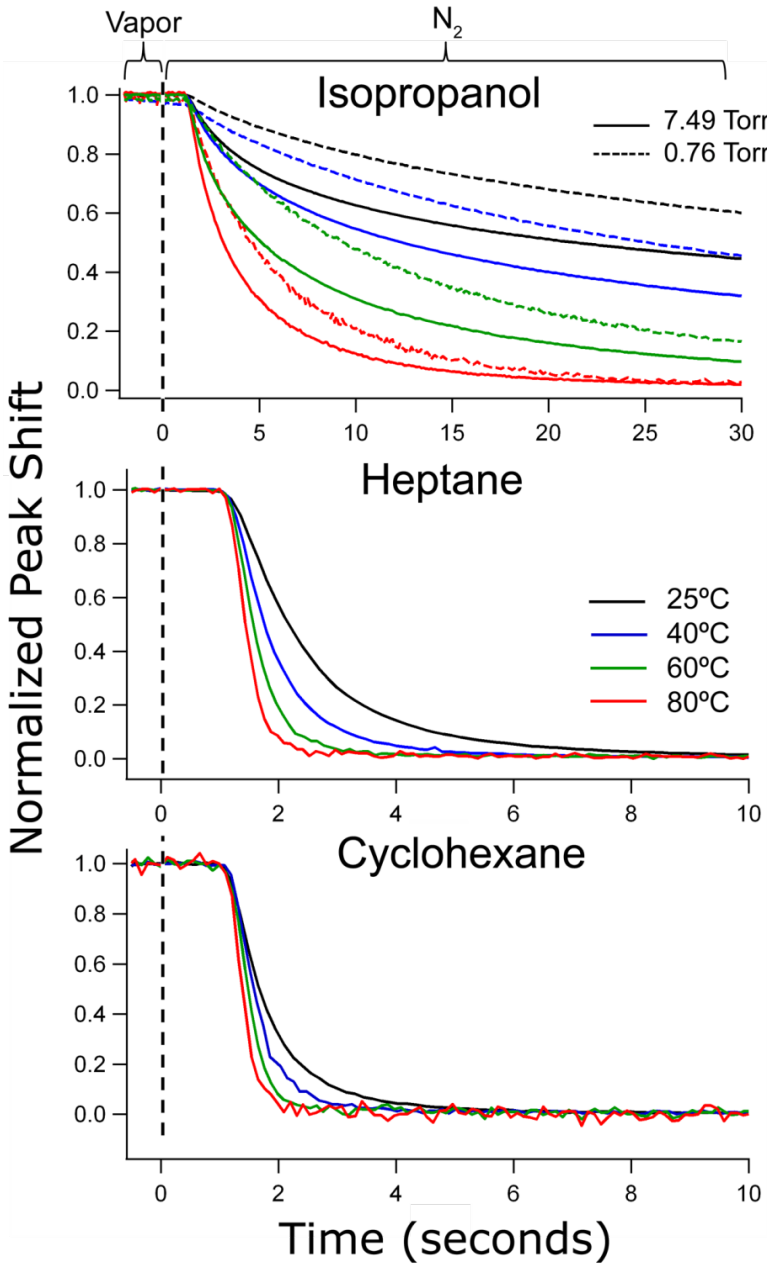

Figure 5.15 Isothermal desorption of vapors from the porous silica sensor showing the slow rate of isopropanol desorption plus diffusion. At each temperature, a constant flow of 1L/min of 7.49 Torr vapor in N_2 was applied and the response allowed to equilibrate. At time t=0, indicated by the dotted vertical line, the four-way valve then switched to a flow of pure nitrogen at the same flow rate. The desorption time for isopropanol is more than an order of magnitude longer than for heptane and cyclohexane. **Top graph:** a lower 0.76 Torr analyte pressure of IPA (dotted lines) was also applied to the sensor to highlight the slower desorption rate of the analyte at lower concentrations.

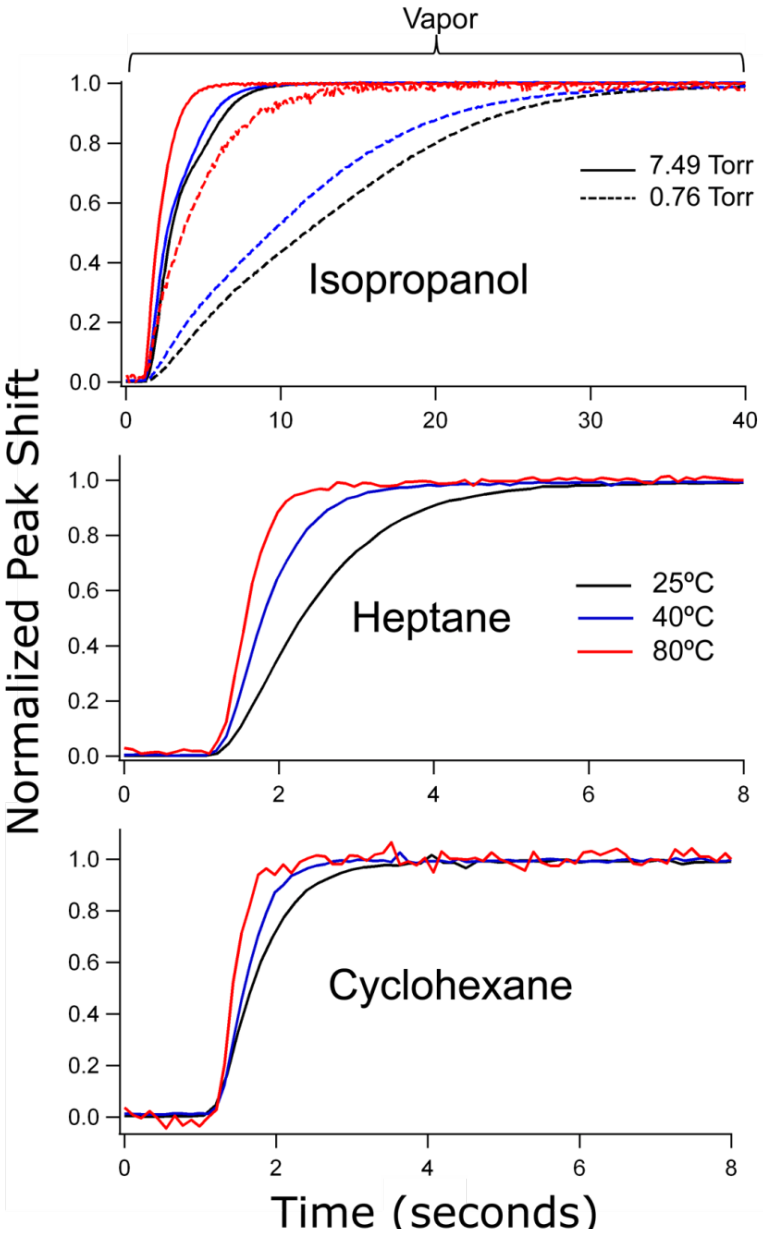

Figure 5.16 Isothermal adsorption of vapors into porous silica. In contrast to the slow desorption of vapors in Figure 5.15, the uptake rates of the vapors are considerably faster. These faster equilibrations, combined with the slower cooling rate of the cycled sensor, resulted in shift-temperature profiles that showed no deviations at lower analyte pressures, even for IPA. At each temperature, a constant flow of 1L/min of vapor in N_2 was applied at time t=0 and the response allowed to equilibrate. An analyte concentration of 7.49 Torr was applied at each temperature. For IPA, a lower 0.76 Torr pressure of IPA (dotted lines) was also applied to the sensor to highlight the slower uptake rate of the analyte at low concentrations.

vapor to a stream of nitrogen (desorption and diffusion out). These equilibration responses to the introduction of analyte vapors are shown in Figure 5.16. In contrast to the heating profiles, the faster vapor uptake rate combined with the slower cooling rate of the sensor resulted in no observed deviation in the peak shift-temperature cooling profiles of the sensor with isopropanol, over the vapor partial pressures tested.

5.4.8 Relating the Rugate Spectral Shift to Porous Volume Filling

The sensor response space displayed in Figure 5.8 relates the sensor response to both the vapor partial pressure of the analyte in the nitrogen stream above the sensor and to the porous silica temperature. The thermodynamics of vapor adsorption in porous media is highly complex and various strategies for determining properties of the vapor-surface equilibrium have been employed[185, 236, 237], but a critical first step in any further analysis of the this porous silica system is to relate the sensor nanometer shift in spectral peak position to the volume of the porous layer filled with adsorbed analyte.

The simplest approach is to linearly scale the spectral peak shift from the spectral position of the rugate in the absence of vapor to the spectral position under saturated vapor pressure, or to the spectral position of a layer filled with liquid analyte. Although this requires little calculation, it assumes complete filling of the porous volume under saturated pressure (or liquid filling, whichever is employed). The assumption of a perfectly linear change in spectral peak shift with volume filling of the layer is also not exact, and is better described by an effective medium approximation. The relationship between the volume fraction of the pores filled to the average refractive index of the

porous layer for porous silica has been commonly described with the Bruggeman effective medium approximation [41, 86]

$$(1-P)\,\frac{{n_{Si}}^2-{n_{eff}}^2}{{n_{Si}}^2+2{n_{eff}}^2}+\;(P-fP)\,\frac{{n_{air}}^2-{n_{eff}}^2}{{n_{air}}^2+2{n_{eff}}^2}+\;(fP)\,\frac{{n_{fill}}^2-{n_{eff}}^2}{{n_{fill}}^2+2{n_{eff}}^2}=0 \qquad (5.8)$$

where f is the volume filling fraction, ranging from 0 to 1, and P is porosity, also ranging from 0 to 1. The term n_{fill} is the refractive index of the analyte filling the pores, and n_{eff} is the average index of the porous layer.

The strategy of relating the spectral peak shift to the fractional volume filling of the porous layer with an analyte thus consists of two steps. First, the relationship between the spectral peak shift and the refractive index is determined by plotting the peak shift against the effective optical thickness (EOT=$2n_{avg}L$) from the fast Fourier transform of the interference fringes in the spectrum that arise from light reflected off the top and bottom interfaces of the porous layer. Since the thickness of the layer L is known (15.9um), the relationship between the peak position and n_{avg} is determined. Second, the relationship between the average refractive index n_{avg} and the fractional filling of the porous layer is determined by the Bruggeman equation for the measured conditions of porosity and layer thickness.

Beginning with a fractional volume fill, the process is thus to convert the fractional volume fill to a shift in n_{avg} using the Bruggeman, then to an EOT shift using the layer thickness, and finally to a nanometer peak shift using the peak position-EOT relationship fitted from the data.

The Bruggeman equation was solved for n_{avg}, the average index of the SiO_2 pillars and void space filled with nitrogen and analyte, for 20 volume fraction steps

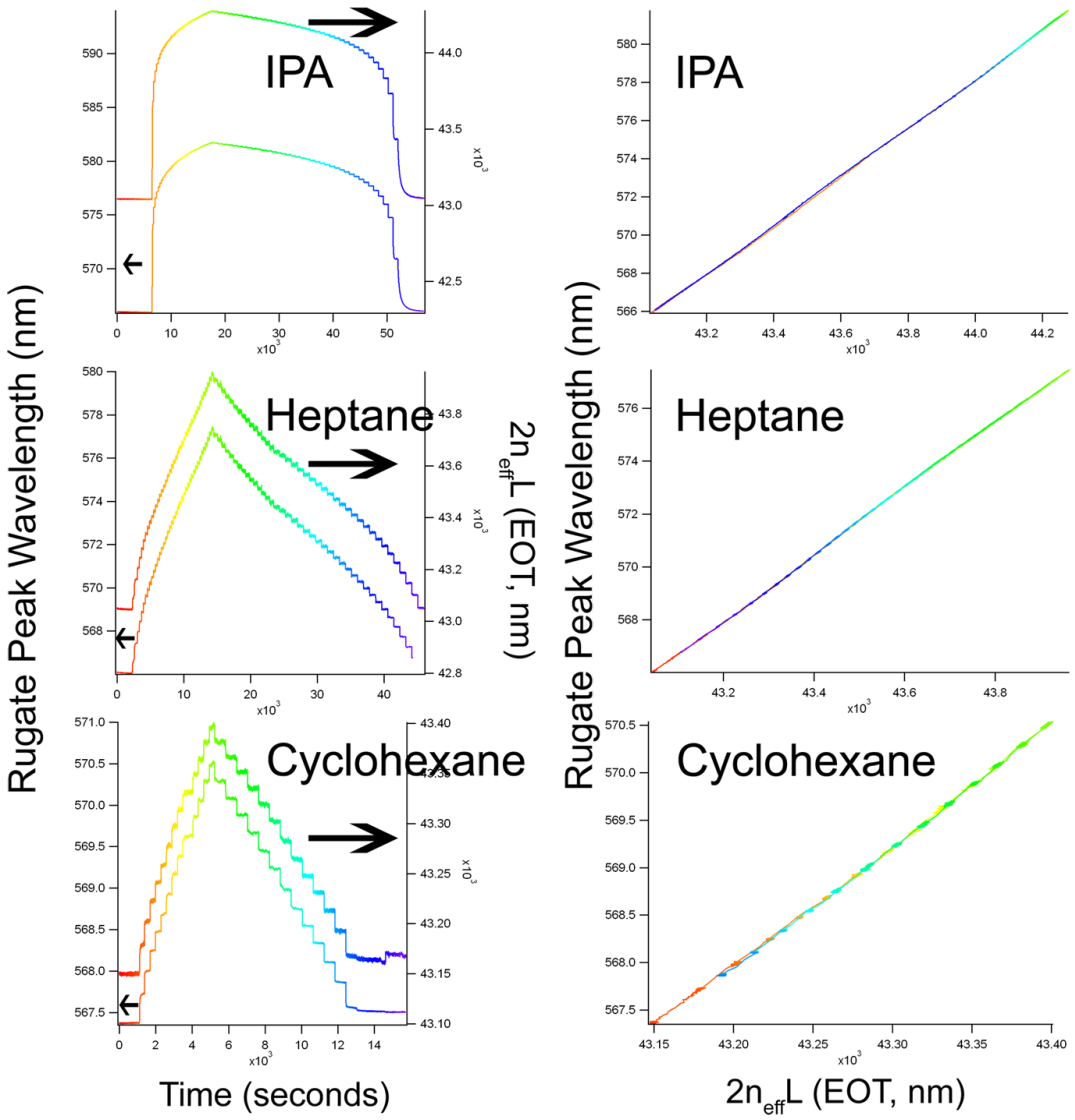

Figure 5.17 Spectral shift versus effective optical thickness (2nL). **Left:** Isothermal equilibrium adsorption-desorption shifts versus time (Figure 5.3, middle row) showing the spectral peak response (left axis) and effective optical thickness (right axis) from the stepwise increase and decrease of analyte concentration for the runs from 0-7.5 Torr at 25° C. The plots are colored as a function of time (red to blue). **Right:** Spectral shift versus effective optical thickness, colored as a function of time (red to blue), showing the linearity of the optical response.

from unfilled to filled for each analyte. The resulting Δn_{avg} shifts were then converted to ΔEOT using the 3-component Bruggeman, as detailed in appendix A.4. The relationship between the rugate peak position and the EOT was then determined by fitting a plot of the two values from the isothermal, step-wise dosed sensor runs from 0-7.5 Torr at 25°C, where each analyte partial pressure was allowed to equilibrate with the sensor, as shown in Figure 5.17. The left column displays the shift in rugate peak position and the shift in effective optical thickness versus time for each analyte, with each stair step corresponding to a dosing concentration of analyte. The right column displays the peak position-EOT (λ_0-EOT) relationship, showing a highly linear relationship for each analyte and no discernible difference between the adsorption and desorption segments. The runs at 40 and 80°C were also highly linear with no adsorption-desorption differences. The value of n_{Si} in the Bruggeman equation was determined by solving the 2-component Bruggeman (f=0) for each run using the value of n_{avg} (EOT/2L) of the sensor exposed to pure nitrogen. The sensitivity of the sensor shift, defined as[132]

$$\text{Sensitivity} = \Delta n / \Delta\lambda \tag{5.9}$$

was consistent for the three analytes with values of 1.28×10^{-2}, 1.27×10^{-2}, and 1.26×10^{-2} for isopropanol, heptane, and cyclohexane respectively, at 25°C.

The result of these fractional volume filling calculations for the 0-7.5 Torr, isothermal equilibrated dosing runs is shown for isopropanol in Figure 5.18. The porosity used in the Bruggeman calculation was gravimetrically determined to be 26%. The porosity of the oxidized layer can also be calculated from that of the freshly etched layers before oxidation by considering the volume change of the porous layer[238].

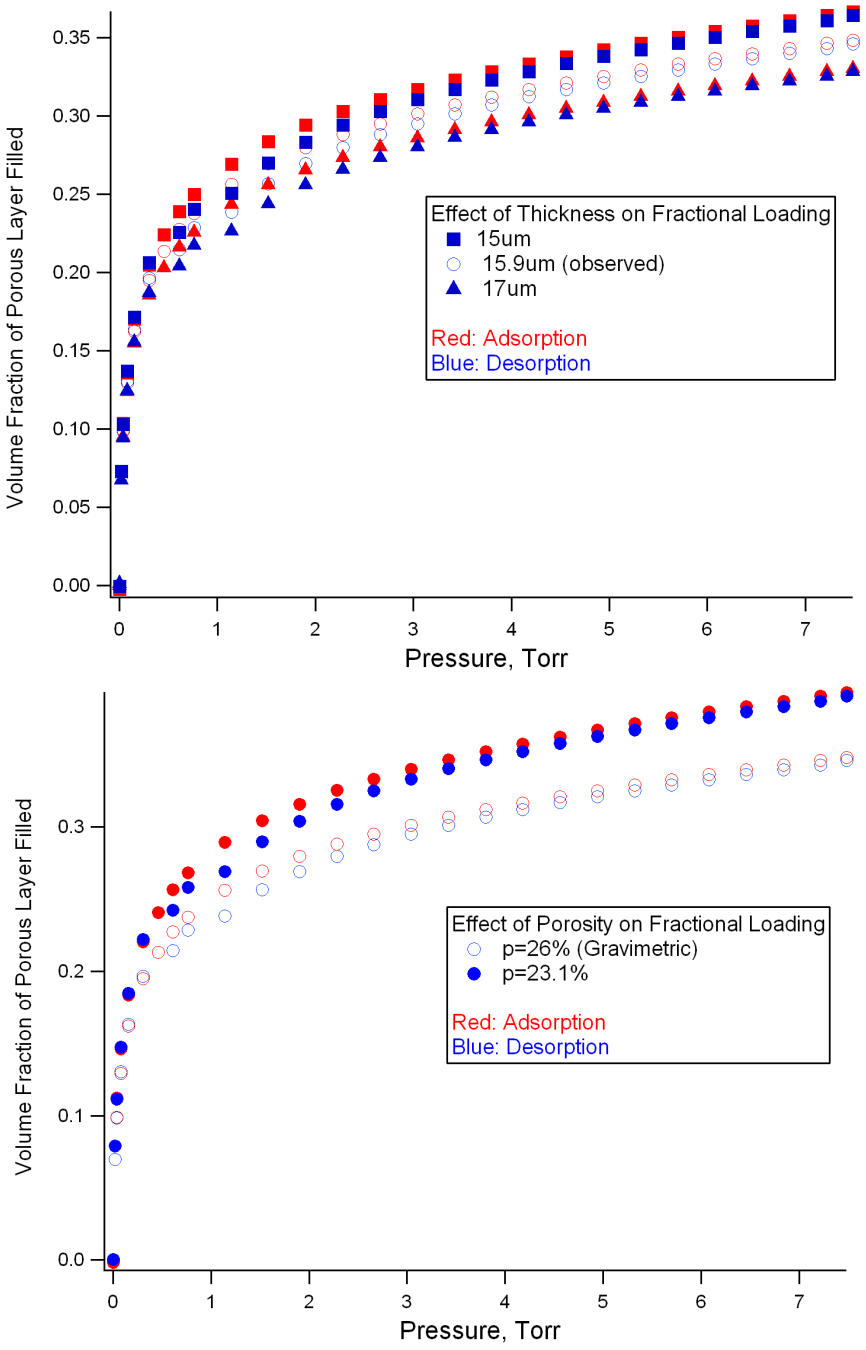

Figure 5.18 Isothermal peak shifts at equilibrated isopropanol partial pressures converted to fractional volume fillings. Responses from 0-7.49 Torr (Figure 5.3, row 2) for isopropanol were converted to fractional filling of the porous volume with analyte, from 0 (empty) to 1 (filled). **Top:** effect of changing the porosity used in the Bruggeman calculation from the measured 26% to 23.1%. **Bottom:** effect of changing the layer thickness from the measured 15.9 um to higher and lower values.

By this method, the 66% fresh porosity is expected to yield a 23.1% oxidized porosity. To examine the effect of changing the porosity in the calculations, the upper plot of Figure 5.18 shows fractional fillings given each porosity. The effect of changing the layer thickness on the resulting filling versus concentration curves was also examined, with the bottom plot showing the effect of a one micron thinner (15um) and thicker (17um) layers than that which was measured.

The volume filling was also applied to the equilibrated isothermal dosing runs taken from zero to saturated vapor pressure, as shown in Figure 5.19, where the top plot shows the calculated spectral peak shift versus volume filling and the bottom plot displays the volume filling versus concentration for the downward, desorption leg of the isothermal hysteresis. The red, solid lines represent the as-observed conditions, and the black lines display the result of a simple linear scaling of the volume filling based on the endpoints of the shift (p=0 and p=saturated). Other curves test the effect that variations in thickness and porosity have on the fractional filling.

The calculated fractional filling, when applied to the isothermal vapor dosings from zero to saturated pressure, results in a saturated pressure estimated to be filled ~20% more than the total porous volume. An offset of more than 2% porosity and more than 1um in thickness would be necessary to align the fractional fill shift at saturated filling to the true 100% pore filling (1.0 fractional fill). Both of these offsets are above the experimental error and so cannot completely account for the difference. One source of error may be due to the gravimetric porosity including porous voids that have been closed off from oxide growth or morphological changes during oxidation. Since vapors and liquids cannot access these porous voids, observed optical thickness

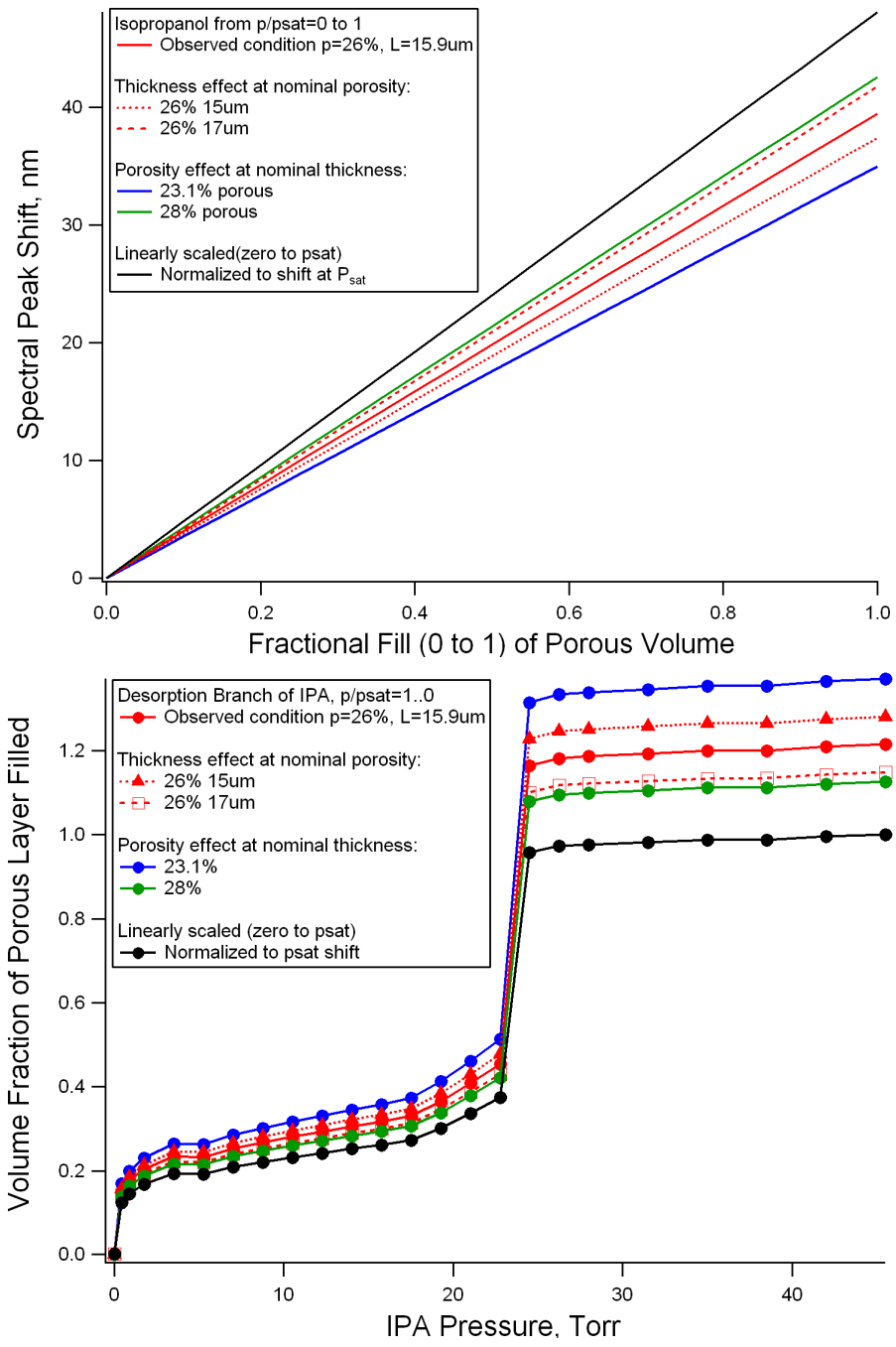

Figure 5.19 Volume fractional filling of the porous SiO_2. Isopropanol was chosen as an example. **Top**: The spectral peak shift versus the volume of pores filled with isopropanol. **Bottom:** The isothermal equilibrium desorption shifts from P_{sat} to zero vapor pressure at 25° C (Figure 5.3, row 1) adjusted to their fractional fill values (empty to filled as 0 to 1). For both, curves based on the measured shifts, porosity, and thickness (red, solid line) are compared to curves based on various other porosities and thicknesses.

changes with analyte loading is less than the shift expected if all porous voids were accessible. The high fractional filling values predicted by the approach above may also be due in part to a breakdown in the linearity of the peak shift (nm) with fractional filling at high concentrations due to changes in analyte density that occur when the analyte condensed fluid is confinement[239]. Further, the Bruggeman method used a constant refractive index value for the value at no filling (f=1) determined by the position of the unshifted rugate peak in nitrogen. While this works well for small fractional volume fillings that result in small peak shifts, for large redshifts the refractive index of the SiO_2 decreases slightly. A value of n_{avg} for a large spectral shift that is based on the initial wavelength of SiO_2 will thus be higher, and yield a greater peak shift, than a value based on the wavelength of the shifted peak.

In conclusion, short-range, small shifts show excellent linearity in their peak shift versus refractive index profiles at all three examined temperatures for all three analytes, but the error for fractional volume fillings approaching f=1 was too great to confidently relate the peak shift to volume or mass filling of the pores.

5.4.9 Thermal Cycling at a Distance with a Halogen Heat Source

The thermally cycled data described above used a thermoelectric Peltier module to actively heat and cool the sensor chip while exposed to isopropanol (IPA) or cyclohexane vapors. The sample was also heated at a distance by illuminating the backside of the chip, mounted on top of an o-ring and glass slide instead of on the thermoelectric, with a halogen lamp under computer control. Heating to temperatures above 100°C was fast and consistent, but the high heating rate resulted in poor data

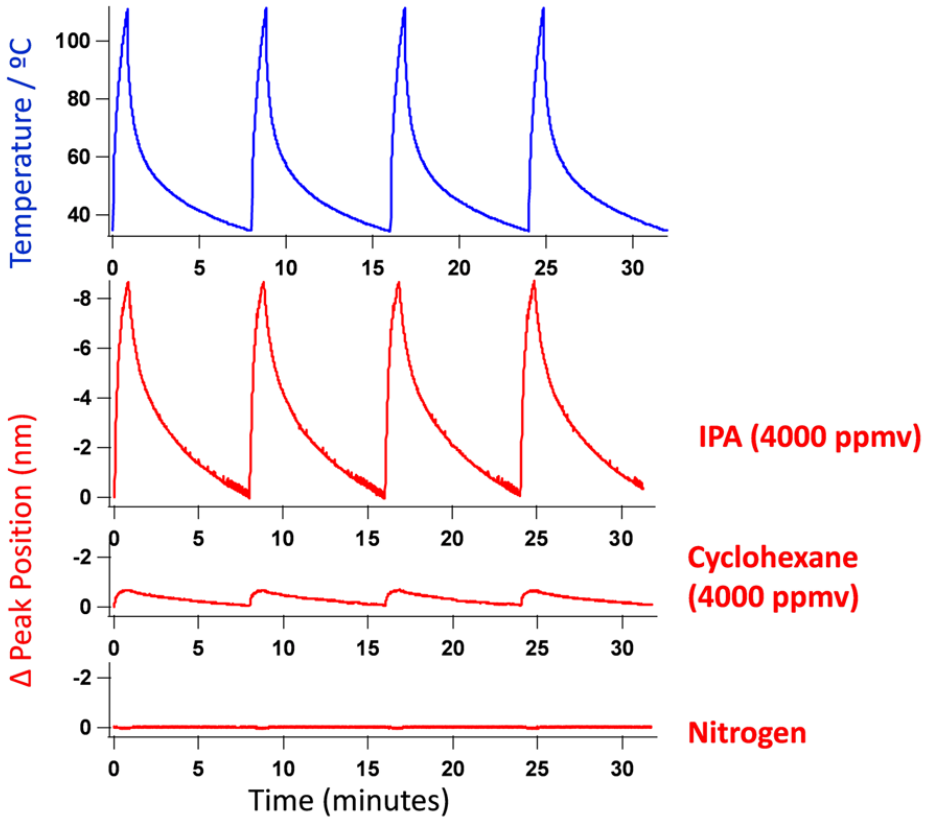

Figure 5.20 Thermal cycling by heating from a distance. A computer controlled halogen lamp illuminated the backside of a sensor chip mounted between two glass slides. Cycling the lamp on-off under flows of analyte (isopropanol (IPA) or cyclohexane) shifted the spectral peak, comparable to the thermoelectric approach.

accuracy between 25-40°C due to the limited acquisition rate, as shown in Figure 5.20. Cooling of the thermal mass under N_2 was also considerably slower than the active cooling provided by the thermoelectric. In Figure 5.19, the heating time was 50s, while the cooling to 25°C required 7 min. Passive cooling is thus undesirable for rapid vapor detection applications.

5.4.10 Cyclic Pressure Modulation of the Sorption Equilibrium in a Closed System

As an alternative to thermally cycling the sensor to modulate the vapor-sensor equilibrium, pressure cycling of the sensor in a sealed system was briefly examined. Figure 5.21 depicts the experimental configuration. A 10mL gas sampling syringe (Vici/Valco A-2 pressureizable), electronic pressure transducer (Omega PX209), vapor inflow, and outflow to the vapor flow cell were connected with Teflon tubing to a Swagelok cross-junction and 7.5 Torr of each vapor flowed through the system at ambient pressure. For each analyte, the outflow after the flow cell and inflow were then sealed with valves, and the pressure of the sealed system modulated with the plunger of the pressure syringe. Here, pressure refers to the total pressure of the sealed system, as shown in Figure 5.22, rather than the analyte partial vapor pressure (concentration). Spectra and pressures were recorded over time at 25°C, shown in Figure 5.22.

In nitrogen, the peak position increases with each successive repressurization, indicated that the system is incompletely sealed and a small amount of ambient relative humidity is entering the nitrogen environment each cycle, since the o-ring seal on the sensor chip may lose contact with the chip when the system is pressurized. The peak shift due to leakage, however, was small compared to the shifts from vapors. For each vapor, the peak shift versus pressure was more consistent after the first cycle. The significant drop in peak position for the first pressure cycle may be due to drawing ambient air into the cell in the first depressurization before a good seal is made. The methodology is a simple demonstration that pressure modulation can, like thermal modulation, be used to change the vapor-surface adsorption equilibrium in the porous

SiO_2. However, pressure modulation in a fielded system would require a sealed chamber and moving parts, and is thus less practical.

5.5 Conclusions

A rugate porous silica photonic crystal was thermally cycled between 25-80°C under flows of analyte vapor in nitrogen to modulate its adsorption equilibrium with three volatile organic vapors. The temperature response of the rugate spectral band enabled discrimination between pure isopropanol, heptane, and cyclohexane vapors with partial pressures ranging from 0-7.5 Torr. At low concentrations (analyte partial pressures), the heating rate was sufficient to observe a delayed isopropanol response to temperature due to its slower equilibration with the porous layer. The methodology suggests a means of discriminating larger numbers of vapors by optically sensing thermally cycled porous SiO_2.

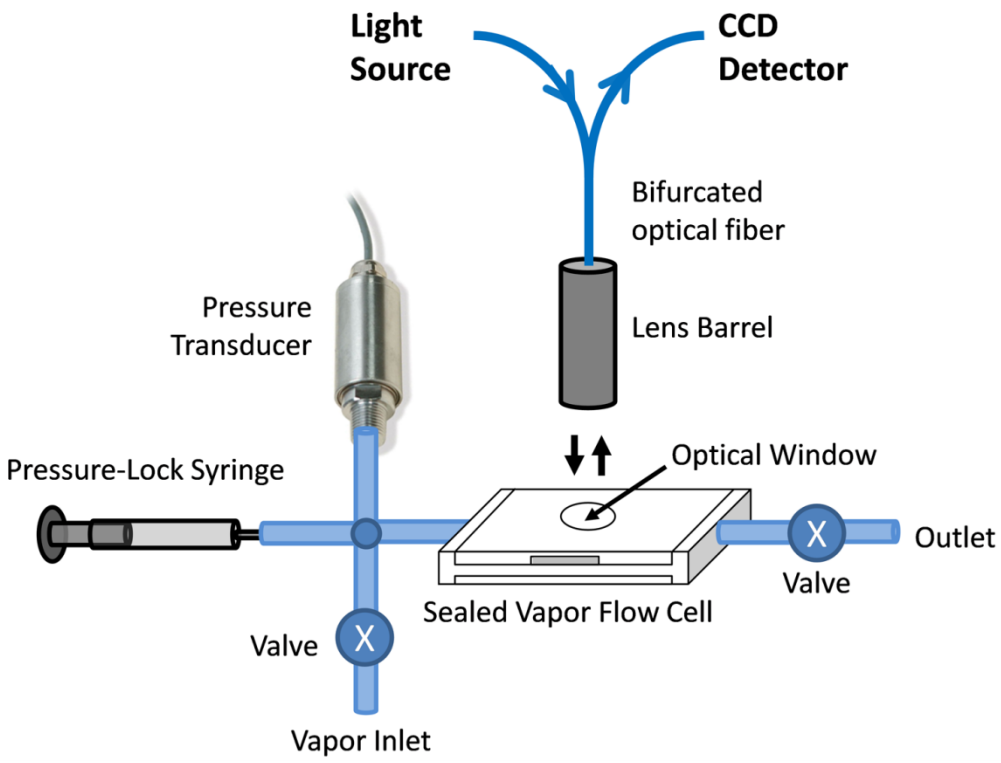

Figure 5.21 Experimental setup of closed chamber pressure modulation approach. A pressure-tight syringe was connected at a junction to an electronic pressure transducer, the inlet vapor flow, and the outflow path to the vapor flow cell and used to modulate the pressure after sealing the inflow and ouflow valves.

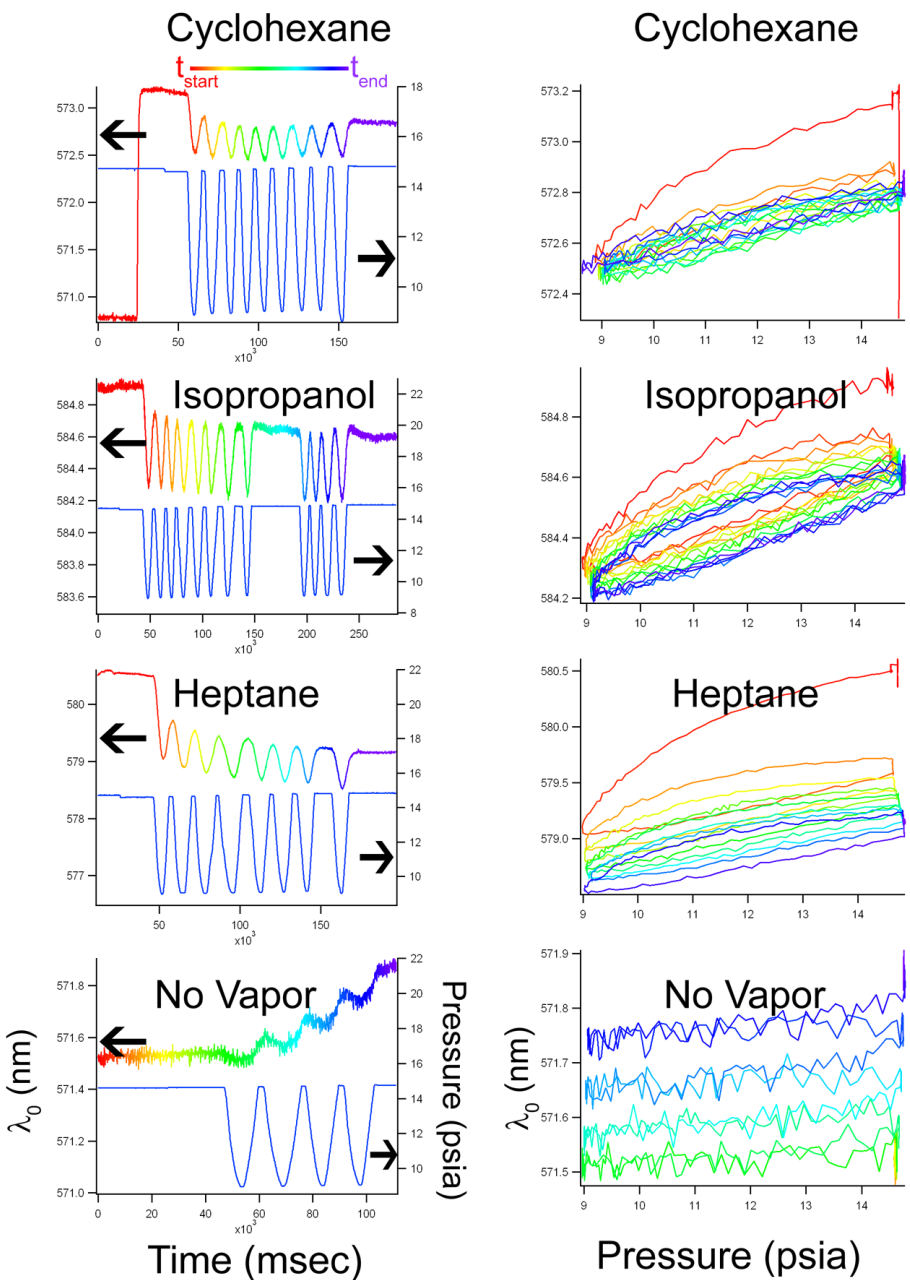

Figure 5.22 Pressure cycling of the sensor response at 7.5 Torr by manually modulating the plunger of a pressure-sealed gas sampling syringe. Here, pressure refers not to the vapor partial pressure of 7.5 Torr of each analyte but to the total pressure inside the sealed vapor flow cell, measured with a pressure transducer. **Left column**: spectral peak position (left axis) and pressure (right axis) over time. Peak positions are colored versus time (red to blue). For cyclohexane, the initial response in nitrogen is shown before vapor exposure at 25 seconds. For the heptane and IPA, the responses are cropped and begin when vapor is already introduced. **Right column:** peak position versus pressure, colored as a function of time (red to blue).

Chapter five, in part or in full, is a reprint (with co-author permission) of the material as it appears in the following publication: King, Brian H.; Wong, Travis; Sailor, Michael J. *Discrimination of pure chemical vapors by optical sensing of a thermally cycled rugate porous silica photonic crystal.* Manuscript in preparation. The author of this dissertation is the primary author of this manuscript.

CHAPTER SIX

GAS SENSING WITH ELECTROCHEMICALLY FABRICATED MEDIUM-WAVE INFRARED POROUS SILICON OPTICAL FILTERS

6.1 Abstract

In Chapters 2-5, direct optical sensing of target analytes with porous silicon photonic crystals was investigated, in which analyte vapors directly interact with the porous layer. The following three chapters explore the use of porous silicon rugate structures as indirect sensors for gases and photoluminescent dyes by leveraging the tunable optical properties of the material. In this chapter, the optical features of rugate porous silicon nanostructures are tailored in the mid-infrared region to match the absorbance peaks of target compounds, enabling sensing of a target gas.

Porous silicon rugate optical filters were electrochemically fabricated to display reflectance peaks in the medium wavelength infrared region from 4um-8um. Etching conditions were tuned to create filters with single and multiple infrared reflectance peaks overlapping specific infrared chemical absorbance bands and containing internal optical reference channels. Rugate optical structures matching the absorbance band of CO_2 at 2350cm^{-1} were used to demonstrate gas sensing with the optical filters, and a structure with a photonic stop band tuned to match the infrared absorbance band of P=O, found in G-series chemical warfare agents, was fabricated. With adequate electrolyte replenishment, calibration of the etching conditions to the spectral band features showed little deviation over increasingly longer etch durations.

6.2 Introduction

Porous silicon optical films produced by the electrochemical etching of silicon[31] have presented an attractive means of creating a film with multiple tunable optical features. The current density applied during the etch process determines the

porosity-depth profile and the resulting refractive index profile of the film with depth, allowing a variety of optical structures to be programmed into the material. Structures including Bragg stacks[4, 74], Fabry-Pérot layers[240], and single and multiple bandgap rugates[8, 33] have been widely produced and applied to gas sensing in the visible and near-infrared. Rugate structures contain a sinusoidal refractive index variation with depth. Multiple sinusoids can be combined into composite profiles that exhibit bandgaps corresponding to each component frequency[33, 85].

This work demonstrates the ability to optically sense target molecules at medium wave infrared wavelengths with rugate porous silicon photonic crystals by matching the rugate reflectance bands to target infrared absorption peaks, with a demonstration of CO_2 sensing using a rugate filter tuned to match the principal νCO_2 stretch of carbon dioxide at 2350cm^{-1}. [241, 242] CO_2 is often sensed at NIR wavelengths like 2.05um[243], but as a proof of principle the 4.2um MWIR absorption band was utilized here. A composite filter based on the superposition of two sinusoid frequencies was also constructed to create a structure that incorporates a tunable reflectance reference channel. Further, to demonstrate the ability to fabricate rugate infrared reflection peaks at the edge of the long-wave infrared region, a filter was constructed with an optical peak at 1250cm^{-1} (8um), the wavelength of the P=O bond vibration in the G-series chemical warfare agents soman, sarin, tabun, and VX [244, 245].

In recent years, rugate porous silicon structures in the infrared region have primarily focused on the near-infrared, particularly at telecommunications wavelengths for applications like broadband mirrors and switches,[8, 10, 246]. Some sensing work at NIR wavelengths has been performed, with Chapron applying NIR rugates in the 1-

3um region to directly sensing liquid analytes with the porous matrix[247]. Since NIR structures are thinner than the thick films required for medium and long wave infrared filters due to their shorter spacing of the dielectric variation, they are less affected by electrochemical fabrication issues of electrolyte diffusion and depletion for long etch times, and face competition from slower fabrication methods like chemical vapor deposition[83], glancing angle deposition[81], and evaporation [80 84], that are less amenable to creating thick medium wave infrared rugate filters.

Medium wave infrared (MWIR) optical structures pose additional fabrication challenges, but open porous silicon to applications including infrared hyperspectral imaging and filters for two dimensional infrared imaging. Recently, Ishikura fabricated MWIR porous silicon structures at 5-10um, demonstrating the ability to create broadband high pass filters[34], and Lo has demonstrated fabrication of rugate filters with broad stop bands at terahertz frequencies[44]. In contrast, the aim of this work is to create narrow band spectral features that overlap the vibrational peaks of target molecules, and to demonstrate the application of these structures to infrared gas sensing through reflectance-mode Fourier-transform infrared (FTIR) spectroscopy.

FTIR is widely used for sensing chemical agents[248] and forensic chemical imaging, with a single scan providing a spectrum analogous to a pixel of a hyperspectral infrared system[249]. The large planar surface area of the porous silicon filter, here 1.2cm^2, further motivates the application of porous Si as optical filters for 2-D infrared imaging since the filters are large enough to cover the infrared imaging elements. In the NIR, 2D imaging has been used for applications including counterfeit pharmaceutical detection[250] and hyperspectral microscopy. In the MWIR, imaging is

of interest to satellite remote imaging[251] and remote sensing[252], as well as military applications in airborne surveillance, target detection and tracking, and thermal imaging. The ability to acquire 2D infrared images developed in the 1970s and blossomed into a variety of detection materials like vanadium oxide bolomoters and barium strontium titanate detectors[253]. In the past decade, quantum dot infrared photodetectors[254] and quantum well infrared detectors (QDIP and QWIP) have enabled cameras with megapixel resolution[255]. Ordered photonic structures have even been used for infrared detection[256], but the work presented here aims not to capture infrared photons with porous Si photonic crystals but rather to complement such detectors with porous silicon filters, by demonstrating infrared sensing using the passive optical filtering properties of porous silicon. Unlike other infrared optical filters, porous silicon is quickly and easily produced, and can be tailored to exhibit sharp spectral features[257]. In contrast, recent developments with voltage tunable multiband infrared focal plane arrays using MEMS technology[253] to create tunable infrared filters has resulted in broad band structures that are not suitable to sensing specific chemical species by matching molecular vibrational absorption bands.

6.3 Experimental

6.3.1 Fabrication of Optical Structures

Porous Si samples were prepared from single-crystal, (100)-oriented highly boron-doped p-type Si (Siltronix,, 0.92 mΩ-cm resistivity) by electrochemical etching in a 3:1 v:v solution of aqueous hydrofluoric acid (HF) to ethanol (49% hydrofluoric acid from Fisher Scientific, Inc). Etching was performed in a Teflon cell with a

platinum mesh counter electrode and a galvanostat (Kepco BOP 50-4D) under computer control (LabView, National Instruments). Single and composite frequency rugate etches were fabricated with a current waveform varying between 25 and 100 mA/cm^2, applied nominally for 45 cycles with other sinusoid conditions as indicated. Fresh HF was introduced to the etch cell during electrochemical fabrication by replacing 1.5mL of the 3:1 etch solution at 5 minute intervals. Lifted-off porous films for use in FTIR transmission mode were achieved by detaching the porous layer from the bulk Si with an electropolishing current of 2.7 mA/cm^2 for 5 minutes in a 3.3% hydrofluoric acid:ethanol solution. Rugate etch currents varied as a function of time t according to:

$$I\,(t) = \frac{\sum_{i=1}^{n} I_i}{n} \tag{6.1}$$

$$I_i(t) = I_{min} + \left[\frac{I_{max} - I_{min}}{2}\right]\left[\sin\left(\frac{2\pi t}{p_i}\right) + 1\right] \tag{6.2}$$

where I_{max} and I_{min} are the high and low currents and p is the period in seconds. For single frequency rugates, n=1. The composite rugate described below contained n=2 components with periods p_1 and p_2.

6.3.2 Gravimetric Determination of Porosity

Samples were weighed before etching (m1), after etching (m2), and after dissolving the porous layer with a 0.1M basic solution of KOH in water and rinsing with ethanol (m3). The following equation was used to determine the porosity:[170]

$$\text{Porosity} = (m_1 - m_2) / (m_1 - m_3) \tag{6.3}$$

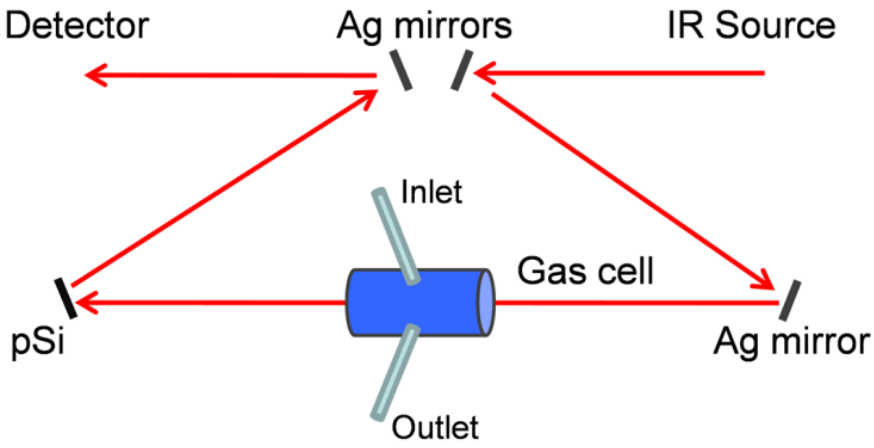

Figure 6.1 Plan view of the reflectance-mode gas sensing configuration inside an FTIR sample chamber. Silver mirrors divert the beam through a gas cell with KBr windows. The porous silicon optical structure is mounted at one of the beam deflection locations, as pictured. A reference spectrum is acquired with a polished silicon chip mounted in the porous silicon location.

6.3.3 Infrared Spectroscopy

Spectra were recorded with a Thermo Scientific Nicolet 6700 FTIR with an MCT/A detector and KBr beamsplitter using a resolution of 2 cm^{-1} and an average of 128 scans. Attenuated total reflectance (ATR) spectra were acquired with a smart iTR diamond accessory. Transmission-mode spectra were acquired by mounting the lifted-off porous Si film between two KBr circular plates (Koch crystal) and placing the assembly on a transmittance accessory stage normal to the infrared beam. Reflectance-mode spectra were acquired with a beam deflector setup as pictured in Figure 6.1 and with filters that were not lifted off from the bulk underlying Si. Four Ag mirrors (Thorlabs), mounted on posts and positioned at a specular angle of 12.5°, diverted the beam path through a gas sample cell. The 2.5" long glass gas cell was positioned in the beam path as depicted and used KBr windows and had Swagelok input and output ports. Reference spectra were taken by replacing one mirror, on the detector side of the gas cell, with polished Si. Sample spectra were taken by replacing the polished Si with a porous Si sample. A flow of ~2L/min of nitrogen , measured with a mass flow controller (Alicat Scientific) was passed through the gas cell. Spectral acquisitions with CO_2 were taken by first purging the cell with a 2L/min flow of CO_2 for 5 minutes, with continuous flow during sampling.

6.3.4 EOT Determination

Reflectance spectra of the samples in the visible region were taken across 530-1200nm with a CCD spectrometer (Ocean Optics USB4000) and a tungsten-halogen light source (Ocean Optics LS-1) connected with a Y-branch bifurcated optical fiber.

The common end of the bifurcated fiber was focused with an objective lens to a 2mm^2 spot size and positioned normal to the porous silicon sample surface. A routine using a fast Fourier transform (FFT) of the optical interference fringes in the visible between 850-1000nm was used to determine the effective optical thickness (2nL) of the layers[86].

6.3.5 Scanning Electron Microscopy

Porous silicon layer thickness was determined by cutting and imaging cross sections of the filters with an FEI XL30 SFEG SEM in ultra high resolution mode with a through lens detector (TLD) at 10kV without prior metallic sputtering of the sample.

6.4 Results and Discussion

6.4.1 Appearance of Rugate Structures in the Infrared

A comparison of spectra from three FTIR acquisition configurations for a filter with a sinusoidal current-time waveform period of p=60s is shown in Figure 6.2. Spectra obtained in the attenuated total reflectance (ATR) configuration clearly exhibit features of the fresh Si-H surface, with $\nu(SiH_x)$ stretches at 2112 and 2087 cm^{-1}, $\delta(SiH_2)$ at 907 cm^{-1}, and $\delta(SiH_x)$ at 623 cm^{-1}. No rugate stop band feature is visible under ATR due to the limited depth of penetration of the infrared beam into the filter layer relative to the physical thickness of the rugate cycles.

The depth of penetration of the ATR beam into a sample is given by[258]:

$$d = \frac{\lambda}{2\pi\,(n_1{}^2 \sin^2\theta - n_2{}^2)^{1/2}} \tag{6.4}$$

where n_1 is the sample refractive index, n_2=2.4 is the diamond crystal index, and θ = 42° is the incident angle. The average refractive index of the porous Si filter is approximately n=1.6 (determined below), yielding a penetration depth ranging from 1.9um at 6000 cm^{-1} to 5.8um at 2000cm^{-1}. Although the filter is inhomogenous and contains a network of pores and voids in contact with the diamond, it may act as a homogenous material since the beam spot size (~1mm) and infrared wavelength are much larger than the dimensions of the pores (~10nm).

In the transmission configuration, the $\nu(SiH_x)$ stretch is very strong, since the light is absorbed in that band as it passes through the optical film. The principal rugate band at 1715 cm^{-1} is observed, as well as higher order harmonics at $2/\lambda$ and $3/\lambda$ [33]. If desired, these higher order harmonics may be suppressed by creating filters with a sinusoidal modulation of the logarithm of the refractive index n with depth [8, 34] rather than a direct sine variation of n. Here, the $2/\lambda$ band was desired and utilized as an optical reference channel. The thickness of the filter balances a tradeoff between increasing the number of sinusoid repetitions to reduce thin film interference fringes and increasing the material's absorbance in the Si-H bands outside of the desired rugate spectral position. Figure 6.3 shows a picture of a mounted lifted-off porous Si filter and the resulting transmission-mode FTIR spectrum for a filter etched for 50% longer than the filter shown in Figure 6.2, resulting in a ~50% thicker film. A comparison of the two filter spectra in transmission mode shows higher absorbance and a sharper rugate band for the thicker layer, but increased Si-H stretch and bend absorbances as well.

To sense absorbing molecules in the beam path, a reflection rather than transmission configuration is desirable. In reflection mode, an absorbing gas is sensed

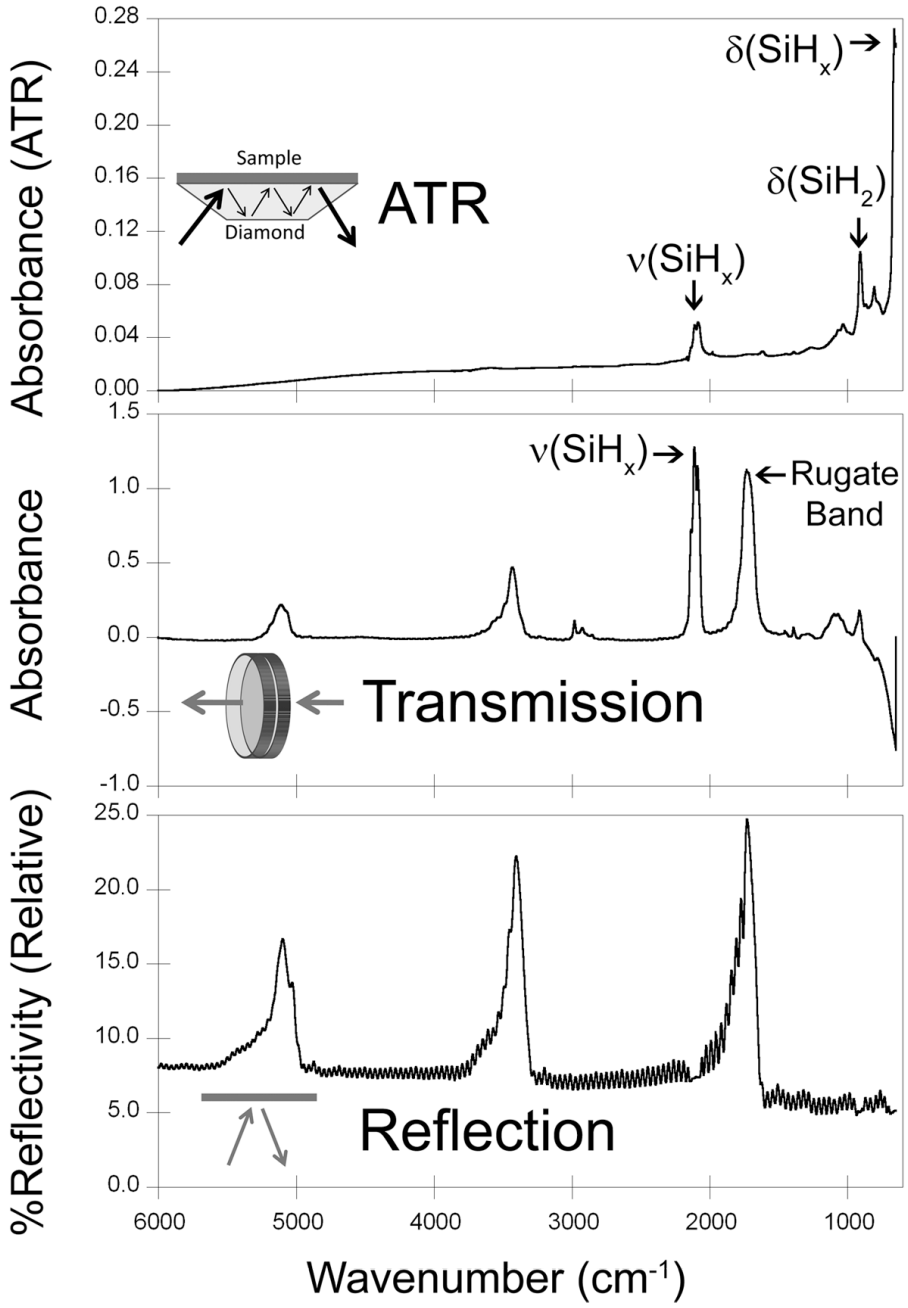

Figure 6.2 Comparison of three FTIR acquisition modes and resulting spectra for an infrared rugate optical structure with a sinusoid etching wave period of 60s. **Top:** Attenuated total reflectance. **Middle:** The optical structure was lifted-off from the bulk and the spectrum acquired in transmission mode. **Bottom:** Reflection-mode interrogation using the beam diversion configuration in Figure 6.1. The percent reflection is relative to the polished Si reference.

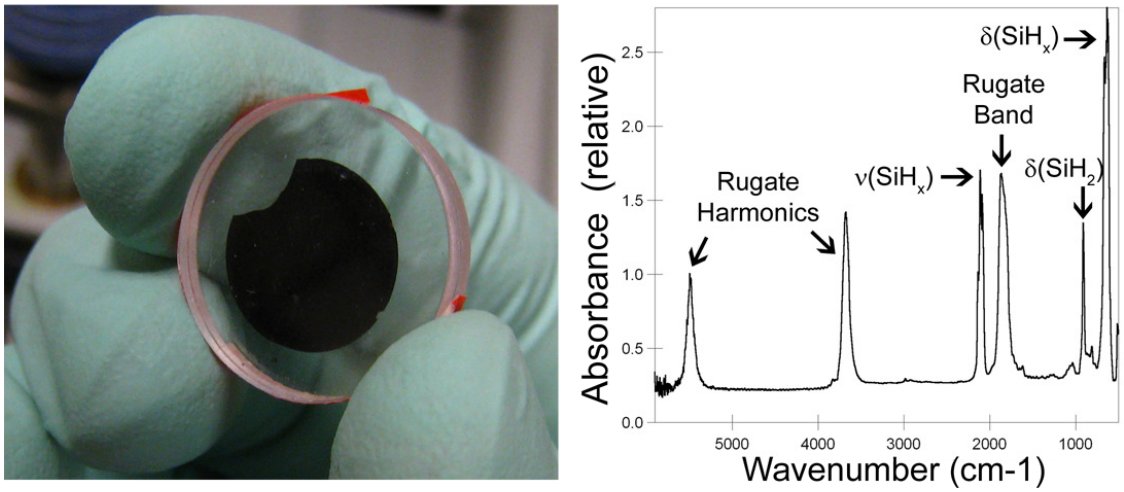

Figure 6.3 Left: Image of a lifted-off porous silicon optical structure mounted between two KBr plates. **Right:** transmission-mode FTIR spectrum of the freshly prepared rugate structure, with the rugate band and overtones labeled.

as a reduction in peak reflectivity, while in transmission mode the absorbing gas results in a slight decrease in the already low filter transmittance of the rugate band. The spectrum in Figure 6.2 taken in the reflection configuration clearly exhibits the rugate reflection band as well as higher order harmonics at $2/\lambda$ and $3/\lambda$, with the Si-H stretches of the material's absorbance appearing as reductions in the reflectivity at ~2100 cm^{-1}. Thin film interference fringes are present due to reflections from the top and bottom interfaces of the optical structure, where the bottom interface consists of the porous Si layer and bulk silicon. Despite mounting the porous Si sample at a 15° angle of incidence, the center wavenumber of the rugate band at 1742cm^{-1} in the reflectance configuration was only slightly lower than its appearance at 1730 cm^{-1} in the transmission configuration, where the filter was normal to the incident beam. This is not surprising, since for an incident angle θ_0, the wavelength of the peak at an angle λ_θ relative to its location at normal incidence λ_0 is[10]:

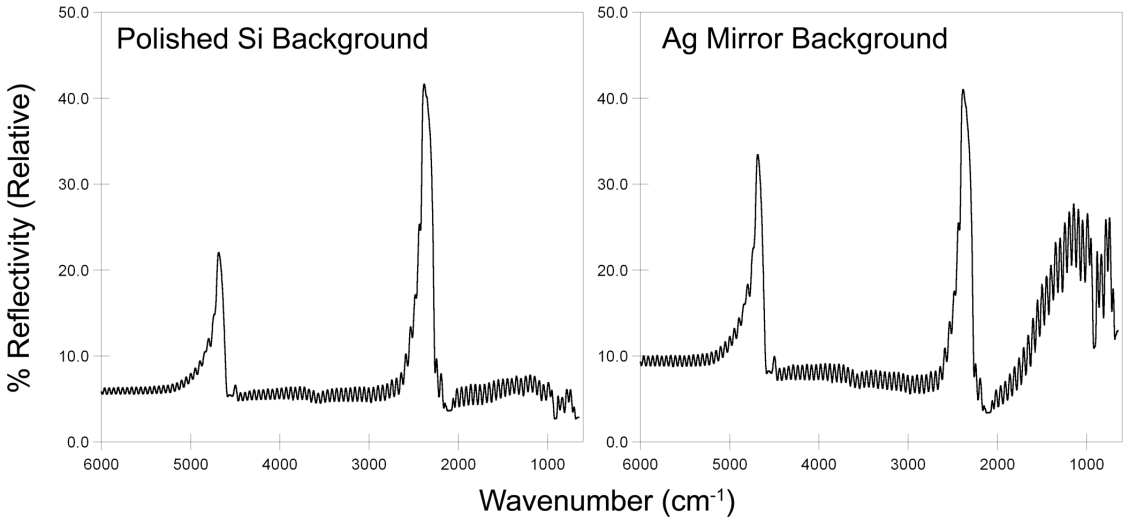

Figure 6.4. Comparison of the reflectance-mode FTIR spectrum of a rugate structure with a sinusoid etchwave period of p=43.5s referenced to the background spectrum of a polished Si wafer (left) to the same structure reference to the background spectrum of an Ag mirror (right), demonstrating the variable reflectivity of the silicon substrate across the FTIR region at low wavenumbers.

$$\lambda_\theta = \lambda_0 \cos(\theta_a) = \lambda_0 \left(1 - \frac{\sin^2\theta_0}{{n_{avg}}^2}\right)^{0.5} \tag{6.5}$$

where θ_a is the angle of propagation through the rugate filter and n_{avg}=1.5 its average refractive index (calculated in section 6.4.7). This yields an expected spectral position in reflectance mode at θ_a=12.5° of 1748 cm^{-1}, with the observed difference due to the tolerance of the mirror positioning. The porous Si filter may be placed at any of the four beam diverter locations pictured in Figure 6.1, but was placed after the gas sample cell for sensing experiments to simulate a filter on an infrared imaging device.

The choice of reference material in reflectance mode influences the resulting spectra, as shown in Figure 6.4. Referencing to a silver mirror increases the reflected intensity above 2000 cm^{-1} due to the silicon absorbance, while referencing to polished Si yields a baseline that is considerably more optically flat.

6.4.2 Comparison to Other Rugate Structures

Typical rugates with stop bands in the visible region are not optically inactive in the infrared. They display fringes throughout the infrared as a result of constructive and destructive interference between light striking the top and bottom interfaces of the filter, as shown in Figure 6.5. In Figure 6.5, the fringes of the filter are widely spaced in the infrared because of the short filter thickness. Figure 6.6 displays a comparison between a thicker (>50um) rugate filter with a stop band at 2000cm^{-1} and a constant-current etch fabricated at the same average etch current density (62.5 mA/cm^2). Both were etched for the same time and at the same average current density. Since the two filters are of comparable thickness, the spacing of the interference fringes is similar. As expected, the constant-current film exhibits interference fringes with a low reflectivity of <6%, along with a cut-out of the fringes at 2100cm^{-1}due to absorption from Si-H stretches.

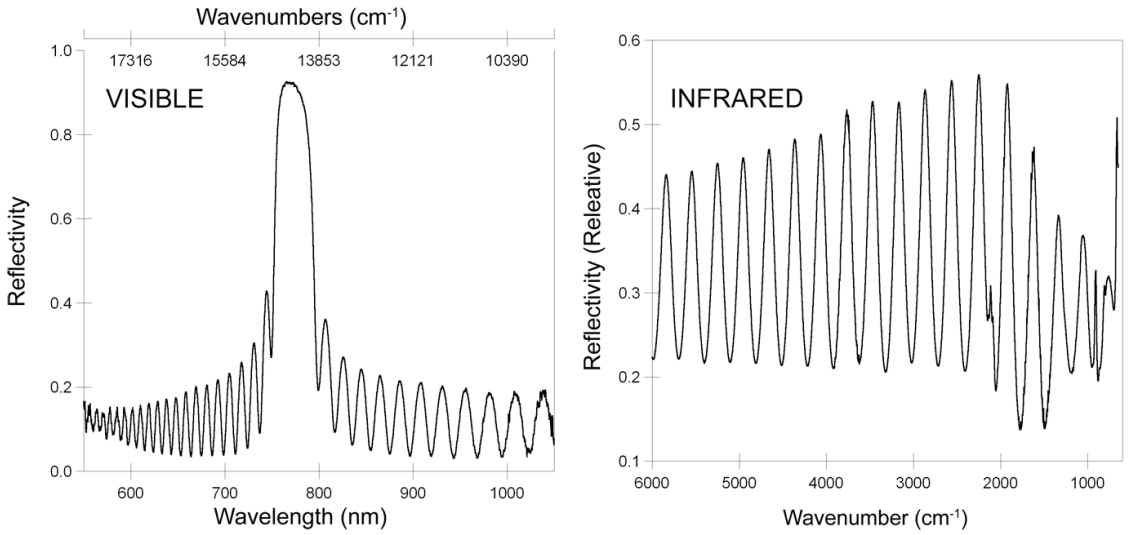

Figure 6.5 Rugate structure with a current-time sinusoid etchwave period of 7s **Left:** Visible-region reflectance at normal incidence taken with a CCD spectrometer and halogen light source. Right: FTIR reflectance-mode spectrum of the optical structure mounted at one of the beam diversion positions in the FTIR optical path.

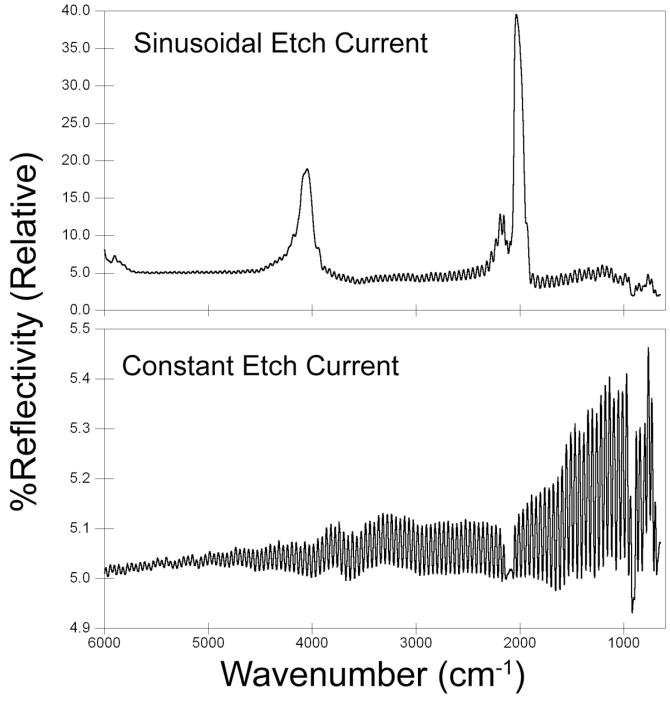

Figure 6.6. Comparison of reflectance-mode FTIR spectra of a rugate porous silicon structure with fabricated with a sinusoid period of p=51s (top) to that of structure etched at a constant current for the same total etching time and at the same average current density (mA/cm^2) of the rugate sinusoidal etch.

6.4.3 Demonstration of Gas Sensing with a Single-Peak Rugate

A rugate filter tuned to the $\nu(CO_2)$ band is shown in Figure 6.7. The CO_2 vibrational transitions from the ground state between 2260-2390 cm^{-1} are easily observed in a reference sample of the gas taken without the porous Si filter by using silver mirrors at all beam deflection locations. The slight sawtoothing visible around 2350 cm^{-1} is due to the Q and R absorption branches, which sawtooth since the step size of 2cm^{-1} is not small enough to show individual peaks. The absorptions at higher wavenumbers are the result of combination vibrational modes, with a doublet at 2.7um and higher members of the same sequence at 2.0um.[241, 242] The "noise" observed from 1400-1800 cm^{-1} is due to a small amount of residual water vapor in the FTIR chamber. The rugate filter displayed in Figure 6.7 was constructed with a current-time sinusoid waveform with a period of 43.7s etched for 45 repetitions, designed to match the 2350cm^{-1} principal absorption band. The resulting filter exhibited a cross sectional thickness of 70.7um. Upon introduction of CO_2 into the gas cell, the principal rugate band was obscured by the absorbing molecules, decreasing the peak area, while the higher order harmonic was unchanged. The ratio of the areas or of the intensities of the principal peak to the harmonic overtone peak can thus be used as a referenced sensor for the presence of CO_2.

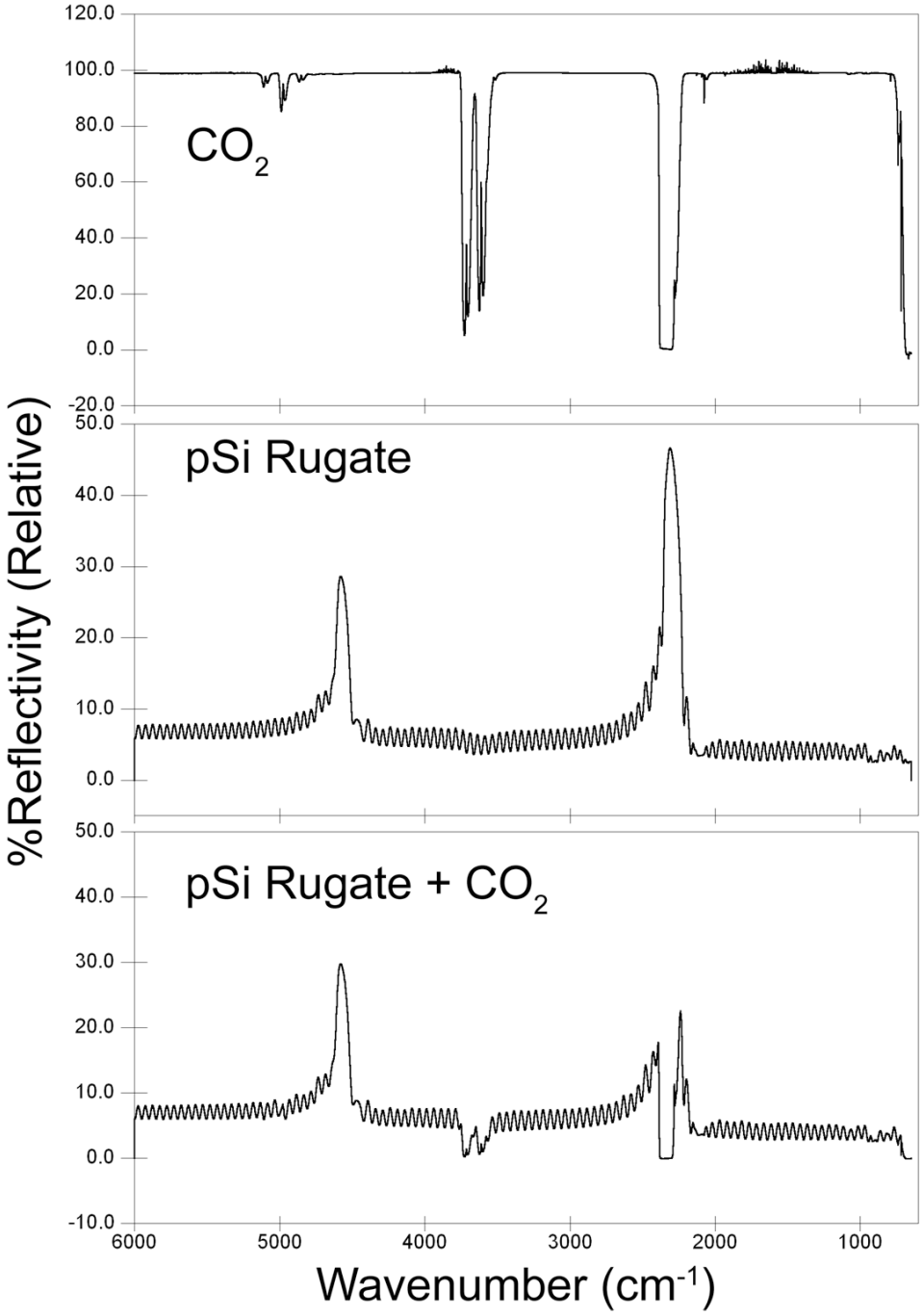

Figure 6.7 Reflectance-mode FTIR sensing of CO_2 with a rugate filter. The rugate was etched with a single-frequency sinusoidal current-time waveform with a period p=43.7. **Top:** Gas chamber purged with CO_2, with silver mirrors mounted in all four beam deflection locations. **Middle:** Gas cell purged with N_2, with porous Si mounted at a deflection position. **Bottom:** Gas cell purged with CO_2, with porous Si at a beam deflection position.

6.4.4 Gas sensing with a Composite Rugate Photonic Crystal

In the single-peak rugate described above, a harmonic band was utilized as a reference channel for the principal rugate band at 2350cm^{-1} that overlaps the CO_2 absorption. The location of the harmonic band is spectrally distant from the principal peak and its location depends upon the principal peak location. To introduce a tunable reference peak that is spectrally closer to the principal band, a composite, infrared rugate was fabricated consisting of a single layer combining two sinusoidal current-time frequencies into the current-time etch wave, as pictured in Figure 6.8. Filters of each single frequency were fabricated for reference (left panel), with the composite filter comprised of p=43.7s and p=51s periods that resulted in rugate bands at 2350 and 2000 cm^{-1} respectively, with a total layer thickness of 72.5um determined by SEM. As shown in the right panels of Figure 6.8, the presence of CO_2 in the gas cell greatly reduced the area of the peak at 2350cm^{-1}, while not affecting the reference channel at 2000cm^{-1}. Figure 6.8 also demonstrates sensing of CO_2 at lower concentrations. A spectrum reflected off the filter was taken for a 50/50 volumetric mix of CO_2 and N_2 in the gas cell, as well as ambient room air. The reflectance scan of the latter exhibits a slight reduction in the 2350cm^{-1} peak area and shows evidence of water vapor outside the rugate bands.

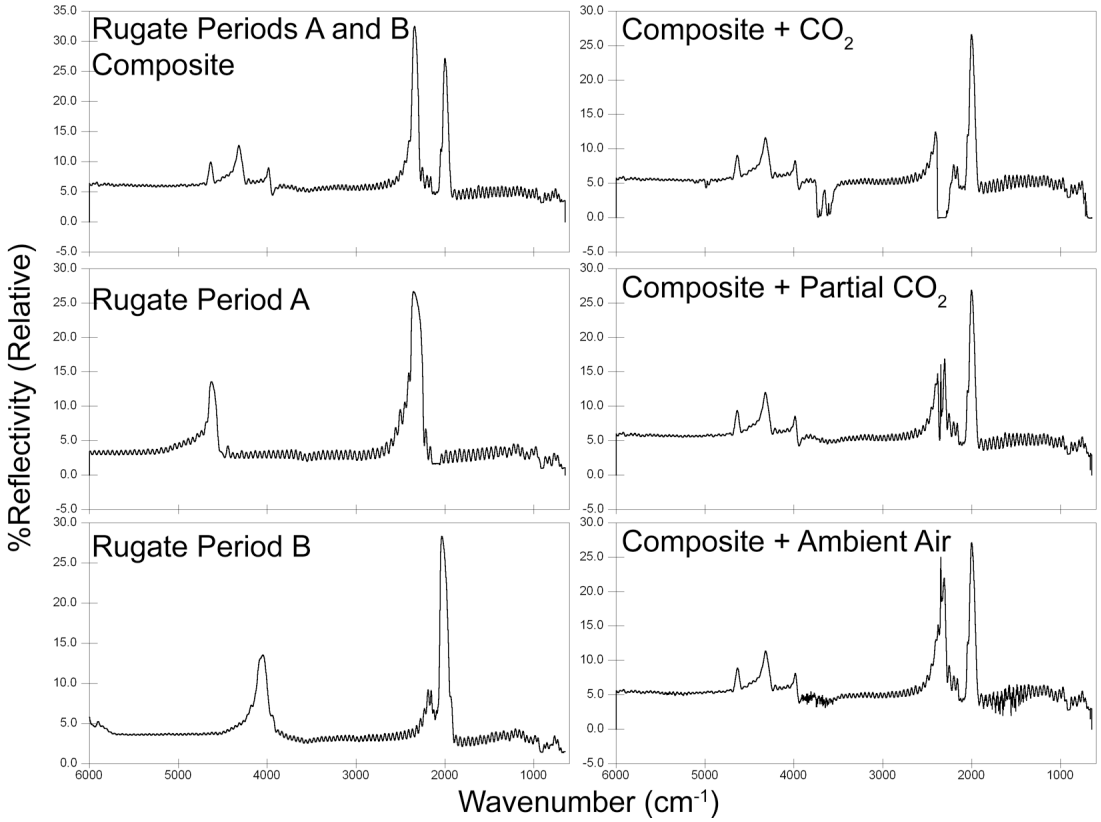

Figure 6.8 Reflectance-mode FTIR sensing of CO_2 using a multi-frequency rugate optical filter. **Left:** Single-frequency components with p=43.7s (middle) and p=51s (bottom) compared to the composite filter (top). **Right:** Spectra of the composite filter with varying levels of CO_2 in the gas sample cell: fully purged with

6.4.5 Matching the P=O Bond Stretch

To demonstrate the ability to tune rugate peaks to the edge of the long wave infrared region, a filter was constructed to match the P=0 stretch at 1250cm^{-1}. This transition is present in the G-series chemical nerve agents sarin, soman, tabun, and VX[244, 245]. The filter shown in Figure 6.9 was etched with a sinusoid current-time period of p=82.5s, resulting in a 123um thick layer as determined by SEM. Several overtone bands are clearly present. A section of the SEM cross section of this filter is pictured in Figure 6.10, clearly showing the contrast in electron density between the alternating regions of high and low porosity with depth and indicating the pitch (spatial period) of the refractive index variation with depth. The pores in the image are much smaller than the pitch and run vertically from the top to bottom of the filter, as pictured in the right panel of Figure 6.10.

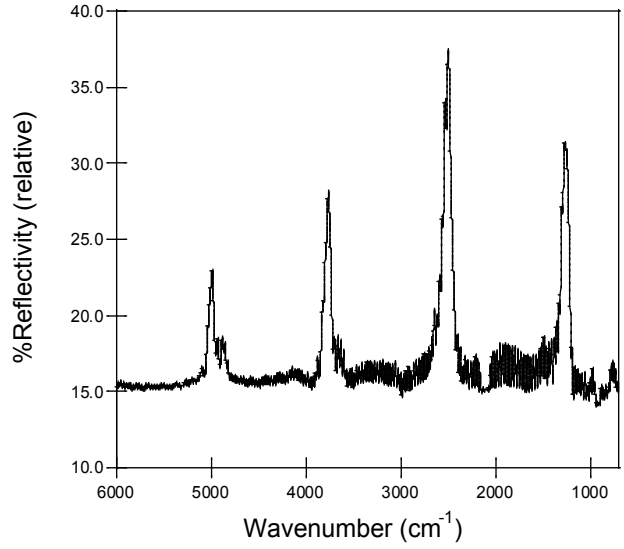

Figure 6.9 Reflectance-mode FTIR of an optical filter with a sine current-time etching waveform period of p=82.5s mounted at one of the beam diversion positions. The principal rugate peak at 1250cm^{-1} was designed to match the P=O bond stretch of G-series chemical nerve agents.

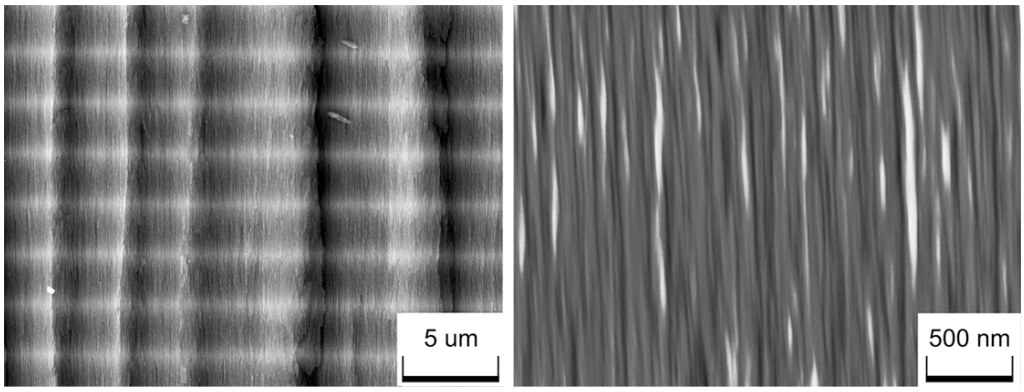

Figure 6.10 Left: SEM cross sections taken at 10kV of a rugate optical structure with a sinusoid etchwave period of p=82.5s showing horizontal bands of varying porosity with depth, corresponding to the sinusoidal variation of the etch current with time. **Right:** the vertical pore channels extending from the top to the bottom of the optical structure, taken at 2kV

6.4.6 Effect of Rugate Repetitions

Increasing the number of sinusoid etch repetitions for a given fixed period reduces the height of the thin layer interference fringes relative to the rugate peak while increasing the etch thickness. Thicker layers result in increased absorption at porous Si-H absorption frequencies. For the gas sensing work above, layers with 45 rugate cycles were chosen as a nominal value exhibiting acceptable thin film fringe reduction. Figure 6.11 displays four etches with varying numbers of rugate cycles for a period of p=43.7s. The effective optical thickness ($2n_{avg}L$) increases linearly with the number of cycles due to the linear increase in the layer thickness L, for the constant average layer refractive index n. This result indicates that issues affecting the etch rate of the porous layer do not dramatically deviate the linearity of the optical thickness with total etch time for very thick (>50um) etches[12]. Specifically, the diffusion of the HF electrolyte into the increasingly thicker film during long etches does not appear to have limited the etch rate.

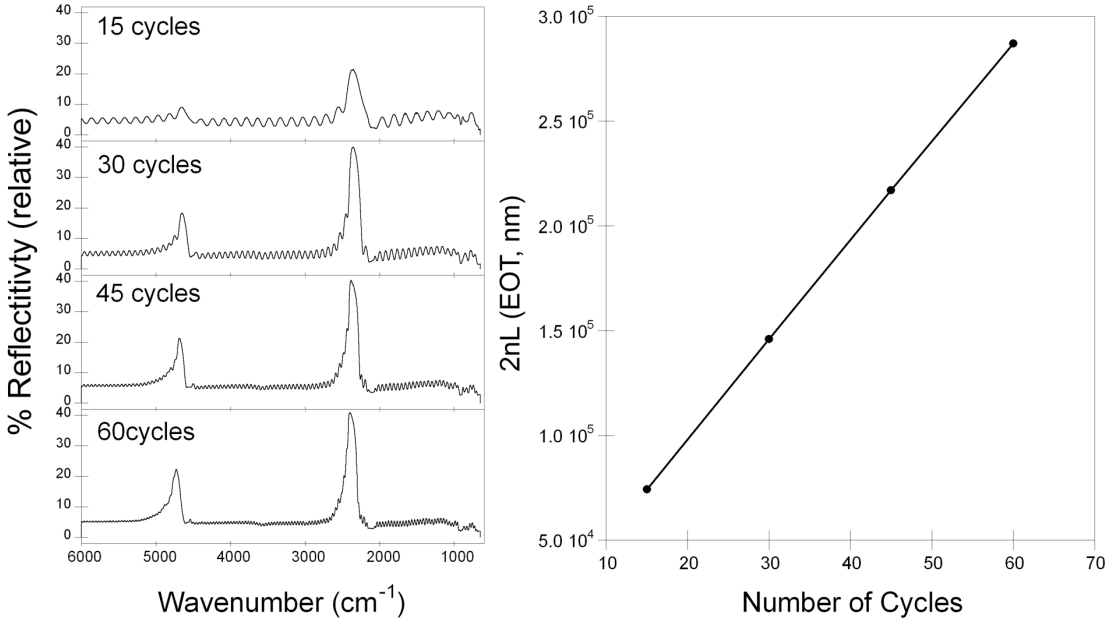

Figure 6.11 Left: Effect of the number of sine wave cycles for an optical structure with a period of 43.7s. **Right:** Linear relationship between the effective optical thickness ($2n_{avg}L$), from an FFT of the visible interference fringes, and the number of sine wave cycles.

6.4.7 Effect of the Etching Period

The period of the current-time etch wave, given in equation 6.2, corresponds directly to the spectral position of the rugate band, and rugates with spectral bands across the MWIR have been created. Figure 6.12 displays reflectance FTIR spectra of several of these filters.

The periodic variation of the current density with time given in equation 6.2 results in a periodic variation of the refractive index with depth z, expressed as [8, 33]:

$$n(z) = n_{avg} + \frac{\Delta n_{avg}}{2}\sin\left(\frac{4\pi n_{avg} z}{\lambda_0}\right) = n_{avg} + \frac{\Delta n}{2}\sin\left(\frac{2\pi z}{d}\right) \quad (6.6)$$

where n_{avg} is the average refractive index of the filter, $n_{avg}z$ is the optical path, λ_0 is the resonance peak wavelength of the rugate, and d is the spatial period of the index modulation, which is the physical thickness of one period. The spectral position of the rugate peak is expressed as $\lambda_0 = 2n_{avg}d$, so longer periods in the current-time etching wave correspond to larger spatial periods and higher rugate peak wavelengths. As seen by comparing equations 6.2 and 6.5, the location of the stop band λ_0 is proportional to the period of the etching sine wave p, and so the frequency 1/p scales with wavenumber ($10^6/\lambda$). The refractive index profile with depth deviates somewhat from the sine waveform of the current etchwave since the etch rate increases with current, biasing the refractive-index depth profile[212]. However, this bias is expected to be constant if the amplitude of the current-time wave is held constant and only the period is changed. Figure 6.12 compares two sets of period versus peak wavelength (λ_0) calibrations of MWIR porous Si filters, one in which the total etch time was held constant and the number of cycles varied (left column), and the other in which the

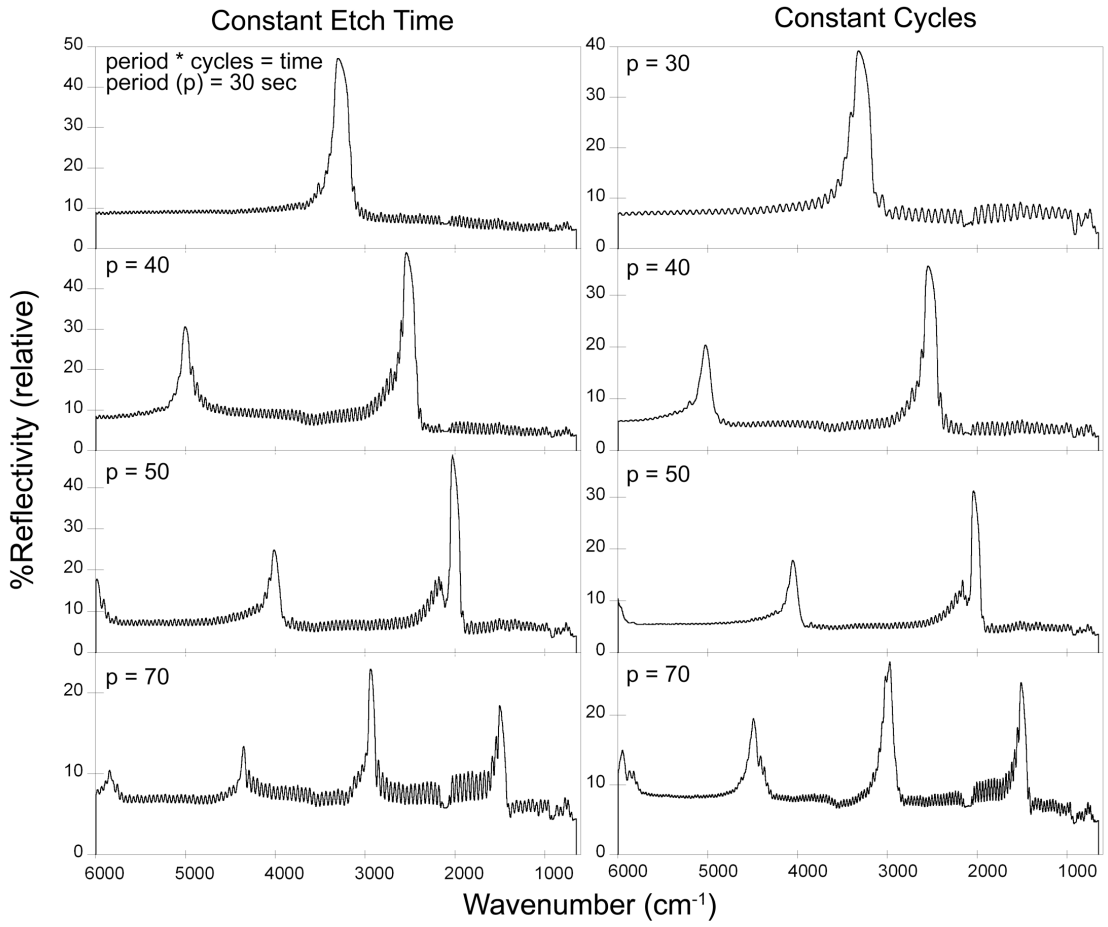

Figure 6.12 Comparison study of a series of etches with constant total etching times but a variable number of cycle repetitions (left) to a series of etches with a constant number of sinusoid cycle repetitions but variable etching times (right). Spectra from structures of four of the sine wave periods in each series are shown. The total etch time was the equal to the period (s) times the number of cycles. The two calibrations coincide at p=50s, where each consisted of 45 repetitions and a total etch time of 2250s.

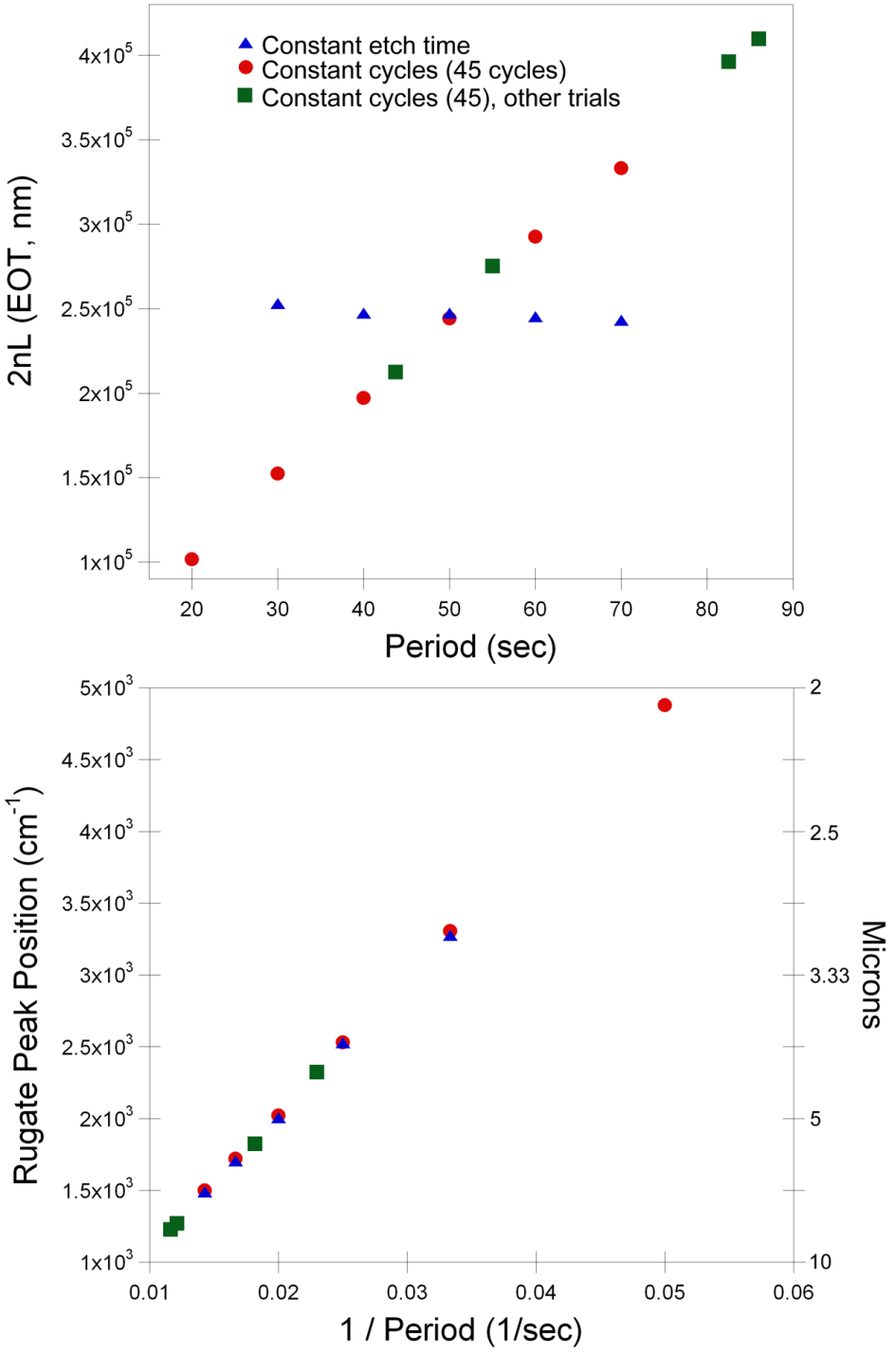

Figure 6.13 Top: Effective optical thickness versus the etchwave period for porous silicon optical filters. Filters fabricated with a constant total etching time (triangles) are compared to those etched for a constant number of sinusoid cycles (circles and squares). **Bottom:** Position of the principal rugate spectral peak as a function of the frequency (1/period) for both constant-time and constant-cycle repetition calibrations.

number of sinusoid cycles was held constant and the total etch time varied. The two calibration series share a coincident point at a sine period of p=50s. As expected, the etches with a constant total etch time have a similar spacing between the thin film interference fringes, while the increasing thickness of the constant cycle etches results tracks with an increasing optical thickness, evidenced by the decrease in fringe spacing.

Figure 6.13 displays the effective optical thickness (EOT, $2n_{avg}L$) and rugate peak position of these etches versus the period. The EOT was determined by an FFT of the thin layer interference fringes in the visible spectrum. EOT values based on an FFT of fringes in the infrared were also calculated and differed by a constant -4% from the visible values taken at normal incidence. The filters with a constant total etch time display a slight decrease in effective optical thickness with increasing period, in contrast to the linearly increasing EOT with period for constant-cycle, variable etch time filters, shown in the top panel of Figure 6.13. The EOT scales linearly with the period since for a constant n_{avg} of the layer, the thickness L is a direct function of the etch rate (nm/sec) times the etch time (sec). The rugate peak position of both the constant-time and constant-repeat etches is linear with the etch period, as shown in the bottom panel of Figure 6.13. As mentioned, this is expected since λ_0 scales with the period p, and so wavenumbers ($1/\lambda_0$) scale with the frequency 1/p. Additional etches that were performed separately from the two trials above are included in Figure 6.13 and show excellent agreement with these trends.

Several issues can affect the etch rate for longer etches, and consequently the EOT and rugate spectral positions. HF diffusion to the etching boundary for thick layers can lead to a decrease in the layer growth rate with depth, and a reduction of the

concentration of HF as it is consumed can influence the etch rate of long etches with low electrolyte volumes[12, 31]. To address this, the volume of HF was mixed and partially replaced every 5 minutes during the etches. Incorporation of etch stops for 1s every cycle to allow equilibration of electrolyte concentration showed no difference in optical properties or layer thickness, though others have utilized shorter etch stops to homogenize electrolyte distribution for creating ~300um rugate filters with stop bands at terahertz frequencies[44]. Further, after a section of the filter has been electrochemically etched, it will continue to be dissolved at a much lower rate while in contact with HF, leading to a high to low porosity gradient from the top to bottom of the etched layer. The linearity of the EOT and peak position in Figure 6.13 with increasingly thicker etches with longer etch times (increasing periods for constant cycles) indicate that these issues were not significant for the etching conditions utilized. The gravimetric porosity was determined for all etched layers as 74%, with no more than a +/-1% variation across all samples, attributable to error in the weighing of the samples. The porosity exhibited no trend with changes in period, indicating uniformity of the etch rate with increasing etch time of the samples.

It is also worth noting the decrease in the width of the rugate peaks in the FTIR spectra with increasing period. This is an expected result of changing the reflectance band position, since width of the spectral band $\Delta\lambda$ centered at λ_0 can be expressed as[10, 89]:

$$\frac{\Delta\lambda}{\lambda_0} = \frac{\Delta n}{2n_{avg}} \tag{6.7}$$

Since the variation in refractive index Δn and average refractive index of the layer n_{avg} are determined by the low and high etch currents of the sine etching wave and do not change with period, an increase in the wavenumber $1/\lambda_0$ of the stop band results in a commensurate decrease of the rugate peak $1/\Delta\lambda$, as seen in the FTIR spectra of Figure 6.12.

The SEM thickness and effective optical thickness ($2n_{avg}L$) of a filter specimen can be used to determine the average refractive index n_{avg} of the porous filter by dividing by 2 times the thickness, where thickness was determined by SEM of film cross sections. For the single-peak CO_2 sensor example with a thickness of 70.7um, n_{avg}=1.51. The refractive index of the silicon pillars in the porous material, n_{Si}, can then be calculated with the Bruggeman effective medium approximation[212] where P is the porosity and n_{air} the refractive index of air:

$$(1-P)\,\frac{{n_{Si}}^2-{n_{avg}}^2}{{n_{Si}}^2+2{n_{avg}}^2}+\;P\;\frac{{n_{air}}^2-{n_{avg}}^2}{{n_{air}}^2+2{n_{avg}}^2}=0 \qquad (6.8)$$

The nSi of filter is 3.67 for an EOT determined by fringes between 850-1000nm, a close match to literature data of n=3.6 at 900nm[218]. This agreement indicates that the optical properties of the filters tuned to MWIR wavelengths are consistent were consistent with expected porous silicon properties.

6.5 Conclusions

Rugate optical filters with reflectance bands in the medium-wave infrared were successfully fabricated from porous silicon and used to detect CO_2, by matching the reflectance peak to a vibrational absorbance band of the molecule. Filters with rugate bands tuned across the MWIR region were fabricated, including porous layers with an optical band at the wavelength of the P=O bond stretch at $1250cm^{-1}$, and the spectral position of the sensing layer reflectivity band in the infrared exhibited excellent linearity with the frequency of the current-time sinusoid etching waveform.

Chapter six, in part or in full, is a reprint of the material as it appears in the following publication: King, Brian H.; Sailor, Michael J. *Gas sensing with electrochemically fabricated medium-wave infrared porous silicon optical filters.* Manuscript in preparation. The author of this dissertation is the primary author of this publication.

CHAPTER SEVEN

TAILORING THE OPTICAL SPECTRUM OF POROUS SILICON FOR SENSING APPLICATIONS

7.1 Abstract

The previous chapter discussed optical sensing with rugate porous silicon at mid-infrared wavelengths, tuning the wavelengths of an optical structure with a single reflectance peak and another with two spectral reflection bands. In this chapter, the customization of rugate porous silicon photonic structures is investigated in greater depth and applied to structures with reflectance bands in the visible spectrum for a digital imaging application based on matching the spectral bands of porous silicon to the optical peaks of fluorescent dyes. As with the infrared rugates, the porous silicon is used as an indirect sensor by acting as a customized optical filter. Here, the optical shift of rugate bands with chemical vapor exposure is additionally utilized to create a filter whose spectrum can by chemically modulated. Difference imaging is then performed by contrasting images of the filter in an ambient environment to those taken with the vapor-shifted porous filter.

7.2 Introduction

Optical filters with customized spectral features have broad application in airborne surveillance imaging[259], medical imaging and microscopy[260], live monitoring of chemical reactions[261], chemical imaging of pharmaceuticals[250], and imaging of fluorescent dyes that bind to explosives, proteins, and toxins[262]. Additionally, customized and tunable spectral filters are of great interest for hyperspectral and difference imaging applications. In hyperspectral imaging, each spatial pixel contains an entire spectrum of data, with wavelengths typically resolved by methods such as sets of bandpass filters, liquid crystal tunable filters[263], or acousto optic tunable

filters[261]. Bandpass filters are inexpensive, but their resolution is poor due to their broad spectral features. Other methods involve systems of higher complexity and cost. In difference or "correlation" imaging, images are often typically acquired through spinning wheels containing filter discs that match optical features of desired gases, dyes, or other compounds of interest. The difference between images taken through target spectrum-matched and unmatched filters is used to contrast the desired target to the rest of the image space[264, 265]. While highly customized spectral filters have been created by techniques including PECVD and glancing angle deposition[81], these processes are slow and expensive in contrast to electrochemical fabrication with porous silicon, and the nonporous optical layers they create lack the additional direct chemical responsiveness of porous silicon. This direct response to chemical vapors is used here to chemically shift the filter and provide an alternate means of difference-imaging target compounds than mechanical wheel-based methods.

This work addresses the need for customized, easily fabricated filters that match target visible wavelength spectra. The first section of this chapter covers a method of matching porous silicon to the photoluminescence peaks of several target dyes. A method of refinement is first described, whereby the spectral peak wavelength, reflectivity, and width are recursively tuned to approximate desired features by changing the period and amplitude of the porous silicon etching wave. These methods, including the superposition of etching wave frequencies to generate composite waves that display more than one rugate spectral peak[8, 33, 78], have been commonly employed with porous silicon for other applications. Following this, a second approach takes a porosity-depth profile generated through optical modeling methods, converts it to a

time dependent current density etching profile, and assesses the resulting spectral features. Optical design of spectral features for creating custom optical coatings has been discussed in depth, especially by Verly[266, 267], Bovard[268], and offers a potentially faster method for creating new optical structures than the refinement approach. An optically designed porosity-depth profile, expected to yield an optical structure that matches the fluorescent spectrum of a target dye, was converted here to a time dependent current density etchwave through a series of calibrations.

The second section of this chapter turns to applying the refinement method to digital imaging of target fluorescent lanthanide dyes, whose spectrum the porous Si is tuned to match. Chelation of dipicolinic acid (DPA) to these dyes greatly increases their fluorescence intensity. DPA is released from bacterial endospores upon germination and constitutes approximately 15 percent of the dry endospore weight[269] but is not commonly found in other substances or the environment. The Terbium dye used here has been widely utilized to quantitatively detect spores through Tb^{3+}-DPA luminescence[270, 271]. Porous Si filters are first used to distinguish ultraviolet illuminated Terbium-DPA and Europium-DPA-impregnated glass fiber swatches by color imaging. The Terbium-matched filter is then used to distinguish the dye from a broadband dye that appears the same color to the naked eye. This is accomplished using a single channel (monochrome) imaging system by chemically shifting the filter spectrum with ethanol vapor in a difference-imaging configuration.

7.3 Experimental

7.3.1 Sensor Preparation

Porous silicon rugate optical films were prepared from single-crystal, (100)-oriented highly boron-doped p-type Si (Siltronix, 1-1.2 mΩ-cm resistivity) by electrochemical etching in 3:1 v:v solution of aqueous hydrofluoric acid (49%, Fisher Scientific):ethanol (Rossville Gold Shield Chemical). Etching was performed in a Teflon cell with a platinum ring counter electrode and a galvanostat (Kepco ATE 25-2DML) under computer control (Lab View, National Instruments.) Optical films used in camera imaging experiments utilized a 5.1cm^2 Teflon cell to produce a larger planar surface area, while all others were performed in a 1.2 cm^2 cell. The current density - time waveforms of the rugate filter etches were designed in Igor Pro (Wavemetrics). The specific current density waveforms for each filter design are described later in the text. For those optical filters that were oxidized, the samples were placed in a tube furnace (Lindberg Blue) for 60 minutes at 800°C in ambient air and allowed to slowly cool.

7.3.2 Porous Silicon Characterization

Gravimetric Determination of Porosity

To calibrate the porosity of the filters to the etching current density, samples were weighed before etching (m1), after etching (m2), and after dissolving the porous layer with a 0.1M basic solution of KOH in water and rinsed with ethanol (m3). The following equation was used to determine the porosity of the freshly etched porous silicon filters[170]:

$$\text{Porosity} = (m_1 - m_2) / (m_1 - m_3) \quad (7.1)$$

Scanning Electron Microscopy

To calibrate the etch rate of the fabrication process to the etching current density, SEM cross sections of samples were examined. Porous silicon layer thickness was determined by cutting and imaging cross sections with an FEI XL30 SFEG SEM in ultra high resolution mode with through lens detector (TLD) at 10kV without prior metal sputtering of the sample.

Reflectance Spectra

Reflectance spectra of the samples in the visible region were taken across 345-1045nm with a CCD spectrometer (Ocean Optics USB4000) and a tungsten-halogen light source (Ocean Optics LS-1) connected with a Y-branch bifurcated optical fiber. The common end of the bifurcated fiber was focused with an objective lens to a $2mm^2$ spot size and positioned normal to the porous silicon sample surface. A silver mirror (Thorlabs) at the same height as the filter chip surface was used as a reflectivity reference.

7.3.3 Digital Difference Imaging

Dye swatches were prepared by impregnating borosilicate glass fiber filter paper (Whatman) with aqueous solutions of sensitized (DPA-bound) and desensitized dyes. Terbium(III) nitrate hexahydrate, and Europium(III) nitrate pentahydrate were purchased from Aldrich. DPA (2,6-Pyridinedicarboxylic acid) was used as a chelating fluorescence sensitizer (Aldrich). The broad-spectrum dye, used in experiments to

separate two similar-color dyes, was the Ruthenium coordination compound $[Ru(bipy)_3]^{2+}$, obtained as the salt tris(2,2′-bipyridyl) dichlororuthenium(II) (Aldrich). Impregnated filter papers were cut and positioned below a cubic beam splitter at a 20cm working distance, with the optical path in the beam splitter reflecting off of the porous Si filter surface (Figure 7.14). The swatches were illuminated with two ultraviolet light sources (365 and 254nm, UVP UVGL-25). Color channel filtering was performed with a color camera (Canon Rebel Xti) while imaging for separating similar-color dyes was performed with a monochrome USB camera sensor (Point Grey Chameleon).

7.4 Results and Discussion

7.4.1 Tailoring Porous Si Optical Properties to Match Spectra of Target Fluorescent Dyes

A simple single-period, sine current density-time etching waveform yields an optical spectrum with a single principal reflectance peak. In the first section below, the wavelength, reflectivity (relative height), and width of the peak are tailored by adjusting the parameters of the sine waveform, with multiple spectral features created by mixing multiple waveforms into a “composite” etch. The result of this approach is first discussed with respect to a target dye with two overlapping spectral peaks, and then applied to several other target dyes. Following this, a second approach to creating custom spectral features took a dye-matching filter design, which was provided from optical modeling, and converted it into an etching waveform, with the result assessed.

7.4.1.1 Decomposition and Refinement Approach

The goal of this approach is to tune the spectral bands of the porous Si filters to match those of target dyes. The overall strategy can be broken into the following parts:

1. If the target spectrum contains overlapping peaks, decompose the spectrum into separate peaks. For spectrally separate peaks, or for individual peaks decomposed from overlapping peaks, the conditions for matching porous Si spectral bands to each individual peak are first determined before combining the etching waveforms into a single composite waveform (step 3).
2. For each single peak in the decomposed spectrum, etch and adjust the sine wave parameters to tune the rugate band as desired. The peak wavelength is tuned by changing the period of the sine wave, the reflectivity or relative height is tuned by adjusting the current density range of the etch wave, and the width of the spectral band is tuned by chirping the etch wave over a narrow range of etchwave periods.
3. Combine each individual waveform by superposition and etch the resulting composite wave.

This process is referred to here as a refinement strategy, since step 2 above involves progressively refining etching parameters until a desired result is achieved. An advantage of this approach is that control of the rugate stop band wavelength and reflectivity have been widely successful[33, 223], as has the fabrication of multiple rugate peaks by the superposition of sine waves with different frequencies[8, 33].

All current-time waveforms applied to the electrochemical etches in this chapter can be described by the following equations:

$$I\,(t) = \frac{\sum_{i=1}^{n} I_i}{n} \tag{7.2}$$

$$I_i(t) = \left[\sin\left(\frac{2\pi t}{q\; p_i(t)}\right) + 1\right]\left[\frac{I_{max_i} - I_{min_i}}{2}\right] + I_{min_i} \tag{7.3}$$

where q is the number of points per second in the etch, typically 1000, and I_{min} and I_{max} are the minimum and maximum currents of the sine waveform. P(t) is the period of the waveform. Typically, p(t) is a constant, but as discussed below p(t) is not constant for chirped etches that aim to broaden the spectral reflectivity band. For rugate filters with a single reflectivity peak, n=1. Multiple peak "composite" filters are etched by combining individual components into one waveform, according to equation (7.2), with n>1. The current-time etchwave profile applied during electrochemical etching results in a corresponding porosity-depth profile in the filter layer. The porosity-depth profile, in turn, corresponds to the refractive index-depth profile of the layer, with the approximately linear relationship between porosity and refractive index commonly described by the Bruggeman effective medium approximation (see Appendix A.4).

Spectral peak position from sine period

The current-time profile defined in equation (7.3) results in a corresponding periodic variation of the refractive index profile with depth, expressed as[8, 33]:

$$n(z) = n_{avg} + \frac{\Delta n_{avg}}{2}\sin\left(\frac{4\pi n_{avg} z}{\lambda_0}\right) = n_{avg} + \frac{\Delta n}{2}\sin\left(\frac{2\pi z}{d}\right) \tag{7.4}$$

where n_{avg} is the average refractive index of the filter, $n_{avg}z$ the optical path, Δn the variation in refractive index in the undulating layers, λ_0 the resonance peak wavelength

of the rugate, and d the spatial period of the index modulation, which is the physical thickness of one period.

The central wavelength of the resonance peak is therefore approximated as[33]:

$$\lambda_0 = 2n_{avg}d \tag{7.5}$$

Thus, changing the spatial period of the modulation by changing the temporal period of the etching wave will shift the spectral band wavelength. For a sine etching profile, the resulting refractive index-depth profile is not truly sinusoidal due to the increase of the etching rate with current density, which results in a high-current bias to the profile[212]. Given a consistent bias, however, calibration of the rugate spectral band position to the period of the current-time etch waveform is highly linear, as is the case for filter made with different etching wave periods but the same high and low current densities of the sine etchwave. Figure 7.1 displays a calibration of the wavelength of the rugate peak to the etching waveform period p(t) of rugate filters made with the same high and low current densities in the sine etchwave (12.5 and 62.5 mA/cm^2). The relationship shows excellent linearity.

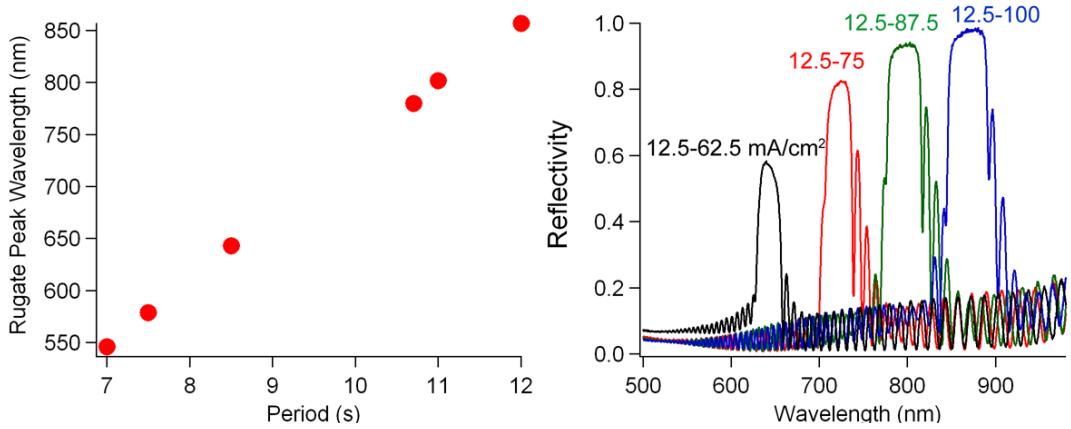

Figure 7.1 Tuning the wavelength and reflectivity of the rugate stop band. **Left:** change in spectral peak position as a function of the current-time etch waveform sine period for a 12.5-62.5 mA/cm^2 waveform. **Right:** Adjusting the reflectivity of the rugate band by changing the index contrast, determined by the minimum and maximum etchwave current densities, for an 8.5s period.

Reflectivity from index contrast

Target spectral features often involve multiple spectral peaks with different relative intensities. To change the relative height of the porous Si reflectivity peak, the index contrast is adjusted by changing the current density range of each sine wave component. The reflectivity of a rugate etch is closely approximated by the reflectivity of a multilayer Bragg stack[72, 272], where:

$$R = \left[\frac{n_{air}(n_1)^{2N} - n_{Si}(n_2)^{2N}}{n_{air}(n_1)^{2N} + n_{Si}(n_2)^{2N}}\right]^2 \quad (7.6)$$

The variable R is the reflectivity, N is the number of Bragg double layer cycles (here, rugate cycles), and n_1 and n_2 are the high and low refractive indices of the rugate cycles corresponding to the high and low current densities of the sine etching waveform. Thus, greater differences between n_1 and n_2, corresponding to a greater current density contrast, result in higher reflectivity. The right panel of Figure 7.1 demonstrates this effect. Each etch consisted of 90 cycles of a sine wave with a period of 8.5sec. Holding I_{min} constant and increasing I_{max} yielded a higher reflectivity of the spectral band.

The spectrum of the first target dye to match in this chapter is displayed in Figure 7.2, as well as the decomposed singular peaks of the multi-peak dye. The deconstructed spectrum contains a spectral peak at 867nm and second, broad peak at 809nm. The lower three plots are reflectivity spectra of three porous Si filters. Each consisted of a composite etch waveform with n=2, with an average etch current

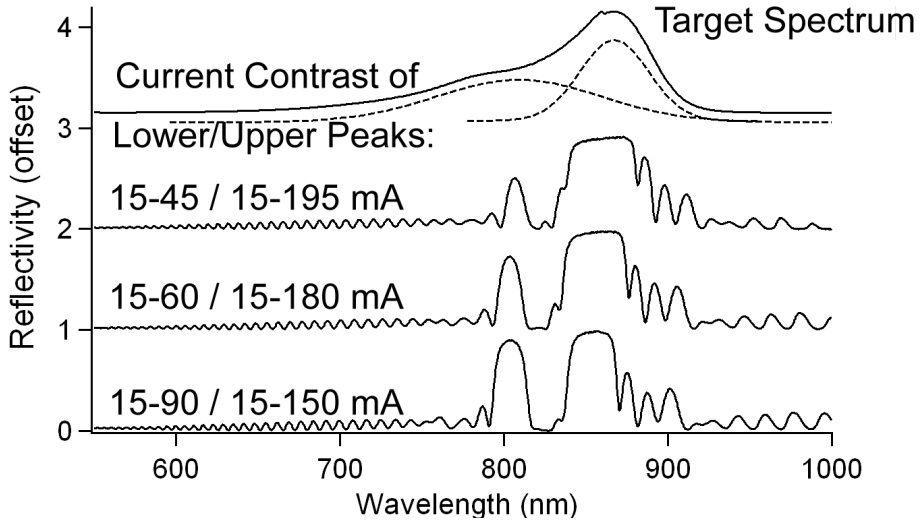

Figure 7.2 Matching the porous Si rugate band to a target dye's fluorescence spectrum (top plot) using a composite wave formed from the superposition of two sine waves with different periods and current ranges. The top plot shows a decomposition of the spectrum into two target rugate peaks to be matched by the porous Si (dotted lines). The three porous Si spectra below the target dye show the results of adjusting the rugate peak height by changing its etch current amplitude.

variation of 15-120 mA (12.5-100 mA/cm^2). The relative etch current ranges, and resulting index contrasts, are progressively adjusted for each component shown in the figure. The increase in reflectivity of the lower wavelength peak, as its etch current range is increased from 15-45mA to 15-90mA, is clearly seen.

Although altering the period and etch current range of the etching waveform resulted in a filter that approximated the peak positions and relative heights of the two spectral components of the target dye, the lower peak must be additionally broadened to match the target spectrum.

Peak broadening by chirping

If the spectral peak position of a rugate stop band is not important, wider spectral bands are easily achieved by increasing the sine wave period to produce spectral bands at higher wavelengths, which exhibit wider peaks. The stop band width $\Delta\lambda$ can be expressed a:[10, 89]

$$\frac{\Delta\lambda}{\lambda_0} = \frac{\Delta n}{2n_{avg}} \tag{7.7}$$

where the rugate band is centered at λ_0. Since the variation in refractive index Δn and average refractive index n_{avg} of the layer are determined by the low and high etch currents and do not change with period, higher periods that result in higher wavelength (λ_0) stop bands result in a commensurate increase in the stop band width $\Delta\lambda$.

For matching spectral features at fixed wavelengths, however, a different approach is required. Waveform chirping consists of combining multiple etch waveforms with closely spaced frequencies into a single current-time etch waveform. Two approaches to waveform chirping are explored below. The first consists of combining many individual waveforms with closely spaced periods into one composite waveform, such that n>>1 in equation 7.2 and each waveform of the superposition has a constant period over the duration of the etch: period(time) = constant. In contrast to this "composite" chirping approach, the second method combines many individual waveforms with closely spaced periods by serial concatenation. Thus, n=1 in equation 7.2 but p(t) is not constant in equation 7.3. For many discrete periods, p(x) is a step function. When the number of steps approaches infinity, p(t) is a continuous function.

The form of various continuous functions of the period over the course of the etch, p(t), influences the spectral characteristics[10].

7.4.1.2 Results of Refinement-Based Approach

In Figure 7.2, porous Si was tuned to match the target spectrum through adjustments to the sine component periods and etch current ranges of the current-time etching waveform. The lower wavelength peak of the porous Si filter, however, was not as wide as the broad secondary peak of the target spectrum. The following approaches aim to broaden this lower peak at 809nm by chirping the etching waveform.

Composite Chirping

As mentioned, composite chirping consists of combining multiple sine wave components over a small period range into a single composite current-time waveform, producing one broadened reflectivity band as depicted in Figure 7.3. Superposition of many closely spaced narrow stop bands is expected to result in a single broad band. Figure 7.4 displays a few results of this approach to broadening the target dye peak at 809nm. For all etches, ΔI=112.5 mA/cm^2 and I_{min} =12.5 mA/cm^2. The top plot displays a chirped wave and its spectral result, made from n=11 sine components with periods from 7.9-8.1sec at increments of 0.2sec. The middle plots display the waveform and spectrum a chirped wave with n=21 components from 7.8-8.0sec in steps of 0.01sec. For comparison, a single period, n=1 rugate filter made with a sine period of p=8.0sec is displayed in the bottom row with its resulting reflectance

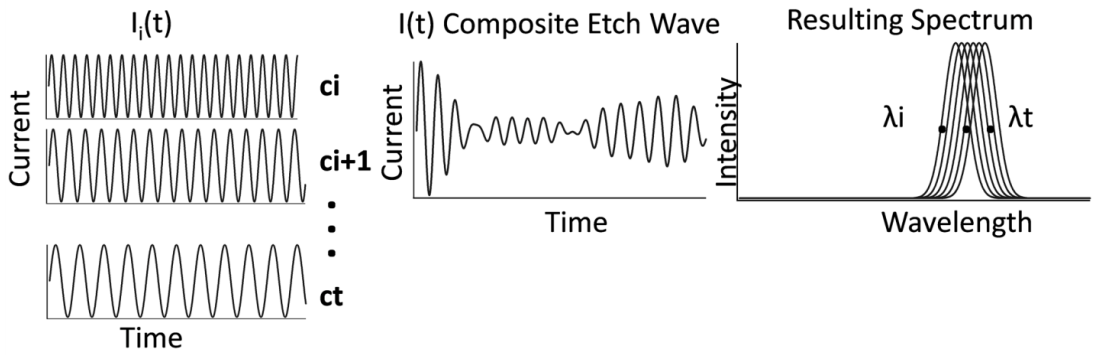

Figure 7.3 Depiction of a chirping with a composite etch wave. Individual waves with different frequencies are combined by superposition into one current-time waveform that is etched into the silicon, resulting in spectral peaks corresponding to each frequency. Closely spaced frequencies will result in closely spaced peaks such that the optical spectrum exhibits one broad region of reflectance.

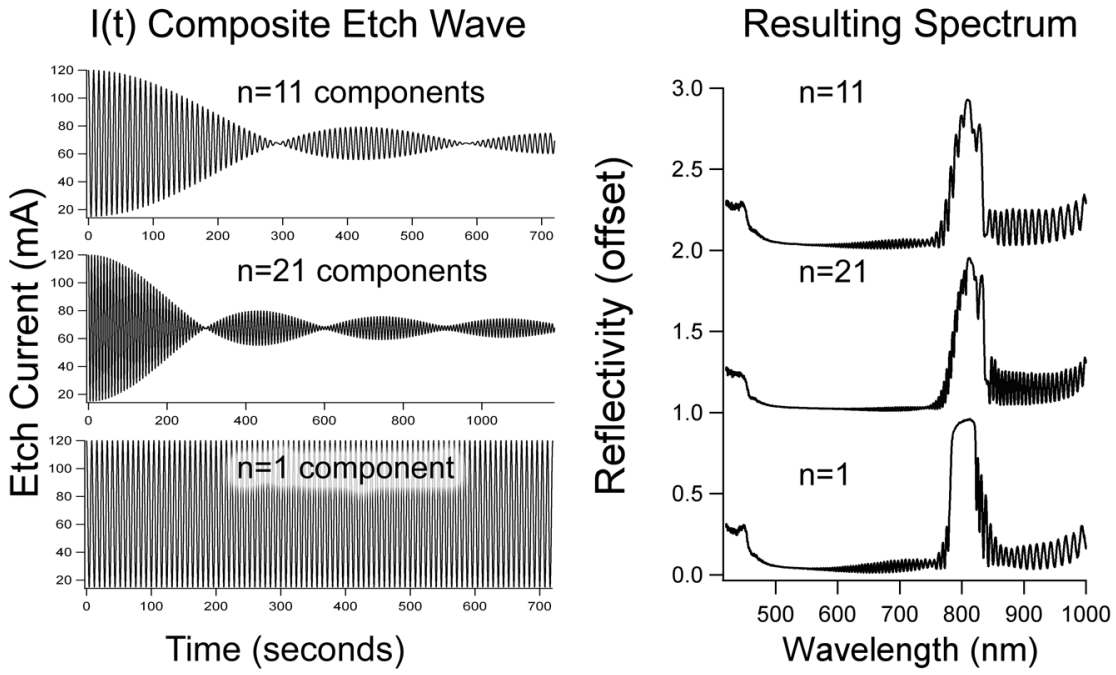

Figure 7.4 Composite waveform chirping of the current-time etch waves (left) and the resulting reflectivity spectra of etched porous Si (right). **Top:** 11 periods were superimposed over a 0.2s period range of the sine etchwave. **Middle:** 21 periods were combined over a 0.2s period range. **Bottom:** a single-period etchwave was utilized. The composite-wave chirping increased the width of the rugate band slightly, but at the cost of significantly increased interfacial reflections

spectrum. Composite waveform chirping resulted in spectral peaks broadened by 10-20nm, but displayed significantly increased interference fringes due to light reflecting off of the top and bottom interfaces of the filter layer[72].

Serial chirping

The serial addition of sine waves with different frequencies[33] was next used to chirp the current-time etch waveform and broaden the porous silicon reflectance peak designed at 809nm.Figure 7.5 depicts two types of serial chirping. The top row of the figure depicts a sine current-time etch waveform with a constant, single period p(t), resulting in single spectral band for comparison. "Discrete" serial chirping concatenates waves of different frequencies into one current-time etch profile. Since each segment of the concatenation has a different period, p(t) is step function. For closely spaced periods, closely spaced spectral peaks are expected to overlap such that a single, broad peak is observed, analogous to the composite method of combining components with closely spaced periods. Serial chirping may also be continuous, with p(t) expressed as a function, as shown for p(t) equal to a linear function in the bottom row of Figure 7.5.

Several period ranges, step sizes, and orders of the layers with different periods were examined, with an example shown in Figure 7.6. In this figure, the result of chirping using a single (n=1) etching wave made of three serially combined frequency segments is compared to a chirped etch with a linear p(t) profile. The reflectivity spectrum of each is also compared to the spectrum of a constant-period, unchirped etch. For all etches, ΔI=112.5 mA/cm^2 and I_{min} =12.5 mA/cm^2, etched for 120 repeats

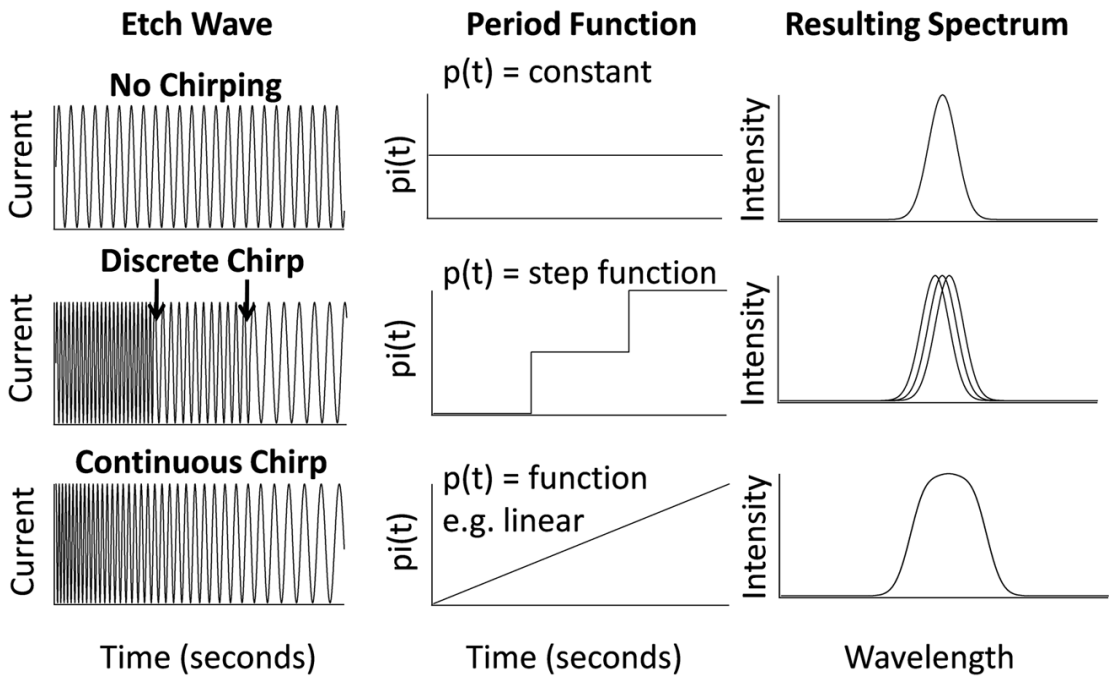

Figure 7.5 Chirping rugate peaks by serial addition of sine waves with different frequencies. **Top:** etchwave with a single, constant period. **Middle:** Discretely chirping the etchwave by serial addition of waves with different periods. **Bottom:** Continuously chirping the etchwave by changing the frequency of the wave over the course of the etch. The period of the etching wave over time can be a simple linear function, shown above, or any other continuous function.

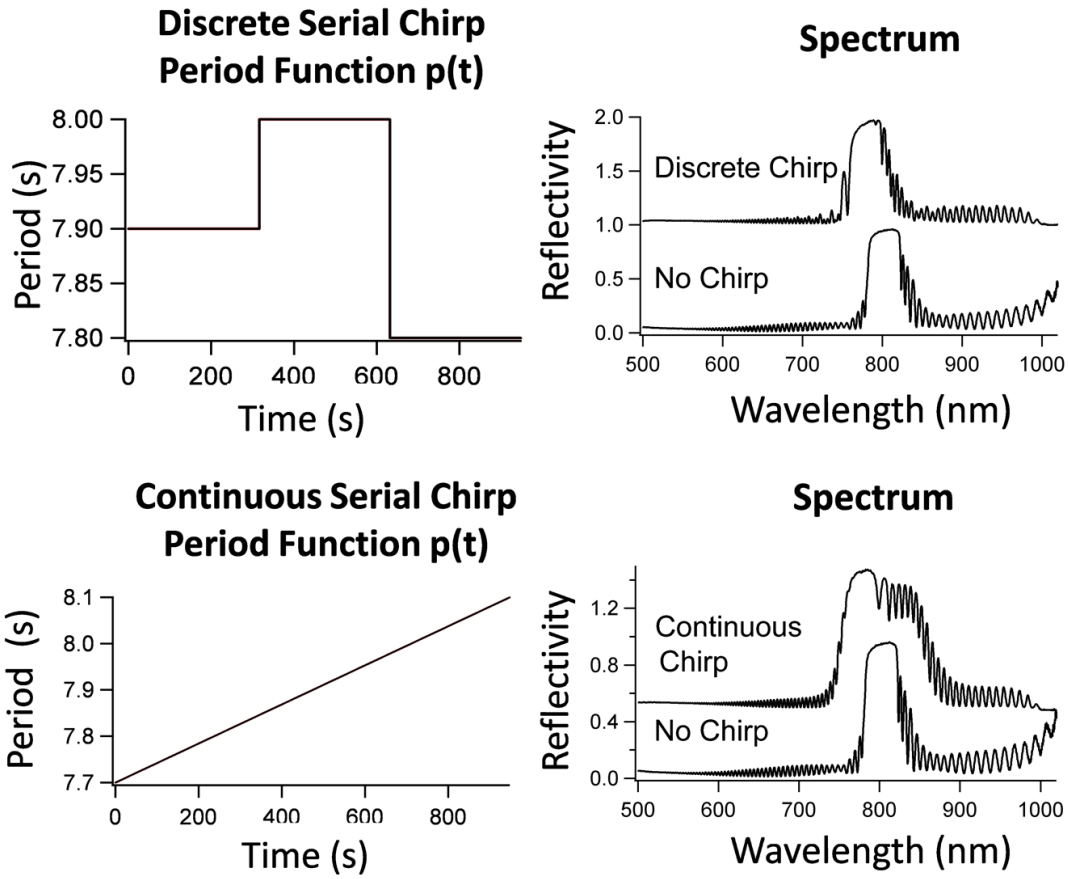

Figure 7.6 Result of a discretely chirped etching waveform compared to a continuously chirped waveform. The discrete chirp (top) consisted of three waves closely spaced in frequency and concatenated together. The continuous chirp used a linearly increasing period function over time. The resulting spectra are shown at right and compared to a single-period etch at the average frequency (7.9s). All etch times were 711s (90 sine cycles for 7.9s period).

of the average period. The unchirped etch, shown for comparison, had a period of 8.0s. The serially chirped, discrete-segment etch had etch waveform segments of 7.9, 8.0, and 7.8sec. The serially chirped etch with the linearly increasing period had a p(t) that ranged from a p_{min} of 7.7 to a p_{max} or 8.1, with the change in the period over time taking the form:

$$p_i(t) = p_{min_i} + \frac{(p_{max_i} - p_{min_i})}{j} t \tag{7.8}$$

where j was the total number of points in etch .

Chirping with continuous, linearly increasing p(t) profile clearly broadened the rugate peak, increasing the width by ~40nm. Each sine component of a multi-peak, composite waveform optical filter takes the form:

$$I_i(t) = \left[\sin\left(\frac{2\pi t}{q\, p_i(t)}\right) + 1\right]\left[\frac{I_{max_i} - I_{min_i}}{2}\right] + I_{min_i} \tag{7.9}$$

as described before. The change in the period over time for each component, $p_i(t)$, can have its own function form, such as a sine or linear function. In Figure 7.7, a single I(t) component with different p(t) functions is examined to assess the chirping of the resulting optical reflectivity peak. These etches with various p(t) profiles used the same parameters of etch current range and average etch current as those shown in Figures 7.5 and 7.6. The parameter (b) in these period functions is the total number of rugate cycles in the etch, which is determined by the average period (total etch time / period = number of cycles). The (b) parameter is used to modulate the number of cycles of the period function p(t) over the course of the etch for a p(t) that takes the form of a sine wave. Quarter-sine and linearly increasing period profiles yielded the best spectral

results, with widened peaks that exhibited lower interference fringing than other profiles. Cyclically varying the period over the duration of the etch resulted in strong interference fringing in the spectrum. This may be due to the introduction of additional interfaces with depth as the period is varied.

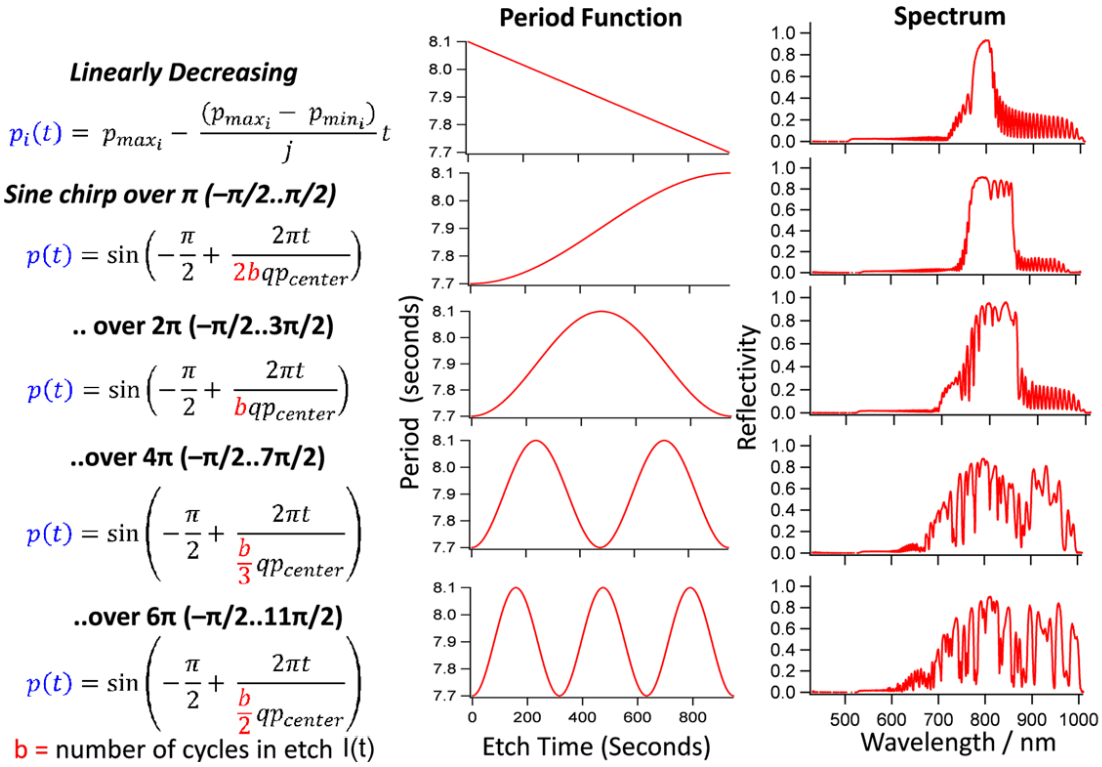

Figure 7.7 Continuously chirped etching waveforms with various period-time functions (left and middle columns) used in a the current-time waveform I(t), and their spectral results (right column). Here, p_{max} and p_{min} are the maximum and minimum periods of period-time function, in seconds. Linear and quarter sine waveforms yield the least interference fringing surrounding the rugate stop band. The function p(t) is the period component of the current-time etch wave I(t)=sin(2πt/p(t)).

Overall results

The result of the refinement process for matching porous Si to the spectrum of the dye with two overlapping emission peaks, discussed above, is shown in Figure 7.8. A single-peak, chirped etchwave (second plot, under the target spectrum) is compared to several double peak, composite waveforms, including composite waveforms that incorporate continuous chirping into one of the peak's component etchwave. All etches utilized an average etch current density range of ΔI=112.5 mA/cm^2 and I_{min} =12.5 mA/cm^2, etched for 120 repeats of the average period. The two double-peak etches utilized differing etch current density range contrasts to adjust the relative reflectivity of the lower wavelength peak. In the figure, the 2-peak composite, linearly increasing chirp shows an example of a combination of composite etching, etch current range contrasting, period tuning, and continuous chirping of the lower peak component. The result matches the general shape of the target dye spectrum, but interference fringes present a significant source of discrepancy between the target and etched filter spectra.

Other dyes with narrower peak features were better matched through the refinement approach. The left panel of Figure 7.9 display a target dye with two spectrally separate peaks of differing intensities, with peaks at 738 and 870nm. A double peak, composite waveform with n=2 components is shown at the bottom of the panel (Figure 7.9, left). Each component of the etching waveform had a separate period and etch current range, with the upper wavelength peak additionally chirped using a linearly increasing period profile. Spectra of intermediate steps in the refinement process are shown in the middle rows of the plot,

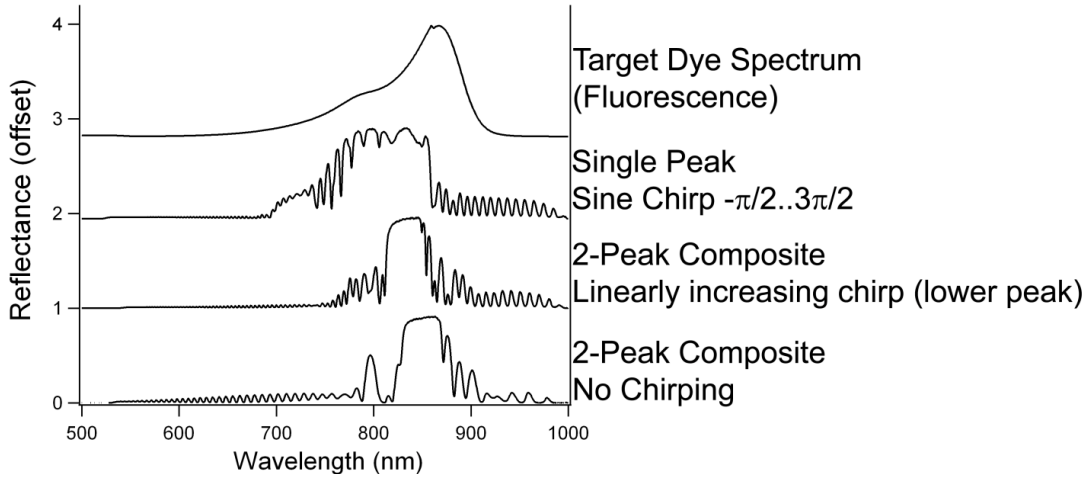

Figure 7.8 Incorporating peak chirping into matching the porous Si double rugate band to a target dye's fluorescence spectrum (top plot). **Second row:** a single-period rugate tuned to the lower peak of the dye and chirped to broaden. **Third row:** a two-component composite rugate to match both of the dye peaks, with the lower peak continuously serially chirped with a linearly increasing period. **Bottom row:** a two-component composite to match both dye peaks, with the lower peak component a single period waveform with no chirping, and with the two peak heights adjusted by index contrast.

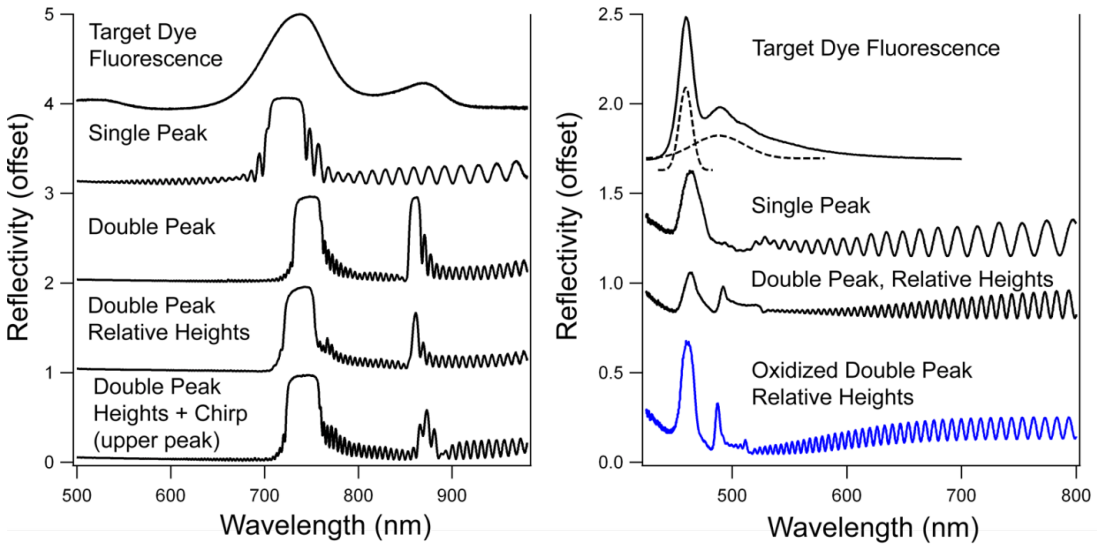

Figure 7.9 Several other target dyes were matched. **Left:** A dye with two spectrally separate peaks was best matched with a two-component composite waveform with index contrast controlling relative peak heights and the upper (higher nm) peak component continuously serially chirped to broaden. **Right:** A dye with two overlapping peaks decomposed into two components (dotted lines). A two-component composite etchwave with the index contrast of each component adjusted to match relative peak heights (third row) had low reflectivity. An oxidized rugate filter made using the same methodology showed significantly increased reflectivity (bottom row) due to decreased absorption of light from the porous layer.

which display (from top to bottom) a single-period, single peak etch, a double peak etch with no etch current range contrast, and a double peak etch with the relative peak heights adjusted through the etch current contrasts of the component sine waveforms.

The right panel of Figure 7.9 displays spectra of porous Si filters fabricated to match a double peak, spectrally overlapping dye with low wavelength peaks at 460 and 490nm. The reflection spectrum of an initial single-period, single peak porous silicon filter is shown below the target spectrum for comparison. Below this, a composite (n=2) waveform with tuned spectral peak positions and with tuned relative peak heights is displayed, showing good agreement with the target dye features but a low reflectivity. Poorly reflective filters are undesirable since they limit their application to filtered imaging. The poor reflectivity is due to the rise in absorbance with decreasing wavelength in freshly prepared porous silicon[218]. Oxidizing the porous layer converts porous silicon to porous silica, with a very low absorption coefficient at low wavelengths. The bottom plot in the right column of Figure 7.9 displays a spectral filter that was thermally oxidized at 800° C for 1 hour. Oxidation decreases the refractive index of the filter, blue shifting the rugate spectral band. For a fixed temperature and time of oxidation this shift is consistent. The refinement method therefore incorporated this oxidation offset into the design of the spectral peaks, as well as the adjustment of the higher wavelength peak's reflectivity as described. The oxidized filter design exhibits over twice the reflectivity of the freshly prepared porous silicon filter.

In summary, the refinement method yielded mixed results in matching porous silicon to the spectra of target dyes. While adjusting the wavelength of the spectral

peaks and their reflectivity worked as expected, widening spectral bands by chirping the etch waveforms showed mixed success, with the best chirping waveforms employing a continuous linearly increasing or quarter-sine increasing period-time profile. Target feature spectral position and relative reflectivity were successfully matched, but distortions due to interfacial interference fringes were greatly exacerbated with chirped profiles. At low visible (near-UV) wavelengths, oxidized filters proved several times more reflective than freshly prepared layers.

7.4.1.3 Optical Design Approach

The iterative process of matching porous Si reflectance to a target spectrum by etching and refinement must be performed for each new dye or desired spectral feature. A more encompassing approach utilizes optical models to design a porosity-depth or refractive index-depth profile that is expected to yield an optical layer with the desired spectral reflectance characteristics. This optical modeling, which typically involves applying Fourier transform techniques to a target spectrum, has been utilized with other materials and fabrication processed to design refractive index profiles that exhibit desired rugate stop band characteristics[268, 273] and to fabricate antireflection coatings with tailored optical features, including stop bands with desired widths, heights, and spectral positions[266, 267]. However, little work has been published applying the profiles designed by this approach to porous silicon filters. Here, a porosity-depth profile was provided that was designed to match the fluorescent dye in the right column of Figure 7.9 with a 25um porous silicon layer. The porosity-depth profile was then converted to an etch current-time profile through a set of calibrations. The advantage of this

approach is that a single set of calibrations should allow for any arbitrary spectral design to be implemented, in contrast to the tuning necessary for each new design made by the refinement method.

To convert the porosity-depth profile to an etch current-time profile, two calibrations are necessary, pictured in Figure 7.10. First, the porosity was calibrated to the etch current density by gravimetrically (equation 7.1) measuring a series of thin film (<10um) etches at constant current densities, ranging from 12.5-500 mA/cm^2. As shown in Figure 7.10, this calibration profile was fit with a power function, yielding the relationship: current density = $(\text{porosity-A})^{1/q}/B$, where A, B, and q are constants of the power function fit. Each porosity in the porosity-depth waveform was then mapped to the corresponding current density using this relationship. Second, the depth of the porosity-depth profile was converted to the time in the etch by fabricating a series of thin layer porous silicon layers at various constant current densities. The cross sectional thickness of each was measured by SEM. The etch rate (nm/sec) is then given by: etch rate = layer thickness / etch time. The relationship between the etch rate and the current density is shown in the lower left panel of Figure 7.10, and was linearly fit to generate a function relating etch rate to etch current. The temporal spacing between each point in the porosity-depth profile was then converted to a time wave by: $\Delta\text{time} = \Delta\text{depth}/\text{etch rate}$ (sec/nm * nm) for each point in the depth profile, so that the temporal spacing of the etch current-time wave differed for each point based on the current density at that point.

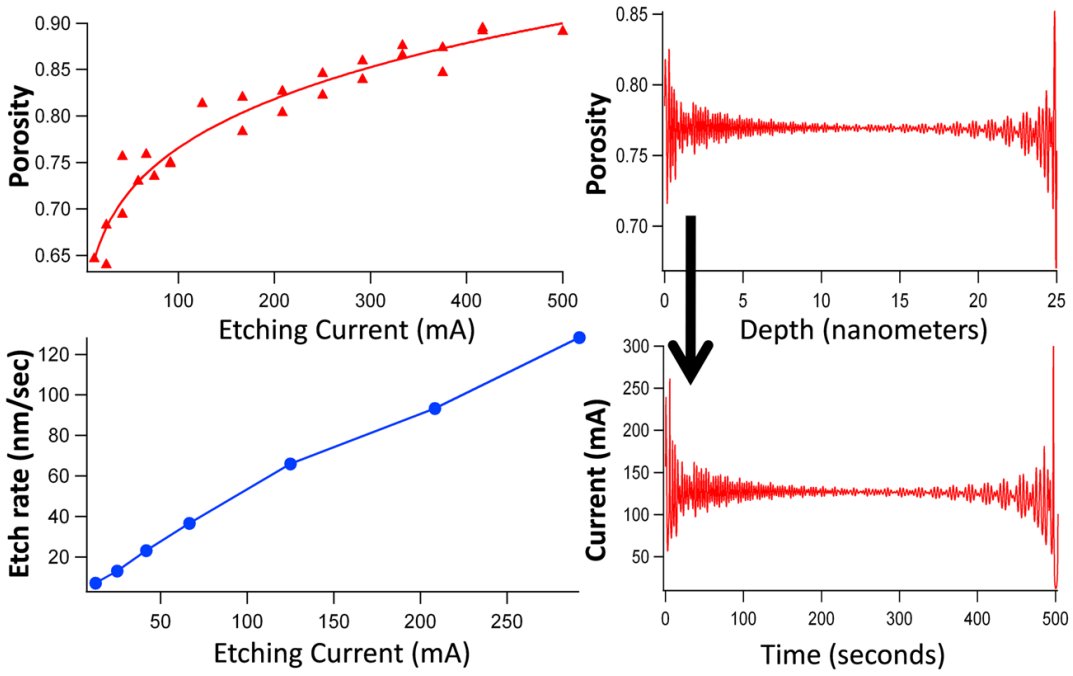

Figure 7.10 Left: the porous Si porosity (top) and etching rate (bottom) were calibrated to the etching current for 1.2cm^2 etches. **Right:** A porosity-depth waveform was designed for a rugate filter to match a target dye spectrum. The calibrations at left allowed translation of this porosity-depth profile to a current-time waveform that was applied during electrochemical etching.

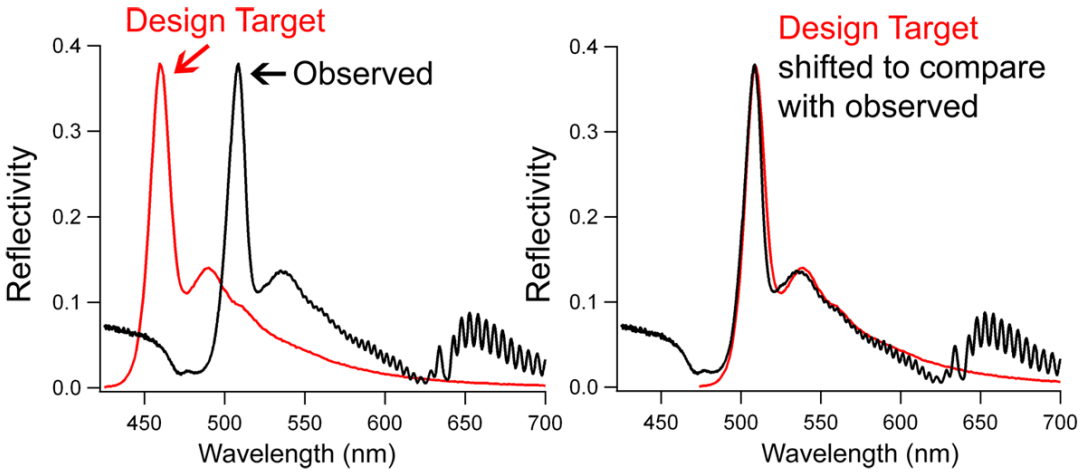

Figure 7.11 Left: the result of the designed waveform (Figure 7.10) etched into porous Si, comparing the target dye fluorescence spectrum to the observed reflectivity spectrum. **Right:** translating the wavelength of the target spectrum to align with the observed peak shows excellent matching of the secondary peak and the width of the spectral features.

The resulting etch current-time profile was electrochemically etched, with the resulting reflectance spectrum shown in Figure 7.11. Both calibration sets of etches, as well as the current-time etch from the design, were performed on silicon chips from the same 4" silicon wafer to promote uniformity of the material used. The principal peak was significantly red-shifted from the design target, but translation of either spectrum such that the principal peaks shows excellent matching of the secondary peak and shoulders between the porous Si filter reflectance spectrum and target spectrum.

Lowering the period of a single-period sine etchwave decreases the spatial variation of the refractive index with depth, blue-shifting the rugate stop band since the wavelength of the rugate peak scales with the spatial period (equation 7.5). This contraction of the sine cycle pitch is a simple means of blue shifting the spectral band. Figure 7.12 shows etches, created using the current-time etch waveform based on the optical model, that were time (pitch) contracted by reducing the x-axis timescale data of the etching wave by 5, 11, and 15% for respective samples. A 15% timescale contraction of the current-time waveform, where the source waveform was the same as that discussed above, yields an optical reflectivity curve with a peak at the same spectral wavelength as that in the target design. The height of the secondary peak and shape of the peak shoulders is distorted, however. Scaling the porosity of the current-time etchwave to align the etched spectral peak with the target peak similarly results in distortion of the lower amplitude secondary peak.

The wavelength offset between the target design and the reflectivity spectrum of the filter etched with the current-time waveform derived from optical modeling can be attributed to several sources of error. Measuring porosity gravimetrically had a +/-

2% variation for samples etched under identical conditions. This variation is large relative to the calibration range of the porosity, from 65-90%, and influences on the functional form used to fit the porosity-current density relationship could lead to significant error in translating a porosity profile to a current density profile. The calibration of the etch rate to the current density also exhibits variation, though layer thicknesses are generally resolved to within several nanometers by SEM (<1% of the total layer thickness) and the overall variation is smaller than that of the porosity. The effective medium model, dielectric function, and methods employed in creating a porosity-depth profile from a target spectrum all present potential sources of error. Here, the porosity-depth profile was provided. Process control is another major factor impacting the etches, with factors like the compression of the o-ring in the etching cell affecting the effective etch area available for etching, altering the actual current density of the etch. Figure 7.13 displays five etches of the current-time etch waveform produced by optical methods, described above. The etches were performed over two hours, and exhibit a standard deviation of only 0.86 nm. Several etches, however, exhibit deviations in spectral shape above 500nm, showing the process variability of the rugate filter designs. The lack of temperature control during etching is also of particular importance. Temperature variations are known to significantly influence etch rate and porosity[12]. Variations over the course of the calibrations, which were performed over several days, increases the error in the data. Importantly, etching a current-time waveform that is designed to match a target spectrum at a temperature significantly different than that of the calibrations used in the design could lead to significant offsets.

In summary, the optical design-based method can in theory, once calibration of porosity and etch rate to the current density is performed, be used to rapidly create a spectral design. In practice, the optical spectrum of the etched design was offset in wavelength from the target spectrum. This offset can be compensated for by contracting the x-scale pitch (timescale) of the current-time etchwave, but at the cost of deviation of the reflectivity profile away from the principal spectral peak. The refinement method requires more work to be performed for each desired spectrum to match, but yielded rapid approximate matching of target spectra.

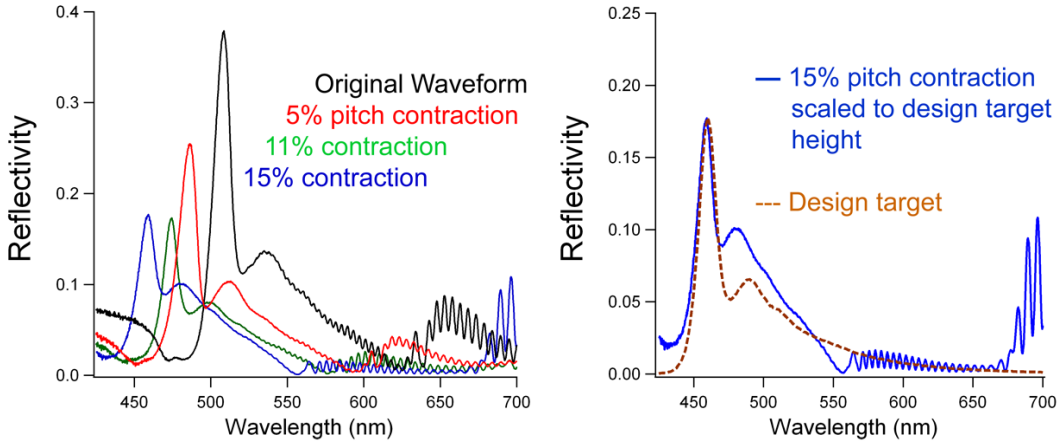

Figure 7.12 Left: Spectra of time-contractions of the current-time etching waveform (pitch contraction) compared to the reflectivity of the porous Si with no time-scale contraction. **Right:** a 15% time contraction of the etching waveform timescale resulted in alignment of the principal dye peak to the target spectrum at 460nm. However, the secondary peak height and location is distorted.

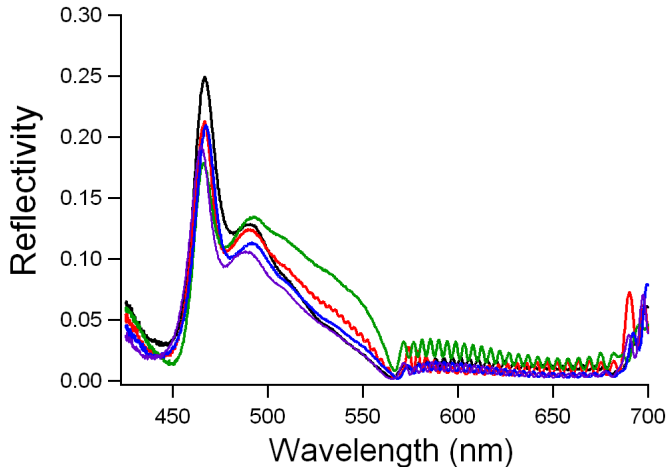

Figure 7.13 The unaltered current-time waveform (Figures 7.10, 7.11) with no timescale contraction was repeatedly etched into porous Si to assess repeatability of the spectral result. Each trace corresponds to a separate porous Si etch of the same waveform. The porous layer was removed by dissolution with 0.1M KOH before the next etch.

7.4.2 Imaging of Dipicolinate-Bound Fluorophores with Tailored Optical Correlation Filters

The refinement approach was applied to fabricating porous Si filters with spectral bands matching the fluorescence spectral peaks of $[Tb(DPA)_3]^{3-}$ and $[Eu(DPA)_3]^{3-}$. First, these two spectrally separate dyes were distinguished by imaging dye-containing filter paper swatches with their respective dye-matched porous silicon filters. The $[Eu(DPA)_3]^{3-}$ swatch was then imaged next to that of a broadband dye that appears a similar red color to the human eye, $[Ru(Bipy)_3]^{2+}$. By exposing the Eu-matched filter to ethanol vapor, images of the filter on and off-resonance with the Europium emission peaks were taken and subtracted from each other, leaving a difference image with only areas of the Europium dye exhibiting a strong intensity.

For both of these imaging experiments, the optical system was configured as shown in Figure 7.14. Glass fiber swatches impregnated with dried aqueous solutions of the dyes were illuminated with two ultraviolet light sources in the short and long UV. Each porous silicon filter was mounted flush to one side of a cubic beam splitter, so that the image of the dye swatches was reflected off of the porous filter before reaching a digital camera. Porous glass filter paper was utilized because of its low UV photoluminescence compared to cellulose paper products, and both imaging experiments also included a dye-free porous glass swatch for a background comparison.

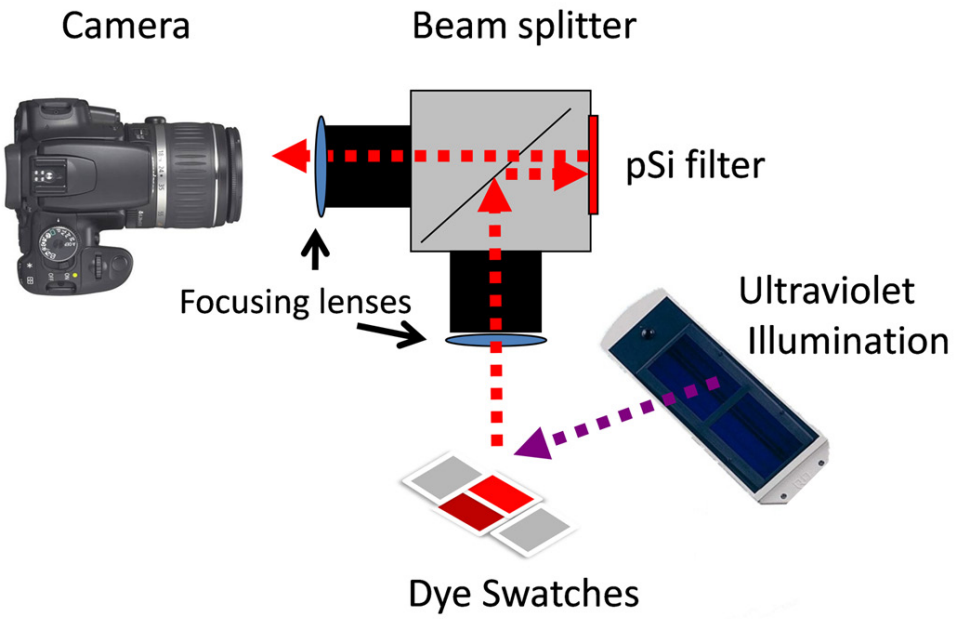

Figure 7.14 Schematic of the imaging setup. The porous Si filter with a reflectance spectrum matched to fluorescence spectrum of one of the dyes was mounted in a cubic beam splitter and used in reflectance mode to optically filter images of the UV-irradiated filter paper swatches impregnated with dyes.

7.4.2.1 Distinguishing Fluorophores in Separate Color Channels with Porous Si Filters

Fabricating porous Si filters to match the Eu and Tb emission spectra posed specific challenges for the digital imaging application. Since the intensity of the reflected light in the image depends on the spectral matching of the rugate porous Si peak to the dye's fluorescence peak, spatial uniformity of the optical filter is necessary. The spectral uniformity of the electrochemical etch deviates spatially, with the greatest deviation at the edges of the round porous Si filters due to physical blocking and shadowing of the electrical field in the etch by the o-ring seal, as well as other effects[31]. To allow for a greater planar surface area to be imaged, the etch cell area was increased from 1.2cm^2 to 5.1cm^2.

The $[Tb(DPA)_3]^{3-}$ fluorescence peak at 545nm was matched by designing a porous silicon reflectance spectrum with a sine current-time etch waveform of ΔI = 91.7 mA/cm^2, I_{min} = 45.8 mA/cm^2, p=3.36, and n=1 in equations (7.2) and (7.3) above. The waveform was applied for 300 cycles to better suppress interference fringes that arise from light reflecting off of the top and bottom interfaces of the layer. The resulting spectrum is shown in Figure 7.15. Three dye swatches were illuminated with a fixed ultraviolet light source and imaged: one impregnated with $[Tb(DPA)_3]^{3-}$, one impregnated with $[Eu(DPA)_3]^{3-}$, and a third containing no dye or dipicolinate. Images taken by reflecting the optical path off of the Tb-matched porous Si filter result in a strong intensity of the Tb swatch compared to the Eu and blank swatches, as shown in Figure 7.15. For comparison, an image of the same swatch configuration reflected off of a polished silicon mirror showed no apparent selectivity for the Tb swatch area.

Two spectral peaks of the $[Eu(DPA)_3]^{3-}$ luminescence spectrum at 594 and 616nm were matched by a separate porous Si filter, as shown in Figure 7.16. A composite etch wave with n=2 (equation 7.2) composed of the superposition of waves I_1 and I_2 with periods of 6.904 and 7.173 was employed, with ΔI = 300mA (58.82 mA/cm^2) and I_{min} = 29.41 mA/cm^2. The etch wave was applied for 180 cycles of the lesser period. The resulting spectrum is compared to the fluorescence of Eu(dpa) in Figure 7.16. The dye swatches were illuminated and imaged as before, this time reflected off of the Eu-matched optical filter mounted in the beam splitter, resulting in selective imaging of the Eu sample swatch compared to a polished Si mirror reference. As shown in Figure 7.16, the intensity of the swatch impregnated with $[Eu(DPA)_3]^{3-}$ dominates the intensity of the image taken with the spectrally matched filter.

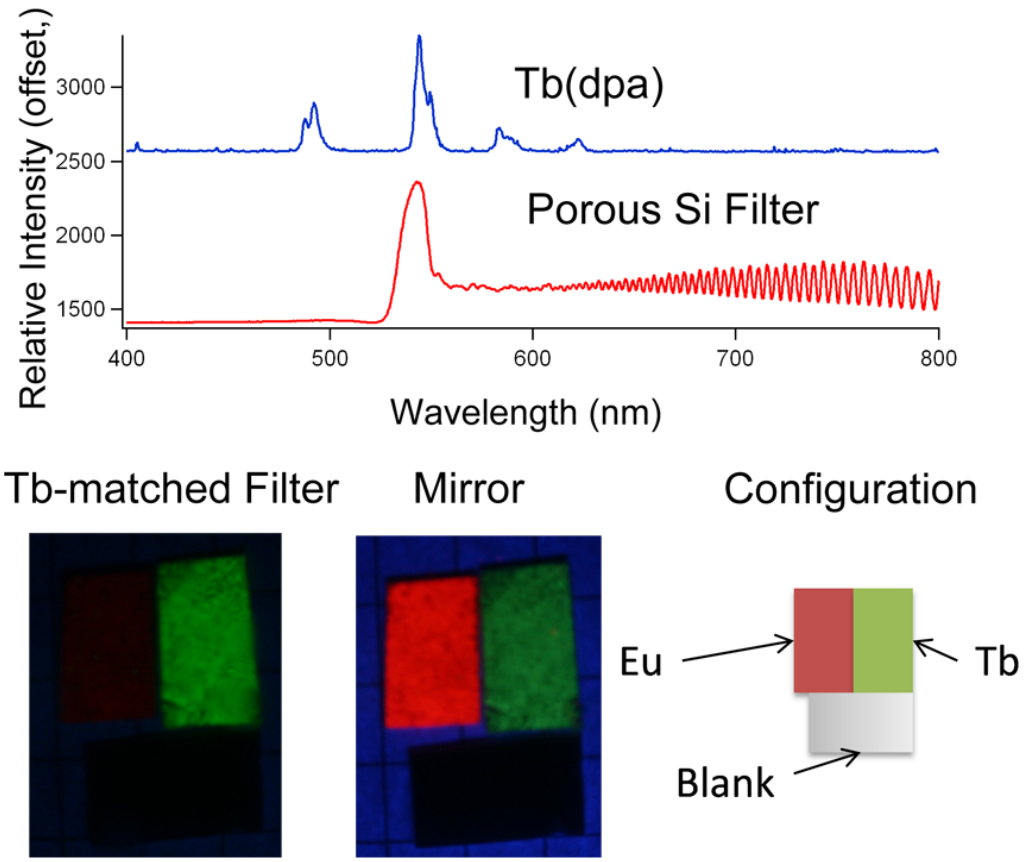

Figure 7.15 Top: A porous Si filter was fabricated to match a principal Terbium emission peak at 545nm**. Bottom:** Images filtered by reflecting off the mounted Si chip filtered spectral regions outside the porous Si rugate peak, resulting in an image dominated in intensity by the Terbium swatch. In image of the same swatch layout using polished Si in place of the rugate filter is shown for comparison.

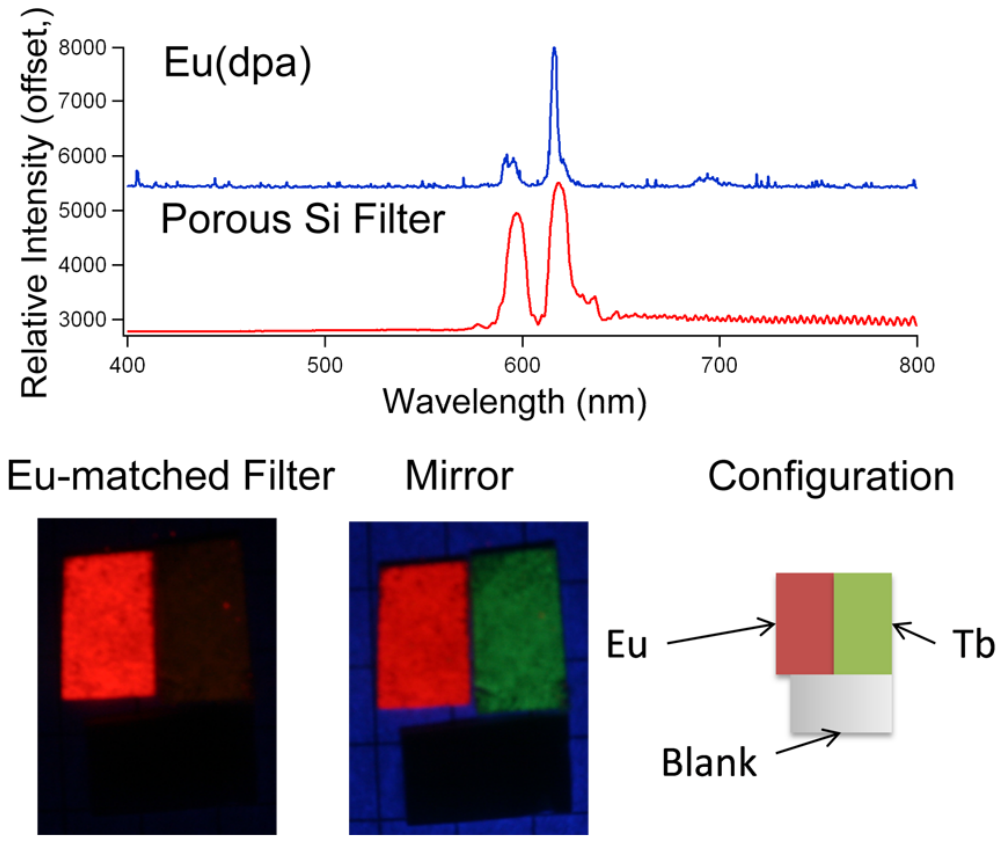

Figure 7.16 Top: A porous Si filter was fabricated to match two of the Europium emission peaks at 594 and 616nm. **Bottom:** Images filtered by reflecting off the mounted Si chip filtered spectral regions outside the porous Si rugate peaks, resulting in an image dominated in intensity by the Europium-impregnated swatch. In image of the same swatches using polished Si in place of the rugate filter is shown for comparison.

7.4.2.2 Distinguishing Similar-Color Fluorophores by Chemically Shifted Difference Imaging with Porous Si

Selective imaging of the Tb and Eu dyes in the previous section was relatively straightforward, since the targeted spectral features did not overlap. Additionally, the red-green-blue mosaic filters on the color imaging sensor act as broadband pass filters with some degree of overlap, so that selective imaging of dyes in separate color channels could be roughly approximated by simply monitoring the desired color channel. To demonstrate the ability of the porous Si filters to match specific spectral features, two dye-impregnated swatches were imaged that appear a similar color to the naked eye. One exhibits broadband luminescence, while the other, designated as the target dye, exhibits sharp spectral features. The porous Si filter matching the target dye's sharp spectral features was used to selectively image dye-containing swatches. An image taken with the filter's reflectivity matched to the target dye was subtracted from an image taken with the filter's reflectance peaks chemically shifted outside of the target dye emission bands. This shift was accomplished by introducing a ethanol vapor over the porous Si filter surface, which red shifted the spectral bands by increasing the refractive index of the filter layer upon analytes infiltration.

Spectra of the two chosen dyes are shown in Figure 7.17. $[Eu(DPA)_3]^{3-}$ has a red luminescence and sharp spectral emission peaks at 594 and 616nm, while the ruthenium complex $[Ru(Bipy)_3]^{2+}$ also appears red but exhibits a broad luminescence between 600 and 700nm. Four dye swatches were prepared: one impregnated with the broadband $[Ru(Bipy)_3]^{2+}$ dye, one impregnated with $[Eu(DPA)_3]^{3-}$, a third impregnated with the desensitized, weakly photoluminescent $[Eu(NO_3)_3]^{3-}$ without DPA, and a

fourth a reference swatch of glass fiber filter paper. The dyes were illuminated with short and long wave ultraviolet light, and a monochrome imaging sensor was used to eliminate the secondary filtering of spectral data by RGB sensor filters found in color cameras. The Eu-matched filter was prepared by etching with a sine waveform with n=2, ΔI_1 = 19.6 mA/cm^2, p_1=5.10, ΔI_2 = 127.5 mA/cm^2, p_2=5.32, and I_{min} = 29.41 mA/cm^2.

Images of the swatches with the Eu-matched filter in air and exposed to a near-saturated dose of ethanol are shown in Figure 7.17. With the optical filter in air, luminescence from the $[Eu(DPA)_3]^{3-}$ and $[Ru(Bipy)_3]^{2+}$ is observed in the image, with the Europium appearing more intense. When the same imaging field is captured using the vapor-shifted filter, the $[Eu(DPA)_3]^{3-}$ intensity decreases dramatically since the filter reflectivity peaks no longer align with the $[Eu(DPA)_3]^{3-}$ emission bands. In contrast, the broadband $[Ru(Bipy)_3]^{2+}$ maintains the same intensity in the image with the vapor-shifted filter, since the shifted rugate bands are still within the broadband emission of the Ruthenium swatch. Subtracting these two images thus leaves only intensity regions of the $[Eu(DPA)_3]^{3-}$ swatch, shown in the right column of the Figure 7.17 images. The desensitized $[Eu(NO_3)_3]^{3-}$ and dye-free glass swatches show very low intensity in both images, resulting in near-zero intensity in the difference image. As a comparison, images reflected off of a mirror instead of the spectrally-matched porous silicon were acquired, shown in the bottom row of the figure. Since the mirror does not selectively image the Europium dye in air or in ethanol, the difference image shows little intensity in any of the swatches.

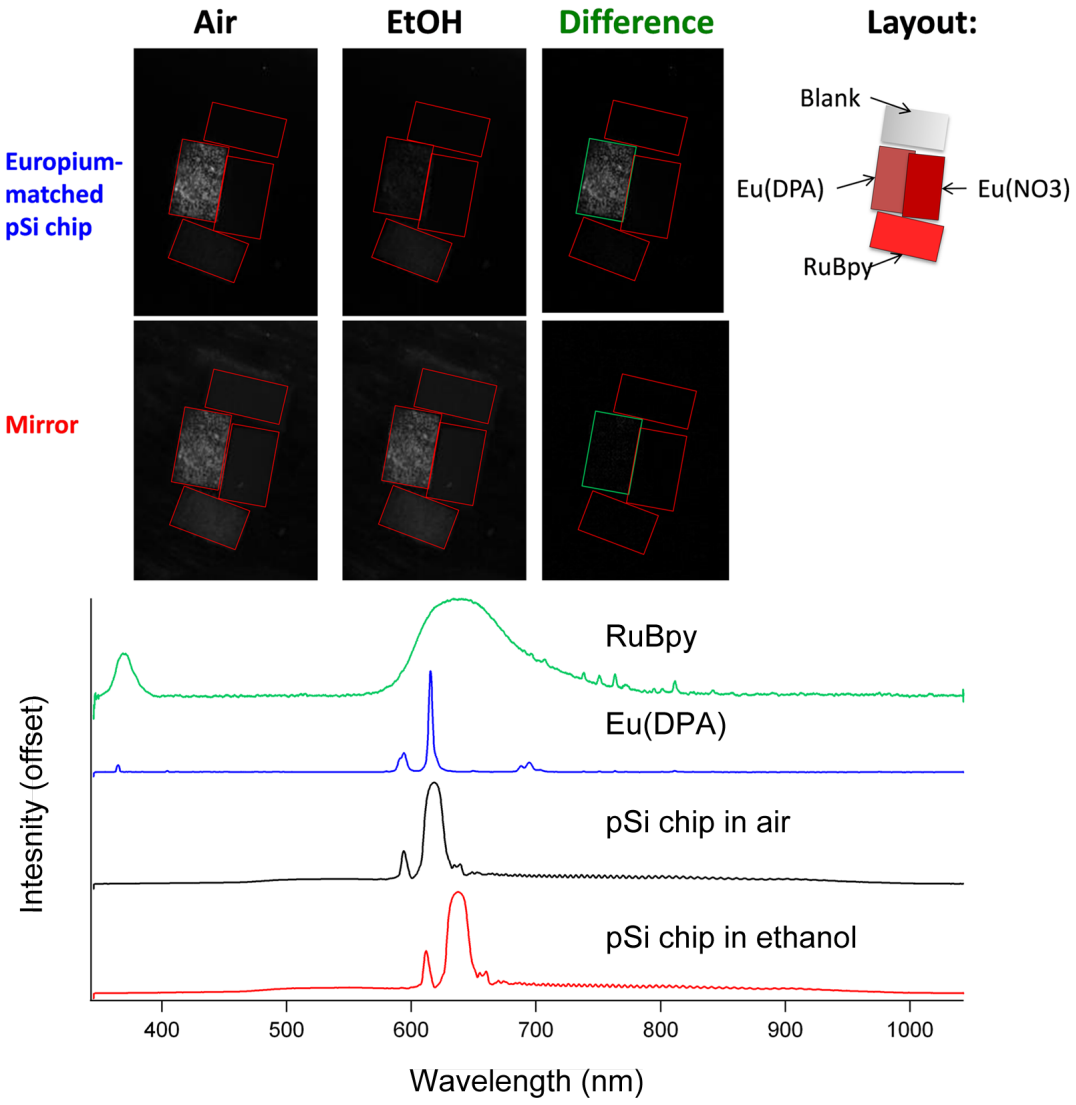

Figure 7.17 Top: Images of dye-impregnated filter paper swatches taken by reflecting the optical path off of a porous Si filter whose reflectivity spectrum matched two of the Eu emission peaks. In air, the filter's reflectivity peaks match the Eu(DPA) swatch's emission spectrum and are within the Ru(bipy) emission spectrum. In ethanol, the filter's spectral peaks shift and no longer match the dye fluorescence, but are still within the Ru(bipy) spectrum. The Eu(DPA) spectrum is only reflected for the unshifted filter while the Ru(bipy) is reflected for both unshifted and shifted filter images, so the difference of the images (third column) separates the Eu(DPA) from other dyes in the image. Unsensitized Europium dye, $Eu(NO_3)$, has a much weaker fluorescence than the dye sensitized with dipicolinic acid and therefore exhibits low intensity in the difference image **Bottom:** Dye fluorescence spectra (top two rows) and porous Si reflectance spectra in air and in ethanol. In air, the Eu(DPA) and porous silicon spectra align.

7.5 Conclusions

Refinement of rugate porous silicon spectral features was successfully employed to match the porous silicon reflectivity peaks to the emission peaks of photoluminescent dyes by adjusting multiple, superimposing current-time etching waveforms, each with specifically calibrated and tailored current density ranges periods, and variations in period over the time of the etch. Selective imaging of two lanthanide dyes by reflecting an image off of spectrally-matched rugate filters, placed in the optical path between the fluorescent dye swatches and a digital imaging sensor, was demonstrated for two spectrally separate dyes. Two dyes of similar fluorescent color were distinguished by imaging with a porous silicon filter matched to one dye's emission spectrum, with chemical vapor used to shift the filter's rugate bands on and off resonance with the spectral emission peaks in proof of concept demonstration of difference imaging.

Chapter seven, in part, is a reprint (with co-author permission) of the material as it appears in the following publication: Garcia Sega, Adrian; King, Brian H.; Sailor, Michael J. *Tunable porous silicon multispectral correlation filters for the remote detection of dipicolinate.* Manuscript in preparation. The author of this dissertation is a co-author of this manuscript.

CHAPTER EIGHT

INTERNALLY REFERENCED POROUS SiO_2 PHOTONIC CRYSTAL SENSOR FOR AMMONIA

8.1 Abstract

The last two chapters described spectrally tailored porous silicon filters used as indirect sensors, where transduction relies on the optical properties of the porous layer but target molecules do not directly bind to the porous matrix. This chapter continues the theme of indirect sensing with porous Si by incorporating a wavelength referencing channel into a porous silica layer that is used as an indirect sensor for ammonia. A one-dimensional photonic crystal possessing two peaks in the reflectance spectrum was prepared by electrochemical etching of Si. The porous photonic crystal was oxidized and infused with a bromothymol blue indicator dye yielding a pH-responsive sensor for $NH_{3(g)}$. The photonic crystal was prepared such that one of the reflectance peaks overlapped the absorbance band of the basic form of the dye (λ_{max} = 636 nm), while the other peak appeared in a "clear" spectral region where the dye has minimal absorbance. Simultaneous monitoring of the area of both reflectance peaks allowed for zero-point drift correction in the sensor response. It was found that the detection methodology inherently corrects for large changes in probe light intensity, providing a consistent measurement that is compatible with low-power, remote sensing applications. Detection of gas-phase NH_3 in the concentration range 15-1300 mg/m^3 is demonstrated. Since the sensor response follows the pH response of the indicator dye, it is not linear with gas-phase NH_3 concentration.

8.2 Introduction

Devices intended for remote sensing applications, such as the detection of environmental pollutants or toxic chemicals in industrial settings, need to be low-power, robust, and insusceptible to zero-point drift over long periods of unattended operation. Ammonia (NH_3) production in 2009 was over 133 million tons worldwide, making its industrial and environmental detection of particular importance.[274] Various sensor elements amenable to remote sensing of NH_3 have been developed, using electrical, mass, or optical-based transduction schemes. For example, Connolly and coworkers [156] described a porous SiC sensor that reliably senses the analyte using a capacitance-based transducer. Electrical transducers tend to be highly sensitive to changes in relative humidity, requiring a separate reference sensor to facilitate zero-point drift correction. Mass-based sensors, such as surface acoustic wave (SAW) devices, are less susceptible to humidity, but also require a reference channel to discriminate background signals.[275] Whereas electrical and mass-based sensors require a power source local to the sensor element, optical sensors, like those based on changes in fluorescence intensity or spectral absorbance, may be probed from a distance, making them amenable to remote detection. For instance, laser-based two-wavelength ratiometric absorption measurements have been used to quantify NH_3 in air.[276, 277] However, the high power and unit cost of such systems makes them less favorable for remote sensing applications. Lower power optical sensors have been developed that rely on pH changes as a means of detection, including silica-bound porphyrins,[278] polymer hydrogels[279] and porous Si.[280-283] Like the electrical or mass-based systems,

detection may suffer from false positives due to humidity or temperature fluctuations and thus requires a reference channel to ensure robust signals in the field.[130]

Photonic crystals provide a useful platform for remote sensing because their sharp spectral features allow them to be probed using eye-safe, low power laser probes.[24, 85, 284-287] Optical sensing of chemical analytes based on reflectance spectroscopy from porous Si films is well-documented,[9, 21, 288-290] and recent reports have addressed the possibility of zero-point correction in aqueous-phase sensing by using a reference channel built-in to the porous Si nanostructure.[86, 291] In this work, two principle remote sensing features of photonic crystals are investigated: incorporation of molecular-class specificity by addition of a chromogenic probe (bromothymol blue), and incorporation of an internal reference channel in the same physical space as the sensing channel, by electrochemical control of the nanostructure during synthesis. The detection of ammonia (NH_3) gas in a pure nitrogen (N_2) carrier stream is demonstrated. The electrochemical method of creating photonic crystals in porous Si is found to be a convenient means of incorporating two separate spectral peaks in the same physical location that can act as reference and sample channels.

8.3 Experimental

8.3.1 Preparation of Porous Si Photonic Crystals

Samples of one-dimensional photonic crystals of porous Si displaying two spectral reflectivity peaks were prepared from single-crystal, highly doped, (100)-oriented, p-type Si (Boron doped, 1-1.5 mΩ-cm resistivity) by electrochemical etching

in a 3:1 solution of 49% aqueous hydrofluoric acid:ethanol (hydrofluoric acid from Fisher, inc.). Etching was performed in a Teflon cell with a platinum mesh electrode and a galvanostat (Princeton Applied Research Model 363) under computer control (LabView, National Instruments). Reference and signal reflectance channels were simultaneously created by electrochemically etching silicon with a time-dependent current density waveform as previously described.[85, 158] Briefly, the current waveform I(t) consisted of a superposition of two sine waves:

$$I(t) = \sum_{i=1}^{n} I_i(t) \tag{8.1}$$

$$I_i(t) = A\sin(k_i t + \phi) \tag{8.2}$$

where A is the current amplitude, k_i is a frequency term corresponding to the position of reflectance spectrum peak i, φ is the phase offset, and n = 2. The 400 s duration current density waveform varied between 130 and 260 mA/cm^2. The resulting porous film was 50 μm in thickness (measured by scanning electron microscopy), with an average porosity of 64% (measured gravimetrically).[170] Samples were subsequently oxidized for 15 minutes at 650 ºC, as depicted in Figure 8.1.

8.3.2 Ammonia Sensing Experiments

A 15 μL aliquot of 1.5 mg/mL bromothymol blue (Sigma-Aldrich 17622HC) in dimethyl sulfoxide (DMSO) (A.C.S. grade) was loaded onto the oxidized porous Si chip and the sample placed in a Teflon gas dosing chamber fitted with a transparent optical window. Nitrogen carrier flow and NH_3/N_2 mixed flow was regulated with a gas mixer/mass-flow controller (Cole-Parmer). Ammonia gas was generated by

bubbling N_2 through an aqueous NH_3 solution. The NH_3 concentration in the gas phase (in mg/m^3) was computed by considering the mass of analyte in a volume of flow: aqueous NH_3 concentrations were first converted to partial pressures using a temperature-dependent Henry's Law constant for NH_3 [292]; partial pressures were then converted to mass using the ideal gas law[293], and the masses were adjusted according to the mixing ratio with the nitrogen carrier stream. Ammonia concentration was verified by performing acid-base neutralization titrations on solutions obtained from bubbling the dosing chamber gas effluent through distilled H_2O. The titration results agreed with concentrations calculated from the gas mixing ratios.

8.3.3 Data Acquisition

Reflectance spectra were recorded using an optical spectrometer (Ocean Optics S2000) coupled to one Y-branch of a bifurcated fiber optic cable with a halogen light source (Ocean Optics) illuminating the other Y-branch and a lens assembly at the distal end of the fiber, mounted above the sample in the dosing chamber. Reflectance spectra were captured at a rate of 1 Hz. The spectra were processed using a custom Igor Pro (Wavemetrics, Inc.) routine that computed the area of each of the two peaks (sample and reference) using trapezoidal integration.

8.4 Results and Discussion

8.4.1 Methodology Overview

The sensing methodology explored in this work combines the chemical specificity of an indicator dye with the sharp spectral features of a photonic crystal.

Many molecules change their absorption or emission properties upon analyte interaction. Some of these molecular systems are highly specific,[294, 295] while others respond to a wide range of analytes.[296, 297] Molecular absorption and fluorescence spectra tend to have broad spectral peaks, and sensing scenarios that involve multiple chromophores typically rely on spatial separation of the sensor elements for chromophore identification.[297] The problem of overlapping spectral peaks can be minimized by narrowing spectral linewidth, as occurs in a resonant cavity.[298] In principle, this allows one to incorporate many chromophores into a single platform without the need for a spatially resolved array. It also allows a chromophore spectrum to be distinguished from background "clutter" arising from interferents present in the sample matrix or in the environment by incorporating a narrow-linewidth, spectrally separated reference channel in the optical spectrum. The photonic crystal in this work utilizes two spectral reflectance peaks to optically reference a dye sensor. The pH indicator dye bromothymol blue is used as a model chromophore in this work. The absorption band of the dye is relatively broad, but only a narrow slice of the spectrum is observed when it is present in the porous photonic crystal used in the study. It is worth noting that leveraging the sharp spectral features of the porous Si host layer allows for better contrast and lower noise for extending the filter to potential digital imaging sensor filtering applications, discussed in Chapter 7. The sensing matrix consists of a one-dimensional photonic crystal of porous Si that has been thermally oxidized (Figure 8.1). The photonic crystal was fabricated to display two narrow spectral reflectivity peaks (Figure 8.2A). The wavelength of one of these peaks

coincides with the maximum of the broad absorption band of deprotonated bromothymol blue pH indicator dye (Figure 8.2B), and the other peak appears in a

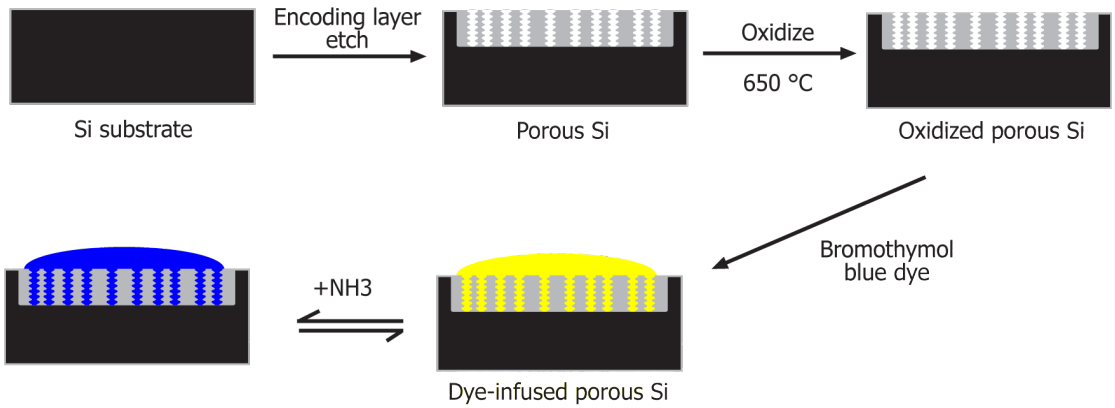

Figure 8.1 Schematic depicting the preparation of the porous photonic crystal gas sensor. A 1-dimensional photonic crystal is first etched into crystalline Si. The photonic crystal possesses two reflectivity peaks, one of which coincides with the absorption maximum of deprotonated bromothymol blue. The film is thermally oxidized, producing a stable porous SiO_2 matrix. Bromothymol blue is infused into the porous matrix, and the resulting sensor is exposed to ammonia to test the response.

region of the spectrum where neither the protonated nor the deprotonated forms of the dye absorbs, acting as a wavelength referencing band. The method allows the incorporation of reference and sample channels in the same physical location, dramatically simplifying the analysis.

Bromothymol blue was chosen as the indicator molecule for this study because of its rapid and well-behaved optical response as a pH-sensitive dye. It was infused into the porous photonic crystal as a solute in the high boiling-point solvent DMSO (Figure 8.1). The DMSO solvent was not removed from the sensor, and remains in the porous film throughout the course of the experiments. In its protonated acidic state, the absorption maximum of the dye occurs at a wavelength shorter than the two reflection peaks of the porous Si photonic crystal (Figure 8.2A). The reflection spectrum of a porous Si photonic crystal is readily controlled by the current density waveform used in its electrochemical preparation.[85, 158] In the present case two spectral reflection peaks were designed into the waveform, with reflection maxima occurring in the oxidized film at 644 and 812 nm. The reflection peak at 644 nm, referred to as the "Signal" channel, coincides with the absorption maximum of the deprotonated bromothymol blue dye (636 nm, Figure 8.2B). The 812 nm "Reference" peak appears in a region of the spectrum where neither protonated nor deprotonated forms of bromothymol blue display significant absorbance.

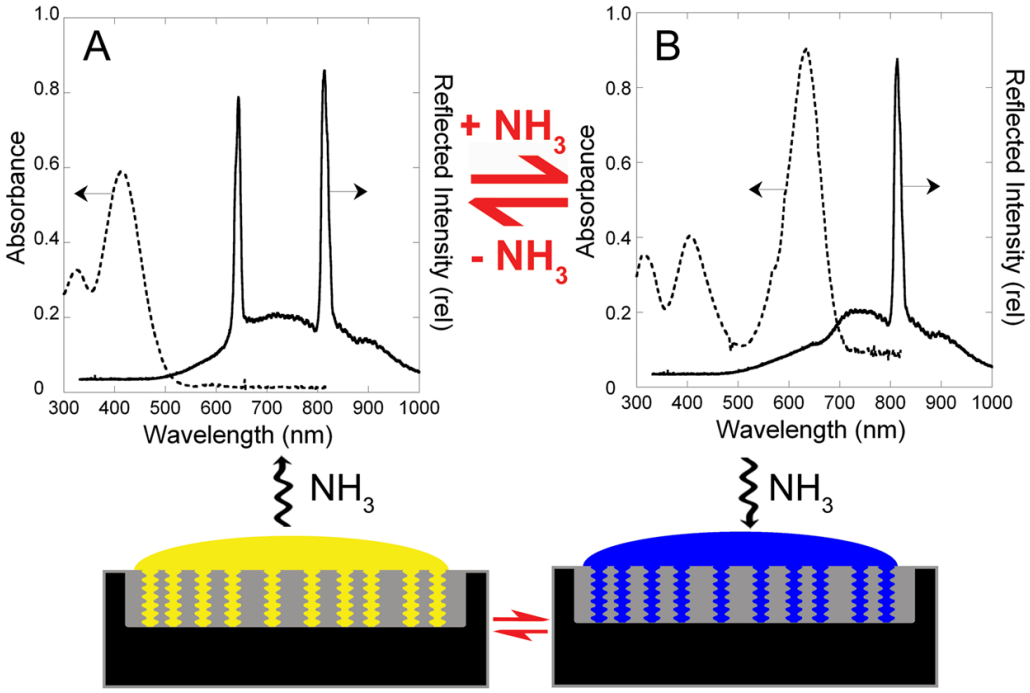

Figure 8.2 Comparison of the absorbance spectrum of bromothymol blue (1.5 mg/mL in dimethylsulfoxide, DMSO) with the reflected white light spectrum of the bromothymol blue-infused porous SiO_2 photonic crystal sensor. The photonic crystal contained two reflectivity maxima (solid curves) at 644 and 812 nm. **Plot A:** With no NH_3 present, the absorbance maximum of bromothymol blue (dashed line) occurs at 415 nm, and both the reflectance peaks of the photonic crystal are observed. **Plot B:** In the presence of NH_3, the absorption maximum of the indicator dye shifts to 636 nm, overlapping the lower reflectance peak of the photonic crystal. A ratio of the areas of the two reflectance peaks thus provides a measure of the amount of NH_3 present that is independent of the intensity of the probing light beam, since the reference peak area will vary accordingly. The bottom row of diagrams depicts the porous layer with infused indicator dye, which shifts from yellow (protonated state, no ammonia, left side) to blue (deprotonated state, ammonia present, right side).

8.4.2 Indirect Sensing of Ammonia

Ammonia was chosen as a test analyte for its importance as a widely used hazardous chemical.[299, 300] With no NH_3 present, the absorbance maximum of bromothymol blue occurs at 415 nm, and both the reflectance peaks of the photonic crystal are observed at 644 and 812 nm (Figure 8.2A). Introduction of ammonia gas to the sensor causes a dramatic change in the reflectivity spectrum of the bromothymol blue-coated porous Si photonic crystal (Figure 8.2B). Consistent with the absorbance spectrum of the indicator dye in its deprotonated form, the absorption maximum of the indicator dye shifts to 636 nm and the 644 nm "Signal" peak is completely obscured (Figure 8.2B). Because the dye has no significant absorbance at 812 nm, the "Reference" peak is still observed.

8.4.3 Light Intensity Compensation by Spectral Referencing

The ratio of the integrated areas of the photonic crystal's two reflectance peaks provides a measure of the concentration of ammonia vapor in the sensor while correcting for experimental fluctuations such as changing probe light intensity (Figure 8.3). The traces in Figure 8.3 represent an experiment in which the sensor was subjected to a sudden change in light intensity and, separately, a dose of NH_3 vapor. In order to test the ability of the sensor to correct for zero point drift, spectrally flat optical filters were used to fluctuate the intensity of the light source. In the region labeled A of Figure 8.3, a neutral density filter (ND) of optical density OD = 0.03 (calibrated at 632.8 nm, Newport Corporation) was placed between the halogen light source and the fiber optic used to illuminate the sample. In segment B, the filter was replaced with a

filter of OD = 0.2. In segment C, the OD = 0.03 filter was reinserted. The "Signal/Reference" ratio is unchanged throughout these segments. Additionally, the measurement noise in the ratio is significantly reduced relative to the "Signal" and "Reference" channels alone. For example, the signal to noise ratio (S/N), measured as the mean ($\bar{x}$) divided by the standard deviation (σ),[301, 302] increased from S/N = 46 in the raw signal channel of segment C (Figure 8.3) to S/N = 142 for the ratio "Signal/Reference" in this segment. The correlated noise is thus a significant portion of the noise in the measurement, and it is attributed to intensity fluctuations in the probe beam and readout noise in the CCD chip used in the spectrometer.

Following the experiment that tested susceptibility to variations in probe light intensity, the sensor was subjected to a dose of 496 mg/m^3 of NH_3 vapor in a nitrogen carrier stream (at 34% RH) for 20 s and then allowed to recover in a stream of pure nitrogen (Figure 8.3, segment D). Introduction of the analyte leads to a differential change in response that is easily discerned in the "Signal/Reference" ratio trace of Figure 8.3. As the analyte dissolves in the DMSO/bromothymol blue solution infused in the sensor film, the indicator dye is titrated to its deprotonated form, reducing the intensity of the "Signal" peak reflected from the photonic crystal. When NH_3 is removed from the N_2 carrier stream, the titration reverses as dissolved NH_3 leaves the sample matrix solution, and the "Signal" reflectance peak recovers to its original intensity.

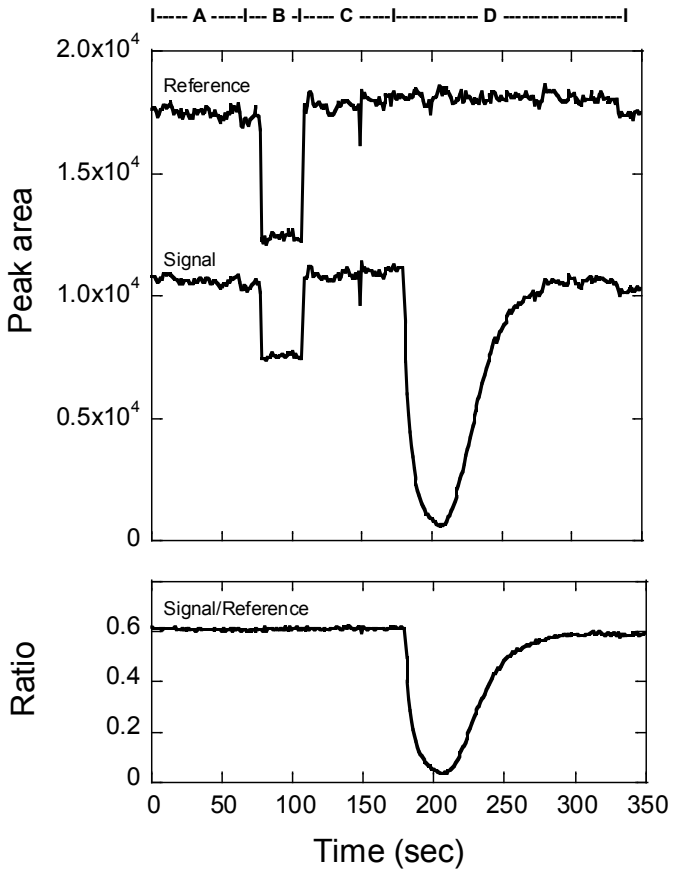

Figure 8.3 Integrated area of the reflectivity peak at 644 nm ("Signal") and at 812 nm ("Reference"), and the ratio of these two signals ("Signal/Reference") as a function of time during an NH_3 dosing run. Region A corresponds to the sample in pure nitrogen. In region B, the intensity of the probing light beam is reduced using a neutral density filter and both channels detect the change. In region C the neutral density filter is removed and both channels recover. In region D, a 20 s dose of 496 mg/m^3 $NH_{3(g)}$ is introduced and the "Signal" channel decreases while the "Reference" channel remains unchanged.

8.4.4 Reversibility

The reversibility of the sensor was tested by repeated dosings with $NH_{3(g)}$ in a pure N_2 carrier gas stream. A representative dose-time plot is presented in Figure 8.4. These data are normalized such that the ratio "Signal/Reference" is unity when the sample is measured in pure N_2 at the beginning of each experiment. Each minimum in the trace corresponds to the end of a 20 s exposure to 496 mg/m^3 of NH_3 gas. The sensor is then allowed to recover for 280 s. Given sufficient time, the sensor exhibits full recovery of the "Signal/Reference" ratio over the investigated concentration range of 15 – 1300 mg/m^3. With a dose of 496 mg/m^3 NH_3, for instance, the ratio recovers to 99% of its initial value after 450 s. The time for full recovery of the "Signal/Reference" ratio varied with analyte concentration for a fixed dosing time, presumably because at higher concentrations of NH_3, more of the bromothymol blue indicator present in the sensor matrix is titrated and more time is required for the larger amount of NH_3 to diffuse out.

8.4.5 Concentration Dependence of the Rate of Sensor Change

Assuming the kinetics of the indicator chemistry are fast relative to the timescale of the rates of dissolution and diffusion of NH_3 in the liquid phase of the sensor matrix, the rate of titration is expected to depend on the concentration of analyte in the gas phase. Thus the slope of the "Signal/Reference" ratio vs. time trace should correlate with the concentration of NH_3 in the gas phase.[303] This is indeed found to be the case, as shown in Figure 8.5. . The slope of the "Signal/Reference" ratio vs time trace, shown in the inset of Figure 8.5 and obtained in the 10s period immediately after

introduction of $NH_{3(g)}$, correlates with the $NH_{3(g)}$ concentration: higher concentrations of ammonia titrate the dye more rapidly and yield a steeper slope of the signal/reference ratio over time.

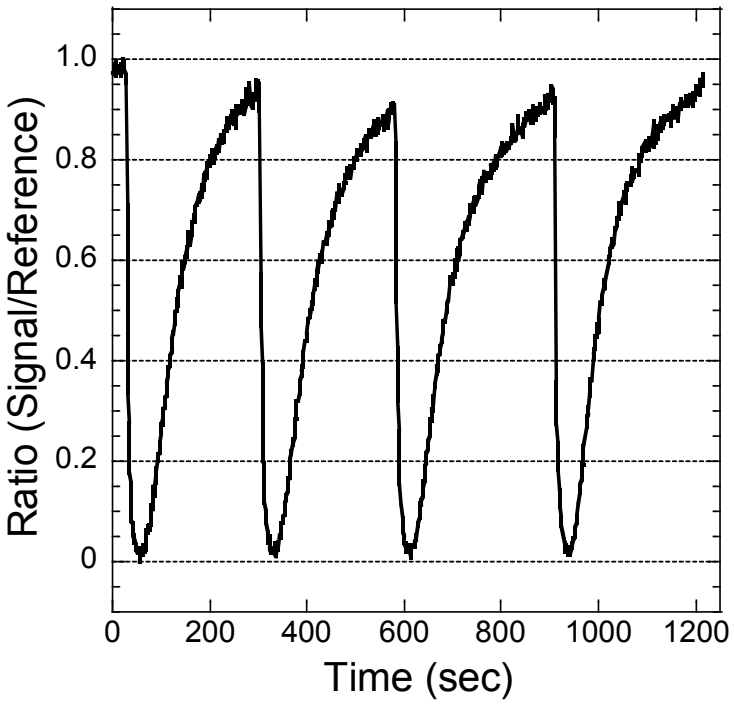

Figure 8.4 Plot depicting reversibility of the sensor to repeated 20s doses of $NH_{3(g)}$. Sensor response (ratio of the area of the "Signal" peak to the "Reference" peak) to four consecutive doses of 496 mg/m^3 of $NH_{3(g)}$ in $N_{2(g)}$ (at 34% RH) is presented as a function of time. Each cycle consists of a decrease in the ratio "Signal/Reference" when the NH_3 dose (20 s duration) is introduced, followed by recovery of the ratio upon analyte removal (return to pure $N_{2(g)}$ for 280 s). The ratio values are normalized to unity at $[NH_{3(g)}] = 0$, t=0.

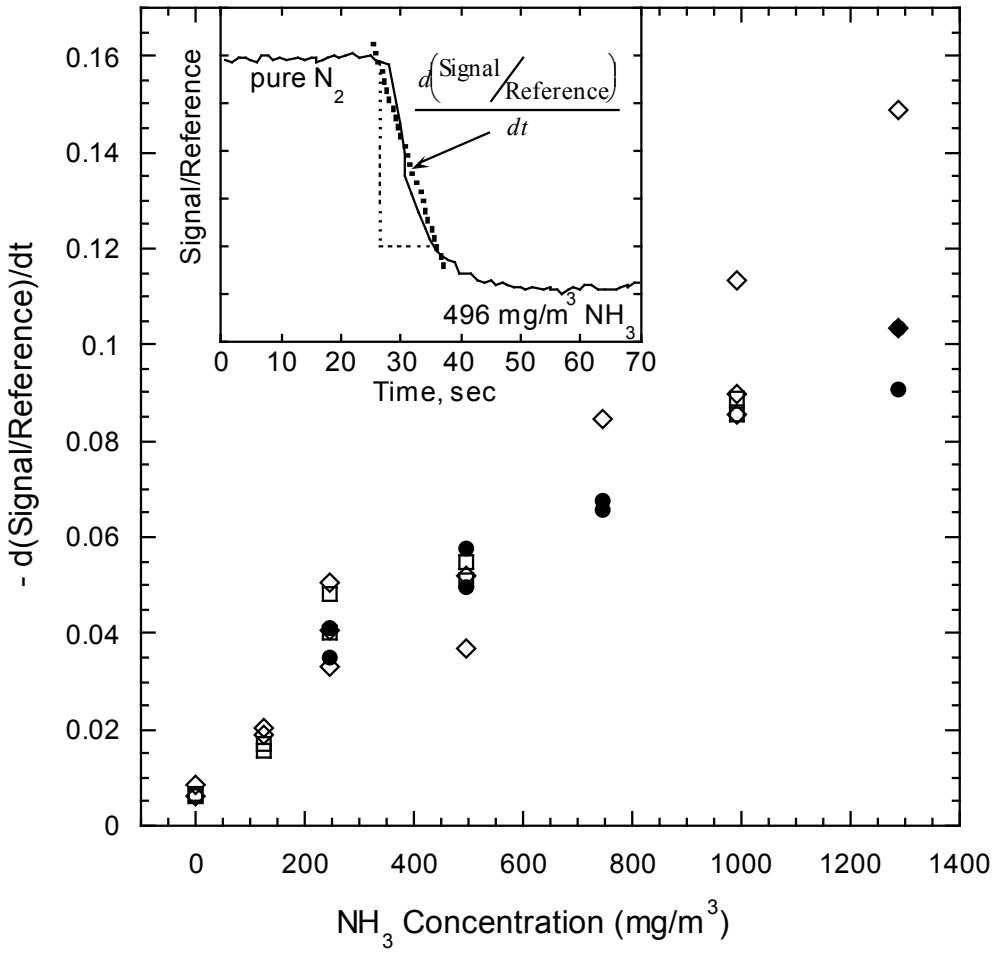

Figure 8.5 Correlation of the initial slope of the "Signal/Reference" vs. time plot, -d(Signal/Reference)/dt, with the concentration of $NH_{3(g)}$. The value -d(Signal/Reference)/dt was determined from the slope of the normalized (Signal/Reference) vs. time plot for the first 10 s of analyte introduction. The total analyte exposure time was 20 s. The inset shows an example of the -d(Signal/Reference)/dt slope for a 496 mg/m^3 dose. The different symbols represent separate chip preparations. Each preparation utilized the same porous Si chip, but with a fresh aliquot of bromothymol blue added after rinsing with pure DMSO and drying in N_2. A linear fit of the data shown has an r^2 coefficient of greater than 0.95.

8.4.6 Sensitivity

The lowest detectable limit (LDL) of the sensor was determined for measurements of the response to $NH_{3(g)}$ over a concentration range of 15 – 1300 mg/m^3. The concentration of $NH_{3(g)}$ in N_2 was varied while the relative humidity was held constant at 34% RH. The detection protocol consisted of measurement of the "Signal/Reference" ratio after a 20 s exposure to the analyte, with the baseline value of the ratio normalized to unity. Even at the lowest concentration tested, the sensor response was several times greater than the noise band of the "Signal/Reference" ratio; at an $NH_{3(g)}$ concentration of 15 mg/m^3, the average value of the normalized "Signal/Reference" ratio was 0.75, while the width of the noise band averaged only 0.03 units.

Since the vapor delivery system consists of a bubbler containing aqueous ammonia, the analyte carrier stream contains water vapor (nominal RH = 34%) that may also influence the indicator dye behavior. The response of the sensor system to water vapor alone was evaluated by replacing the aqueous NH_3 bubbler with a bubbler of distilled H_2O. The temperature of the system under the test conditions was 20 ºC. The response to water vapor was found to be greater than the measurement noise level, with the normalized "Signal/Reference" ratio decreasing from unity to 0.88 ± 0.06 when switching from the baseline stream of pure $N_{2(g)}$ (RH = 0%) to the water bubbler stream at RH = 34%. For this reason, the detection limit of the sensor was also evaluated at the threshold of three times the standard deviation of the sensor response due to water vapor, rather than the smaller threshold of three times the standard deviation of the noise band in the "Signal/Reference" ratio. Using this more stringent

standard, a practical detection limit of 124 mg/m^3 was determined, well under the NIOSH IDLH (immediate danger to life and health) limit of 210 mg/m^3 and the fatal dose limit of 3500–7000 mg/m^3.[188]

While the 124 mg/m^3 practical detection limit for the $NH_{3(g)}$ sensor is below the NIOSH IDLH limit, it is above the OSHA permissible exposure limit (PEL) of 35 mg/m^3. The OSHA PEL is for continual analyte exposure over many minutes. Since longer periods of analyte exposure titrate more of the indicator dye, protocols using a dose time of greater than 20 s yield a lower limit of detection. This was demonstrated at an analyte concentration of 62 mg/m^3 in three separate dosing cycles on the oxidized porous Si/indicator dye sensor chip; a 20 s exposure resulted in a drop of the normalized "Signal/Reference" ratio to 0.58, while a 30 s exposure yielded a value of 0.42, and an 18 minute exposure decreased the ratio to 0.08. The limit of detection can thus be reduced by increasing the analyte exposure time until an equilibrium concentration of ammonia in the liquid phase is achieved. However, longer exposure times are also subject to greater error because the DMSO solvent gradually evaporates from the sensor surface under the conditions of the experiment.

8.5 Conclusions

This chapter reported a new approach for incorporating an internal reference channel into the same physical location as a sensing channel, for a sensor material amenable to remote sensing applications. A pH-responsive sensor for $NH_{3(g)}$ was constructed by infusing an indicator dye into a porous photonic crystal. Both the "Signal" and "Reference" channels were incorporated into the photonic crystal in the

form of two spectrally separate reflectance peaks, allowing for correction of intensity fluctuations in the probing light beam. The wavelength of the "Signal" peak coincides with the absorption maximum of the deprotonated indicator dye, while the wavelength of the "Reference" peak appears in a region of the spectrum where no dye absorbance occurs. This wavelength-based referencing methodology is extendable to other colorimetric sensing motifs. Taking into account the effect of relative humidity, a "practical" limit of detection for $NH_{3(g)}$ was determined to be 124 mg/m^3. This ratiometric method is insensitive to large fluctuations in probe light intensity, providing a robust approach for remote analyte detection.

Chapter eight, in part or in full, is a reprint (with co-author permission) of the material as it appears in the following publication: King, Brian H.; Gramada, Andrei; Link, Jamie R; Sailor, Michael J. *Internally Referenced Ammonia Sensor Based on an Electrochemically Prepared Porous SiO_2 Photonic Crystal.* Advanced Materials (2007), 19 (22), 4044-4048. The author of this dissertation is the primary author of this publication.

APPENDIX A

KEY PROGRAMMING EXAMPLES

A.1 Construction of a Low-Power Porous Si Sensor on an Arduino Platform

A.1.1 Introduction

Optical transduction of sensor binding events are amenable to low-power, portable sensor systems[132]. A simple sensor configuration consisting of a porous silicon rugate film attached to a phototransistor and illuminated with an LED was packaged on top of an Arduino microcontroller, as shown in Figure A.1. The spectrum of the rugate was tuned to match the spectral emission of the LED at 650nm. When vapors infiltrate the porous structure, the reflected light spectrum shifts to higher wavelengths, allowing more of the LED light centered at 650nm to pass through the film to the photransistor and increasing the current through the detector, read by the Arduino as the voltage drop. This sensing scheme is depicted in Figure A.2. Various sensing principles such as dark spectrum correction and dynamic threshold levels are incorporated.

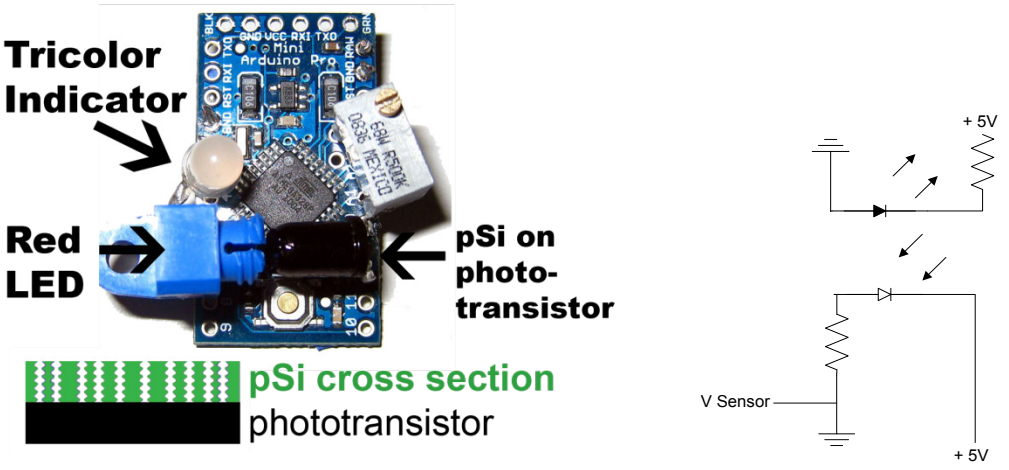

Figure A.1 Left: A low power porous Si sensor on an Arduino mini microcontroller board. The board performs dark correction, and other functions and provides various outputs to the user. Right: the simple LED-phototransistor arrangement of the sensor. The porous Si film is mounted atop the phototransistor.

A.1.2. Experimental

Porous Si samples displaying a single spectral reflectance peak were prepared from single-crystal, (100)-oriented highly boron-doped p-type Si (Siltronix, 1.0-1.2 mΩ-cm resistivity) by electrochemical etching in a 3:1 v:v solution of aqueous hydrofluoric acid:ethanol (49% hydrofluoric acid from Fisher Scientific, Inc). Etching was performed in a Teflon cell with a platinum mesh counter electrode and a galvanostat (Princeton Applied Research Model 363) under computer control (LabView, National Instruments). The current waveform was sinusoidal, with a period of 8.9 s, varying between 10 and 50 mA/cm^2, applied for 75 cycles (592 s). The porous layer was detached from the bulk Si by applying a current of 2.7 mA/cm^2 for 2 minutes in a 3.3% hydrofluoric acid:ethanol solution. Detached layers were carefully oxidized at 700C for 45 minutes in a high temperature furnace (Lindberg/Blue). The detached films were affixed to the phototransitor (Everlight PT334-6C) with epoxy after curing for 20 minutes in air (Devcon, No. 14310). The phototransistor was first polished to a smooth surface with optical fiber lapping film (Thorlabs). The Arduino and electrical components were purchased from Sparkfun, Inc. The assembled board, with the sensor-coupled phototransistor facing the red LED (Industrial Fiber Optics, Inc. IFE97) in Figure A.1.

Visible light spectra, shown in Figure A.2, were taken in the visible region from 400-1100nm with a CCD spectrometer (Ocean Optics USB4000) and a tungsten-halogen light source (Ocean Optics LS-1) connected with a Y-branch bifurcated optical fiber. The common end of the bifurcated fiber was focused with an objective lens to a $2mm^2$ spot size and positioned normal to the porous silicon sample surface of the film

not attached to the phototransistor. Vapor dosing of this film served as a comparison to samples attached as films to the phototransistor. The LED emission spectrum was taken by butting the LED to the common distal end of the optical Y-branch.

Vapor dosing of the sensor and the porous Si comparison chip were performed using the computer controlled vapor dosing system detailed in section A.2. The outflow of the vapor delivery system was connected to a large volume syringe, and the sensor package placed inside. The open side of the syringe was lightly packed with glass wool to prevent disruption of chamber concentration by air currents.

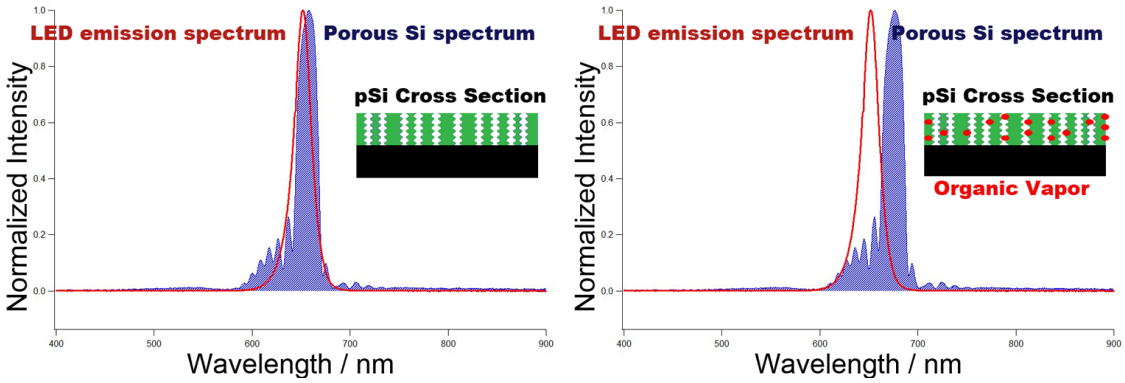

Figure A.2 The reflected light spectrum of the porous Si compared to the LED emission spectrum. Both spectra were recorded by CCD spectrometer. Left: The porous Si has been fabricated to match the LED emission in air. Right: when vapors infiltrate the optical film, the porous Si rugate spectrum shifts, allowing more of the LED light to pass through the layer into the phototransistor. The sensing is thus a function of the overlapped areas of the porous Si rugate peak and the LED emission.

A.1.3 Construction and Calibration of a Microcontroller-driven Porous Si Sensor

The assembly of the sensor unit on top of an Arduino 3.3V Mini board is pictured in Figure A.1. The board incorporates several processing features. The LED is pulsed, and the voltage before and after the LED turn-on used as a dark current reading and subtracted from the on-state reading to correct for ambient light levels. A tricolor LED indicator flashes and changes color based on changes in voltage from the initial sample-minus-dark baseline set on powering on. Serial communication to log voltages by computer is also provided through the top row of pins in Figure A.1. A dual sampling rate is programmed into the controller that increases when the first Δvoltage threshold is passed and reverts to the slower, power saving mode after a given number of samples are taken that are under the threshold. A voltage reading outside the bounds set in the program, indicating a broken circuit, results in a unique indicator LED flash pattern. To minimize ambient light entering the phototransistor, the epoxy "can" section of the phototransistor package has been painted black. The sensor was exposed to various concentrations of isopropanol and heptane vapors, as shown in Figure A.3. The voltage response clearly differs from the shift of the rugate stop band central peak position with vapor concentration. This is due to the different optical components in each system. The phototransistor acts to integrate the radiant power striking the detector over all wavelengths. The voltage is thus a function of the area of

overlap between the transmittance of the porous Si and the LED emission spectrum, the sensitivity of the phototransistor across the wavelength spectrum, and the transfer functions of irradiance to current and current to voltage in the phototransistor[39].

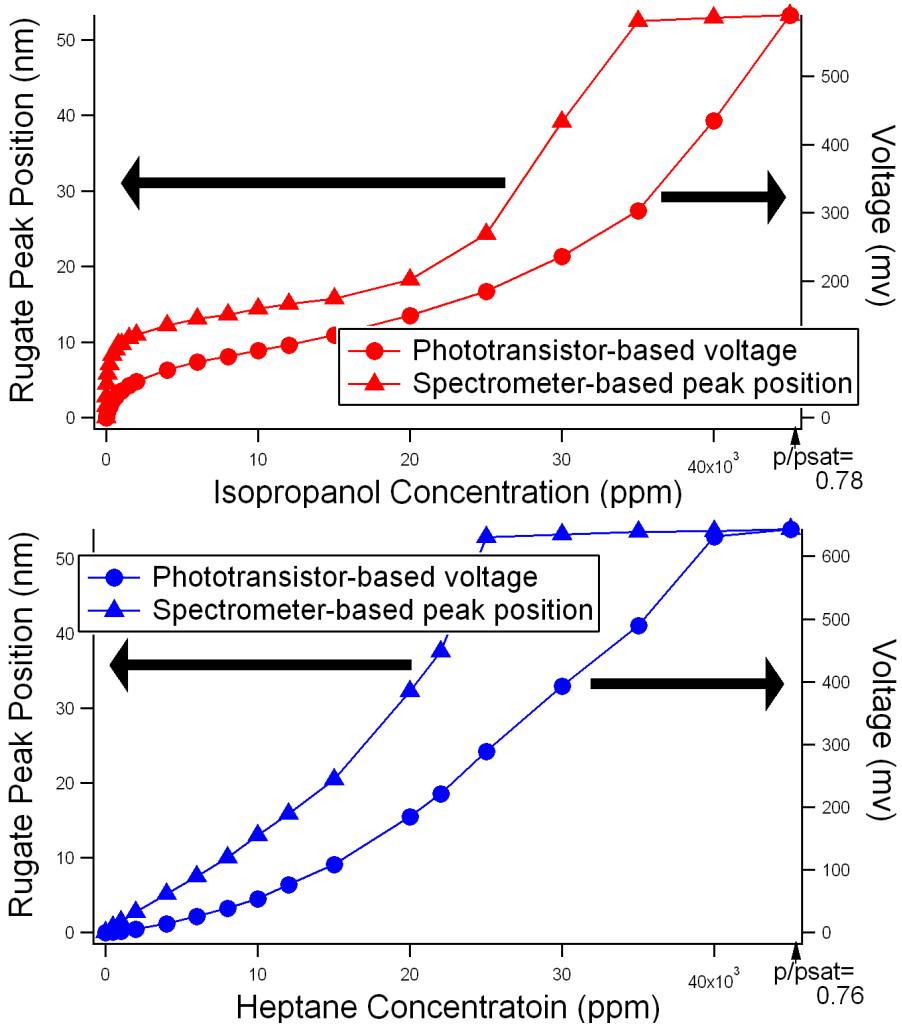

Figure A.3 Comparison of calibration of the sensor board voltage to analytes (right axes) to calibration of the CCD-recorded rugate spectral position of same sensor material to versus analytes (left axes). The curves differ since the voltage reading is based on the total flux of light passing through the porous silicon film to the phototransistor and so depends principally on the area of overlap between the rugate

peak and the LED, while the peak position depends only the central peak wavelength shift of the rugate band.

The thin-film interference fringes appearing at lower wavelengths from the rugate peak in Figure A.1 confound the voltage readings by reflecting LED light when the rugate stop band of reflectivity is outside of the LED emission band. Power consumption of the entire unit is small, measured as 4.5mA at 3.6V.

A.1.4 System Integration with Other Sensor Inputs and User Outputs

A larger prototype was constructed to test sensor integration, as shown in Figure A.4, with the Arduino board connected to a temperature and humidity sensor, USB-serial interface for easy programming, LCD display, two banks of indicator lights, and a cell phone. The SHT15 temperature and humidity sensor allowed temperature compensation of the sensor by calibrating the temperature response of the sensor in a vacuum oven (at ambient pressure) and correcting for the sensor response in the programming code. The response with temperature was found to be very small over the 25C-60C range tested (less than 10mV shift for a full range of 3.3 volts), consistent with observations of oxidized refractive index shifts with temperature in Chapter 4.

Separate banks of indicator lights for the ΔV voltage shifts and the dV/dT derivative of the voltage change are provided so that rate of change thresholds can be set if desired. Both banks operate as green-yellow-red corresponding to nominal vapor threshold-medium threshold –high threshold, with the specific thresholds set in the

program. An LCD displays the temperature, humidity, voltage and dV values, and red-threshold LED trip levels. Serial communication to a cell phone to send a text message notification is also implemented, with code adapted from the SSerial2Mobile library. The text message can be customized to indicate the type of threshold passed (rate of change or absolute change in voltage).

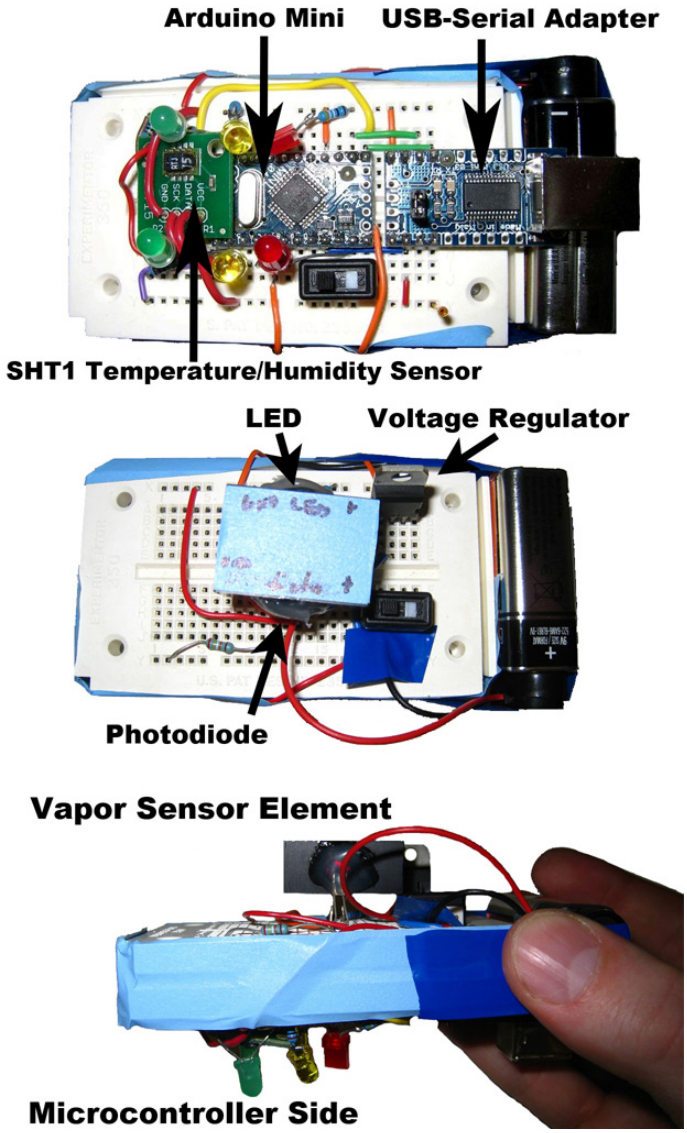

Figure A.4 Arduino microcontroller board integrated with other sensing components. In this prototype, the porous Si-photodiode and LED are mounted in a separate block placed on a backside breadboard for ease of diagnostics. The Arduino is linked to two banks of LEDS to indicate voltage and derivative of voltage (dV) thresholds, as well as a temperature and humidity sensor (SHT1) and USB adapter. Additional pins were used (not shown here) to perform serial communication with a cell phone to send text message warnings when threshold levels are met, and to output voltage, temperature, and humidity measurements and alerts to an LCD screen.

A.1.5 Programming Examples of Standalone Sensors

Miniature sensor platform in pulsed acquisition mode: The code of the sensor described in section A.1.3 is provided below, with comments in bold.

```
//Declare Vairables
int trired = 2; int triblue = 4; int trigreen = 3; int redLED = 6;
int sensePin = 0; //pin for taking voltage readings
int phototransistor = 12; float currentvalue = 0.0;
float darkvalue = 0.0; //dark voltage reading variable
int i =10;
int blue = 0; int green = 0; int red = 0;

//Set input and output modes
void setup()
{ pinMode(sensePin, INPUT);  pinMode(trired, OUTPUT);  pinMode(triblue, OUTPUT);
 pinMode(trigreen, OUTPUT); pinMode(redLED, OUTPUT);
 Serial.begin(19200); // Open serial connection to report values to host
 Serial.println("Starting up"); //Serial messages are for debugging
delay(500);
digitalWrite (phototransistor, HIGH); delay(500);

 // Take the first reading (dark corrected) and use that to establish the trip levels
 darkvalue= analogRead(sensePin);
 digitalWrite (redLED, HIGH); delay(110);
 currentvalue = analogRead(sensePin); delay(10);
 digitalWrite(redLED, LOW);
 currentvalue = currentvalue - darkvalue;
 Serial.print("Initial Value is:");
 Serial.println(currentvalue);
 blue = currentvalue - 40; //these are the trip levels based on voltage shift
 green = currentvalue + 10;
 red = currentvalue + 90; delay(100); }

void loop()    //Loop of continuous operation
{
   //Turn on the LED, take a reading, and turn it off
  darkvalue= analogRead(sensePin);
  digitalWrite (redLED, HIGH);  delay(110);
  currentvalue = analogRead(sensePin);  delay(10);
  digitalWrite(redLED, LOW);
  currentvalue = currentvalue - darkvalue;
  Serial.println(currentvalue);
```

```
if(currentvalue <blue)   //this indicates an electrical connection is bad - flash red/blue
  { digitalWrite (triblue, HIGH);   delay(100); digitalWrite (triblue, LOW);   delay(100);
     digitalWrite (trired, HIGH);     delay(100);digitalWrite (trired, LOW);   delay(100);
     digitalWrite (triblue, HIGH);   delay(100);digitalWrite (triblue, LOW);  delay(100);
     digitalWrite (trired, HIGH);     delay(100);digitalWrite (trired, LOW);    delay(100); }


//below is the evaluation for absolute voltage level triggering. Voltage triggering is reversible -
lights go off when voltage drops below threshold.
     if(currentvalue >=blue && currentvalue < green)
     {  digitalWrite (triblue, HIGH);delay(200);
      digitalWrite (triblue, LOW);
      i=i+1;  //this increments a counter to handle switching the acquisition period }

 if(currentvalue >=green && currentvalue < red)
   { digitalWrite (trigreen, HIGH); delay(200);
    digitalWrite(trigreen, LOW); i=0; }

 if(currentvalue >= red) //flash the red LED several times when the red threshold is reached
    {  digitalWrite(trired, HIGH);     delay(100);
    digitalWrite(trired, LOW);  delay(100); digitalWrite(trired, HIGH);     delay(100);
    digitalWrite(trired, LOW);  delay(100); digitalWrite(trired, HIGH);     delay(100);
    digitalWrite(trired, LOW);  i=0;  }

 // The sampling interval increases when an event is detected
  if(i >= 10) {  delay(2000);  }
//set so that 10 samples must be taken at the blue threshold to revert to power save mode
  else{ delay (200);  }
}
```

Multisensor package with temperature correction and text messaging features: The code of the sensor described in section A.1.4 is provided below, with comments in bold.

```
//the following lines are for setting up the SHT1x sensor
#include <SHT1x.h>
#define dataPin  10
#define clockPin 11
SHT1x sht1x(dataPin, clockPin);

//the following lines are for setting up the text messaging
#include <SoftwareSerial.h>  // include the SoftwareSerial library so you can use its functions:
#define rxPin 2 //orange wire
#define txPin 3 //red wire
// set up a new serial port
SoftwareSerial sserial =  SoftwareSerial(rxPin, txPin);

//the following lines are for setting up the LED output and sensor pins
int redPin = 13;  int yellowPin= 12; int greenPin = 9; int sensePin = 0; int vgreenPin = 8;
int vyellowPin = 7; int vredPin = 6;

//delta voltage thresholds
int reddelta = 80;  int yellowdelta = 10; int greendelta = 5;

//absolute voltage thresholds
int greenv = 245; int yellowv = 235; int redv = 190;

//other variables
int currentvalue;   //the value is read in the currently running loop
int firstvalue;       //the value from the last loop
int delta; int i=0; //this counts every other loop for alternating what is shown on the LCD
int temperature =25;
boolean triggered = false;  //this boolean is used to ensure a text message is sent only once

void setup()
{
  pinMode(redPin, OUTPUT);  pinMode(yellowPin, OUTPUT);
  pinMode(greenPin, OUTPUT); pinMode(vgreenPin, OUTPUT);
  pinMode(vyellowPin, OUTPUT);  pinMode(vredPin, OUTPUT);
  pinMode(sensePin, INPUT);
  //Communication setup:
  pinMode(rxPin, INPUT);   pinMode(txPin, OUTPUT);   sserial.begin(4800);
  sserial.println("AT*SWRESET");
 // LCD display setup:
  Serial.begin(19200); //open serial connection to display output
```

```
  Serial.print(12,BYTE);  //clear display
  delay(10); Serial.print(22, BYTE); //turn on display with no cursor or blinking
  Serial.print(17,BYTE); //turn on backlight
  Serial.print("Chemical Sniffer");
  Serial.print("Brian King 2010"); delay(4000);

 //print all the trigger levels to the display
  Serial.print(12, BYTE);  delay(20);  Serial.print("dT trips:");  Serial.print(13, BYTE);
  Serial.print("Green dT: ");  Serial.println(greendelta); delay(3000);  Serial.print(12, BYTE);
  delay(40);  Serial.print("Yellow dT: ");   Serial.println(yellowdelta);  Serial.print(13, BYTE);
  Serial.print("Red dT: ");  Serial.println(reddelta);  delay(3000);  Serial.print(12, BYTE);
  delay(40);  Serial.print("Voltage trips:");  Serial.print(13, BYTE);  Serial.print("Green:");
  Serial.print(greenv);  delay(3000);  Serial.print(12, BYTE);  delay(20);  Serial.print("Yellow:");
 Serial.print(yellowv);  Serial.print(13, BYTE);  Serial.print("Red:");  Serial.print(redv);
 delay(3000);  Serial.print(18, BYTE); //turn off LCD
  //take a sensor reading before the loop starts
  firstvalue = analogRead(sensePin);    }

void loop()   {
  Serial.print(12,BYTE);   delay(40);
    //linear temperature correction based on calibration
  currentvalue = analogRead(sensePin) + 0.5*(temperature-25);
  delta = firstvalue - currentvalue;

  //evaluate the delta for triggering lights and turn on/off based on threshold
  if(delta >=greendelta)
     { digitalWrite (greenPin, HIGH);
     }  else { digitalWrite (greenPin, LOW); }

    if(delta >= yellowdelta)
     { digitalWrite (yellowPin, HIGH);
     } else { digitalWrite (yellowPin, LOW); }

    if(delta >= reddelta)
     {     digitalWrite(redPin, HIGH);

    //send text message here
   if(triggered == false) {  //send only one text message
     sendtxt("There is a chemical alert, dV/dT trip"); }
    triggered = true;  //so that no more text messages sent

    //LCD backlight on, clear LCD, and print warning
    Serial.print(17,BYTE); //turn backlight on
    Serial.print("Chemical Alert!");  Serial.print(13, BYTE);
    Serial.print("dV/dT triggered"); delay(5000); Serial.print(18,BYTE); //turn backlight back off
    Serial.print(12, BYTE); delay(20);
    }  else { digitalWrite (redPin, LOW); } }
```

```
//now evaluate the absolute voltage levels
    if(currentvalue <=greenv)
      { digitalWrite (vgreenPin, HIGH);  }
     else { digitalWrite (vgreenPin, LOW); }
    if(currentvalue <=yellowv) { digitalWrite (vyellowPin, HIGH); }
     else {digitalWrite (vyellowPin, LOW);}
    if(currentvalue <= redv)  { digitalWrite(vredPin, HIGH);
    Serial.print(17,BYTE); //turn backlight on
    Serial.print("Chemical Alert!"); Serial.print(13, BYTE);Serial.print("Voltage alert!");

  //send text message here
   if(triggered == false) {  //send only one text message
     sendtxt("There is a chemical alert, voltage trip"); }
    triggered = true;  delay(5000);
    Serial.print(18,BYTE); //turn backlight back off
    Serial.print(12, BYTE);  delay(20); } else {digitalWrite (vredPin, LOW);  }

//print out the voltage and delta voltage for each reading
  Serial.print("V:");  Serial.print(currentvalue);
  Serial.print(" dV:"); Serial.print(delta); Serial.print(13, BYTE);
  Serial.print("V!:");  //trip value for voltage
  Serial.print(redv);
  Serial.print(" dV!:");  Serial.print(reddelta);

 //get and print out the temp and humidity every other cycle so bottom line of 2-line display
 //alternates between the red LED trip values for V and dV and the temp/humidity
  if(i=1) {  float temp_c; float humidity;  temp_c = sht1x.readTemperatureC();  humidity =
sht1x.readHumidity();

 //basic error handling to ensure temp is within acceptable range, then update the global
temperature variable to the current temperature
  if(temp_c > 15) { temperature = temp_c; }

  //print values to LCD
  Serial.print(13, BYTE); Serial.print(13, BYTE);  Serial.print("Temp:"); Serial.print(temp_c,
 DEC);  Serial.print(" RH:");  Serial.print(humidity, DEC);  Serial.print("%  ");
  } else {delay(200);}
   firstvalue = currentvalue; //update the voltage stored in memory to the latest reading
  delay(1200);

  //keep track of every other iteration of main loop
  if(i>=1) {i--;} else {i++;}}

//this is the text message sending function
void sendtxt(char message[])
{ sserial.println("AT+++");   //this is the "tickle" command to wake up the phone
delay(500); sserial.println("AT+CMGF=1");  //set to text messaging mode
delay(500); sserial.print("AT+CMGS=\"");  //sending text messaage
sserial.print("5555555555"); //phone number
sserial.println("\""); delay(500); sserial.print(message); sserial.println(26, BYTE);
delay(2000); }
```

A.2 Construction and Programming of a Vapor Delivery System with LabView Control

A.2.1 Introduction

The purpose of this section is to provide supporting information on the configuration and programming of the vapor delivery system used in chapters 2-5. A description and diagram of the delivery system is followed by a brief example of programming and operating the system.

A.2.2 Vapor Delivery System Configuration

The overall vapor delivery system is described. Individual experiments utilized subsets of the system components and rearrangement of the mass flow controllers for the vapor and nitrogen purge lines, as detailed in the relevant experimental descriptions.

A nominal system configuration is shown in Figure A.5, and consists of four electronic mass flow controllers (Alicat Scientific) pooled into a vapor delivery line with another electronic mass flow controller regulating a nitrogen purge line. Serial communication lines from all flow controllers pooled into a DB9 drop box connected to a serial port breakout cable of the computer. Exiting the mass flow controllers, the Teflon tubing of each branch of the vapor line flowed horizontally into respective heated stainless steel vaporization blocks maintained at 50°C to promote full vaporization. Small diameter Peek tubing from the outflow of a low-flow liquid pump (MilliGAT 6nl-10ml/min, GlbalFIA) was inserted into a vertical tap in the heated block, fitted with Swagelok seals to inject analytes into the flow stream. The calibrated

pump rate of liquid analyte delivery, combined with the nitrogen flow rate, determined the vapor concentration. Solenoid valves before and after the block prevented back pressure to the flow controllers, controlled by LabView through a set of relays. Three injection blocks and pumps allowed for rapid switching between desired analyte vapor streams. The outflow of the vaporization block was united with the nitrogen flow line at a computer controlled four-way valve, with the nitrogen and vapor lines switched between two valve outlets, one to the flow cell and the other to a waste stream. This allowed for continuous flow of vapor to the waste stream while sending pure nitrogen to the sample dosing cell, preventing pressure buildup and allowing for fast switching between vapor and nitrogen flows. The sample was mounted in a Teflon dosing cell with Kapton o-ring seals, with an outflow flow meter used to verify seal integrity. Vapor concentrations were validated with a gas chromatograph (SRI Instruments 8610C with FID detector). Some experiments incorporated temperature control, temperature sensing, and pressure sensing as described in Chapter 5.

A.2.3 Example Program

LabView was used to control all system components, including spectral acquisition from a USB spectrometer (Ocean Optics USB4000) and spectral processing. Each experiment demanded a customized application, with approximately 12 top-level programs sharing several dozen subroutines used to control each component of the system. The example described here is a program used to deliver desired vapor concentrations of an analyte to the sensor chip while thermally cycling

the chip with a computer controlled thermoelectric Peltier unit. The front panel of the program is shown in Figure A.6. The programming panel is shown in Figure A.7. Since many loops are stacked sequences, presentation of the entire programming structure is not possible in a single image. Additionally, only the top-level of the example program is presented here, not the programming of the individual subroutines. However, the points below, corresponding to the sections of graphical programming in the images, describe the overall logic and flow of the program.

The overall logic is a sequence of initialization, acquisition, and termination. Initialization consists of setting pumps, the spectrometer, the thermoelectric Peltier module, and the solenoid valves to an initial state ready to accept commands. The run consists of an outermost loop that determines the concentration for each run within. At each concentration, the a two part sequence is implemented consisting of waiting while the concentration equilibrates and the performing the desired run. The desired run within each concentration loop consists of two principal parts. The upper loop (7 and 9 in the programming panel) acquires spectra, fits peaks, and saves data at a given rate. The lower loop controls the heating cycles for each run at each concentration, progressing the loop containing the heating and acquisition control to the next concentration when all cycles at the current concentration are complete. The termination consists of stopping the liquid pump and turning off heaters and valves.

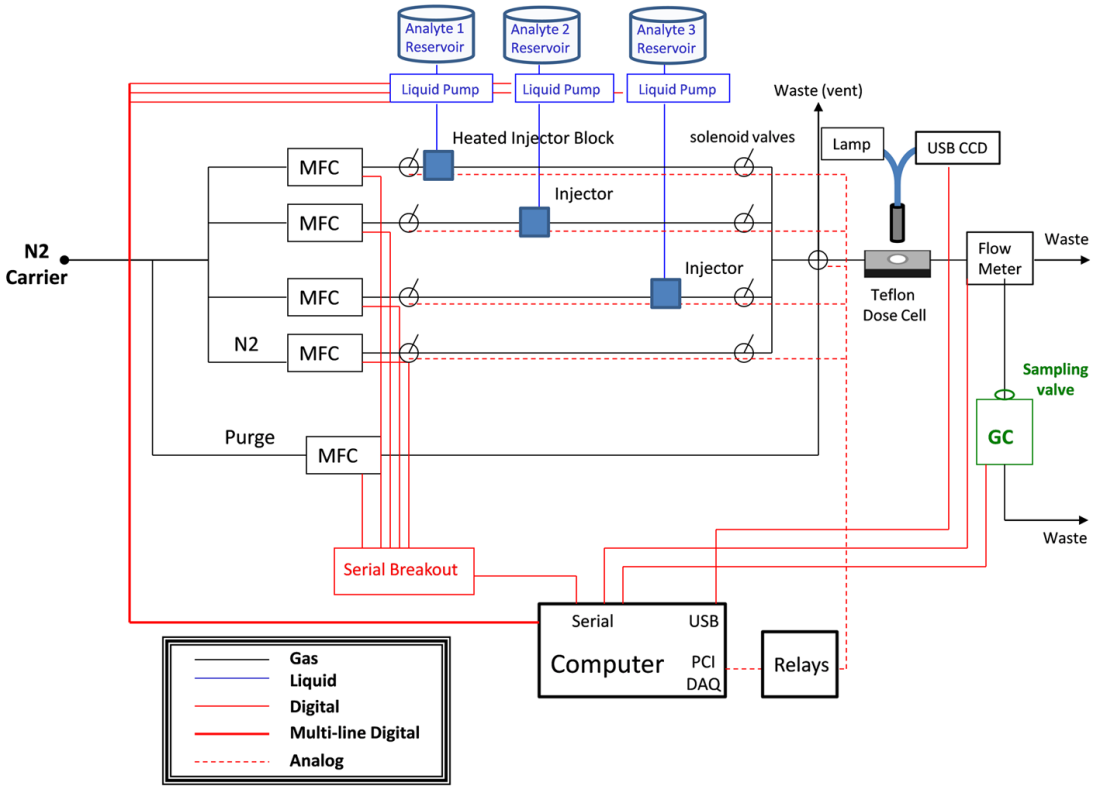

Figure A.5 A nominal configuration of the liquid pump-based vapor delivery system. Serial communication, USB communication, and a digital-analog acquisition card in a PCIe slot are depicted. The four-way valve to the immediate left of the Teflon flow cell allowed rapid switching between vapor and purge lines. The system is pictured without a ballast between the dose cell and the last 4-way valve, but a ballast consisting of several sealed Erlenmeyer flasks connected in series was sometimes used to ensure homogeneity of the vapor flow.

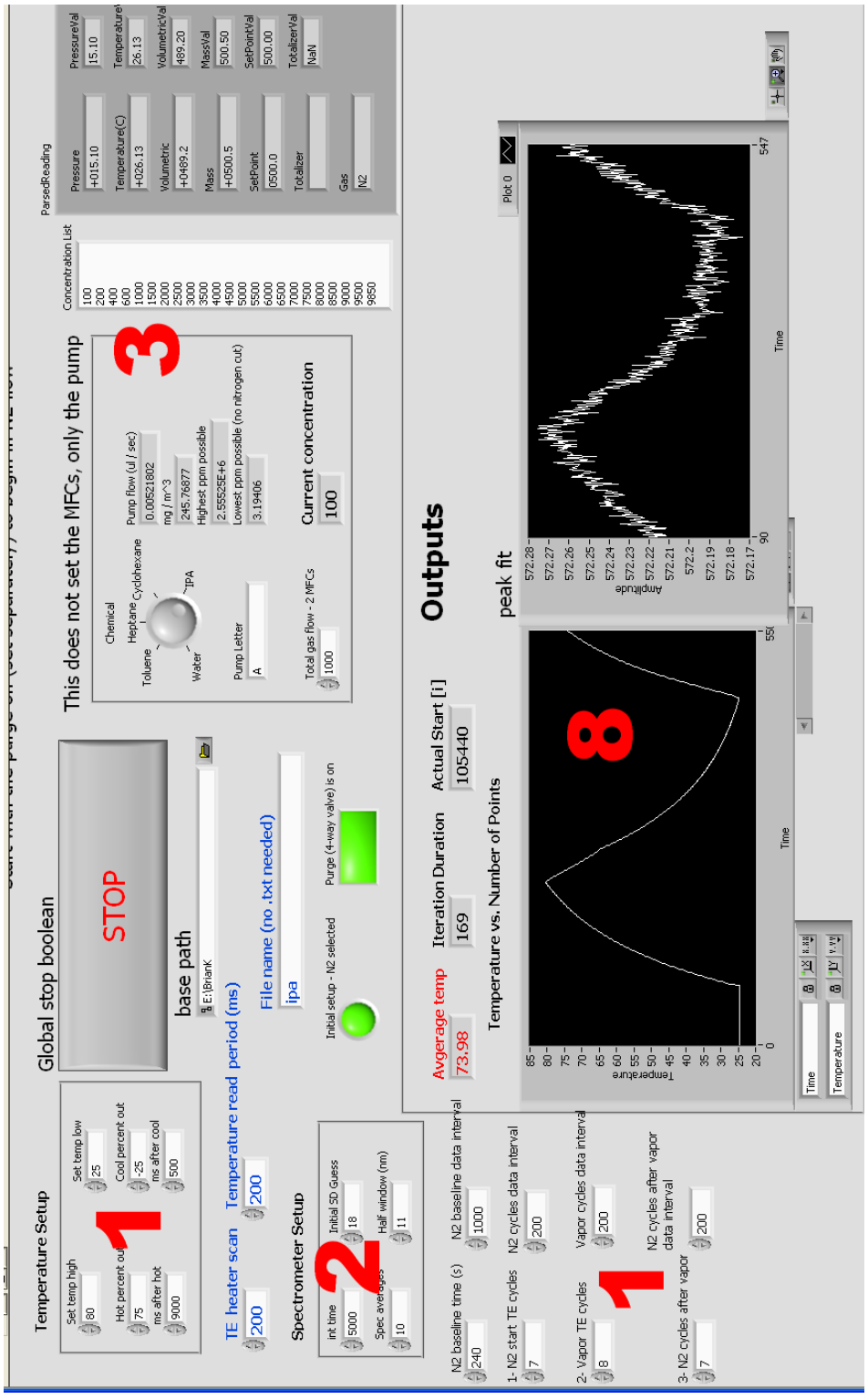

Figure A.6 LabView programming example front panel

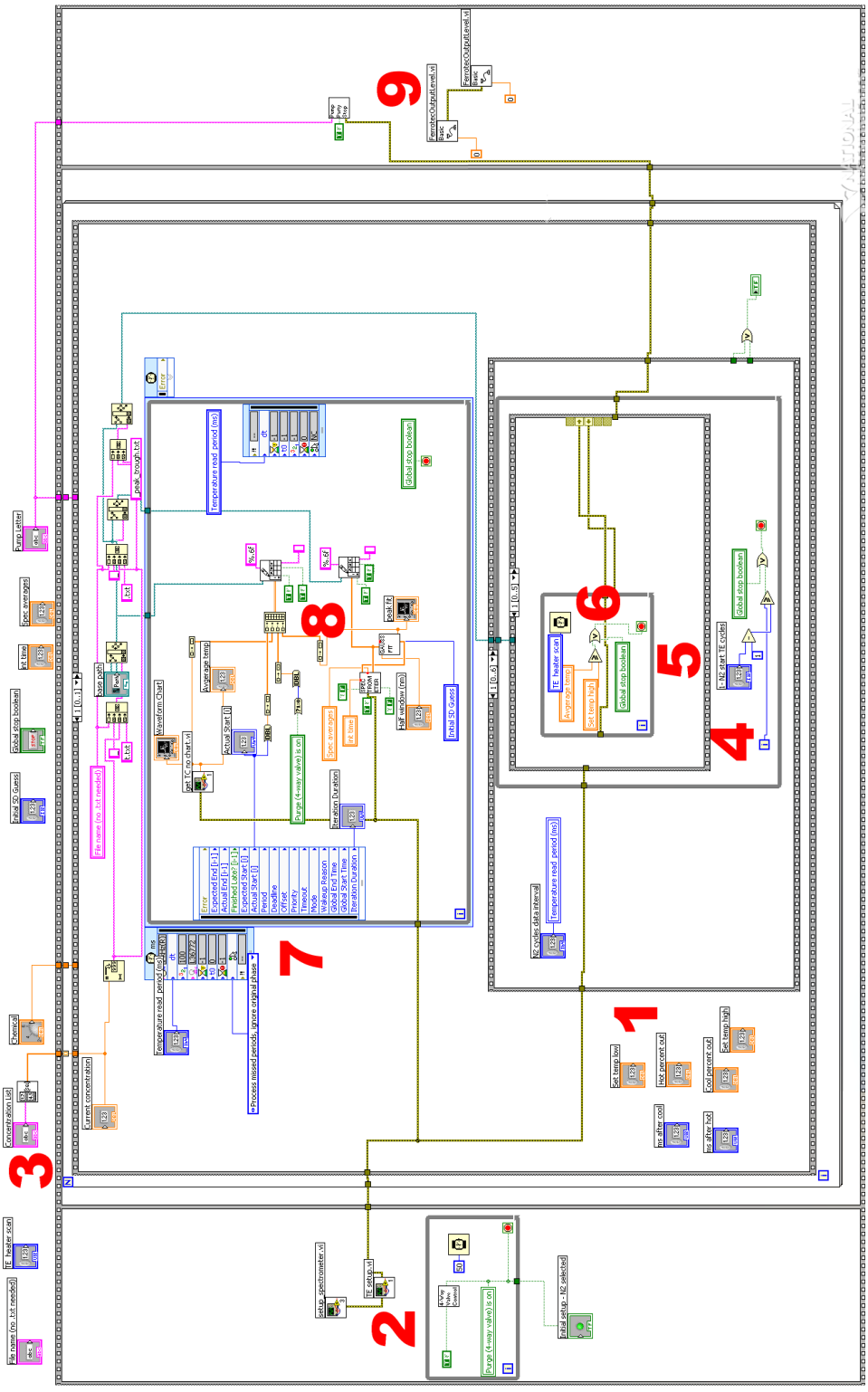

Figure A.7 LabView programming example front panel

1) **Temperature control.** The thermoelectric Peltier is controlled by a PID box (FTC100) with serial communication. For direct control of the heater power output, the unit is placed in manual control mode and power settings sent by serial text strings. The lower, large loop in Figure A.7 to the right of number (1) is used to cycle the thermoelectric as described in numbers 4-6 below. The upper left box in the front panel sets variables for the high and low temperatures to cycle the thermoelectric between, and for the percent heater output for the heating and cooling, as well as the number of seconds to allow the thermoelectric to rest before switching the heating direction to prevent burnout of the unit. The lower left section of the front panel controls the number of thermal cycles for each concentration of vapor in the experiment, as determined by the loops to the right of (1) in the programming panel. In this experiment, at each concentration 7 thermal cycles in nitrogen were followed by 8 cycles under vapor and then 7 more cycles in nitrogen, as set in the front panel. The front panel also sets the "scan" rate in milliseconds of each segment, which is the rate at which thermocouple readings are acquired and compared to the set high and low temperatures to determine when to switch the direction of the heating/cooling. The thermoelectric was operated in this example in an on-off-reverse mode with a single power setting used for the heating and cooling cycles. In other experiments, a power was controlled as a ramping function over time for more controlled heating and cooling.

2) **Initialization of the system.** In the front panel, the acquisition parameters of the subroutine used to acquire spectra from the USB spectrometer are set (integration time and averages), as well as the post-acquisition Gaussian fitting parameters for determining the rugate spectral band position (initial standard deviation guess and window). In the programming panel, the flow is initialized to select the pure nitrogen purge line (4-way valve subroutine), initialize the spectrometer by taking initial dark spectra and setting parameters (setup_spectrometer subroutine), and set the thermoelectric to manual control mode (TE setup subroutine).
3) **Vapor concentrations**. In the front panel, the user inputs a list of concentrations to be dosed. The cycles of heating/cooling are applied to each concentration. Concentration is switched by placing all cycling and spectral acquisition functions inside a *for* loop (largest loop in the middle section of the programming panel) to run through the cycled acquisition sequence at each concentration. A selector knob in the front panel sets the analyte used for concentration calculations throughout the run. The corresponding letter assignment of the liquid pump is input, as well as the total flow through that pump's vaporization block. A subfunction calculates the concentration, outputs the required pump rate to the selected pump unit, and returns concentration information displayed in the front panel. For each new concentration, flow rate information is acquired from the mass flow controllers and saved to a log file to track the proper operation of the system.

4) **Temperature cycles.** The box to the right of (1) is a stacked sequence that is run at each concentration tested. It consists of a baseline period in nitrogen, temperature cycling the sensor chip in nitrogen, temperature cycles under vapor flow, and more temperature cycles in nitrogen. The number of cycles for each segment is set in the front panel (1). The loop containing (4) is for one of these cycled segments. The logic to the right of (4) determines how many cycles have been iterated and stops the loop when the desired number is reached, progressing the run to the next cycling segment. The box immediately above (4) is a stacked sequence controlling one heating-cooling cycle.

5) **One cycle**. The stacked sequence containing (5) is one heating-cooling cycle consisting of : sending an output power level to the thermoelectric; comparing the most recent thermocouple reading (taken in part 8) to the set high temperature value at a comparison rate (set in part 1 on the front panel), recording the Gaussian-fit peak wavelength (from 8); temperature, and time of the high point and setting the heater to zero power; setting the thermoelectric Peltier module to a cooling power; comparing the most recent temperature value to the low temperature setpoint, and recording the peak position, time, and temperature data at the low temperature value while setting the heater power to zero for a set number of milliseconds, set in the front panel area (1). The global stop Boolean local variables throughout the sequence allow the sequence and loops to immediately break before finishing if the user presses "Stop" on the front panel

6) **Comparison of PV to SV**. In this inner loop, the set point value (SV) for the high temperature of the thermoelectric cycle is compared at a given interval (TE heater scan) to the actual process temperature (PV), acquired in part 8 at a similar fast (>5Hz) data interval, until the maximum temperature is reached.
7) **Data acquisition.** In this timed loop, spectra are acquired (at the rate "Temperature read period") using a spectrometer subfunction and temperature is acquired from the DAQ card with another subfunction ("get TC no chart"). The spectra are Gaussian fit using a third subfunction.
8) **Saving data to file and user output.** To the right of (8), the raw, full spectra are saved to one file, and the processed peak position along with the temperature, time, and position of the four-way valve that switches between vapor and nitrogen are recorded in a separate file. In the front panel, plots of the temperature versus time and peak position versus time are displayed.
9) **Termination.** At the end of all concentrations, the pump is stopped (pump party stop subfunction) and the heater is set to zero power.

The speed of spectral acquisition is primarily limited by the USB driver. Each ~70KB spectra should be able to transfer at USB 2.0 speeds (60 MBps maximum) at thousands of hertz, yet the minimum spectral acquisition time for one spectral average and 10ms integration time was ~40ms acquired using only the subfunction with no additional processing or writing to disk. A 15ms integration increases the acquisition time to 45ms, indicating a roughly ~20-30ms overhead due to the device driver and interface with LabView.

Gaussian fitting the rugate peak for single-peak rugates was performed by determining the highest intensity point in the spectrum and fitting a window (determined in part 2 of the front panel) around that point. This method yielded a noise band of less than 0.03nm, as can be seen on the front panel in A.6. A separate method that was implemented using autocorrelation of the spectrum resulted in a >0.05nm noise band. Spectra can be stored in an array and processed after each sequence of interest and then written to disk all at once, in order to increase processing time and therefore the acquisition rate for fast acquisitions. However, writing to disk and processing for each acquisition was very fast (<5ms) compared to the acquisition rates needed (50-200ms) and, and writing memory contents to disk each acquisition ensured sufficient physical memory resources over long runs.

A.3 Modeling the Effect of a Ballast Volume in a Vapor Delivery System

In Chapter 4, a 125 mL ballast was used in the vapor delivery flow line as a mixing volume and placed between the output line of the bubbler system and the sample dosing cell, where the output line consisted of a split and then recombination of a saturated concentration bubbler vapor line and an air dilution stream. The effect of the ballast on the concentration changeover time from zero to the final concentration, corresponding the beginning of a vapor dose, and from a concentration to zero, corresponding to the end of a vapor dose when the line is switched to a purge of pure carrier gas, is modeled here.

The one box model common to many atmospheric chemistry problems is applied with the balance equation[304] expressing the change in time of the mass in the ballast, m:

$$\frac{dm}{dt} = \sum sources - \sum sinks = F_{in} - F_{out} \quad \text{(A.1)}$$

where Fin and Fout are the mass flows into and out of the ballast. The source flowing into the ballast for a flow rate R_{in} (L/min) and input concentration C_{in} (mg/L) is:

$$F_{in}\ (\text{mg/min}) = R_{in}\ C_{in} \quad \text{(A.2)}$$

and losses are assumed as first order so that F_{out} = km. Thus:

$$\frac{dm}{dt} = F_{in} - km \quad \text{(A.3)}$$

Separation of variables yields:

$$\frac{dm}{S-km} = dt \quad \text{(A.4)}$$

And integrating both sides over time from 0 to t yields:

$$-\frac{1}{k}\ln\left(\frac{S-km(t)}{S-km(0)}\right) = t \quad \text{(A.5)}$$

Rearranged to:

$$m(t) = m(0)e^{-kt} + \frac{F_{in}}{k}(1-e^{-kt}) \quad \text{(A.6)}$$

The initial mass for the ballast system is m(0) = $C_{ballast,\ initial}$*$V_{ballast}$, in mg/L for the units above. To find the constant k, we can take the situation where the mass in the ballast approaches the steady state value of m(inf***) = F_{in}/k. At this steady state, the mass flow into the ballast equals the ballast concentration, so we have the concentrations [Inflow] = C_{in} (mg/L) and

[Flask] = F_{in}/ k $V_{ballast}$. Setting these equal and rearranging, we have, substituting equation (2) for F_{in}:

$$k = \frac{F_{in}}{C_{in}V_{ballast}} = \frac{R_{in}C_{in}}{V_{ballast}C_{in}} = \frac{R_{in}}{V_{ballast}} \quad \text{(A.7)}$$

Inserting k and (A.2) into equation (A.6) yields:

$$m(t) = C_{ballast,initial}V_{ballast}e^{-\frac{R_{in}}{V_{ballast}}t} + C_{in}V_{ballast}\left(1-e^{-\frac{R_{in}}{V_{ballast}}t}\right) \quad \text{(A.8)}$$

The initial increase in concentration upon vapor dosing is thus the right side of equation 8, since Cballast, initial =0. When the vapor dose is switched back to nitrogen (or air), only the left side of equation 8 applied since Cin = 0.

Figure A.8 displays an increase from zero concentration to an arbitrary concentration of 90 mass units per Liter (the pre-exponential factor in equation 7) given a 500sccm flow rate R_{in} and two different ballast sizes for V_{flask}. For the heating time of 160s, a 125 mL ballast was deemed acceptable since the concentration approaches C_{final} in ~2 seconds.

For the rapid thermal cycling work of Chapter 5, where spectra were acquired at 5 Hz and greater, a ballast of any size was undesirable. Instead, sudden changes in concentration due to the liquid pumps delivering liquid to the nitrogen line were monitored with a second gas dosing cell and spectrometer system connected in series to the output of the principal experimental dosing cell. Runs with anomalous concentration behavior were excluded and re-run.

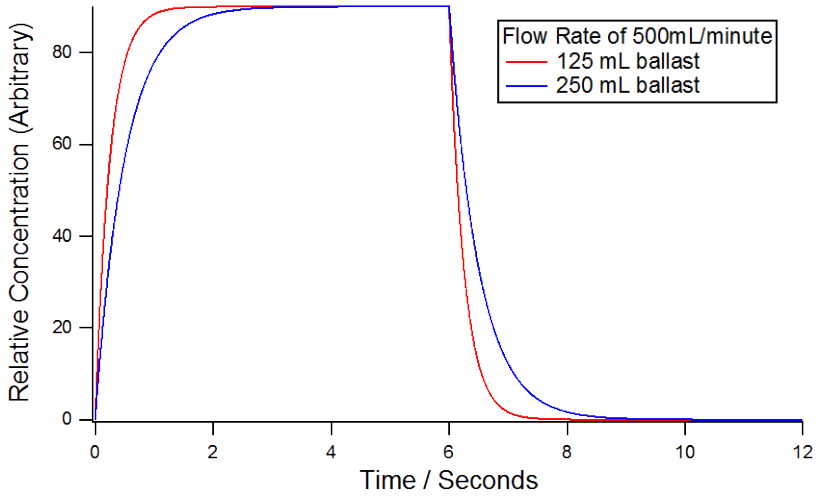

Figure A.8 Concentration (mass over volume, arbitrary scale) of analyte in the ballast as a function of time for a flow rate of 0.5L/min and two ballast sizes. The flow rate was chosen to match the conditions in Chapter 4.

A.4 Implementation of the 3-Component Bruggeman Effective Medium Approximation

This appendix describes how the filling of porous silicon and silica can be related to the change in the average refractive index of the layer, n_{eff}. A cross section depiction of the porous layer and the volume components is shown in Figure A.9. The three component Bruggeman can be written as[86]:

$$(1-P)\,\frac{{n_{Si}}^2-{n_{eff}}^2}{{n_{Si}}^2+2{n_{eff}}^2}+\;(P-fP)\,\frac{{n_{air}}^2-{n_{eff}}^2}{{n_{air}}^2+2{n_{eff}}^2}+\;(fP)\,\frac{{n_{fill}}^2-{n_{eff}}^2}{{n_{fill}}^2+2{n_{eff}}^2}=0 \qquad \text{(A.9)}$$

where f is the volume filling factor, ranging from 0 to 1, and P is porosity, from 0 to 1. The term n_{fill} is the refractive index of the analyte filling the pores, and n_{eff} is the average index of the porous layer. Thus, given the porosity and refractive index of the material (typically n_{Si} or $nSiO_2$), $n_{effective}$ can be obtained for a given fractional filling of the pore volume. The refractive index n_{eff} versus various fractional fills can be readily calculated in Maple, shown in Figure A.10.

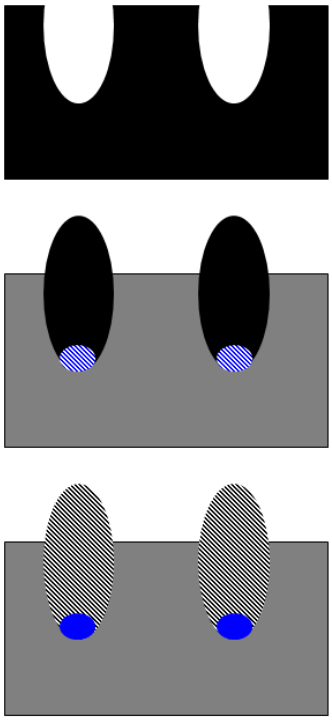

Component 1: Pillars of silicon
1 – Porosity

Component 2: Void space (air or N2) minus analyte fill

P – F * P

Component 3: Analyte fill
F*P where fill F is a fractional fill of the volume from 0 to 1.

Figure A.9 Components of the Bruggeman equation: silicon, void space, and analyte fill (blue)

```
v := Vector(21);
p := .26;
nsi := 1.49944;
nsolvent := 1.3776;
for t from 1 by 1 to 21 do
S := (1 − p) * ( (nsi^2 - n^2) / (nsi^2 + 2*n^2) ) + (p − (t/20 − 0.05) * p)
     * ( (1 - n^2) / (1 + 2*n^2) ) + ((t/20 − .05) * p)
     * ( (nsolvent^2 − n^2) / (nsolvent^2 + 2*n^2) );
P := solve(S, n);
if t = 1 or t = 21 then v[t] := P[nops([P])] else v[t]
     := P[nops([P]) − 4] end if
end do;
```

Figure A.10 Maple code to calculate n_{eff} of a porous layer given pore filling fractions from unfilled (0) to completely filled (1) split into 21 fractional filling levels. The code above uses a porosity of 26% and an n_{Si} material refractive index of 1.49944. The solvent refractive index of 1.3776 is for isopropanol.

A.4.1 Procedure for Plotting the Change in n_{eff} or Change in λ_0 by Pore Filling with Analytes

1) Determine n_{Si} with the 2-component Bruggeman equation. Experimentally this can be performed for a rugate by:
   a) Recording the nm peak location of a rugate with no vapor present (zero point)
   b) Calculating the effective optical thickness (EOT=2neffL) from an FFT of the interference fringes at that point
   c) Using the thickness as measured by SEM to calculate:
   $(2n_{eff}\,L)/2L = n_{eff}$
   d) Applying the 2-component Bruggeman using the gravimetric porosity to obtain n_{Si}.
2) Calculate n_{eff} for various fractional fillings of the pores using n_{Si} from step 1 using the 3-compoenent expression.
3) To relate the n_{eff} for each fractional filling to the rugate peak location λ_0, plot and fit λ_0 vs. EOT for various concentrations. Plots of λ_0 vs EOT were found to be highly linear as shown and discussed in chapter 5.

Figure A.11 shows the refractive index of the layer, n_{eff}, as a function of volume fill for various analytes. Conditions were chosen for a fully oxidized silicon material with a refractive index of n_{Si} = 1.46 and a porosity of 26%, typical for material oven oxidized at 800°C for long times. In Chapter 5, the experimental values of n_{Si} and

porosity were utilized Multiplying the volume fill per volume of chip by the density of each analyte or density times molar mass yields the mass fill and molar fill per volume of sensor chip, respectively. The fractional volume can be converted to the volume of the chip filled by multiplying by the total volume of the chip determined by BET or other means.

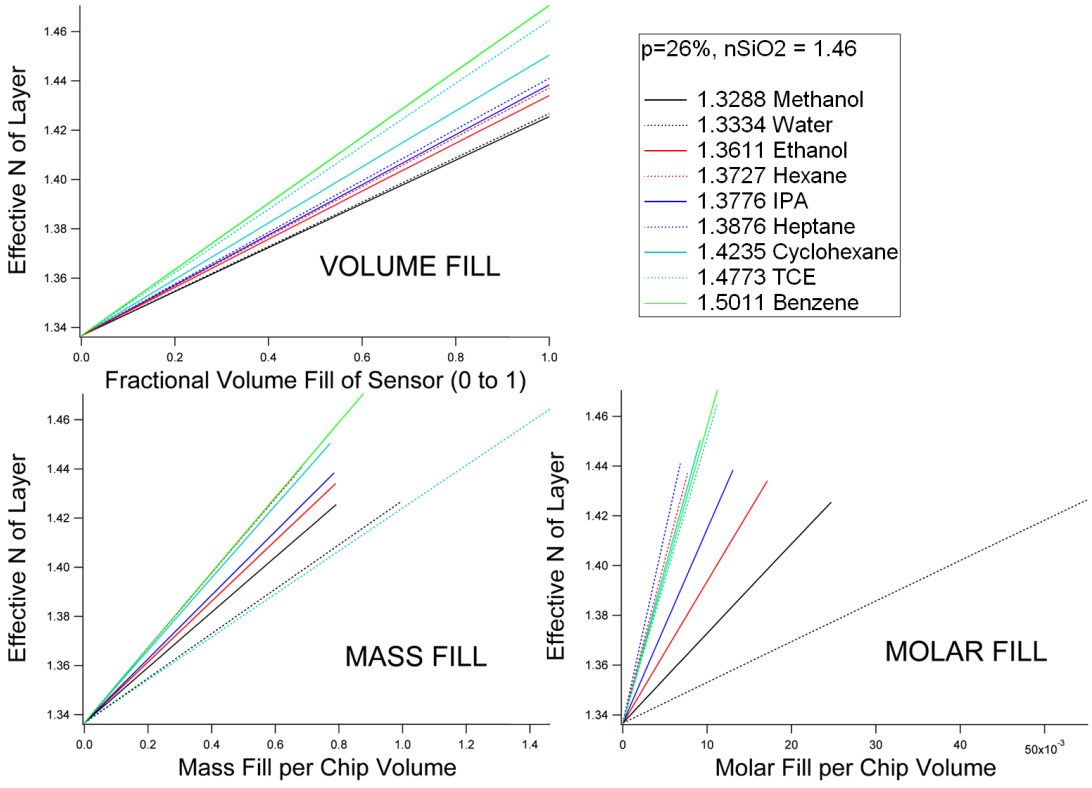

Figure A.11 Fractional volume fill (upper left) influence on the average refractive index of a porous silicon sensor layer. Lower panels display the shift for various analytes fillings in term of mass and moles per volume fraction of the chip, where mass fill is the fractional volume fill times density and molar fill is the mass fill divided by the molecular weight of the analyte.

APPENDIX B

TEMPORAL OBSERVATIONS OF A MULTILAYER RUGATE STRUCTURE

B.1 Introduction

Chapter 5 investigates the thermal desorption of volatile organic compounds from a single layer of porous silicon. Two quasi-equilibrium parameters were utilized to discriminate pure analyte vapors: the spectral shift from 25-40°C and the shift from 25-80°C.

One way to increase the discrimination capability of the porous silicon optical sensor is to introduce an orthogonal measurand based on a property other than the spectral peak shifts between temperatures, such as the rate of the spectral shifts or another temporal parameter related to the kinetics of the system. A temporal parameter based on the desorption and diffusion of vapors from a single layer, at thermal equilibrium of when heated, can inform vapor discrimination. A similar approach is to construct a multilayer stack of porous silicon layers. Temporal differences between the desorption of analyte vapors from each layer of a multilayer rugate stack can provide analyte discrimination based on kinetic information to augment the information obtained from the transient-equilibrium differences in spectral shifts between temperatures. Multilayer stacks provide the advantage of being able to independently tune the pore size and surface chemistry of each layer to create an analogue of the retention column in a gas chromatograph, with the tailored specificity of each layer influencing the rate at which different vapors desorb from the pore channels.

This appendix section lays a brief preliminary groundwork for this concept by constructing a bilayer rugate stack with a spectral peak corresponding to each layer, exposing the stack to analyte vapor, and observing the temporal difference in the

spectral shift of each layer. For comparison, a composite rugate etch, with two peaks at the same spectral positions as the bilayer and of the same thickness, is also exposed to vapor and shows no temporal difference between the shifts of each peak. This composite layer consists of a single layer etched with a waveform of the superposition of the two bilayer etch waveforms, a method of creating multiple spectral peaks in a single etch waveform described previously and extensively in the literature[8, 78]. Following this isothermal adsorption experiment, the rugate stack is heated, and a difference in the time of the spectral shifts from desorption from each layer is observed.

Multilayer rugate porous silicon stacks have been constructed previously for applications including referencing for biological sensing[86], monitoring enzyme activity with a bilayer stack of different pore sizes[93], and mitigating the influence of relative humidity in vapor sensing with a hydrophilic/phobic bilayer stack[90]. Vapor dosing of a bilayer was studied by Fuertes for multilayers of mesoporous thin films with different pore sizes in each layer, but the kinetics of the sorption were not assessed[305]. Additionally, Salem dosed a multilayer rugate stack with organic vapor to observe the response, but did not evaluate differences in the timings of each layer response, focusing instead on equilibrium responses[7].

B.2 Experimental

Sensor Preparation

Porous Si samples were prepared from single-crystal, (100)-oriented highly boron-doped p-type Si (Siltronix,, 1.3 mΩ-cm resistivity) by electrochemical etching in a 3:1 v:v solution of aqueous hydrofluoric acid:ethanol (49% hydrofluoric acid from Fisher Scientific, Inc). Etching was performed in a Teflon cell with a platinum mesh counter electrode and a galvanostat (Kepco BOP 50-4D) under computer control (LabView, National Instruments).

The bilayer stack was fabricated by the serial concatenation of two sine waves of different frequencies, with each varying between 12.5-50 mA/cm^2. The top layer of the stack (see Figure B.1) was etched with a sine wave with a period of 6.5sec for 81 cycles, followed by the bottom layer of the stack etched with a sine wave period of 8.4sec for 63 cycles. The composite layer current density-time waveform consisted of the superposition of two single-frequency sine components, expressed as functions of current density I over time t:

$$I\,(t) = \frac{\sum_{i=1}^{n} I_i}{n} \tag{B.1}$$

$$I_i(t) = I_{min} + \left[\frac{I_{max} - I_{min}}{2}\right]\left[\sin\left(\frac{2\pi t}{p_i}\right) + 1\right] \tag{B.2}$$

where n=2, I_{max}=12.5 mA/cm^2, I_{min}=50 mA/cm^2, p_1 =6.5sec and p_2=8.4sec. The composite layer was etched for a total of 1056sec to match the total etching time of the bilayer. Both the bilayer and composite layer were then oxidized for 30 minutes at 650°C in a tube furnace (Lindberg Blue).

Vapor dosing:

The vapor dosing configuration was similar to that described in Chapter 4. Briefly, a manual mass flow controller (Cole-Parmer) regulated a flow of nitrogen through a glass bubbler filled with liquid analyte. The outflow of the vapor bubbler, containing saturation analyte vapor, was diluted by joining at a T-junction with a regulated flow of nitrogen, with the resulting mix delivered to a vapor flow cell containing the sensor chip. Adsorption measurements were performed with saturation vapor pressures of analytes. Thermal desorption was performed with saturation vapor pressure of analyte and with 50% saturation vapor pressure (shown). The vapor cell consisted of a Teflon top and bottom plate, with the sensor sandwiched between and sealed with Kapton o-rings. Swagelok input and output ports of the flow cell connected it to the flow of analyte vapor from the liquid bubbler, and a glass optical window allowed visible light interrogation of the sample.

Reflectance spectra of the samples in the visible region were taken across 345-1045nm with a CCD spectrometer (Ocean Optics USB2000) and a tungsten-halogen light source (Ocean Optics LS-1) connected with a Y-branch bifurcated optical fiber. The common end of the bifurcated fiber was focused with an objective lens to a 2 mm^2 spot size on the sensor chip and positioned normal to the porous silicon sample surface. Reflectance spectra were acquired at 20Hz using SpectraSuite software (Ocean Optics).

Heating:

To heat the sensor, the backside of the bilayer sensor was coated with a thin layer of thermal compound (AOS) and placed on a resistive heater (8.0 volts applied to a 7.8Ω thin film strip heater, Minco) atop the Teflon bottom plate of the cell. A fine-

gauge thermocouple (Omega) was attached to the top of the sensor with Kapton high temperature tape (VWR) in an area not covered by the interrogating light beam, and temperature readings recorded by converting the thermocouple signal to 1mV/°C (Omega TAC80B-K) and acquiring with a digital to analog acquisition module (USB-6009, National Instruments).

B.3 Results and Discussion

The bilayer exhibits a spectral peak corresponding to each layer, with the top layer of the stack (the layer not connected to the bulk silicon) corresponding to the lower wavelength spectral band. The composite layer exhibits peaks at the same wavelengths as the bilayer, since it was constructed with sine components of the same frequency. These peaks are encoded into the entire layer structure.

The bilayer and composite layer were exposed to doses of saturation vapor pressures of isopropanol and toluene in a carrier flow of nitrogen at ambient temperature (22°C), as shown in Figure B.1. For both vapors, the bilayer exhibited a shift in the top layer stack before the bottom layer stack began to shift. In contrast, the spectral peaks of the composite layer shifted simultaneously upon analyte exposure, since the spectral peaks are encoded into the entire composite layer. The top layer adsorbs analyte before the bottom layer and shifts first, since the analyte vapor must physically traverse the top porous layer before reaching the bottom rugate stack. The timescale of the difference between the shifts of each layer is significantly faster than Knudsen diffusion and is consistent with capillary flow of condensed analyte through the top layer[235], as is expected for exposure to a dose of saturated vapor.

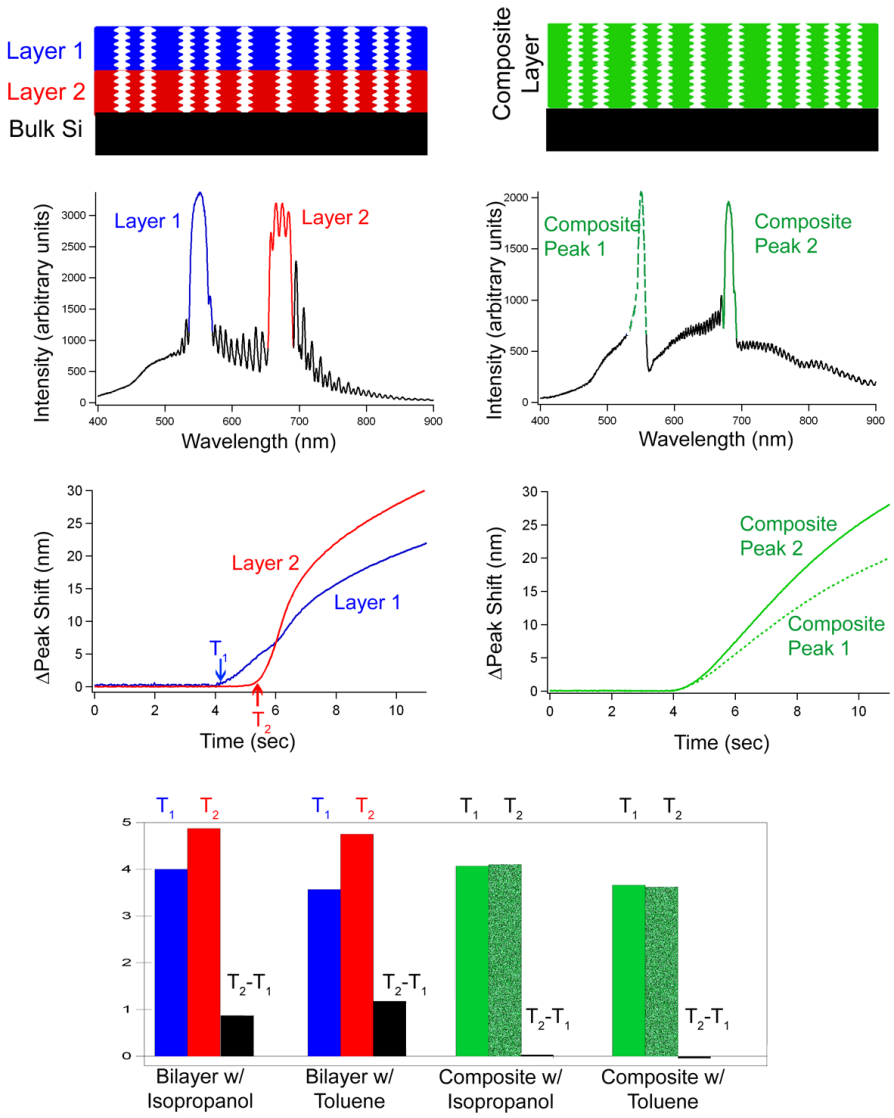

Figure B.1 A bilayer rugate stack of porous Si with two discrete layers, each exhibiting a different spectral peak (left column), and a composite layer etched with a waveform combining the two current-time single-frequency wave of the bilayer into a single etching waveform (right column). **First row:** depiction of the layer stacks**. Second row**: spectra of the bilayer and composite layer. **Third row:** dosing the rugate layers with saturated isopropanol. The bilayer shows a difference in the response times between the layers, while the spectral peaks of the composite shift simultaneously. Analyte exposure began at time T=0 sec. **Fourth row:** Time at which the lower spectral peak (upper bilayer) and upper spectral peak (lower layer stack) shifted for IPA and Toluene and the time difference between the shifts. At right, the time at which each peak of the composite peak shifted and the differences are shown for comparison.

Three vapor exposures were performed for each analyte showing excellent consistency of the temporal responses, with changes in the times at which each layer began to shift of less than 0.1sec. The sensor was purged with nitrogen to its initial baseline between each vapor exposure. In the third row of Figure B.1, the time at which the spectral peak of each layer in the bilayer, or each peak of the composite layer, began to shift is indicated. T_1 corresponds to the lower wavelength spectral peak, and T_2 to the upper wavelength peak. These times were determined as the time at which the sensor shift increased by 0.2nm above the baseline value in nitrogen (approximately 3 times the noise band). The last row of the figure plots the time at which the spectral peak for each layer (in the bilayer) shifted, as well as the difference in time between the layers. This difference in time is a kinetic parameter that could inform analyte discrimination. As expected, the composite layer showed no difference in the times at which each layer shifted, since the physically coincident peaks responded simultaneously. The bilayer exhibited a longer time delay between the layer shifts for toluene exposure than for isopropanol. This is consistent with the higher vapor pressure of isopropanol (45.5 Torr) than toluene (28.5 Torr, both at 25°C[178], since the higher vapor pressure of isopropanol may result in a lower surface affinity and a faster traversal of the top layer of the stack[185], thereby reducing the difference in shifting times between layers.

In Figure B.2, the bilayer was exposed to isopropanol vapor (segment B) and the sensor response allowed to equilibrate. The porous rugate bilayer was then heated under a continual flow of isopropanol, as shown in the left panel of Figure B.2. As with the isothermal vapor dosing shown in Figure B.1, a temporal lag between the

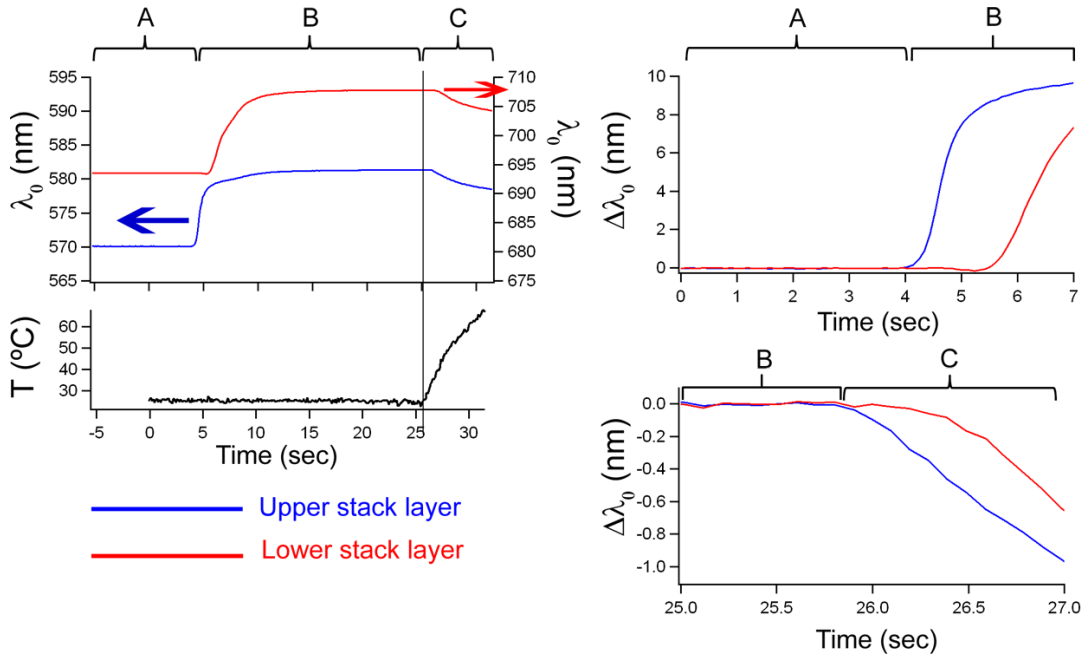

Figure B.2 Exposure of a bilayer rugate stack with two spectral peaks, one per layer, to 50% saturation isopropanol vapor, followed by heating. **Segment A**: sensor under a flow of nitrogen. **Segment B:** sensor exposed to 50% saturation IPA vapor. **Segment C:** Bilayer rugate heated, expelling the analyte from the stack**.** **Left:** spectral peak positions and temperature over the entire run. **Right top:** magnified section of the peak shifts upon vapor exposure, zeroed to the baselines in nitrogen, showing the shift of the upper stack before the lower stack peak shifts. **Right bottom:** magnified section of the peak shifts under vapor exposure when heated, zeroed to the equilibrium levels in section (B). The upper stack shifts before the lower stack when heated.

shifts of the spectral peaks for each layer were again observed, shown in the upper right panel of B.2. Upon heating (segment C), the spectral band of the upper layer of the bilayer stack shifted before the lower layer. This indicates a pore blocking mechanism[185], where the liquid analyte condensed in the upper layer of the filter must desorb and exit the layer before analyte in the underlying layer can traverse the upper layer. The difference in time between the desorption and shift of the upper layer and that of the bottom layer provides a kinetic parameter that could be applied to vapor discrimination.

B.4 Conclusions

In these preliminary observations, a temporal lag was observed between the spectral shift of the upper and lower layers of a bilayer rugate structure, upon exposure of the rugate stack to high concentrations of organic analyte vapors. As a control, a composite, single stack layer, exhibiting two rugate peaks at the same spectral positions as the bilayer and of the same thickness and porosity variation as the bilayer, showed no temporal difference in its spectral peak shifts upon vapor exposure. Heating the porous silicon bilayer under a flow of isopropanol vapor resulted in a temporal lag between the spectral shift of the upper rugate layer and lower rugate layers, paralleling the temporal lag observed for isothermal adsorption. The upper layer of the bilayer shifted first when exposed to analyte, indicating flow of liquid adsorbed from the upper to bottom layers[235], and shifted first when heated under constant vapor exposure, indicating pore blocking of the bottom layer by analyte adsorbed on the upper layer.

The temporal differences between layers suggest a means of discriminating analytes by heating multilayer porous silicon rugate structures and using the kinetic (temporal) parameter of each set of layers layer. A nanoscale analogue to a gas chromatograph retention column could be constructed by fabricating layers with different pore sizes, morphologies, and surface functionalities.

REFERENCES

1. Jane, A., R. Dronov, A. Hodges, and N.H. Voelcker, *Porous silicon biosensors on the advance.* Trends in Biotechnology, 2009. 27(4): p. 230-239.

2. Shi, J., Y. Zhu, et al., *Recent developments in nanomaterial optical sensors.* TrAC Trends in Analytical Chemistry, 2004. 23(5): p. 351-360.

3. Buriak, J.M., *Organometallic Chemistry on Silicon and Germanium Surfaces.* Chem. Rev., 2002. 102(5): p. 1272-1308.

4. Snow, P.A., E.K. Squire, P.S.J. Russell, and L.T. Canham, *Vapor sensing using the optical properties of porous silicon Bragg mirrors.* Journal of Applied Physics, 1999. 86(4): p. 1781-1784.

5. Gao, J., T. Gao, Y.Y. Li, and M.J. Sailor, *Vapor Sensors Based on Optical Interferometry from Oxidized Microporous Silicon Films.* Langmuir, 2002. 18: p. 2229-2233.

6. Stefano, L.D., L. Moretti, I. Rendina, and A.M. Rossi, *Quantitative optical sensing in two-component mixtures using porous silicon microcavities.* Phys. Status Solidi A, 2004. 201(5): p. 1011–1016.

7. Salem, M.S., M.J. Sailor, et al., *Sensitivity of porous silicon rugate filters for chemical vapor detection.* Journal of Applied Physics, 2008. 103(8).

8. Lorenzo, E., C.J. Oton, et al., *Porous silicon-based rugate filters.* Applied Optics, 2005. 44(26): p. 5415-5421.

9. Sailor, M.J. and J.R. Link, *Smart Dust: nanostructured devices in a grain of sand.* Chem. Commun., 2005: p. 1375-1383.

10. Imenes, A.G. and D.R. McKenzie, *Flat-topped broadband rugate filters.* Applied Optics, 2006. 45(30): p. 7841-7850.

11. Pacholski, C. and M.J. Sailor, *Sensing with porous silicon double layers: A general approach for background suppression.* Physica status solidi (c), 2007. 4(6): p. 2088-2092.

12. Lehmann, V., *Electrochemistry of Silicon*. 2002, Weinheim, Germany: Wiley-VCH. 51-75.

13. Uhlir, A., *Electrolytic shaping of germanium and silicon.* Bell System Tech. J., 1956. 35: p. 333-347

14. Canham, L.T., *Silicon Quantum Wire Array Fabrication by Electrochemical and Chemical Dissolution.* Appl. Phys. Lett., 1990. 57(10): p. 1046-1048.

15. Lehmann, V. and U. Gosele, *Porous Silicon Formation: a Quantum Wire Effect.* Appl. Phys. Lett., 1991. 58(8): p. 856-858.

16. Anderson, R.C., R.S. Muller, and C.W. Tobias, *Investigations of Porous Si for Vapor Sensing.* Sens. Actuators, 1990. A21-A23: p. 835-839.

17. Baratto, C., G. Faglia, et al., *A novel porous silicon sensor for detection of sub-ppm NO2 concentrations.* Sensors and Actuators B-Chemical, 2001. 77(1-2): p. 62-66.

18. Angelucci, R., A. Poggi, et al., *Porous silicon layer permeated with Sn-V mixed oxides for hydrocarbon sensor fabrication.* Thin Solid Films, 1997. 297(1-2): p. 43-47.

19. Lewis, S.E., J.R. DeBoer, J.L. Gole, and P.J. Hesketh, *Sensitive, selective, and analytical improvements to a porous silicon gas sensor.* Sensors and Actuators B-Chemical, 2005. 110(1): p. 54-65.

20. Kim, J., S. Jang, et al., *Fabrication of Multi-Optical Filters Based on Encoded Rugate Porous Silicon.* Journal of Nanoscience and Nanotechnology, 2008. 8(10): p. 4951-4957.

21. Snow, P.A., E.K. Squire, P.S.J. Russell, and L.T. Canham, *Vapor sensing using the optical properties of porous silicon Bragg mirrors.* J. Appl. Phys., 1999. 86(4): p. 1781-1784.

22. Lauerhaas, J.M., G.M. Credo, J.L. Heinrich, and M.J. Sailor, *Reversible Luminescence Quenching of Porous Si by Solvents.* J. Am. Chem. Soc., 1992. 114: p. 1911-1912.

23. Zangooie, S., R. Jansson, and H. Arwin, *Ellipsometric characterization of anisotropic porous silicon Fabry-Perot filters and investigation of temperature effects on capillary condensation efficiency.* J. Appl. Phys., 1999. 86(2): p. 850-8.

24. Schmedake, T.A., F. Cunin, J.R. Link, and M.J. Sailor, *Standoff detection of chemicals using porous silicon "Smart Dust" particles.* Adv. Mater., 2002. 14: p. 1270-1272.

25. Sohn, H., S. Létant, M.J. Sailor, and W.C. Trogler, *Detection of fluorophosphonate chemical warfare agents by catalytic hydrolysis with a porous silicon interferometer.* J. Am. Chem. Soc., 2000. 122: p. 5399-5400.
26. Song, J.H. and M.J. Sailor, *Quenching of Photoluminescence from Porous Silicon by Aromatic Molecules.* J. Am. Chem. Soc., 1997. 119(31): p. 7381-7385.

27. Janshoff, A., K.-P.S. Dancil, et al., *Macroporous p-type silicon Fabry-Perot layers. Fabrication, characterization, and applications in biosensing.* J. Am. Chem. Soc., 1998. 120(46): p. 12108-12116.

28. Chan, S., P.M. Fauchet, et al., *Porous silicon microcavities for biosensing applications.* Phys. Status Solidi A-Appl. Res., 2000. 182(1): p. 541-546.

29. Létant, S.E., B.R. Hart, et al., *Enzyme immobilization on porous silicon surfaces.* Adv. Mater., 2004. 16(8): p. 689-693.

30. Content, S., W.C. Trogler, and M.J. Sailor, *Detection of Nitrobenzene, DNT and TNT Vapors by Quenching of Porous Silicon Photoluminescence.* Chem. Europ. J., 2000. 6(12): p. 2205-2213.

31. Canham, L., *Properties of Porous Silicon*. EMIS Datareviews, ed. B.L. Weiss. Vol. 18. 1997, London: Institution of Engineering and Technology. 1-405.

32. Lu, C.J., W.H. Steinecker, et al., *First-generation hybrid MEMS gas chromatograph.* Lab on a Chip, 2005. 5(10): p. 1123-1131.

33. Johnson, W.E. and R.L. Crane. *Introduction to rugate filter technology*. in *Inhomogeneous and Quasi-Inhomogeneous Optical Coatings*. 1993. Quebec City, Canada: SPIE.

34. Ishikura, N., M. Fujii, et al., *Porous silicon based extended-bandwidth rugate filters for mid-infrared application.* Infrared Physics & Technology, 2010. 53(4): p. 292-294.

35. Cunin, F., T.A. Schmedake, et al., *Biomolecular screening with encoded porous silicon photonic crystals.* Nature Mater., 2002. 1: p. 39-41.

36. Meade, S.O., M.Y. Chen, M.J. Sailor, and G.M. Miskelly, *Multiplexed DNA Detection Using Spectrally Encoded Porous SiO2 Photonic Crystal Particles.* Analytical Chemistry, 2009. 81(7): p. 2618-2625.

37. King, B.H., A.M. Ruminski, J.L. Snyder, and M.J. Sailor, *Optical fiber-mounted porous silicon photonic crystals for sensing of organic vapor breakthrough in activated carbon.* Adv. Mater., 2007. 19(24): p. 4530 - 4534.

38. Wolfbeis, O.S., *Fiber-Optic Chemical Sensors and Biosensors.* Anal. Chem., 2006. 78(12): p. 3859-3874.
39. *Optical Fiber Sensor Technology*, ed. K.T.V. Grattan and B.T. Meggitt. 2000, Boston: Kluwer Academic Publishers.

40. Korposh, S., R. Selyanchyn, and S.W. Lee, *Nano-assembled thin film gas sensors. IV. Mass-sensitive monitoring of humidity using quartz crystal microbalance (QCM) electrodes.* Sensors and Actuators B-Chemical. 147(2): p. 599-606.

41. Moretti, L., I. Rea, L. De Stefano, and I. Rendina, *Periodic versus aperiodic: Enhancing the sensitivity of porous silicon based optical sensors.* Applied Physics Letters, 2007. 90(19): p. 191112-3.

42. Archer, M., M. Christophersen, and P.M. Fauchet, *Electrical porous silicon chemical sensor for detection of organic solvents.* Sensors and Actuators B-Chemical, 2005. 106(1): p. 347-357.

43. Archuleta-Garcia, R., D. Moctezuma-Enriquez, and J. Manzanares-Martinez, *Enlargement of Photonic Band Gap in Porous Silicon Dielectric Mirrors.* Journal of Electromagnetic Waves and Applications. 24(2-3): p. 351-361.

44. Lo, S.Z.A. and T.E. Murphy, *Nanoporous silicon multilayers for terahertz filtering.* Optics Letters, 2009. 34(19): p. 2921-2923.

45. Richard, C., A. Renaudin, V. Aimez, and P.G. Charette, *An integrated hybrid interference and absorption filter for fluorescence detection in lab-on-a-chip devices.* Lab on a Chip, 2009. 9(10): p. 1371-1376.

46. Bjorklund, R.B., S. Zangooie, and H. Arwin, *Color changes in thin porous silicon films caused by vapor exposure.* Appl. Phys. Lett., 1996. 69(20): p. 3001-3.

47. Wei, J., J.M. Buriak, and G. Siuzdak, *Desorption-ionization mass spectrometry on porous silicon.* Nature, 1999. 399: p. 243-246.

48. Chan, S., S. Kwon, et al., *SERS of small molecules from silver-coated silicon nanopores.* Adv. Mater., 2003. 15(19): p. 1595-1598.

49. Rittersma, Z.M., A. Splinter, A. Bodecker, and W. Benecke, *A novel surface-micromachined capacitive porous silicon humidity sensor.* Sens. Actuators B, 2000. B68(1-3): p. 210-17.

50. Ben-Chorin, M., A. Kux, and I. Schechter, *Adsorbate effects on photoluminescence and electrical conductivity of porous silicon.* Appl. Phys. Lett., 1994. 64(4): p. 481-483.
51. Yarkin, D.G., *Impedance of humidity sensitive metal/porous silicon/n-Si structures.* Sensors and Actuators a-Physical, 2003. 107(1): p. 1-6.

52. Barillaro, G., A. Diligenti, et al., *Low-Concentration NO2 Detection With an Adsorption Porous Silicon FET.* IEEE Sensors Journal, 2006. 6(1): p. 19-21.

53. Sa'ar, A., *Photoluminescence from silicon nanostructures: The mutual role of quantum confinement and surface chemistry.* J. Nanophotonics, 2009. 3: p. 032501.

54. Gaburro, Z., N. Daldosso, et al., *Monitoring penetration of ethanol in a porous silicon microcavity by photoluminescence interferometry.* Applied Physics Letters, 2001. 78(23): p. 3744-3746.

55. Canaria, C.A., M. Huang, et al., *The effect of surfactants on the reactivity and photophysics of luminescent nanocrystalline porous silicon.* Adv. Funct. Mater., 2002. 12(8): p. 495-500.

56. Curtis, C.L., V.V. Doan, G.M. Credo, and M.J. Sailor, *Observation of Optical Cavity Modes in Photoluminescent Porous Silicon Films.* J. Electrochem. Soc., 1993. 140(12): p. 3492-3494.

57. Ouyang, H., M. Christophersen, et al., *Macroporous silicon microcavities for macromolecule detection.* Adv. Funct. Mater., 2005. 15(11): p. 1851-1859.

58. Volk, J., T. Le Grand, et al., *Porous silicon multilayer stack for sensitive refractive index determination of pure solvents.* Journal of Physics D-Applied Physics, 2005. 38(8): p. 1313-1317.

59. Dancil, K.-P.S., D.P. Greiner, and M.J. Sailor, *A porous silicon optical biosensor: detection of reversible binding of IgG to a protein A-modified surface.* J. Am. Chem. Soc., 1999. 121(34): p. 7925-7930.

60. Letant, S.E. and M.J. Sailor, *Molecular identification by time-resolved interferometry in a porous silicon film.* Advanced Materials, 2001. 13(5): p. 335-338.

61. Link, J.R. and M.J. Sailor, *Smart Dust: Self-assembling, self-orienting photonic crystals of porous Si.* Proc. Nat. Acad. Sci., 2003. 100(19): p. 10607-10610.

62. Shih, S., K.H. Jung, et al., *Photoluminescence and Formation Mechanism of Chemically Etched Silicon.* Applied Physics Letters, 1992. 60(15): p. 1863-1865.

63. Zhang, X.G., *Morphology and Formation Mechanisms of Porous Silicon.* J. Electrochem. Soc., 2004. 151(1): p. C69-C80.

64. Lowell, S., J.E. Shields, M.A. Thomas, and M. Thommes, *Characterization of Porous Solids and Powders: Surface Area, Pore Size and Density*. 2004, The Netherlands: Kluwer Academic Publishers.

65. Lehmann, V. and H. Foll, *Formation Mechanism and Properties of Electrochemically Etched Trenches in n-Type Silicon.* J. Electrochem. Soc., 1990. 137(2): p. 653-659.

66. Lehmann, V. and U. Gosele, *Porous Si: Quantum Sponge Structures Grown via a Self-Adjusting Etching Process.* Adv. Mater., 1992. 4: p. 114-116.

67. Foll, H., M. Christopherson, J. Carstensen, and G. Haase, *Formation and application of porous silicon.* Mater. Sci. Eng. R, 2002. 39: p. 93-141.

68. Beale, M.I.J., J.D. Benjamin, et al., *An Experimental and Theoretical Study of the Formation and Microsctructure of Porous Silicon.* Journal of Crystal Growth, 1985. 73(3): p. 622-636.

69. Agarwal, V. and J.A. del Rio, *Tailoring the photonic band gap of a porous silicon dielectric mirror.* Applied Physics Letters, 2003. 82(10): p. 1512-1514.

70. Pavesi, L. and P. Dubos, *Random porous silicon multilayers: application to distributed Bragg reflectors and interferential Fabry-Perot filters.* Semicon. Sci. Tech., 1997. 12(5): p. 570-5.

71. Pacholski, C., C. Yu, et al., *Reflective interferometric Fourier transform spectroscopy: A self-compensating label-free immunosensor using double-layers of porous SiO2.* Journal of the American Chemical Society, 2006. 128(13): p. 4250-4252.

72. Macleod, H.A., *Thin-Film Optical Filters, Third Ed.* 2001, London: Taylor & Francis.

73. Parker, G. and M. Charlton, *Photonic crystals.* Physics World, 2000. 13(8): p. 29-34.

74. Choi, S.Y., M. Mamak, et al., *Mesoporous Bragg Stack Color Tunable Sensors.* Nano Lett., 2006. 6(11): p. 2456-2461.

75. Kronenberg, P., P.K. Rastogi, P. Giaccari, and H.G. Limberger, *Relative humidity sensor with optical fiber Bragg gratings.* Optics Letters, 2003. 27(16): p. 1385-1387.
76. Berger, M.G., R. Arens-Fischer, et al., *Dielectric filters made of PS: advanced performance by oxidation and new layer structures.* Thin Solid Films, 1997. 297(1-2): p. 237-240.

77. Jalkanen, T., V. Torres-Costa, et al., *Optical gas sensing properties of thermally hydrocarbonized porous silicon Bragg reflectors.* Optics Express, 2009. 17(7): p. 5446-5456.

78. Meade, S.O. and M.J. Sailor, *Microfabrication of freestanding porous silicon particles containing spectral barcodes.* Phys. Status Solidi-Rapid Res. Lett., 2007. 1(2): p. R71-R73.

79. Bartholomew, C.S., M.D. Morrow, et al., *Rugate Filters by Laser Flash Evaporation of SiOxNy on Room-Temperature Polycarbonate.* Journal of Vacuum Science & Technology a-Vacuum Surfaces and Films, 1988. 6(3): p. 1703-1707.

80. Gunning, W.J., R.L. Hall, et al., *Codeposition of Continuous Composition Rugate Filters.* Applied Optics, 1989. 28(14): p. 2945-2948.

81. Robbie, K., A.J.P. Hnatiw, et al., *Inhomogeneous thin film optical filters fabricated using glancing angle deposition.* Electronics Letters, 1997. 33(14): p. 1213-1214.

82. Jankowski, A.F., L.R. Schrawyer, and P.L. Perry, *Reactive Sputtering of Molybdenum-Oxide Gradient-Index Filters.* Journal of Vacuum Science & Technology a-Vacuum Surfaces and Films, 1991. 9(3): p. 1184-1187.

83. Swart, P.L., P.V. Bulkin, and B.M. Lacquet, *Rugate filter manufacturing by electron cyclotron resonance plasma-enhanced chemical vapor deposition of SiNx.* Optical Engineering, 1997. 36(4): p. 1214-1219.

84. Kaminska, K., T. Brown, G. Beydaghyan, and K. Robbie, *Vacuum Evaporated Porous Silicon Photonic Interference Filters.* Applied Optics, 2003. 42(20): p. 4212-4219.

85. Meade, S.O., M.S. Yoon, K.H. Ahn, and M.J. Sailor, *Porous silicon photonic crystals as encoded microcarriers.* Adv. Mater., 2004. 16(20): p. 1811-1814.

86. Pacholski, C., M. Sartor, et al., *Biosensing using porous silicon double-layer interferometers: reflective interferometric Fourier transform spectroscopy.* J. Am. Chem. Soc., 2005. 127(33): p. 11636-11645.

87. Orosco, M.M., C. Pacholski, G.M. Miskelly, and M.J. Sailor, *Protein-coated porous silicon photonic crystals for amplified optical detection of protease activity.* Adv. Mater., 2006. 18: p. 1393-1396.

88. Ilyas, S., P.J. Reece, et al. *Porous Silicon Based Rugate Filters*. in *Optoelectronic and Microelectronic Materials and Devices, 2004 Conference on*. 2004.

89. Abusafia, H.A., A.I. Alsharif, and I.O. Abualjarayesh, *Rugate Filter Sidelobe Suppression Using Half-Apodization.* Applied Optics, 1993. 32(25): p. 4831-4835.

90. Ruminski, A.M., M.M. Moore, and M.J. Sailor, *Humidity-Compensating Sensor for Volatile Organic Compounds using Stacked Porous Silicon Photonic Crystals.* Adv. Funct. Mater., 2008. 18(21): p. 3418-3426.

91. Jang, S., Y. Koh, et al., *Detection of organophosphates based on surface-modified DBR porous silicon using LED light.* Materials Letters, 2008. 62(3): p. 552-555.

92. Gao, J., T. Gao, and M.J. Sailor, *Porous-silicon vapor sensor based on laser interferometry.* Applied Physics Letters, 2000. 77(6): p. 901-903.

93. Orosco, M.M., C. Pacholski, and M.J. Sailor, *Real-time monitoring of enzyme activity in a mesoporous silicon double layer.* Nature Nanotech., 2009. 4: p. 255 - 258.

94. Pacholski, C., L.A. Perelman, M.S. VanNieuwenhze, and M.J. Sailor, *Small molecule detection by reflective interferometric Fourier transform spectroscopy (RIFTS).* Phys. Status Sol. A, 2009. on line: p. NA.

95. Salem, M.S., M.J. Sailor, et al., *Electrochemical stabilization of porous silicon multilayers for sensing various chemical compounds.* Journal of Applied Physics, 2006. 100(8).

96. Gao, J., T. Gao, and M.J. Sailor, *A porous silicon vapor sensor based on laser interferometry.* Appl. Phys. Lett., 2000. 77(6): p. 901-3.

97. Gao, T., J. Gao, and M.J. Sailor, *Tuning the response and stability of thin film mesoporous silicon vapor sensors by surface modification.* Langmuir, 2002. 18(25): p. 9953-9957.

98. Jang, S.H., Y.D. Koh, et al., *Detection of organophosphates based on surface-modified DBR porous silicon using LED light.* Materials Letters, 2008. 62(3): p. 552-555.

99. Lin, V.S.-Y., K. Motesharei, et al., *A Porous Silicon-Based Optical Interferometric Biosensor.* Science, 1997. 278(5339): p. 840-843.

100. Kolasinski, K.W., *Silicon nanostructures from electroless electrochemical etching.* Current Opinion in Solid State & Materials Science, 2005. 9(1-2): p. 73-83.

101. Dudley, M.E. and K.W. Kolasinski, *Structure and photoluminescence studies of porous silicon formed in ferric ion containing stain etchants.* Physica Status Solidi a-Applications and Materials Science, 2009. 206(6): p. 1240-1244.

102. Israelachvili, J.N., *Intermolecular and surface forces*. 2nd ed. 1992, London: Academic Press London. 331.

103. Adamson, A.W., *Physical Chemistry of Surfaces*. 5th ed. 1990, New York: John Wiley & Sons, inc. 58-59.

104. Casanova, F., C.E. Chiang, C.P. Li, and I.K. Schuller, *Direct observation of cooperative effects in capillary condensation: The hysteretic origin.* Applied Physics Letters, 2007. 91(24).

105. Albert, K.J., N.S. Lewis, et al., *Cross-reactive chemical sensor arrays.* Chemical Reviews, 2000. 100(7): p. 2595-2626.

106. Rickert, J., T. Weiss, and W. Gopel, *Self-assembled monolayers for chemical sensors: Molecular recognition by immobilized supramolecular structures.* Sensors and Actuators B-Chemical, 1996. 31(1-2): p. 45-50.

107. Jaras, K., A. Ressine, et al., *Reverse-Phase versus Sandwich Antibody Microarray, Technical Comparison from a Clinical Perspective.* Analytical Chemistry, 2007. 79(15): p. 5817-5825.

108. Schwartz, M.P., S.D. Alvarez, and M.J. Sailor, *Porous SiO2 interferometric biosensor for quantitative determination of protein interactions: Binding of protein a to immunoglobulins derived from different species.* Analytical Chemistry, 2007. 79(1): p. 327-334.

109. Rocchia, M.A., E. Garrone, et al., *Sensing CO2 in a chemically modified porous silicon film.* Phys. Status Solidi A-Appl. Mater., 2003. 197(2): p. 365-369.

110. Lin, H., T. Gao, J. Fantini, and M.J. Sailor, *A Porous Silicon-Palladium Composite Film for Optical Interferometric Sensing of Hydrogen.* Langmuir, 2004. 20: p. 5104-5108.
111. Letant, S.E. and M.J. Sailor, *Detection of HF gas with a porous silicon interferometer.* Advanced Materials, 2000. 12(5): p. 355-+.

112. Buriak, J.M., *Organometallic chemistry on silicon surfaces: formation of functional monolayers bound through Si-C bonds.* Chem. Commun., 1999. 12: p. 1051-1060.

113. Lewis, N.S., *Progress in understanding electron-transfer reactions at semiconductor/liquid interfaces.* J. Phys. Chem. B, 1998. 102(25): p. 4843-55.

114. Chazalviel, J.-N., *Surface methoxylation as the key factor for the good performance of n-Si/methanol photoelectrochemical cells.* J. Electroanal. Chem., 1987. 233: p. 37-48.

115. Salonen, J., V.P. Lehto, et al., *Studies of thermally-carbonize porous silicon surfaces.* Phys. Status Solidi A-Appl. Res., 2000. 182(1): p. 123-126.

116. Heilig, A., N. Barsan, et al., *Gas identification by modulating temperatures of SnO2-based thick film sensors.* Sensors and Actuators B-Chemical, 1997. 43(1-3): p. 45-51.

117. Lee, A.P. and B.J. Reedy, *Temperature modulation in semiconductor gas sensing.* Sensors and Actuators B-Chemical, 1999. 60(1): p. 35-42.

118. Nakata, S., M. Nakasuji, N. Ojima, and M. Kitora, *Characteristic nonlinear responses for gas species on the surface of different semiconductor gas sensors.* Applied Surface Science, 1998. 135(1-4): p. 285-292.

119. Collins, B.E., K.-P. Dancil, G. Abbi, and M.J. Sailor, *Determining protein size using an electrochemically machined pore gradient in silicon.* Adv. Funct. Mater., 2002. 12(3): p. 187-191.

120. Malnic, B., J. Hirono, T. Sato, and L.B. Buck, *Combinatorial receptor codes for odors.* Cell, 1999. 96(5): p. 713-723.

121. Jurs, P.C., G.A. Bakken, and H.E. McClelland, *Computational methods for the analysis of chemical sensor array data from volatile analytes.* Chemical Reviews, 2000. 100(7): p. 2649-2678.

122. Aernecke, M.J. and D.R. Walt, *Optical-fiber arrays for vapor sensing.* Sensors and Actuators B-Chemical, 2009. 142(2): p. 464-469.

123. Raman, B., D.C. Meier, J.K. Evju, and S. Semancik, *Designing and optimizing microsensor arrays for recognizing chemical hazards in complex environments.* Sensors and Actuators B-Chemical, 2009. 137(2): p. 617-629.
124. Li, B., S. Santhanam, et al., *Inkjet printed chemical sensor array based on polythiophene conductive polymers.* Sensors and Actuators B-Chemical, 2007. 123(2): p. 651-660.

125. Severin, E.J., B.J. Doleman, and N.S. Lewis, *An investigation of the concentration dependence and response to analyte mixtures of carbon black/insulating organic polymer composite vapor detectors.* Analytical Chemistry, 2000. 72(4): p. 658-668.

126. Lonergan, M.C., E.J. Severin, et al., *Array-based vapor sensing using chemically sensitive, carbon black-polymer resistors.* Chemistry of Materials, 1996. 8(9): p. 2298-2312.

127. Grate, J.W., *Acoustic wave microsensor arrays for vapor sensing.* Chemical Reviews, 2000. 100(7): p. 2627-2647.

128. Lin, H., J. Mock, et al., *Surface-Enhanced Raman Scattering from Silver-Plated Porous Silicon.* J. Phys. Chem. B, 2004. 108(31): p. 11654 -11659.

129. Walt, D.R., *Molecular Biolgoy:Bead-based Fiber-Optic Arrays.* Science, 2000. 287(5452): p. 451-452.

130. Wolfbeis, O.S., *Materials for fluorescence-based optical chemical sensors* J. Mater Chem., 2005. 15: p. 2657.

131. Lee, B., *Review of the present status of optical fiber sensors.* Optical Fiber Technology, 2003. 9(2): p. 57-79.

132. *Optical Sensors: Industrial, Environmental, and Diagnostic Applications*. Optical Sensors, ed. O.S. Wolfbeis. Vol. 1. 2004, New York: Springer.

133. Barnard, S.M. and D.R. Walt, *Fiber-optic organic vapor sensor.* Environ. Sci. Technol., 1991. 25(7): p. 1301-1304.

134. Wang, A., G.Z. Wang, K.A. Murphy, and R.O. Claus, *Fiber-optic temperature sensors based on differential spectral transmittance/reflectivity and multiplexed sensing systems.* Applied Optics, 1995. 34(13): p. 2295-2300.

135. Mitschke, F., *Fiber-optic sensor for humidity.* Optics Letters, 1989. 14(17): p. 967-969.

136. Bureau of Labor Statistics / NIOSH, *Respirator Usage in Private Sector Firms.* 2001.

137. Moyer, E.S., M.W. Findlay, G.J. Maclay, and J.R. Stetter, *Preliminary Evaluation of an Active End-of-Service-Life Indicator for Organic Vapor Cartridge Respirators.* American Industrial Hygiene Association journal, 1993. 54(8): p. 417-425.

138. Favas, G., *End of Service Life Indicator (ESLI) for Respirator Cartridges. Part I: Literature Review*. 2005, Australian Government Department of Defense, DSTO-TN-0657.

139. NIOSH, *Certification Criteria.* Certification Criteria, 2005. Procedure No. RCT-APR-STP-0066.

140. OSHA, *Respiratory Protection*. 2006, U.S. Department of Labor.

141. Lorenzo, E., C.J. Oton, et al., *Porous silicon-based rugate filters.* Appl. Opt., 2005. 44(26): p. 5414.

142. Linstrom, P.J. and W.G. Mallard, *NIST Chemistry WebBook, NIST Standard Reference Database Number 69.* June 2005, Gaithersburg, MD: National Institute of Standards and Technology.

143. *CRC Handbook of Chemistry and Physics*. 87th ed, ed. D.R. Lide. 2007, Boca Raton, FL: CRC Press, Inc.

144. Cheng, H. and M. Reinhard, *Sorption of Trichloroethylene in Hydrophobic Micropores of Dealuminated Y Zeolites and Natural Minerals*. Environ. Sci. Technol., 2006. 40(24): p. 7694-7701.

145. Farrell, J., B. Hauck, and M. Jones, *Thermodynamic Investigation of Trichloroethylene Adsorption in Water-Saturated Microporous Adsorbents.* Environmental Toxicology and Chemistry, 1999. 18(8): p. 1637-1642.

146. Linders, M.J.G., L.J.P. van den Broeke, et al., *Binary adsorption equilibrium of organics and water on activated carbon.* AIChE Journal, 2001. 47(8): p. 1885-1892.

147. Yang, R.T., *Adsorbents: fundamentals and applications*. 2003, Hoboken, N.J.: Wiley-Interscience.

148. Adams, L.B., C.R. Hall, R.J. Holmes, and R.A. Newton, *An examination of how exposure to humid air can result in changes in the adsorption properties of activated carbons.* Carbon, 1988. 26(4): p. 451-459.

149. Tanaka, S., Y. Tsuda, et al., *A Simple Method for Detecting Breakthroughs in Used Chemical Cartridges.* AIHAJ - American Industrial Hygiene Association, 2001. 62(2): p. 168-171.

150. Caron, S., P. Bernard, M. Vernon, and J. Lara, *Porous glass optical fiber sensor as an end-of-service indicator for respiratory cartridges.* Sensors and Actuators B: Chemical, 2004. 102(2): p. 198-206.

151. Boukherroub, R., J.T.C. Wojtyk, D.D.M. Wayner, and D.J. Lockwood, *Thermal hydrosilylation of undecylenic acid with porous silicon.* J. Electrochem. Soc., 2002. 149(2): p. 59-63.

152. Linders, M.J.G., L.J.P. Van Den Broeke, et al., *Effect of the adsorption isotherm on one- and two-component diffusion in activated carbon.* Carbon, 1997. 35(9): p. 1415-1425.

153. Linders, M.J.G., L.J.P. van den Broeke, et al., *Modelling sorption and diffusion in activated carbon: a novel low pressure pulse-response technique.* Carbon, 2001. 39(14): p. 2113-2130.

154. Stakgold, I., *Gas-solid reaciton with porosity change.* Electronic Journal of Differential Equations, 2000. 5: p. 247-252.

155. Lauerhaas, J.M. and M.J. Sailor, *Chemical Modification of the Photoluminescence Quenching of Porous Silicon.* Science, 1993. 261: p. 1567-1568.

156. Connolly, E.J., B. Timmer, et al., *A porous SiC ammonia sensor.* Sens. Actuators B, 2005. 109: p. 44-46.

157. Sailor, M.J., *Sensor Applications of Porous Silicon*, in *Properties of Porous Silicon*, L. Canham, Editor. 1997, Institution of Engineering and Technology: London. p. 364-370.

158. Berger, M.G., R. Arens-Fischer, et al., *Dielectric filters made of porous silicon: advanced performance by oxidation and new layer structures.* Thin Sol. Films, 1997. 297(1-2): p. 237-240.

159. Song, J.H. and M.J. Sailor, *Chemical modification of crystalline porous silicon surfaces.* Comments Inorganic Chem., 1999. 21(1-3): p. 69-84.

160. Gurtner, C., A.W. Wun, and M.J. Sailor, *Surface modification of porous silicon by electrochemical reduction of organo halides.* Angew. Chem. Int. Ed., 1999. 38(13/14): p. 1966-1968.

161. Linford, M.R., P. Fenter, P.M. Eisenberger, and C.E.D. Chidsey, *Alkyl monolayers on silicon prepared from 1-alkenes and hydrogen-terminated silicon.* J. Am. Chem. Soc., 1995. 117: p. 3145-3155.

162. Buriak, J.M. and M.J. Allen, *Lewis Acid Mediated Functionalization of Porous Silicon with Substituted Alkenes and Alkynes.* J. Am. Chem. Soc., 1998. 120(6): p. 1339-1340.

163. Stewart, M.P. and J.M. Buriak, *Photopatterned hydrosilylation on porous silicon.* Angew. Chem. Int. Ed. Engl., 1998. 37(23): p. 3257-3260.

164. Salonen, J., E. Laine, and L. Niinisto, *Thermal carbonization of porous silicon surface by acetylene.* J. Appl. Phys., 2002. 91(1): p. 456-461.

165. Salonen, J., M. Bjorkqvist, E. Laine, and L. Niinisto, *Stabilization of porous silicon surface by thermal decomposition of acetylene.* Appl. Surf. Sci., 2004. 225(1-4): p. 389-394.

166. Salonen, J., J. Tuura, M. Bjorkqvist, and V.P. Lehto, *Sub-ppm trace moisture detection with a simple thermally carbonized porous silicon sensor.* Sens. Actuator B-Chem., 2006. 114(1): p. 423-426.

167. Bjorkqvist, M., J. Paski, J. Salonen, and V.P. Lehto, *Studies on hysteresis reduction in thermally carbonized porous silicon humidity sensor.* IEEE Sens. J., 2006. 6(3): p. 542-547.

168. Bjorkqvist, M., J. Paski, J. Salonen, and V.P. Lehto, *Temperature dependence of thermally-carbonized porous silicon humidity sensor.* Phys. Status Solidi A-Appl. Mat., 2005. 202(8): p. 1653-1657.

169. Bjorkqvist, M., J. Salonen, and E. Laine, *Humidity behavior of thermally carbonized porous silicon.* Appl. Surf. Sci., 2004. 222(1-4): p. 269-274.

170. Halimaoui, A., *Porous silicon formation by anodisation*, in *Properties of Porous Silicon*, L. Canham, Editor. 1997, Short Run Press Ltd.: London. p. 12-22.

171. Masayuki, N., *Dehydration of Gels and Glasses in the Systems B2O3-SiO2 and ZrO2-SiO2 Prepared by the Sol-Gel Process from Metal Alkoxides.* J. Am. Ceram. Soc., 1984. 67(12): p. C-258-C-259.

172. Brinker, C.J., E.P. Roth, G.W. Scherer, and D.R. Tallant, *Structural evolution during the gel to glass conversion.* Journal of Non-Crystalline Solids, 1985. 71(1-3): p. 171-185.

173. Brinker, C.J. and S.P. Mukherjee, *Conversion of monolithic gels to glasses in a multicomponent silicate glass system.* J. Mater. Sci., 1981. 16(7): p. 1980-1988.

174. Salonen, J., E. Laine, and L. Niinisto, *Thermal carbonization of porous silicon surface by acetylene.* Journal of Applied Physics, 2002. 91(1): p. 456-461.

175. Bateman, J.E., R.D. Eagling, et al., *Alkylation of porous silicon by direct reaction with alkenes and alkynes.* Angew. Chem. Int. Ed., 1998. 37(19): p. 2683-2685.

176. Kurokawa, A. and S. Ichimura, *High purity ozone oxidation on hydrogen passivated silicon surface.* Appl. Surf. Sci., 1996. 100/101: p. 436-439.

177. Paski, J., M. Bjorkqvist, J. Salonen, and V.-P. Lehto, *Effects of treatment temperature on thermally-carbonized porous silicon hygroscopy.* Physica status solidi (c), 2005. 9: p. 3379-3383.

178. Kent, J.A., *Kent and Riegel's Handbook of Industrial Chemistry and Biotechnology*. 2007, Springer-Verlag.

179. Donaldson, S.L. and D.B. Miracle, *ASM Handbook*. Vol. 21: Composites. 2001: ASM International.

180. *Formulating with Dow Epoxy Resin.* Dow Chemical Company, form No. 296-346-1289.

181. *Chemical Resistance for Ambient Cure Epoxy Formulations.* Air Products and Chemicals, Inc., 1996. Pub No. 125-9326.

182. *Dow Liquid Epoxy Resins.* Dow Chemical Company, form No. 296-00224-0199 WC+M, 1999.

183. *Dow Epoxy Novolac Resins.* Dow Chemical Company, form No. 296-00279-1098 SMG, 1998.

184. *Epoxy Additives and Resins.* Air Products and Chemicals, Inc., 2006. Pub No. 125-06-014-US.

185. Do, D.D., *Adsorption Analysis: Equilibria and Kinetics*. Series on Chemical Engineering. Vol. 2. 1998, London: Imperial College Press.

186. Salonen, J., M. Bjorkqvist, E. Laine, and L. Niinisto, *Stabilization of porous silicon surface by thermal decomposition of acetylene.* Applied Surface Science, 2004. 225(1-4): p. 389-394.

187. Salonen, J., M. Bjorkqvist, and J. Paski, *Temperature-dependent electrical conductivity in thermally carbonized porous silicon.* Sensors and Actuators a-Physical, 2004. 116(3): p. 438-441.

188. *NIOSH Pocket Guide to Chemical Hazards*. 2005: National Institute of Occupational Safety and Health of the United States, Publication #2005-149.

189. Ferguson, J.A., B.G. Healey, et al., *Simultaneous monitoring of pH, CO2 and O2 using an optical imaging fiber.* Analytica Chimica Acta, 1997. 340(1-3): p. 123-131.

190. Epstein, J.R. and D.R. Walt, *Fluorescence-based fibre optic arrays: a universal platform for sensing.* Chem. Soc. Rev., 2003. 32(4): p. 203-214.

191. Ferguson, J.A., T.C. Boles, C.P. Adams, and D.R. Walt, *A fiber-optic DNA biosensor microarray for the analysis of gene expression.* Nat. Biotechnol., 1996. 14: p. 1681-1684.

192. Brogan, K.L. and D.R. Walt, *Optical fiber-based sensors: application to chemical biology.* Current Opinion in Chemical Biology, 2005. 9(5): p. 494-500.

193. Schwartz, M.P., S.D. Alvarez, and M.J. Sailor, *A Porous SiO2 Interferometric Biosensor for Quantitative Determination of Protein Interactions: Binding of Protein A to Immunoglobulins Derived from Different Species.* Anal. Chem., 2007. 79: p. 327-334.

194. Lee, J.W., D.Y. Choi, et al. *Adsorption dynamics of water vapor on activated carbon*. 2005.

195. Wood, G.O., *Estimating service lives of organic vapor cartridges II: A single vapor at all humidities.* Journal of Occupational and Environmental Hygiene, 2004. 1(7): p. 472-492.

196. Wood, G.O. and J.L. Snyder, *Estimating service lives of organic vapor cartridges III: Multiple vapors at all humidities.* Journal of Occupational and Environmental Hygiene, 2007. 4(5): p. 363-374.

197. Qi, N., W.S. Appel, M.D. LeVan, and J.E. Finn, *Adsorption dynamics of organic compounds and water vapor in activated carbon beds.* Industrial & Engineering Chemistry Research, 2006. 45(7): p. 2303-2314.

198. Tien, C., *Adsorption Calculations and Modeling*. 1994, Newton: Butterworth-Heinemann.

199. Franke, M.E., T.J. Koplin, and U. Simon, *Metal and metal oxide nanoparticles in chemiresistors: Does the nanoscale matter?* Small, 2006. 2(1): p. 36-50.

200. Rittersma, Z.M., *Recent achievements in miniaturised humidity sensors--a review of transduction techniques.* Sensors and Actuators A: Physical, 2002. 96(2-3): p. 196-210.

201. Kang, U.S. and K.D. Wise, *A high-speed capacitive humidity sensor with on-chip thermal reset.* Ieee Transactions on Electron Devices, 2000. 47(4): p. 702-710.

202. Semancik, S., R.E. Cavicchi, et al. *Microhotplate platforms for chemical sensor research*. 2001.

203. Rittersma, Z.M., W.J. Zaagman, M. Zetstra, and W. Benecke, *A monitoring instrument with capacitive porous silicon humidity sensors.* Smart Materials & Structures, 2000. 9(3): p. 351-356.

204. Rittersma, Z.M., A. Splinter, A. Bodecker, and W. Benecke, *A novel surface-micromachined capacitive porous silicon humidity sensor.* Sensors and Actuators B-Chemical, 2000. 68(1-3): p. 210-217.

205. Foucaran, A., B. Sorli, et al., *Porous silicon layer coupled with thermoelectric cooler: a humidity sensor.* Sensors and Actuators a-Physical, 2000. 79(3): p. 189-193.

206. Das, J.O., S. Dey, et al., *A hygrometer comprising a porous silicon humidity sensor with phase-detection electronics.* Ieee Sensors Journal, 2003. 3(4): p. 414-420.

207. Kaltsas, G., A.A. Nassiopoulos, and A.G. Nassiopoulou, *Characterization of a silicon thermal gas-flow sensor with porous silicon thermal isolation.* Sensors Journal, IEEE, 2002. 2(5): p. 463-475.

208. Riviere, J.E., C.E. Smith, et al., *Use of methyl salicylate as a simulant to predict the percutaneous absorption of sulfur mustard.* Journal of Applied Toxicology, 2001. 21(2): p. 91-99.

209. Minco (2005) *Estimating Power Requirements of Etched-Foil Heaters*. Volume,

210. Casanova, F., C.E. Chiang, et al., *Gas adsorption and capillary condensation in nanoporous alumina films.* Nanotechnology, 2008. 19(31).

211. Yaws, C.L., *Chemical Properties Handbook*. 1999, McGraw-Hill.

212. Salem, M.S., M.J. Sailor, T. Sakka, and Y.H. Ogata, *Electrochemical preparation of a rugate filter in silicon and its deviation from the ideal structure.* Journal of Applied Physics, 2007. 101(6): p. 063503-6.

213. Della Corte, F.G., M.E. Montefusco, et al., *Temperature dependence analysis of the thermo-optic effect in silicon by single and double oscillator models.* Journal of Applied Physics, 2000. 88(12): p. 7115-7119.

214. Cocorullo, G., F.G. Della Corte, and I. Rendina, *Temperature dependence of the thermo-optic coefficient in crystalline silicon between room temperature and 550 K at the wavelength of 1523 nm.* Applied Physics Letters, 1999. 74(22): p. 3338-3340.

215. Jellison, G.E. and H.H. Burke, *The Temperature Dependence of the Refractive Index of Silicon at Elevated Temperatures at Several Laser Wavelengths.* Journal of Applied Physics, 1986. 60(2): p. 841-843.

216. Li, H.H., *Refractive Index of Silicon and Germanium and its Wavelength and Temperature Derivatives.* Journal of Physical and Chemical Reference Data, 1980. 9(3): p. 561-658.

217. Toyoda, T. and M. Yabe, *The Temperature Dependence of the Refractive Indexes of Fused Silica and Crystal Quartz.* Journal of Physics D-Applied Physics, 1983. 16(5): p. L97-L100.

218. Palik, E.D., *Handbook of Optical Constants of Solids*, Elsevier.

219. Sze, S.M., *Semiconductor Devices*. 2002, New York: John Wiley & Sons.

220. *SCHOTT Optical Glass Data Sheets*. 2009.

221. Weiss, S.M., M. Molinari, and P.M. Fauchet, *Temperature stability for silicon-based photonic band-gap structures.* Applied Physics Letters, 2003. 83(10): p. 1980-1982.

222. White, G.K., *Thermal Expansion of Reference Materials: Copper, Silica, and Silicon.* Journal of Physics D-Applied Physics, 1973. 6(17): p. 2070-2078.

223. Lhomme, F., C. Caucheteur, et al., *Synthesis of fiber Bragg grating parameters from experimental reflectivity: a simplex approach and its application to the determination of temperature-dependent properties.* Applied Optics, 2005. 44(4): p. 493-497.

224. Jellison, G.E. and F.A. Modine, *Optical Functions of Silicon Between 1.7 and 4.7 EV at Elevated Temperatures.* Physical Review B, 1983. 27(12): p. 7466-7472.

225. Bach, H. and N. Neuroth, *The Properties of Optical Glasses*. 1998, Berlin: Springer-Verlag.

226. Socrates, G., *Infrared and Raman Characteristic Group Frequencies: Tables and Charts.* 3rd ed. 2001, New York: John Wiley & Sons, Ltd.

227. Varghese, H.T., C.Y. Panicker, et al., *IR, Raman and SERS studies of methyl salicylate.* Spectrochimica Acta Part a-Molecular and Biomolecular Spectroscopy, 2007. 66(4-5): p. 959-963.

228. Casanova, F., C.E. Chiang, et al., *Effect of surface interactions on the hysteresis of capillary condensation in nanopores.* Epl, 2008. 81(2).

229. Semancik, S. and R. Cavicchi, *Kinetically controlled chemical sensing using micromachined structures.* Accounts of Chemical Research, 1998. 31(5): p. 279-287.

230. Mizukami, M. and K. Kurihara, *Hydrogen-bonded macrocluster formation of 1-propanol and 2-propanol on silica surfaces.* Australian Journal of Chemistry, 2003. 56(10): p. 1071-1080.

231. Adamson, A.W. and A.P. Gast, *Physical Chemistry of Surfaces*. 1997, New York: John Wiley & Sons.

232. Bandosz, T.J., *Analysis of silica surface heterogeneity using butane and butene adsorption data.* Journal of Colloid and Interface Science, 1997. 193(1): p. 127-131.

233. Schenk, M., B. Smit, T.L.M. Maesen, and T.J.H. Vlugt, *Molecular simulations of the adsorption of cycloalkanes in MFI-type silica.* Physical Chemistry Chemical Physics, 2005. 7(13): p. 2622-2628.

234. Fox, J.P. and S.P. Bates, *Simulating the adsorption of binary and ternary mixtures of linear, branched, and cyclic alkanes in zeolites.* Journal of Physical Chemistry B, 2004. 108(44): p. 17136-17142.

235. Choi, J.G., D.D. Do, and H.D. Do, *Surface diffusion of adsorbed molecules in porous media: Monolayer, multilayer, and capillary condensation regimes.* Industrial & Engineering Chemistry Research, 2001. 40(19): p. 4005-4031.

236. Gusev, V.Y., *Hysteresis thermodynamics of capillary condensation in mesopores.* Journal of Colloid and Interface Science, 1997. 194(1): p. 256-259.

237. Yortsos, Y.C. and K.S. Athanassios, *Phase change in porous media.* Current Opinion in Colloid & Interface Science, 2001. 6(3): p. 208-216.

238. May, G.S. and S.M. Sze, *Fundamentals of Semiconductor Fabrication*. 2003, New York: John Wiley & Sons.

239. Heuberger, M., M. Zach, and N.D. Spencer, *Density fluctuations under confinement: When is a fluid not a fluid?* Science, 2001. 292(5518): p. 905-908.

240. Janshoff, A., K.P.S. Dancil, et al., *Macroporous p-type silicon Fabry-Perot layers. Fabrication, characterization, and applications in biosensing.* Journal of the American Chemical Society, 1998. 120(46): p. 12108-12116.

241. Martin, P.E. and E.F. Barker, *The infrared absorption spectrum of carbon dioxide.* Physical Review, 1932. 41(3): p. 291-303.

242. Herman, R.C., *Vibrational Energy Levels of the Carbon Dioxide Molecule.* Astrophysical Journal, 1948. 107(3): p. 386-388.

243. Zeninari, V., A. Vicet, et al., *In situ sensing of atmospheric CO2 with laser diodes near 2.05 mu m: a spectroscopic study.* Infrared Physics & Technology, 2004. 45(3): p. 229-237.

244. Soderstrom, M.T. and R.A. Ketola, *Identification of Nerve Agents and Their Homologs and Dialkyl Methylphosphonates by Gas-Chromatography-Fourier-Transform Infrared Spectrometry (GC-FTIR) .1. Spectral Interpretation.* Fresenius Journal of Analytical Chemistry, 1994. 350(3): p. 162-167.

245. Braue, E.H. and M.G. Pannella, *FT-IR Analysis of Chemical Warfare Agents.* Mikrochimica Acta, 1988. 1(1-6): p. 11-16.

246. Deubel, M., G. Von Freymann, et al., *Direct laser writing of three-dimensional photonic-crystal templates for telecommunications.* Nature Materials, 2004. 3(7): p. 444-447.

247. Chapron, J., S.A. Alekseev, et al., *Analysis of interaction between chemical agents and porous Si nanostructures using optical sensing properties of infra-red Rugate filters.* Sensors and Actuators B-Chemical, 2007. 120(2): p. 706-711.

248. Shao, L.M., C.W. Roske, and P.R. Griffiths, *Detection of chemical agents in the atmosphere by open-path FT-IR spectroscopy under conditions of background interference: I. High-frequency flashes.* Analytical and Bioanalytical Chemistry. 397(4): p. 1511-1519.

249. Tahtouh, M., J.R. Kalman, et al., *The detection and enhancement of latent fingermarks using infrared chemical imaging.* Journal of Forensic Sciences, 2005. 50(1): p. 64-72.

250. Sando, G. and J. Dubois, *"Seeing" the chemicals in pharmaceutical tablets with NIR chemical imaging.* Chimica Oggi-Chemistry Today. 28(1): p. 40-42.

251. Goetz, A.F.H. and B. Curtiss, *Hyperspectral imaging of the Earth: Remote analytical chemistry in an uncontrolled environment.* Field Analytical Chemistry and Technology, 1996. 1(2): p. 67-76.

252. Dsouza, A.I., L.C. Dawson, et al., *VSWIR to VLWIR MBE grown HgCdTe material and detectors for remote sensing applications.* Journal of Electronic Materials, 1997. 26(6): p. 656-661.

253. Rogalski, A., J. Antoszewski, and L. Faraone, *Third-generation infrared photodetector arrays.* Journal of Applied Physics, 2009. 105(9): p. 44.

254. Stiff-Roberts, A.D., *Quantum-dot infrared photodetectors: a review.* Journal of Nanophotonics, 2009. 3: p. 17.

255. Gunapala, S.D., S.V. Bandara, et al., *Demonstration of Megapixel Dual-Band QWIP Focal Plane Array.* Ieee Journal of Quantum Electronics. 46(2): p. 285-293.

256. Xu, J.M. *Highly ordered carbon nanotube arrays and IR detection*. 2001.

257. Ilyas, S., T. Bocking, et al., *Porous silicon based narrow line-width rugate filters.* Optical Materials, 2007. 29(6): p. 619-622.

258. James P. Lodge, J., Ed., *Methods of air sampling and analysis*. 3rd ed. 1988, New York: Lewis Publishers.

259. Kolodner, M.A., *Automated target detection system for hyperspectral imaging sensors.* Applied Optics, 2008. 47(28): p. F61-F70.

260. Katari, S., M. Wallack, et al., *Fabrication and evaluation of a near-infrared hyperspectral imaging system.* Journal of Microscopy-Oxford, 2009. 236(1): p. 11-17.

261. Fischer, M. and C.D. Tran, *Investigation of solid phase peptide synthesis by the near-infrared multispectral imaging technique: A detection method for combinatorial chemistry.* Analytical Chemistry, 1999. 71(13): p. 2255-2261.

262. Woodfin, R.L., *Trace Chemical Sensing of Explosives*. 2007, Hoboken: John Wiley & Sons.

263. Brauns, E.B. and R.B. Dyer, *Fourier transform hyperspectral visible imaging and the nondestructive analysis of potentially fraudulent documents.* Applied Spectroscopy, 2006. 60(8): p. 833-840.

264. Johnson, T.J., *Methods and systems for remote detection of gases*, USPTO, Editor. 2007, Battelle Memorial Institute: United States.

265. Flanigan, D.F., *System and method for remote detection of hazardous vapors and aerosols*, USPTO, Editor. 2001, The United States of America as represented by the Secretary of the Army: United States.

266. Verly, P.G., J.A. Dobrowolski, W.J. Wild, and R.L. Burton, *Synthesis of High Rejection Filters with the Fourier-Transform Method.* Applied Optics, 1989. 28(14): p. 2864-2875.

267. Verly, P.G., *Hybrid approach for rugate filter design.* Applied Optics, 2008. 47(13): p. C172-C178.

268. Bovard, B.G., *Rugate Filter Theory - an Overview.* Applied Optics, 1993. 32(28): p. 5427-5442.

269. Zourob, M., S. Elwary, and A. Turner, *Principles of Bacterial Detection: Biosensors, Recognition Receptors and Microsystems*. 2008, New York: Springer.

270. Rosen, D.L., C. Sharpless, and L.B. McGown, *Bacterial spore detection and determination by use of terbium dipicolinate photoluminescence.* Analytical Chemistry, 1997. 69(6): p. 1082-1085.

271. Pellegrino, P.M., N.F. Fell, D.L. Rosen, and J.B. Gillespie, *Bacterial endospore detection using terbium dipicolinate photoluminescence in the presence of chemical and biological materials.* Analytical Chemistry, 1998. 70(9): p. 1755-1760.

272. Sheppard, C.J.R., *Approximate calculation of the reflection coefficient from a stratified medium.* Pure and Applied Optics: Journal of the European Optical Society Part A, 1995. 4(5): p. 665.

273. Aguayo-Rios, F., F. Villa-Villa, and J.A. Gaspar-Armenta, *Dichroic rugate filters.* Applied Optics, 2006. 45(3): p. 495-500.

274. *Mineral Commodity Summaries 2010*. United States Geological Survey. 2010: U.S. Government Printing Office, GPO Stock #024-004-02576-0.

275. Varghese, O.K., D. Gong, et al., *Ammonia Detection Using Nanoporous Alumina Resistive and Surface Acoustic Wave Sensors.* Sens. Actuators B, 2003. 94: p. 27-35.

276. Ming, C., T. Tian-Tong, and L. Cheng-Lao, *New technique for in-situ measurement of ammonia distribution in industrial combustion systems.* Waste Management & Research, 2002. 20: p. 382-385.

277. Bozoki, Z., A. Mohacsi, et al., *Near-Infrared Diode Laser Based Spectroscopic Detection of Ammonia: A Comparative Study of Photoacoustic and Direct Optical Absorption Methods.* Applied Spectrocopy, 2002. 56(6): p. 715.

278. Gulino, A., P. Mineo, et al., *Optical pH Meter by Means of a Porphyrin Monolayer Covalently Assembled on a Molecularly Engineered Silica Surface.* Chemistry of Materials, 2005. 17(16): p. 4043.

279. Galindo, F., J.C. Lima, et al., *Water/humidity and ammonia sensor, based on a polymer hydrogel matrix containing a fluorescent flavylium compound.* J. Mater Chem., 2005. 15: p. 2840-2847.

280. Chandler-Henderson, R.R., B. Sweryda-Krawiec, and J.L. Coffer, *Steric Considerations In The Amine-Induced Quenching Of Luminescent Porous Silicon.* J. Phys. Chem., 1995. 99(21): p. 8851-8855.

281. Sweryda-Krawiec, B., J.L. Coffer, and S. Gancopadhahay, *Time-resolved spectroscopic studies of the photoluminescence of nanoporous silicon: Effects of Lewis acid/base exposure.* J. Cluster Sci., 2002. 13(4): p. 637-645.

282. Chun, J.K.M., A.B. Bocarsly, et al., *Proton Gated Emission from Porous Silicon.* J. Am. Chem. Soc., 1993. 115: p. 3024-3025.

283. Kelly, M.T., J.K.M. Chun, and A.B. Bocarsly, *General Bronsted acid behavior of porous silicon: A mechanistic evaluation of proton-gated quenching of photoemission from oxide-coated porous silicon.* J. Phys. Chem. B, 1997. 101(14): p. 2702-2708.

284. Holtz, J.H. and S.A. Asher, *Polymerized colloidal crystal hydrogel films as intelligent chemical sensing materials.* Nature, 1997. 389(6653): p. 829-32.

285. Lee, K. and S.A. Asher, *Photonic Crystal Chemical Sensors: pH and Ionic Strength.* J. Am. Chem. Soc., 2000. 122(39): p. 9534-9537.

286. Reese, C.E., M.E. Baltusavich, J.P. Keim, and S.A. Asher, *Development of an intelligent polymerized crystalline colloidal array colorimetric reagent.* Anal. Chem., 2001. 73(21): p. 5038-5042.

287. G. Pan, R.K., and S. A. Asher, *Optically Nonlinear Bragg Diffracting Nanosecond Optical Switches.* Physical Review Letters, 1997. 78: p. 3860-3863.

288. Schechter, I., M. Ben-Chorin, and A. Kux, *Gas Sensing Properties of Porous Si.* Anal. Chem., 1995. 67(20): p. 3727-3732.

289. Zangooie, S., R. Bjorklund, and H. Arwin, *Vapor sensitivity of thin porous silicon layers.* Sens. Actuators B, 1997. 43(1-3): p. 168-174.

290. Barillaro, G., A. Nannini, and F. Pieri, *APSFET: a new, porous silicon-based gas sensing device.* Sens. Actuators B, 2003. 93(1-3): p. 263-270.

291. Pacholski, C., C. Yu, et al., *Reflective Interferometric Fourier Transform Spectroscopy: A Self-Compensating Label-Free Immunosensor Using Double-layers of Porous SiO2.* J. Am. Chem. Soc., 2006. 128: p. 4250-4252.

292. Clegg, S.L. and P. Brimblecombe, *Solubility of Ammonia in Pure Aqueous and Multicomponent Solutions.* J. Phys. Chem., 1989. 93: p. 7237-7248.

293. Perry, R., *Perry's Chemical Engineers' Handbook.* 1997, New York: McGraw-Hill.

294. Thomas, S.W., J.P. Amara, R.E. Bjork, and T.M. Swager, *Amplifying fluorescent polymer sensors for the explosives taggant 2,3-dimethyl-2,3-dinitrobutane (DMNB).* Chem. Commun., 2005(36): p. 4572-4574.

295. Zhang, S.W. and T.M. Swager, *Fluorescent detection of chemical warfare agents: Functional group specific ratiometric chemosensors.* J. Am. Chem. Soc., 2003. 125(12): p. 3420-3421.

296. Rakow, N.A., A. Sen, et al., *Molecular recognition and discrimination of amines with a colorimetric array.* Angew. Chem.-Int. Edit., 2005. 44(29): p. 4528-4532.

297. Suslick, K.S., N.A. Rakow, and A. Sen, *Colorimetric sensor arrays for molecular recognition.* Tetrahedron, 2004. 60(49): p. 11133-11138.

298. Wun, A.W., P.T. Snee, et al., *Non-linear transduction strategies for chemo/biosensing on small length scales.* J. Mater. Chem., 2005. 15(27-28): p. 2697-2706.

299. *Homeland Security and the Private Sector*. 2004, Washington, D. C.: Publication of the Congressional Budget Office, Congress of the United States

300. *Homeland Security: Federal and Industry Efforts are Addressing Security Issues at Chemical Facilities, but Additional Action is Needed*. 2005: Publication #GAO-05-631T, United States Government Accountability Office.

301. Kirkland, L.E., K.C. Herr, and J.W. Salisbury, *Thermal Infrared Spectral band Detection Limits of Unidentified Surface Materials.* Applied Optics, 2001.

302. Desurvire, E., *Global Telecommunications*. 2004, Hoboken, NJ: John Wiley & Sons.

303. Homola, J., *Present and future of surface plasmon resonance biosensors.* Anal. Bioanal. Chem., 2003. 377: p. 528-539.

304. Jacob, D.J., *Introduction to Atmospheric Chemistry*. 1999, Princeton: Princeton University Press.

305. Fuertes, M.C., S. Colodrero, et al., *Sorption properties of mesoporous multilayer thin films.* Journal of Physical Chemistry C, 2008. 112(9): p. 3157-3163.